MODELING AND MONITORING OF THE DYNAMIC RESPONSE OF
RAILROAD BRIDGES USING WIRELESS SMART SENSORS

BY

ROBIN EUNJU KIM

DISSERTATION

Submitted in partial fulfillment of the requirements
for the degree of Doctor of Philosophy in Civil Engineering
in the Graduate College of the
University of Illinois at Urbana-Champaign, 2015

Urbana, Illinois

Doctoral Committee:

      Professor Billie F. Spencer, Jr., Chair
      Professor Gul Agha
      Professor Larry Fahnestock
      Professor Tomonori Nagayama, The University of Tokyo

ABSTRACT

Railroad bridges form an integral part of railway infrastructure in the USA, carrying approximately 40 % of the ton-miles of freight. The US Department of Transportation (DOT) forecasts current rail tonnage to increase up to 88 % by 2035. Within the railway network, a bridge occurs every 1.4 miles of track, on average, making them critical elements. In an effort to accommodate safely the need for increased load carrying capacity, the Federal Railroad Association (FRA) announced a regulation in 2010 that the bridge owners must conduct and report annual inspection of all the bridges. Until now, visual inspection has been the most prevalent practice in monitoring this infrastructure, although high-cost and unreliability can limit the efficiency and accuracy of such assessments. With recent advances in sensing technology, structural health monitoring can be a promising solution for providing a reliable and inexpensive ways for assessing the bridges. Nonetheless, because damage is a local phenomenon, to be able to detect/ monitor existing/potential damage, densely deployed sensors are required, which can be inefficient and still expensive. Alternatively, model-based monitoring strategies can help identifying critical elements using fewer sensors, utilizing a numerical model that has been calibrated with measured field data. Such approaches have been adopted and applied for highway bridges, while railroad bridges have received comparably less attention. The main reason for the limited number of studies is due, in part, to fundamental differences between the loading being applied to highway bridges and railroad bridges. Usually, the mass of the vehicles crossing highway bridges is assumed to be relatively small compared to the mass of the bridge itself; as a result, the mass of the vehicles are often neglected in the problem. In contrast, the mass of a train crossing a railroad bridge can be as large as the mass of the bridge itself. Moreover, trains are typically composed of an engine, followed by multiple cars resulting in a nearly deterministic

moving mass/load being applied to the bridge. As a consequence, numerous models have been developed to understand the dynamic response of bridges under in-service train loads, but most fail to provide a simple, yet flexible, representation of the salient features of the responses of the bridge.

The objective of this research is to develop appropriate modeling and monitoring techniques for railroad bridges toward understanding the dynamic responses under a moving train. To achieve the research objective, the following issues are considered specifically. For modeling, a simple, yet effective, model is developed to capture salient features of the bridge responses under a moving train. A new hybrid model is then proposed, which is a flexible and efficient tool for estimating bridge responses for arbitrary train configurations and speeds. For monitoring, measured field data is used to validate the performance of the numerical model. Further, interpretation of the proposed models showed that those models are efficient tools for predicting response of the bridge, such as fatigue and resonance. Finally, fundamental software, hardware, and algorithm components are developed for providing synchronized sensing for geographically distributed networks, as can be found in railroad bridges. The results of this research successfully demonstrate the potentials of using wirelessly measured data to perform model development and calibration that will lead to better understanding the dynamic responses of railroad bridges and to provide an effective tool for prediction of bridge response for arbitrary train configurations and speeds.

ACKNOWLEDGMENTS

First and foremost, I would like to express my sincere gratitude and respect to my advisor, Professor Billie F. Spencer Jr., for his advice on my research as well as his support in my life. Sending him the first email on 28th of April 2009 to show my interest in his research laboratory is one of the best things I've done in my life. He is my ultimate mentor and was very fortunate to learn how he handles his research, colleagues, students, as well as his life and family. So much of me as a researcher is made from what I learned from him.

I would also like to thank my committee members, Professor Gul Agha, Professor Larry Fahnestock, and Professor Tomonori Nagayama. Their advice and comments on my research have improved my dissertation significantly.

I appreciate Professor Yozo Fujino and Professor Tomonori Nagayama for their hospitality while I was a visiting scholar in their research laboratory at the University of Tokyo for twelve weeks. Professor Fujino and Professor Nagayama gave me lifelong memories in Japan,

In the first several years in my Ph.D., I was very fortunate to engage myself in various projects for implementing full-scale monitoring systems, including the Jindo Bridge project. I would like to express special gratitude to our team members, a.k.a. the 'Korean Mafia'; Sung-Han Sim, Hongki Jo, and Shinae Jang for their sincere advice and Kirill Mechitov, for his intelligence in helping me to resolve critical issues. I truly enjoyed our sleepless nights in B119, preparing enclosures for the Jindo Bridge deployment!

During my time at UIUC, I have met and worked with many exceptional people in the Smart Structures Technology Laboratory (SSTL). I would like to thank them for their friendship, support, and advice: Brian Phillips, Jian Li, Chia-Ming Chang, Ryan Giles, Lauren Linderman, Nicholas

Wierschem, Hyung-chul Yoon, Takehiko Asai, Fangzhou Dai, Guillermo Dias-Fanas, Gaston Fermandois-Cornejo, Parya Moinzarde (a former student in Computer Science Department), Susu Lei (visiting student from the University of Science and Technology Beijing, China), and JingJing Wang. (visiting student Tongji University, China). I also would like to express thanks to Yuguang Fu, Martha Cuenca, and Zachary Treece, for their kind friendship.

Friends I met inside and outside the department were another big part of finishing Ph.D. journey. I would like to express my gratitude to friends in the Korean Student Association of Civil and Environmental Engineering (KSACEE): Dr. Moochul Shin, Dr. Sungwoo Moon, Dr. DoSoo Moon, Youngjib Ham, Kookin Han, and Donghyuck Jung. I truly enjoyed all our daily chats and big and small parties for memorable events. I also would like to thank my 'the' roommate, Sylvia Kyungmin Choi. Being a roommate with you for two years was a joy with many unforgettable good memories. I am also grateful for the unconditional friendship from my dear friends in both Korea and the United States: Dawoom Chung, Eunjung Kim, Enyoung Kim, Namhwa Song, Yeowool Yoon, Lara Fling, Grace Wang, and Yi-Chin Chen. I miss you all.

Last, but not least, I thank my parents, parents-in-law, sister, and brother for their love, support, and prayers. Most of all, I would like to deliver my sincere gratitude to my husband, Sunkyu Kim. His unbounded love and understanding made me strong, allowing me to get through the rough times and complete my Ph.D.

Table of Contents

CHAPTER 1. INTRODUCTION

1.1. Motivation

Railroads have been an important part of the transportation network for over 150 years in the United States (US). The freight rail industry has been the fastest growing segment since 1980, accounting approximately 40 percent of the total freight tonnage moved nationwide (FRA, 2010). Due to continuous growth in freight demand, the Association of American Railroad forecasts that rail lines exceeding their capacity will increase from 108 miles today to nearly 16,000 miles by 2035 (AAR, 2007). In an effort to accommodate safely the expected increase in the demand, the private US freight railroads have been emphasizing maintenance of their infrastructure, by organizing the majority of their revenue to ensure or to maintain the good state of their network. To date, as much as 15 to 20 percent of their total capital is used to enhance/maintain the railroad capacity (FRA, 2010). Thus, research to assess the health of such infrastructure is of great importance.

Amongst railroad networks, bridges form a critical link. According to the Federal Railroad Administration (FRA) documents in 2002, the U.S. railroad network contained an average of one bridge for every 1.4 miles of track (FRA, 2002). Ensuring good condition for those bridges is important, because they are the most expensive components of railroad networks; replacement and construction of railroad bridges can cost from 11 to 550 times more per linear foot than regular track (GAO, 2007). At the same time, bridges are susceptible for severe wear or deterioration when the structures age and serve heavier traffic than their original design to meet the increased demands. Thus, to accommodate increased axle loads, train speeds, and greater volume of freight traffic associated with predicted increases in network demand, the load carrying capacity and serviceability of existing bridges must be assessed.

The FRA recently mandated annual inspection of all bridges in the network; visual inspection has been the most prevalent method to meet this requirements. However, the high-cost and unreliability nature of visual inspections can limit the use of the approach to a full-scale bridge. With the recent advances in sensing technology, structural health monitoring (SHM) has shown promising potential of inspecting a bridge with reduced cost. However, because damage is a local phenomenon, examining a full-scale bridge employing a densely distributed sensor network is critical; this requirement can still result in high costs for inspection and can be inefficient. Thus, a practical approach that can enable monitoring/detecting any existing/potential damage of a bridge is still lacking.

Alternatively, model-based structural health monitoring (SHM) can be employed to assess the state bridge infrastructure. In the case of highway bridges, where the mass of the vehicles crossing highway bridges is assumed to be relatively small compared to the mass of the bridge itself, the vehicles can often be treated as random loads on the bridge (i.e., neglecting the mass of the vehicles in the problem), or even ambient vibration. This assumption allows for application of a wide variety of simulations for predicting bridge responses under a certain circumstances. However, these methods cannot be applied directly to railroad bridges, because the mass of train is of the same order of magnitude as the mass of the bridge.

The primary load on the railroad bridges is the train; thus, the effect of the train mass cannot be neglected in assessing the capacity of a railroad bridge. As a consequence, the resulting problem is time-dependent and coupled; developing adequate models is a challenging task. Although numerous models have been proposed, most fail to provide a simple, yet flexible, representation of the salient features of the responses of the train, bridge, and track.

1.2. Overview of dissertation

The objective of this research is to develop appropriate modeling and monitoring techniques for railroad bridges toward understanding the dynamic responses under a moving train. The effort is comprised of five distinct research tasks; (1) development of a simple model which can capture salient features of the bridge under a moving train; (2) development of a flexible and efficient hybrid model for estimating bridge responses under arbitrary train configurations and speeds; (3) use a monitoring system to evaluate the performance of numerical models and improve safety of critical structures; (4) interpret predictive capability of the numerical model to enhance the maintainability of a critical bridges; and (5) develop hardware and software components for creating geographically distributed monitoring systems. The results of this research will be the realization of model-based monitoring for railroad bridges that overcomes the challenges posed by lack of an appropriate numerical model and framework that supports the system.

Chapter 2 provides the background of this research, including an overview of existing numerical models of railroad bridges, historical SHM systems, WSSs, and SHM applications on railroad bridges.

Chapter 3 presents formulation of a traditional beam model and a new hybrid models for dynamics analyses of the bridge. A simple beam model of a bridge is first presented using the assumed modes method. An example of the model is devised to demonstrate the effects of vehicle mass on the dynamic response of the bridge. Then, a hybrid model is developed, which interconnects an FE model and an assumed mode model to represent bridge-track interaction. The model can be applied both for a single-track and double-track bridges. Having the bridge responses as the major interests, vehicles are simplified to a series of moving point masses, with the locations of the masses are determined by the train wheel distances. The performance of the simple and hybrid models are validated in the subsequent two chapters.

Chapter 4 describes the monitoring of a railroad bridge, the data from which was used for validation and calibration of a numerical model. A set of WSSs that is suitable for both campaign-type and long-term monitoring service were deployed on a steel truss railroad bridge, the Calumet Bridge, located near Chicago, IL. A careful selection of sensor locations to ensure collection of high-fidelity response data is also presented. From the campaign type system, inputs and outputs of the structure were collected, and examples of those measurements provided. The long-term monitoring service, which was for over a year in duration, demonstrated that the current system can promise a sustainable long-term SHM system producing a rich collection of measurements. Such a database allowed understanding the state of the bridge through system identification. Subsequently, a preliminary FE model of the Calumet Bridge, based on the original drawings is developed, which is then updated using measured data. To validate the updated FE model, an output-only system identification method, peak-picking algorithm, is applied to extract fundamental characteristics of the bridge and compared with the model, i.e. natural frequencies and mode shapes. Using the calibrated FE model, validation of the hybrid model and the simple beam model of the Calumet Bridge are presented. The dynamic analyses of those models are compared with measured field data to demonstrate that the developed models are well calibrated, not only in global sense, but also at the element level of the truss bridge.

Chapter 5 demonstrates that the proposed models are efficient tools for predicting the response of the bridge under undesirable and local phenomena. In the first part of the chapter, the strain response is investigated. Understanding the strain at an element level is important, because high strains can result in fatigue failures, which is one of the most critical issues in steel bridges. The strain map based on dynamic analyses of the hybrid model is generated for the entire bridge under in-service train loads, and used to locate the maximum stresses/strain at arbitrary locations on the bridge. Then, the second part of the chapter performs the resonance study of the bridge for predicting the

critical speeds of a train. Results from moving mass, load, and simple beam models are compared to highlight the effects of mass in predicting critical speeds. The results demonstrate that the proposed models are highly efficient tools for assessing the bridge response under arbitrary train loads and speeds. Studies presented in this chapter promise the potentials of understanding railroad bridge dynamics using the calibrated models.

Achievements from the previous Chapters open questions in utilizing WSSs for capturing the vehicle-track-bridge interaction, which is one of the key issues for characterizing bridge responses under high-speed passenger trains, as well as the train response. Some critical challenges of current wireless sensing technologies and solutions for enabling monitoring railroad bridges are discussed in the next two chapters.

Chapter 6 develops a new synchronization strategy, which can achieve high-accuracy synchronized sensing in geographically distributed WSS networks for extended sensing events. The method combines hardware- and software-based methods to achieve the necessary accuracy in an efficient manner. The Coordinated Universal Time (UTC) information and the Pulse-Per-Second (PPS) signal provided by low-cost GPS receivers are employed. The protocol has been implemented and verified on the Imote2 sensor platform, showing high-accuracy and long-term synchronized sensing performance for an arbitrary number of sensor nodes. This new synchronization algorithm shows potential of obtaining highly synchronized input loads and output responses for railroad bridges by forming two networks, one on the bridge and the other on a train approaching the bridge.

Chapter 7 proposes a new approach to assess the reliability of the WSS networks for monitoring structures. The chapter first illustrates the failure-prone nature of WSSs, which cannot be expressed with communication-level reliability. The traditional communication-level reliability uses temporal state of the sensors. To meet the needs of the SHM systems, that often require a large amount of data transfer, application-level reliability, which can assess the network quality based on

the completion of a task, should be considered. The proposed model uses readily available communication-level indicators such as radio signal strength and link quality indicators to determine the reliability of an application. To estimate the probability of failure, first-order reliability methods and Monte Carlo simulation are used. Due to its simplicity, the proposed approach will inform future applications for monitoring railroad bridges, by optimizing sensor topology in the SHM system design-phase and enhancing data collection strategies to deliver robust and reliable performance of WSS networks.

Finally, Chapter 8 summarizes the research in the dissertation and presents possible direction for future research on understanding railroad bridge dynamics using WSSs.

CHAPTER 2. LITERATURE REVIEW

This chapter describes literature related to the proposed research in this thesis. Topics covered include; numerical models for railroad bridges; structural health monitoring (SHM), wireless smart sensors (WSSs), SHM monitoring systems on railroad bridges. Literature review begins with introducing numerical models that has been developed for understanding railroad bridge dynamics. Introduction and chronological overview of SHM systems (i.e., from traditional wired sensor systems to recent wireless smart sensor network (WSSN) systems) are followed. Then, a brief introduction to the Illinois Structural Health Monitoring Project (ISHMP) Toolsuites, which is a WSSN system developed for monitoring civil infrastructure is presented. Examples of wired and wireless SHM systems that have been implemented is discussed followed by a review of SHM systems of railroad bridges in real practice. Some limitations of the current WSSN systems that prohibit realization of monitoring systems are listed. The goal of this chapter is to identify gaps in knowledge that need to be filled to achieve an effective understanding of dynamic behaviors of railroad bridges.

2.1. Railroad bridge dynamics

Having the primary load on the railroad bridges as the train, understanding railroad bridge dynamics are challenging. The problem is time-dependent, coupled, and nonlinear. Initial motivation in railroad bridge dynamics arose from the collapse of the Chester Rail Bridge, in 1847. Willis (1849) was the pioneer who first published an approximate solution for a load moving over a beam in 1849. Afterwards, the equation was solved by Stokes in 1896 using differential equations (Stokes, 1896). Timoshenko (1922) contributed greatly to solving the bridge vibration problem by deriving a number of approximate solutions under harmonic excitation. Similar work was done thereafter by numerous researchers including Jeefcot (1929), Ayre et al. (1950), Vellozzi (1967), Wen (1960), and Frýba

(1973). However, earlier work neglected the mass of the vehicle or concentrated mostly on the response of the bridge. Such approaches are efficiently applicable to highway bridges, while the bridge and vehicle response of railroad bridges needs to be considered differently from that of highway bridges for the following reasons.

- Moving vehicle loads are repetitive in railroad bridges. Sequential load is generated from the wheel loads of the train implying that a certain frequency of excitation is exerted on the bridge. Random excitation cannot be applied on a vehicle-bridge interaction problem for a railroad bridge unlike for a highway bridge.

- The speed of the vehicle is higher in railroad bridges. Depending on the track condition, the speed of a train can be as high as 100 MPH. Moreover, attention on the replacement of existing passenger railways with a high-speed railway system has been addressed by the government. High-speed trains have a higher risk of exciting the fundamental frequency of a bridge resulting in the resonance phenomenon. Such problems are rarely observed in highway bridges.

- The mass ratio of a bridge to the vehicle is higher in railroad bridges. Railroad bridges are usually narrower than highway bridges. At the same time, trains consist of a number of cars containing heavier freight. This problem cannot be ignored, because of the recent increasing trend of freight loadings within the past 20 years. Thus, interaction between a moving train and a railroad bridge may be stronger than that of a moving vehicle on a highway bridge.

- The existence of a track system affects the vehicle and bridge dynamics. In a railroad bridge, force is transmitted from the vehicle to the bridge through the track system, which consists of rail, sleepers, and ballast layers. The track system usually provides softer stiffness than the stiffness of a bridge, and may magnify or minimize the response of the vehicle and the bridge.

8

Therefore, when modeling a railroad bridge, mass effects must be considered. In the following sections, a review of numerical models for vehicle, bridge, and track is provided. Then the parametric study of affecting railroad bridge dynamics will be discussed. Finally, experiments which utilized vehicle-bridge interaction will be discussed.

2.1.1. Numerical models

Early efforts to understand the dynamic responses of bridges under train loads modeled the train as a point load and represented the bridge as a simple Euler-Bernoulli beam (see Figure 1). Stokes (1849) and Willis (1849) were the first to explore this problem. They considered a beam traversed by a single load, which the mass of the beam is negligible compared to the moving load. Subsequently, Timoshenko (1922) studied the case when the moving mass is negligibly small, compared to the mass of the beam. Ayre et al. (1950) and Ayre and Jacobsen (1950) adopted a similar approach to derive exact solutions for the resulting partial differential equations of a symmetric two-span beam under a moving-load at a constant speed. Other variations of the original approach include studies by Jeffcott (1929), Lowan (1935), and Inglis (1934). They proposed analytical solutions for simplified and fundamental problems, with some variations on the elastic foundation and a moving force. This work provided the foundation for an extensive body of subsequent research.

Figure 1. Beam model under a constant moving force.
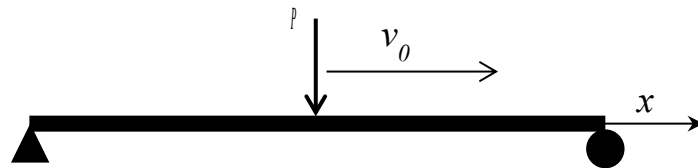
Researchers have explored solutions to multiple moving loads to simulate trains with multiple cars for single-span and multi-span beams. Numerous contributions have been made, including Sridharan and Mallik (1979), Gbadeyan and Oni (1995), Zheng et al. (1998), Rao (2000), and Dugush and Eisenberger (2002). Because moving-load models do not consider the inertia effect

9

of the moving vehicle, those approaches are valid only when the mass of the vehicle is small relative to the mass of the bridge; such models are not sufficient for understanding bridges carrying freight trains, because the mass of a train is comparable to that of the bridge and cannot be neglected.

To overcome this limitation, researchers developed moving-mass models to represent the train/bridge system, with various solutions being proposed. For example, Jeffcott (1929) adopted the method of successive approximations; Stanišić (1985) derived closed form solutions, given by means of an expansion of the eigenfunctions in a series; and Lee (1996) adopted an assumed mode methods. Stanišić and Hardin (1969) examined a series of masses moving on a beam by using a Fourier series expansion. Later, mass representations that are more complicated were developed to include vehicle dynamics (e.g., Biggs, 1964; Yang et al. 1999; Pesterev et al. 2001 and 2003; Siringoringo and Fujino, 2012). Comparing solutions from simple moving mass, moving oscillator, and moving rigid body problem, Yang et al. (2004) demonstrated that the complexity of vehicle representation has insignificant effect to the dynamic responses of the bridge. As such, when the primary concern for monitoring railroad bridges is to assess their performance and capacity under train loadings, the moving-mass model for the train apparently is adequate.

More detailed models of a bridge using the Finite element (FE) method also have been proposed using an FE approach with various train representations being used. Wang et al. (1991) developed an FE model with condensed mass and stiffness matrix retaining vertical and lateral DOFs of the bridge only at the deck level. Yang and Yau (1997) developed an FE model with a beam-like representation to understand the dynamic responses of bridges and detailed vehicle models. Kawatani and Kim (2001) used an FE model to understand the behavior of steel plate girder bridges under moving rigid multi-body system. Zhang et al. (2010) and Wu et al. (2010) studied a three-dimensional FE model with a detailed vehicle model to gain insight into bridge responses subject to an asymmetrically moving train. However, in the FE approaches, inconsistencies in the loads that

10

were applied to the substructure can occur because time dependent and coupled features of the problem require transformation of the moving forces into discrete equivalent nodal forces..

Due to challenges of applying train loads to the substructure when an FE bridge representation is used, researchers have adopted approximate approaches to solve the problem. For example, Yang and Yau (1997) developed two sets of equations of motion, each for the vehicle and the bridge; in this work, two separate equations are solved recursively through transfer of the contact forces to the bridge. As the first step of the approach, values of displacements of the bridge system are assumed for the contact points at a time step, t. Using the assumption, contact forces are explicitly calculated from the vehicle system. Then, the forces are substituted into the subsystem, i.e. bridge and track system, to solve the displacements of the system at the next time step, $t+\varDelta t$. The procedures are iterated until the vehicle reaches to a desired exit location.

Cheng et al. (2001) and Lou (2005) adopted the concept of contact forces to derive augmented equations of motion, in which the track-bridge-vehicle are solved concurrently in the integration procedure. To capture higher frequency components of the railroad bridge response, Luo et al. (2013) proposed combining the FE and a statistical energy analysis to model the bridge. The global and local DOFs of the bridge are partitioned, with the global equations developed using the FE method, while the local equations are derived with a set of admissible functions. Then, a four-layer track is modeled as segmented beams using the set of admissible functions for each segment, in which each length is the same as the length of an element in the FE model. The equations of motion for the two subsystems (i.e., (i) the vehicle and one-layer of track and (ii) three-layer of track and bridge models) are solved separately using the Newmark-β approach. Although the aforementioned studies successfully captured the effect of the vibrating track system and the dynamic response of the bridge, due to computational complexities, this approach is limited to a small number of train cars with the equidistance bogies.

2.1.2. Parametric studies on railroad bridges

The interaction between vehicle, track, and bridge is a coupled, nonlinear problem. Analytical approaches to differentiate the essential factors affecting this interaction have been investigated using the aforementioned vehicle, track, and bridge models. Although highly sophisticated vehicle, track, and bridge models can be derived to represent the reality, simpler models are still favorably used to identify the key parameters governing the railroad bridge dynamics (Humar and Kashif, 1993). In this section, numerical formulations of resonance and cancellation, which are critical factors dominating bridge response, are presented. Then, the speed parameter, which is a non-dimensional property that is adopted to demonstrate the relationship between the speed of the vehicle and the responses of the bridge, is defined. Finally, a parametric review of railroad bridge is follows.

Resonance

Resonance is a phenomenon in which the inherent frequency of the force from a moving vehicle coincides with the fundamental frequencies of the bridge to amplify the bridge response. Consider a simply supported beam with a sequence of N moving loads as shown in Figure 2. Here, the moving loads are apart by d and both run over the beam at speed v. The length of the beam is L with constant young's modulus E, moment of inertia I, and cross section A. Then, with neglecting the weight of each load and the damping effect of the bridge, the equation of motion for the system can be written as below (Yang, 2004).

$$m\ddot{u}(t) + EIu''''(t) = -\sum_{j=1}^{N} p\delta\left[x - v(t - t_j)\right]\left[H(t - t_j) - H(t - t_j - L/v)\right] \tag{1}$$

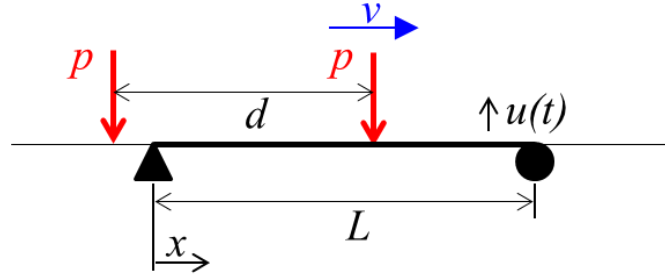where,

$$t_j = (j-1)d/v \tag{2}$$

12

Figure 2. Model of simple beam with a sequence of moving loads.

In Eqn.(1), the beam displacement $u(t)$ is positive in the upper direction, with x the coordinate of the beam. δ denotes Dirac delta function, and $H(\ )$ represents the unit step function. Thus, the j-th moving load with magnitude p will be effective at the entrance of the load at t_j until the load leaves the beam at $t_j + L/v$. Yang (2004) derived and presented the closed form solution of the response of the beam due to the moving loads as below:

$$u(x,t) = -\frac{2pL^3}{EI\pi^4}\sin\left(\frac{\pi x}{L}\right)\left[Q_1(v,t)H(t-t_N) - Q_2(v,t)H(t-t_{N-1}-\frac{L}{v})\right] \quad (3)$$

$$Q_1(v,t) = \frac{\sin\Omega_1(t-t_N) - (\Omega_1/\omega_1)\sin\omega_1(t-t_N)}{1-(\Omega_1/\omega_1)^2}, \quad (3a)$$

$$Q_2(v,t) = \frac{2(\Omega_1/\omega_1)}{1-(\Omega_1/\omega_1)^2}\cos\frac{\omega_1 L}{2v}\left[\sin\omega_1\left(t-\frac{L}{2v}\right)+\sin\omega_1\left(t-\frac{L}{2v}-\frac{t_N}{2}\right)\frac{\sin\omega_1\left(\frac{t_N}{2}-\frac{d}{2v}\right)}{\sin\frac{\omega_1 d}{2v}}\right], \quad (3b)$$

where, $\Omega_1 = \pi v/L$ represents the fundamental frequency of the moving load and ω_1 denotes that of the beam. As can be seen in Q_2, the last term become indeterminate and hence the bridge response gets maximized when $\sin(\omega_1 d/2v) = 0$. Such a phenomenon is so-called resonance of the beam under repetitive moving loads. The term Q_2 can further be organized using the relation that $t_N = (N-1)d/v$ and L'Hospital's rule (Yang, 2004).

13

$$Q_2(v,t) = 2(N-1)(\Omega_1 / \omega_1)\cos\frac{\omega_1 L}{2v}\sin\omega_1\left(t-\frac{L}{2v}\right)$$

(3c)

With the unit step function, $H(t-t_{N-1}-L/v)$, multiplied to Q_2, the bridge response will continuously accumulate until all number of loads pass the beam. Therefore, the critical car lengths that would cause the resonance are:

$$d = 2i\frac{\pi v}{\omega_1}, \qquad i = 1,2,3,...$$

(4)

Cancellation

Cancellation is another phenomenon in which the inherent frequency of the force from a moving vehicle results in the diminishment of the effects of residual effects of vehicle. As can be seen in Eqn. (3), the residual response effect arises from the unit step function, $H(t-t_{N-1}-L/v)$. The term can be eliminated when $\cos(\omega_1 L/2v) = 0$ in Eqn. (3b). When this condition is met, the response of the beam will only be subjected to the excitation of the load while it is passing the beam and all the loads that have passed will sum to zero. The cancellation conditions are:

$$\frac{\pi v}{\omega_1 L} = \frac{1}{2i-1}, \qquad i = 1,2,3...$$

(5)

Eqn. (3b) also show that cancellation conditions are more decisive than the resonance condition. The result is highly idealized due to the simplified model and assumptions such as ignoring inertial effect of the mass, suspension systems and the track system. Nevertheless, derived formulations clearly extract the impact of repetitive loading on the response of a simple beam.

Speed parameter

The speed parameter is devised to efficiently monitor the effect of vehicle speeds. The dynamic behavior of a train with a number of cars traveling over a long span bridge may be different from that over a short span bridge, even with the same speed of train. For instance, responses of train and

14

bridge are generally transient in a short span bridge, while response of the train moving over a long

bridge can reach a steady state (Wu and Yang, 2003). Moreover, as shown in the resonance and

cancellation condition in Eqns. (4) and (5), the conditions are a function of vehicle speed (v),

fundamental frequency (ω) of the bridge, and length (L). For this reason, the speed parameter, S, in

Eqn. (6). is defined as the ratio of the exciting frequency of the moving vehicle to the fundamental

frequency of the beam (Yang 2004). The speed parameter was first used by Tan and Shore in 1968

and later widely adopted by other researchers (Tan and Shore, 1968a, 19968b; Yau et al. 2001; Wang

et al. 1992).

$$S = \frac{\pi v}{\omega L} \tag{6}$$

An advantage of the speed parameter is that the parameter is dimensionless and especially

useful in expressing the interaction between the vehicle and the bridge. For instance, from a

parametric study on speed parameter, Green and Cebon (1997) showed that interaction becomes

significant as the speed parameter increases, and, when ignored, the results may be conservative in

bridge displacement responses. For highway bridges, Green and Cebon (1997) proposed a parametric

guideline of the speed parameter where the interaction should not be neglected. Moreover, Yang et al.

(1995) found that more concise relationships can be obtained if the speed parameter is used for

plotting bridge responses.

Parametric study

An overview on parametric study is provided to give a general overview of the effects of each

component in a railroad bridge; vehicle-track-bridge (VTB) system. Stiffness and damping of the

vehicle's suspension system, rail irregularities, ballast stiffness, and bridge topologies are selected as

the factors that affect VTB system. For example, damping in the vehicle's suspension system is

likely much larger than that of a bridge. Thus, when a vehicle passes along the bridge and the two

systems are combined, the net damping of the systems will be larger compared to the case when interaction is neglected. As a result, the bridge responses when considering VTB interaction will have smaller responses. Similarly, insertion of a track system in the numerical model affects the response of the interaction because the track systems act as vibration absorbers or amplifiers in the VTB system. So far, not many researchers have focused on parametric studies with interaction, but extensive research was done by Green and Cebon (1997), Wu et al. (2001), and Yang et al. (2004). Relative sensitivities of each parameter on the bridge and the vehicle responses studied by aforementioned authors are summarized in Table 1.

Table 1. An overview of parametric studies.

	Track System	Surface Irregularity	Ballast Stiffness	Vehicle Suspension System	
				Stiffness	Damping
Bridge	↓†	↑†	↓	↓	↓
Vehicle	↑↑↑†	↑↑↑†	↓↓↓†	↑↑	↑

- ↑: Slight increase in the response ;   ↓: Slight reduction in the response
- ↑↑ : Moderate increase in the response;
- ↓↓↓ : Significant reduction in the response; ↑↑↑ : Significant increase in the response
- † :Presence of resonance condition

In Table 1, an upward arrow, ↑, indicates that ignoring the property may underestimate the response, while a downward arrow, ↓, indicates that the response may have been overestimated, which also can result in a conservative decision. Generally, the interaction arising from the insertion of a track system, increase in surface irregularities, ballast stiffness or properties of the vehicle suspension system result in a slight increase or decrease in the response of the bridge. Thus, when only bridge response is of concern, a simple moving-mass model can sufficiently capture the general

16

trends of the bridge. Nonetheless, absence of a track system underestimates the bridge response and overlooks the resonance condition that may occur.

The vehicle responses, however, show great influence on the interactions from track systems. Especially, the insertion of a track system, surface irregularity with a certain wavelength, and ballast layer showed the presence of resonance on vehicle response over the speed parameter. The response of the vehicle is directly related to riding comfort and risk of derailment. Thus, when vehicle response is an important concern, track systems in the numerical model should be considered carefully to incorporate the interaction of vehicle and track.

The studies on numerical models for the VTB system indicate that each component is highly coupled to the others and time dependent. However, because the numerical models are derived with assumptions and simplifications, the models need to be updated and verified through experiments.

2.1.3. Experiment efforts on vehicle-bridge interaction system

The mobility of wireless smart sensors has made it possible to monitor the interaction dynamics of a bridge with the moving vehicle. Kim et al. (2011) established a campaign WSSN system on a 4 m long highway bridge consisting of four spans in Korea and a 20-ton truck that crosses over the bridge at 30 km/h. The instrumentation on the bridge deck included twenty uniaxial wireless accelerometers and five tactile sensors. The tactile sensors are piezoelectric strip sensors that each are interfaced to a wireless sensor and bonded on the bridge deck to identify the points in time when the truck steps on the sensor. Wireless sensors were also installed on the center of gravity of the truck to monitor vertical acceleration, horizontal acceleration, and pitching acceleration. The network was triggered as the sensors on the truck approached: The base station on the bridge sent periodic beacon signals to detect whether the sensors were within communication range (within 500 m). When truck sensors were closer and recognized, the base station started time synchronization of all wireless sensors, both

on the truck and the bridge. As soon as the base station acknowledged that sensing had been finished, it started querying data transmission. Because all data was retrieved to a base station, the truck had to stay within reachable range (within 500 m) to successfully send measurements.

The experiment results were able to reveal the existence of dynamic coupling between the bridge and the truck. From the truck response, the interaction of the vehicle with the surface roughness and bridge was identified. Two dominant bridge vibration responses formed the complex dynamic behavior of the bridge. Low-frequency responses corresponded with the global behavior of the girder, and high-frequency responses represented the member-level localized response containing interactions with the truck vibration (Kim et al. 2011). Although the proposed method showed the applicability of capturing interaction dynamics between the bridge and the moving vehicle, an intrinsic limitation exists in the system's use for a general vehicle-bridge interaction system or VTB system. The algorithm stands for a single network. That is, the boundary of the network is limited by physical distance. The selected bridge was small enough (150 m long) to be covered by a single network of wireless sensors with a 500 meter communication range. A reliable network may be hard to form with a single network system for longer bridges. Moreover, single networks bring up further issues in data collection: The truck needs to remain at a nearby location to the bridge to assure that data has been transmitted to a stationary base station on the bridge. Considering the length and operational mechanism of a train, which is usually longer and more difficult to stop within communication range, current WSSNs cannot be directly used for monitoring VTB dynamics.

Other attempts to utilize vehicle-bridge interaction dynamics has been made by other researchers. For example, extracting bridge natural frequencies using instrumented vehicles with acceleration sensors has been performed (Yang et al. 2004; Lin and Yang, 2005; Lu et al. 2012; Siringoringo and Fujino, 2012). Further, approaches utilizing the extracted information on damage detection have been studied by many researchers including Bu et al. (2006) and Zhang et al. (2012).

However, only the first natural frequency was able to be detected from the field tests and none are applicable for a train system.

2.2.   Structural health monitoring

The collapse of the Silver Bridge in 1967 resulted in the loss of 46 lives and focused attention on systematic inspection of our nation's bridge infrastructure. Nonetheless, unforeseen bridge deteriorations brought the collapse of other bridges, such as the Mianus River Bridge on Interstate 95 in Connecticut in 1983 and the Schoharie Creek Bridge in New York in 1987. Over the last few decades, much has been learned that has improved inspection technologies, giving rise to Structural Health Monitoring (SHM) strategies that seek to provide early warning that can prevent catastrophic failures.

SHM is a process of capturing the condition or changes in the condition of a structure by assessing the collected data. The objectives of SHM may include: (i) continuously monitoring the integrity of civil infrastructures; (ii) quantifying the severity of damage; (iii) increasing serviceability; (iv) offering the possibility of reducing cost of maintenance and inspection; and (v) predicting the remaining serviceable life (Spencer et al. 2007; Rytter 1993). Existing SHM systems can be categorized into wired sensor networks (the traditional approach) and wireless smart sensor networks.

In the early stages of SHM, wired sensors were used most frequently. Some representative examples of such systems include work done by Abdel-Ghaffar et al. (1985), Caicedo et al. (2002), Celebi (2006), Wong (2004), Wong (2007), Ni et al. (2010), and Fujino et al. (2000). The applications varied in the purpose of the systems, size of the networks, sensor types installed, monitoring durations, and the ages of the bridges when instrumented. For example, Abdel-Ghaffar et al. (1985) installed an SHM system on The Golden Gate Bridge in San Francisco, California, to analyze the bridge response under ambient vibration. This campaign-type experiment included 28

accelerometers (18 on the main span and 10 on one of the two towers) and an anemometer. A real-time seismic monitoring system was implemented on the Bill Emerson Memorial Bridge in Cape Girardeau, Missouri (Caicedo et al. 2002; Celebi, 2006). This permanent instrumentation consists of 84 accelerometers and anemometers, and data collection is done via the internet. Also, Tsing Ma Bridge in Hong Kong (Wong 2004, Wong 2007, Ni et al. 2010) was instrumented with over 600 sensors. Although the contributions of earlier implementations were remarkable to advance SHM, wide-spread use of SHM was not easily available.

The main challenge of the wired SHM system is that the cost of the system increases as the size of the network increases. Despite the lowered cost of sensors with the recent development of micro-electro-mechanical system (MEMS), the cost of installation still remains high due to cabling of the network. Instrumenting 63 sensors on the Humber Bridge in the UK required 32 km of cabling (Brownjohn, 2007). And the SHM system on the Tsing Ma Bridges in Hong Kong with 326 sensor channels is estimated at $8 million (Lynch and Loh, 2006). Thus, engineers need to devise a system that can reduce the cost of a system and the labor.

In addition, wired systems also require men-labored handling of large amount of data .Because a vast amount of unrefined data floods into a data acquisition system, and processing the data is not a trivial task. For instance, the data generated from 326 sensor channels implemented on the Tsing Ma Bridge and the Kap Shui Mun Bridge in Hong Kong was about 63 MB per hour (Wong, 2004). This issue inspired engineers to develop a newer SHM system that can extract only data that are of interest. In other words, a Smart SHM system was needed.

2.3. Wireless smart sensor (WSS)

2.3.1. Overview of WSS networks

Advances in MEMS technology, along with the prevalence of wireless radio systems, have opened the possibility of wireless sensing applications in SHM. Because structural damage is a local phenomenon, a dense array of sensor systems is desirable to facilitate effective damage detection. However, realizing such systems with traditional wired sensor systems is not only expensive but also time consuming, mainly due to the cabling work necessary to connect the sensors to the central base station. In addition, the network topologies in such systems are intrinsically centralized and lack flexibility, hence, the systems are likely to suffer from data inundation. Thus, over the decades, steady developments have made to each component of wireless smart sensors for commercial and academic uses.

The basic features that comprise a wireless smart sensor are a radio, processors, memory, and sensing interface and power. A radio enables the wireless sensors to communicate within a network and transfer data wirelessly. A majority of wireless sensors operate on 900 MHz, 2.4 GHz, or 5 GHz radio frequencies (Rice, 2009). A careful choice of radio is required, because energy cost may be dominated by the power consumed during communication and transmission of data (Pottie and Kaiser, 2000). A processor on the wireless sensor provides computations of all of the functions and thereby makes the wireless sensor "smart". The speed of a processor is defined by the speed of a clock embedded in the sensor. Data storage capability is governed by Random Access Memory (RAM) and Read Only Memory (ROM). Although a sensor with large storage space and a faster processor is desired, power requirement should be considered. Generally a sensor interface can be categorized two ways, with respect to interface of the sensor: an interface with onboard analog-to-digital converter (ADC) or without onboard ADC. Since an ADC may limit the resolution and the quality of the data, an interface needs to be chosen accordingly. Because wireless smart sensors are

self-powered, power is a key factor that may limit other components of a sensor. Thus, low power consumption with long duty cycle power sources and low cost is desirable. Efforts have been made by many researchers to design a wireless sensor platform that moves toward balancing desired components.

The first wireless sensor platform tailored for SHM purpose was made by Straser and Kiremidjian (1998) and was named WiMMS. Subsequent efforts have been made by academic researchers including Bennett el al. (1999), Lynch et al. (2001), Mitchell et al. (2002), Farr et al. (2005), and Wang et al. (2005). Nonetheless, not many of these platforms were used in full-scale monitoring because there were only a limited number of users; this resulted in less contribution to SHM (Rice, 2009). On the commercial side, a number of wireless sensor platforms were designed and provided. Some representative companies include Ember (2008), Micro Strain (2008), and Crossbow (2007). Especially, Crossbow commercialized Mica motes, which were originally called Berkeley motes, and provided open source hardware and software designs. Later, Intel (now MEMSIC Inc.) adopted the Mica mote and developed Imote (Kling, 2003) and the second generation platform, called Imote2 (Kling et al. 2005; Adler et al. 2005). An intensive overview of commercial wireless platforms can be found in Lynch and Loh (2006).

Among many wireless smart sensor platforms, Imote2 and Mica motes have been adopted extensively for SHM purposes. Both platforms provide stackable modular design, so that any type of daughter board may be attached. Efforts have been made by various researchers to customize those sensor platforms to fit their purposes. Ruiz-Sandoval et al. (2003) developed a high-sensitivity accelerometer board for the Mica2 platform. Pakzad and Fenves (2004) also developed a similar accelerometer board for the Mica2 platform. Nagayama et al. (2004) developed a strain sensor board for the Mica 2 platform. In 2008, Rice and Spencer developed an accelerometer board for the Imote2 platform. And Jo et al. (2010, 2012) developed various sensor boards for the Imote2 platform

including a high sensitivity accelerometer, strain, pressure sensor board, and data acquisition board (DAQ). With numerous developments in sensor boards, wireless smart sensors have established great potential for SHM applications.

Although many attempts have made to verify the applicability of WSSN on full-scale monitoring of civil infrastructures, none have yet been able to accomplish a full-fledged SHM system (Nagayama and Spencer, 2007). Difficulties in establishing full-scale SHM systems mainly occur due to the distributed nature of wireless networks, which includes: time synchronization error, unreliable communication within a WSSN, data loss, and limited network resources (such as battery power, memory, etc.). The effects of the aforementioned issues on general SHM systems can be found in Nagayama et al. (2007).

2.3.2. The ISHMP service toolsuites

The ISHMP is a collaborative work between the Civil and Environmental Engineering Department and the Computer Science Department at the University of Illinois at Urbana-Champaign. The purpose of the project is to develop hardware and software systems for the continuous and reliable monitoring of civil infrastructure using Imote2 platforms (http://shm.cs.illinois.edu). The project has released a library of open-source services, the ISHMP Service Toolsuites, on top of Imote2's operating system TinyOS (http://www.tinyos.net). The software services include Foundation Services; Application Services; Continuous and Autonomous Monitoring Services; and Tools and Utilities Services. Some of the key services are briefly introduced below, and more details can be found in Rice and Spencer (2009), and Sim and Spencer (2009).

<u>Foundation Service</u> provides functionally required applications to support other applications

23

- *Time Synchronization service* [1] (Mechitov et al. 2004) provides consistent and global timestamps for sensor data so that comparable data collection can be achieved within a network.

- *Reliable Communication service* (Nagayama and Spencer, 2007) builds reliable communication within a network to reduce data loss.

  Application Service provides the numerical algorithm needed for SHM applications. Each service may be verified on Imote2s as well as on PCs (Rice and Spencer, 2009).

- *SyncSensing* (Nagayama and Spencer, 2009) resamples time stamped data in order to reduce local clock error and initial start time errors.

Continuous and Autonomous Monitoring Service provides a power efficient method of continuous and autonomous operations for WSSN (Sim and Spencer, 2009).

- *SnoozeAlarm* provides greatly reduced power management for long-term monitoring. The sensor may sleep for a period of time and wake up periodically for a short time to interact with the network (Rice and Spencer, 2009).

- *ThresholdSentry* forms a part of the network to act as sentry nodes to periodically wake up from the *SnoozeAlarm* and sense data to check if an event of interest occurs.

- *AutoMonitor* schedules a number of applications to perform various events. The applications may include sensing events, transferring data events and *ThresholdSentry* events.

Tools and Utilities Service provides basic testing and debugging functionalities needed for long-term or full scale WSSN deployments.

- *TestRadio* (Linderman et al. 2009) tests the bidirectional communication quality between a sender node and a receiver node.

---

[1]An *italic* font refers to the name of application found in the ISHMP Service Toolsuites.

- *RemoteSensing* is used to collect synchronized data from multiple sensors in a network. Collected data is stored as a flash memory in each node until retrieved. A network composed of various kinds of sensor boards, the multi-metric sensing, is supported by the application.

- *SensingUnit* (Sim and Spencer, 2009) is a service component for higher-level applications, such as synchronized sensing applications.

Using the services in the ISHMP Toolsuites, a full scale long-term SHM system was implemented on the Jindo Bridge, a cable-stayed highway bridge in Jindo, Korea. The first attempt at deployment was made in 2010 with a total of 70 wireless sensor nodes (Rice et al. 2010; Jang et al. 2010; Cho et al. 2010). The measurement lasted for four months focusing on demonstrating the performance and usability of the Imote2 platform, acceleration sensors, and the software from ISHMP Toolsuites. With remarkable improvements made from the lessons learned in the deployment, a second full-scale monitoring system was deployed (Jo et al. 2011). In the second deployment, 116 sensor nodes with 669 sensing channels were installed to realize a larger, autonomous, power-harvesting network for multi-metric sensors with centralized and decentralized data acquisition strategies. The measurement lasted about a year with a daily autonomous e-mail reporting system embedded. The total coverage of monitoring systems was large, over 480 m long, so the network was divided into four sub-networks using two base stations (centralized data acquisition PCs): Haenam deck network, Haenam cable network, Jindo deck networkm and Jindo cable network. (Detailed network configurations can be found in Jo et al. 2011). Also, each base station was equipped with an antenna boost to enhance the radio strength. Two sub-networks sharing the same base station (e.g., Haenam deck and cable networks) are perfectly time synchronized with a clock on the base station PC. However, the sub-networks with different Base Stations (e.g., Haenam deck and Jindo deck networks) were roughly time synchronized based on their own base station PC clocks.

The Government Bridge at the Rock Island Arsenal is another example of a bridge that has been used to test the use of ISHMP services for long-term SHM. The bridge is a 115-year-old swing bridge that carries highway and railway traffic. In 2011, autonomous WSSNs that consist of 22 sensing nodes with 66 acceleration channels were deployed (Giles et al. 2012). Because the bridge is a steel truss bridge, the signal blockage from the bridge itself was significant. Thus, the network was divided into two sub networks in which the base stations were shared by one PC to provide synchronization of the PC clock. The main purpose of the WSSN for the bridge was to automatically detect classified events, swinging of the bridge, and train events, and record the acceleration measurements. The measurements at each event are used in a damage detection algorithm to locate damage indices for the members of the truss bridge (Giles et al. 2011). However, analyses were only to determine the health of the bridge under its live load and swing events, and not interpreted in the context interaction dynamics between vehicle (train), track, and the bridge.

2.3.3. Remaining challenges in the use of WSSs for railroad bridge applications

Although SHM using WSSs has the potential to provide rich information, due to their distributed nature, some critical challenges remain for implementation on railroad bridges. One is providing synchronized sensing among input force and output responses. Because the effect of trainloads on the response of the railroad bridge is significant, the system should provide means to measure input to the structure. Although a number of synchronization methods have been developed, most provide only clock synchronization within a limited distance from a central base station (i.e., so that the central base station can reach the nodes through either single-hop or a limited number of hops to maintain certain accuracy). Note that synchronized sensing requires not only clock synchronization among wireless nodes, but also synchronization of the measured data; if the measurements are not synchronized, the measured data can be rendered useless.

Another issue is maintaining highly robust and reliable networks. Due to distributed nature of wireless network, communication uncertainty is always present. Wireless radio signals on field-deployed nodes are influenced by communication range, physical interference, multi-path effect, thermal effect, and noise (Shankar, 2002; Grimmer and Suh, 2005). To use failure prone WSSs in a SHM application requiring high data throughput, a means to assess the WSS network communication quality before and after finalizing a deployment is important. Early studies on WSS network reliability mostly focused on communication-level reliability using temporal signal indicators. However, because the WSS networks for SHM purpose often require a large amount of data transfer, communication-level reliability is not sufficient. Instead, an application-level reliability, which can assess the network quality based on the completion of a task, should be considered.

As a result, studies to fill the gaps to achieve the full potential of WSS technology for in-depth understanding of railroad bridge dynamics have been lacking so far.

2.4.   Monitoring railroad bridges

Railroad bridges in railroad industry are a critical component for the transportation system consisting one bridge within every 1.4 miles of a railway. However, most bridges in the United States are old, nearing their expected life time: Although age is not necessarily an indicator of capacity, most railroad bridges in the United States are over 100 years (GAO, 2007). Moreover, railroad bridges need special more care in their inspections, because they vary in type and materials used, and carry heavier loads compared to highway bridges. Due to public concerns about railroad bridge safety, the Federal Railroad Administration (FRA) has regulated periodic inspection plans for railroad bridges. Also researchers have been inspired to diagnose the structural deficiencies or capacities of railroad bridges using monitoring systems.

2.4.1. Railroad bridges in the United States

According to the FRA, railroad bridges are defined as "any structure with a deck, regardless of length, which supports one or more railroad tracks, and any other under grade structure with an individual span length of 10 feet or more located at such a depth that it is affected by live loads". To date, over 770,000 railroad bridges are operated to form railroad networks all over the United States, and the length of total railroad bridges corresponds to a bridge track at every 1.4 miles of track.

The Majority of railroad bridges in the United States are made of steel, timber, or masonry. As shown in Figure 3, approximately 36% are wood or timber, 32% are steel, and 18% are masonry (FRA, 1992). Timber bridges, which are commonly used in the United States, are rarely used in Europe or China. At the same time, railroad bridges made of stone or concrete are common in Europe and China while relatively rare in the United States. Railroad bridges also can be classified by bridge type, such as truss bridges, plate girder bridges, etc. Some of the railroad bridge designs that are commonly used in the United States are introduced below.
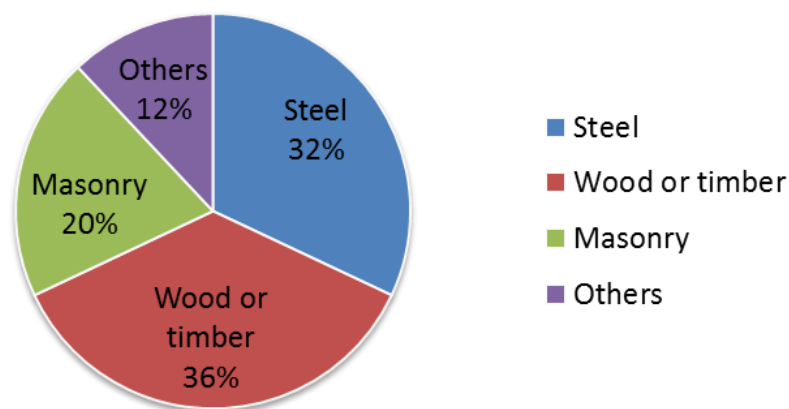
Figure 3. Population of railroad bridges in the United States by material.[2]

Truss Bridges are the most commonly designed railroad bridge not only in the United States but all over the world due to their efficiency in construction and in use of materials. The Bollman Truss

---

[2]Source: FRA 1992–1993 Railroad Bridge Safety Survey

Railroad Bridge at Savage, Maryland, was the first all-metal truss railroad bridge. The bridge is a 160-foot-long, double-span truss bridge, which was originally built in 1852 to economically fulfill the nationwide need to safely carry iron (Jackson, 1998). Truss railroad bridges may be classified as one of three basic types depending on the location of the roadbed and the bridge deck to form a box truss (Mee et al. 1994):

- Through Truss Bridges: Truss members are both above and below the roadbed, and the track system passes between the trusses.

- Deck Truss Bridges: The roadbed and track systems are located atop the truss.

- Suspended or Under Slung Deck Truss Bridges: Track systems are located on top of the truss, and the truss structure is supported at the end of the top chord through an inverted truss.

Plate Girder Bridges, such as the beam or girder bridges for railways, are one of the simplest bridge types. Before long-span beam railroad bridges appeared in the modern era, steel was primarily used for their construction. Plate girder bridges are mostly limited to a length of 100 feet. Two typical plate girder designs used for railroad bridges are (Mee et al. 1994):

- Through Plate Girder Bridge: Similar to the through truss bridge type, the bridge consists of a deep girder with track systems resting on the floor system. Usually through plate girder bridges have an open deck with ties resting directly on the stringer or a ballast deck and may be between 40 and 150 feet long.

- Deck Plate Girder Bridge: Deck plate girder bridges for railroads consist of two girder plates which may act compositely and are located under the track systems. The railroad ties themselves can form the bridge deck, or the deck may be supported by ballast layers. This type of bridge does not require an additional flooring system, and thus is more economical than a through plate girder bridge. The bridge length varies from 10 feet to 120 feet.

29

Timber Trestle Bridges consist of a rigid frame used as a support system or frame of the bridge that is composed of a number of short spans which are supported by such frames. In the context of a timber trestle bridge, each frame consists of a series of bents, the vertical supporting frames, capped with a large timber (Foster, 1897). Timber trestle bridges were widely built in 19th century for temporary uses to serve railways. Throughout several generations, timber trestle railway bridges have been replaced by steel or other material bridges. However, in the south and west of the United States many timber trestle bridges are still in service, with more than 1500 miles of these bridges (Ritter, 1990).

Concrete Spans show in many railroad bridges built during the 1920s and 1930s due to a Federal Highway boom of reinforced structures. Bridge designs with concrete became airier, slimmer, and cheaper to construct than masonry bridges. Nowadays, newer concrete structures, such as pre-cast, pre-stressed concrete slab, are constructed on top of concrete piles or concrete abutment and piers (Mee et al. 1994).

Moveable Railroad Bridges are designed to be turned, raised, or lifted from their original position in order to allow passage for boats or barges. The major advantage of such bridges is that designing a moveable bridge is cost efficient than designing taller bridges. At the same time, a disadvantage of moveable bridges is that traffic must be delayed when they are used in the opened position. Therefore, such bridges are rarely designed for busy channels. Typical types of moveable bridges are:

- Vertical Lift Bridges: A span of the bridge is lifted by counterweighted cables that are mounted on towers remaining parallel with the deck. Compared with other types of moveable railroad bridges, vertical lift bridges cost less to construct and are available for longer span lengths. However, after construction, height restrictions for the barges passing underneath exist.

- Bascule Bridges: A moveable part of the span is hinged with a counterweight that balances throughout the swing event.

- Swing Bridges: A moveable span rotates about a fixed point, usually at the center part. Swing bridges are usually lighter because they require no counterweights. Also, vessel collision risks are reduced due to a sufficient channel and no height restrictions. However, depending on the position of the bridge, whether opened or closed, some members of the bridge may experience changes from compression to tension.

2.4.2. FRA regulations in inspections

The train derailment that occurred in 1979 at Devil's Slide in Utah was a remarkable accident that resulted in the requirement to systematically inspect and report the condition of all railroad bridges. Since then, with a number of modifications on recordkeeping and requirements from the FRA, a current monthly inspection reporting system has been established. Figure 4 summarizes the most recent ten years of railroad accident records reported to the FRA. Throughout this period, the total number of railroad accidents, including train accidents, highway-rail grade crossing incidents, and other incidents related to any death or injury of a railroad employee, has been continually reduced (Figure 4a). Among entire railroad accidents, incidents related to train derailments make up roughly 18%. Except for 2011, the report shows that the number of derailments has also been continually reduced over the period. In 2012, fewer than half as many train derailment accidents occurred than in 2004 (Figure 4b). Because of the strict definition of railroad bridge accidents, that an accident occurred while a train is crossing or attempting to cross the bridge, only a few incidents are reported throughout the period (Figure 4c) (Mee et al. 1994). The portion of incidents caused by the bridge is only a small fraction of the total number of derailment accidents.
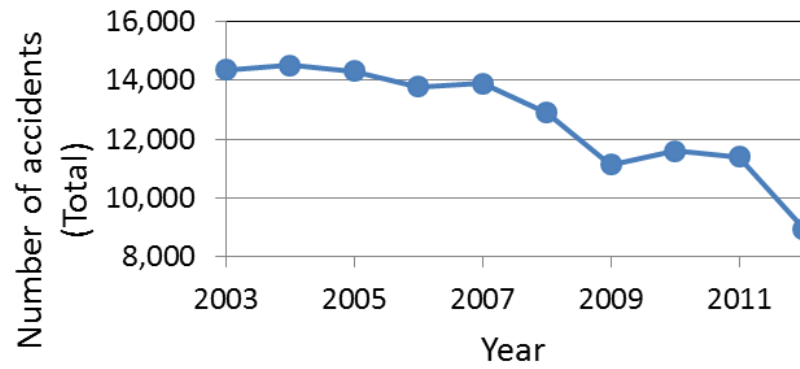
(a) Number of total railroad accidents.
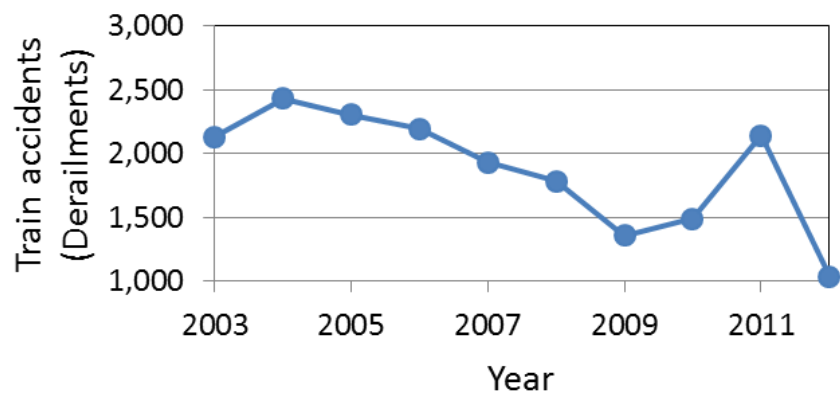
(b) Railroad accidents caused by train derailments.

(c) Railroad accidents due to bridge misalignment or failure.

Figure 4. Railroad accident records for the past 10 years.

Although historical reports imply that the accidents caused by structural deficiencies of a railroad bridge are rare, the importance of structural health monitoring of railroad bridges cannot be overlooked for following reasons.

- Accidents caused by structural failure of railroad bridges exist. According to the FRA accident records, 58 train accidents were caused by structural failure of railroad bridges from 1982 to 2008 (FRA, 2010).

- Consequences of a bridge failure may be catastrophic. One reported failure of a railroad bridge incurred approximately $26 million of damage to railroad facilities, car, and locomotives, which is nearly 18% of the annual damage loss (FRA, 2010).

- Train accidents may have consequences beyond injuries and fatalities, as can be seen from the railroad bridge failure that occurred in November 2012, which caused emission of hazardous chemicals into a creek in New Jersey.

- Public concerns about the structural integrity railroad bridges are increasing as bridges get older. According to a survey conducted by the FRA in 1992 and 1993 regarding bridge safety, more than half of the railroad bridges in the U.S. were constructed before 1920 (FRA, 1999). Considering that most of bridges are built to last 50 years, some railroad bridges are nearing of have exceeded their expected life.

- Increased demands on hauling more loads and dense networks require more frequent inspections of the status of the bridge. The amount of freight carried over the track in 2006 increased over three times from the amount in 1980 (AAR, 2007).

Accordingly, the rules on Bridge Safety Standards (FRA, 2010) have promulgated. The regulations on bridge inspections include scheduling of bridge inspection, requirements on bridge capacity, and bridge inspection procedures. The details of the promulgation are as follows:

33

Scheduling of bridge inspection regulates that each bridge be given regular comprehensive inspections at least once every year with no more than 540 days between two successive inspections. More frequent or special inspections may be performed under a railroad bridge engineer's decision.

Bridge inspection procedures must be determined independently for each railroad bridge. Decisions may vary depending on the configuration of the bridge, conditions found during earlier inspections, characteristics of railroad traffic moving over the bridge (such as train weights, frequencies, and length, and the hazardousness of freight that trains carry over the bridge), and the bridge's exposure to potential damage. The procedure of the inspection may include:

- Inventory: Inventory is not an inspection, but includes a list of information about the bridge under inspection which may not change over time, i.e., construction dates, bridge characteristics, and the like.

- Preliminary: A cursory inspection to roughly estimate the condition of the bridge. The inspection aims to identify serious potential causes for the collapse of a bridge or derailments. Major crack identification or foundation issues may be noted.

- Periodic: Most railroad bridge inspections are the regular or periodic type. An annual inspection may include visually available defects of the bridge. The visual inspection includes identifying any signs of distress, distortions, latent defects, loss of sections and deteriorations.

- Detailed: Detailed inspection thoroughly examines the bridge above the waterline when any sign from visual inspection is observed. Non-destructive tools such as dye penetrant and radiographic may be used on all primary and secondary elements.

- Underwater: Underwater inspections are generally performed on bridges where the water depth is greater than 30 inches at any part of the substructure. The procedure may involve

visual and / or remote inspection. Examination may be applied to scour problems, abutments, piers, and piles.

- Special: All other procedures can be categorized Special; includes interim inspections, damage inspections, flood surveys, and fracture and fatigue monitoring. Techniques such as Ultrasonic and strain sensor testing on steel bridges or movement monitoring using accelerometers may be employed.

Structural evaluation of bridges. The FRA requires a report on condition rating to describe the existing, in-place bridge as compared to the as-built condition. This rating of physical condition applies to the Commonly Recognized (CoRe) Structural Elements from the American Association of State Highway and Transportation Officials (AASHTO) Guide, which include bridge deck, superstructure, and substructures. The aim of the rating is not to localize the deterioration or disrepair of the bridge but to characterize the general condition of the entire components of the bridge that are being rated (FHA, 1999). As such, load-carrying capacity will not be used in the condition rating. In other words, "structurally deficient", or "functionally obsolete" classified bridges do not necessarily imply lack of safety.

The capacity rating is used to determine the maximum absolute permissible live load level that the structure may be subjected to with respect to the AASHTO Manual. The evaluation may be conducted by the choice of three load rating methods: the load and resistance factor (LRFR) method, allowable stress (AS) method, and load factor (LF) method. Through the evaluation procedure, bridges are rated at three different stress levels: inventory rating, operating rating, and posting rating. The inventory rating corresponds to the design level of stresses. This rating reflects the existing bridge condition due to deterioration and loss of section. The operating rating determines the maximum capacity of the bridge under occasional use. The posting rating levels are determined by

each state to rate bridges based on vehicle type used. Posting is required only if the maximum legal load configuration in the state exceeds the permissible load under the operating rating. Based on load capacity determination, bridge management plans and judgments will be followed (FRA, 2010).

2.4.3. Common monitoring strategies for railroad bridge

With increased concerns from public and railroad agencies about the status of railroad bridges, many researchers have focused on the instrumenting and monitoring of bridges to meet these needs. A survey done by Moreu and LaFave (2012) shows that the key railroad issues ranked by engineers shifted from 1987 to 2010–2011. In 1987, researchers concentrated on field stress measurements, impact factor, fatigue life, and determining longitudinal forces. However in 2010–2011, the topics of deflection measurement, high speed trains, and long-span bridges drew more interest, while issues of longitudinal forces and the like were still of concern. Representative railroad bridge monitoring systems are introduced in this section with a focus on inspections and instrument systems used.

In-situ experiments to provide design guidelines for the American Railway Engineering and Maintenance-of-Way Association (AREMA) were conducted in the 1990s. Especially, the longitudinal forces transmitted to a bridge under crossing of a vehicle have been found to be considerably larger than previous analyses from extensive tests on both open deck bridges and ballast deck bridges (Foutch et al. 1996, 1997; Otter and LoPresti, 1997, 1998; Tobias et al. 1999; Otter and LoPresti, 1999; Uppal et al. 2001; Otter et al. 2001). In those tests, temporal wired strain sensors were installed on rails to measure longitudinal rail forces. Displacements were also measured using string potentiometers. Although these experiments gave a broader understanding of the longitudinal behaviors of bridges, wired instruments intrinsically segmented and unsynchronized the network into nearby sub-networks. Thus, the global behaviors of the bridges were not captured.

Attempts to monitor railroad bridges long term using wired strain sensors also have been made. Lee et al. (1999) installed 16 fiber optic sensors on a stringer (longitudinal girder parallel to the rail), a hanger (vertical member of the truss bridge), and clip angles. The system is triggered to record 2 min. of strain data as a train approaches and signals the stain sensor on a rail. The bridge was monitored remotely for a year by transferring collected data via telephone connection at the bridge site. The system requires care in selecting fatigue-critical components in the structure, as installation of a wired system may get complicated.

Today, a number of wired instruments integrated with newer sensor technologies are in use for various purposes. Multi-Depth Deflectometers (MDDs) along with strain gages are embedded in ballast and subgrade layers to investigate differential movement at railroad bridge approaches (Mishra et al. 2012). Fiber Bragg grating (FBG) based strain sensors were installed in 32 different locations on a railroad bridge under a rehabilitation procedure (Rodrigues et al. 2012). At each stage of reconstruction, the strain level was monitored and usability of the FBG sensors was verified. However, global inspection of railroad bridges with dense implementations is rarely achieved via such wired systems.

2.4.4. System identification of a bridge

In civil engineering structures, measuring input to the structure is difficult in most cases; hence, the modal parameters can identified from output-only system identification. A number of researchers provided frequency domain approaches to estimate the natural frequencies and mode shapes of the structure reasonably. Some widely used techniques are the frequency domain decomposition (FDD), Eigensystem Realization Algorithm (ERA), and peak-picking methods (Brincker et al. 2001; Juang and Pappa, 1985; Brownjohn, 2003). The expansion of those techniques uses acceleration measurement due to the ease of measuring acceleration rather than velocity and displacement of the

structure. Among those, the peak-picking method is one of the simplest and fastest implementation for ambient vibration response (Brincker et al. 2001).

Felber (1993) introduced the peak-picking method for reliable estimation of modal frequencies and mode shapes for ambient vibration measurements. The basic theory of this method is that the frequency response goes to an extreme around the fundamental frequency. The method assumes that the structure is linear, the excitation is ambient, and the damping of the structure is light with well-separated modes (Felber, 1993). The natural frequencies of the structure are identified from the peaks of normalized the cross power spectral densities (PSD)s, and the mode shapes are found from the ratio of the cross PSDs. Although the theory behind peak-picking may be comprehensive, this method is highly practical and user-friendly. During the process, peaks in the PSDs are selected based on the physical understanding. This feature allows the method to be understood by a group of variety background. For this reason, this method has been chosen in this study.

To obtain accurate results in the peak-picking method, both low noise levels in the signals and clear, distinctive peaks are essential. Low accuracy in the lower frequencies in the MEMS based low-cost accelerometers may harm the use of the methods for civil structures, where the fundamental frequencies are usually low (Su et al. 2010; Nagayama et al. 2005). To enhance the accuracy, Nagayama et al. (2010), suggested using limited number of high-sensitivity acceleration for the reference signals when calculating the cross-PSDs. Such multi-metric network offers cost-effective extraction of the system identification with increased accuracy for peak-picking method.

2.4.5. System identification of an in-service railroad bridge

Numerous researchers have employed system identification to develop models of highway bridges that can help in assessing the state of bridge infrastructure. Because initial models for the bridge may not be 100% successful for assessing dynamic properties, models are usually updated using

measurements from dynamic testing. Various model updating approaches have been proposed (e.g., Brownjohn and Xia, 2000; Jaishi and Ren, 2005; Deng and Cai, 2009; Morassi and Tonon, 2008). While aforementioned literature used models that well represent global features of the bridge, Catbas et al. (2007) asserted that for accurate and practical condition evaluation of a structure, models should not only be updated with global attributes, but also with local data; when local responses are estimated from global-only calibrated model, results may be render meaningless. As such, in some of applications, global responses are measured from ambient vibration tests using accelerometers. Then, local characteristics, such as strain, are captured from controlled tests; the bridge is usually closed for the revenue traffic while a truck of known mass runs over the bridge (Catbas et al. 2008 and Brenner et al. 2010). Although this type of test strategies is relatively easy to achieve in highway bridges, in the case of railroad bridges, performing such tests can be much expensive and hard. In consequence, railroad bridges received comparably less attention in this topic. Thus, a framework for monitoring railroad bridges that can efficiently reach global and local calibration of a model for system identification under revenue traffic needs to be devised.

To date, only a limited number of studies have conducted system identification of in-service railroad bridges. Ahmadi and Daneshjoo (2012) implemented a full-scale monitoring system on a railroad bridge (Firoozeh Railroad Bridge, Iran). They collected acceleration responses of the bridge under a train of known speed and weight passing and extracted key parameters of the bridge. Giles et al. (2011 and 2012) implemented a full-scale monitoring system on the Government Bridge at the Rock Island Arsenal using wireless smart sensors (WSSs). The efficient and multi-metric system allowed understanding of the global behavior of the bridge (Cho et al. 2014). Local responses are also measured from fiber optic strain sensors. However those sensors were only suitable for static measurements, because of the aliasing effects (Van Damme et al. 2007). In their application, however, because the bridge could swing to allow river traffic (i.e. barges) to pass, and thus traffics

39

are closed and static loads governed during the period, use of those sensors were adequate. From the member strain under self-weight, the health of the bridge was assessed. In addition, system identification of the bridge was performed comparing global responses of the bridge with a finite element (FE) model (Cho et al. 2014). While these methods have been successful in monitoring railroad bridges, a framework for dynamic tests and calibrated models that can help practically assess in-service railroad bridges based on global and local responses has not been provided.

A framework that can experimentally monitor the interaction dynamics of a railroad bridge and a moving vehicle has yet to be realized. The gap may arise from little experiences on the railroad bridge SHM compared with SHM on highway bridges and lack of ability to establish the network that can synchronize a network on a bridge and on a moving vehicle.

2.5.   Challenges on wireless sensing technologies for monitoring railroad bridges

The mobility of WSSN systems leveraged the potential applicability of monitoring physically discrete objects. However, past researches indicate that current WSSN systems have intrinsic limitations in their use for monitoring railroad bridges. Because input to railroad bridges, such as train dynamics, is important, the WSSN has to be fully scalable to accommodate several networks. For example, two distinct networks, which are reliable within a network and precisely time synchronized for both networks is a desirable feature. However, because of the distributed feature of WSSNs, the quality of the network relies on radio communication. Thus, understanding and design of the networks based on assessments of the radio environment is required. In this section, an overview of the two critical features for establishing a monitoring system tailored for railroad bridge applications, time synchronization and radio communication, will be provided.

2.5.1. Time synchronization on WSSs

Wireless sensor technology promise to improve our ability to monitor the structural integrity of civil infrastructure in real time, which is often large in dimension and extremely complex. Traditional wired sensors limit their potential for such applications due to the associated high cost of equipment, labor-intensive installation of the cabling plant, and data inundation due to centralized data collection (Rice, 2009). Wireless smart sensors (WSSs) offer the possibility of addressing these limitations. Recent advance in micro-electro-mechanical systems (MEMS) technology has reduced the cost of sensors. Wireless communication has eliminated the need for much of the cabling. The on-board computational capability of WSSs also reduced the risk of data inundation by extracting the important features of the data, only transmitting essential information to the central base station. Characteristics such as small size and self-powered have led to a few successful long-term monitoring applications (Lynch, et al. 2005 and 2006b; Pakzad, et al, 2008; Jang, et al. 2010; Cho, et al. 2010; Jo, et al. 2012). While WSSs have seen great advancement and offer tremendous opportunities, several challenges remain.

One of the critical issues in WSSs for Structural Health Monitoring (SHM) is providing synchronized sensing. In wireless sensor networks, each WSS operates based on its own clock; the WSS network lacks a centralized time reference, and its performance is susceptible to the quality of the clock's oscillator (e.g., offset, jitter, frequency error and stability; Windl, et al. 2006). Nagayama, et al. (2007) investigated the effect of synchronized sensing error on the accuracy of modal analysis. Because synchronization error causes substantial phase shift in mode shapes, inaccurate synchronized sensing protocol may lead to false positive or false negative results in damage detection. Thus, for successful use of WSSs for SHM, an accurate synchronized sensing protocol which is able to minimize the error down to an acceptable level must be used (Spencer, et al. 2008).

Several researchers have proposed time synchronization schemes for WSS networks. These protocols can be categorized as software-based and hardware-based approaches. A typical software-based protocol can time-synchronize the network by periodically sending beacon signals to estimate clock offset of the nodes. (Lynch, 2007). Hardware-based time synchronization schemes provide communication-free time synchronization among WSSs. Such schemes typically consist of hardware interrupts for each WSS node to adjust the internal clock oscillator (Chen, 2011). These hardware-based solutions can be costly, due to the need for interrupt hardware on each node. In addition, synchronization of the network depends on the precision of the selected hardware (Elson and Römer, 2003; Elson and Estrin, 2003). In general, clocks on wireless nodes can be synchronized to a high level of precision. However, synchronized clocks do not necessarily yield synchronized data.

Traditional synchronization approaches aim to share the reference clock time with all remote sensor nodes. Such protocols cannot control sensing tasks as in a wired network (Nagayama, et al. 2008). The reason lies in the fact that, although the clocks are accurately synchronized, random differences are present in the time at which data collection begins and in the realized sampling rate; non-real time operating system (OS) and non-negligible individual differences in ADC clock frequency, which are typical on WSSs, introduce the random differences unless appropriately designed. To utilize the measured data for civil infrastructure monitoring, these differences must be eliminated. Additionally, because of the large scale of civil engineering structures, multiple networks are often necessary to monitor the entire structure, and sensing duration can be quite long, requiring measurements to remain synchronized over extended periods of time.

A number of software-based protocols have been developed to achieve synchronization of the clocks on CPUs distributed in a network. An example is the Network Time Protocol (NTP). NTP synchronizes CPU clocks with the precision of few milliseconds using a hierarchical, semi-layered system of time sources (Mills, 1991). The protocol may not have sufficient accuracy for applications

that require precise clock synchronization and suffers from delays associated with asymmetric round-trip message delivery (Elson, et al, 2002). Advanced clock synchronization protocols to minimize the cost, power for communication, and delays have been introduced. Reference Broadcast Synchronization (RBS), Timing-sync Protocol for Sensor Network (TPSN), and Flooding Time Synchronization Protocol (FTSP) are examples of such protocols used for WSSs. RBS uses receiver-to-receiver clock synchronization by exchanging the clock information among nodes in the network. Thus, RBS is usually not adequate for large networks or multi-hop applications. TPSN is a typical sender-to-receiver clock synchronization using two-way communication. FTSP is similar to TPSN, which uses sender-to-sender synchronization. The protocol provides time information through the Media Access Control (MAC) layer, which eliminates error from propagation time, reduces jitter, and increases the reliability (Maróti, 2004). On initialization, the sender node broadcasts a data packet, which contains time information as a format of a timestamp at the end of the packet. Upon the reception of the packet by the receivers, the nodes timestamp the local clock reading and calculate the bit offset required to reconstruct the message. The design of FTSP allows high accuracy to be obtained and easy handling of dynamic topology changes and multi-hop. The protocol can synchronize all nodes in a network to the sender node with high accuracy (Roche, 2006). Easy implementation and relatively inexpensive cost to realize the protocol in software-based approaches encouraged wide adoption of the method in WSS networks.

A critical problem in software-based approaches is that the nodes are synchronized to the sender node. Any drift in the sender clock is propagated to the entire network. Moreover, multiple networks cannot easily be synchronized. In an effort to eliminate such problems, hardware-based approaches have been proposed by several researchers. One of the popular hardware-based clock synchronization protocols uses a GPS receiver. The GPS system time is referenced to UTC which is within 50 ns accuracy and is transmitted in the C/A (Coarse/Acquisition) and P(Y) messages from

the satellites. However, to use the UTC information, the signals should be decoded. This process may add time delays that degrade the synchronization accuracy. Instead, most stand-alone GPS receivers are capable of outputting PPS signals when they are locked with satellites. PPS signals is an electrical signal with a width less than one second and a sharp rising edge (or falling edge) corresponds to the clock change in the satellites. The known accuracy of the PPS signals is less than 200 ns (Mannermaa, 1999). The pulses can easily interrupt hardware without introducing delays. Although stand-alone type GPS receivers give accurate time information, implementing a GPS receiver on each wireless node would be expensive, both in terms of cost and power consumption.

Several of these software-based clock synchronization protocols have been implemented for structural health monitoring. Wang, et al. (2005) employed a rough software-based protocol on a low-power wireless sensor unit developed for SHM using commercially available embedded components. In their approach, the network is composed of leaf nodes, each of which has a gateway node to coordinate activities, including time synchronization (see Figure 5). The leaf nodes in the network synchronize their clocks to the gateway node upon receiving a beacon signal from the gateway node. The measurement is also initialized as the signal arrives, eliminating any time delays. The protocol assured reliable communication regarding packet loss during operation of the monitoring system (Wang, et al, 2005, Lynch and Loh, 2006, Lynch, et al. 2004, Lynch, et al. 2006a, and b). Lynch, et al. (2006b) implemented the system on the Geumdang Bridge in Korea and validated the protocol. A network composed of 14 wireless sensor nodes was deployed to monitor the bridge, which has a total length of 273 m. Comparing the acceleration signals collected from wireless sensors to that from wired sensors, the protocol showed 5-10 ms clock synchronization accuracy among 15 sensors (Lynch, et al, 2006b). These papers did not explore the synchronization errors associated with random delays in initial start-up, nor did they consider clock drift that can dominate measurements over extended sensing period.
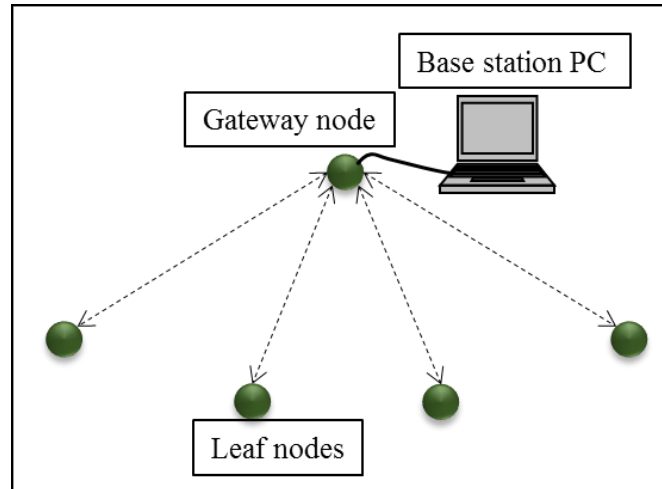
Figure 5. An example of a WSS network topology.

To overcome the some limitations of the software-based methods that incorrect time information propagates to the network and hardware-based methods that establishing the network may be inefficient, Sazonov, et al. (2010) proposed a clock synchronization protocol combining two approaches and implemented it in their Wireless Intelligent Sensor and Actuator Network (WISAN). The gateway node periodically broadcasts beacon signals to the leaf nodes. As a leaf node receives beacon signals, the internal timer is updated to compensate time difference. When stabilized, the estimated maximum drift on each gateway node is ±30 μs per second (Sazonov, et al. 2010). A laboratory scale test using two GPS receivers validated that the proposed protocol achieved about 15 μs synchronization error within two separate sub-networks. A field test composed of forty-four leaf nodes on a four-steel-girder bridge located in NY, USA also validated the protocol. The maximum time error among respective leaf nodes was about 23 μs.

However, synchronized clocks do not necessarily yield synchronized sensing. Nonlinear drift in the gateway node clocks and the randomness in the clock speed should also be adjusted to achieve synchronized sensing in the systems.

2.5.2. Radio communication quality on WSSs

In a wireless sensor network, unreliability in radio communication is a common and non-negligible phenomenon. The cause and significance of the radio irregularities vary with selected hardware. Thus, this overview will focus on reviewing the characteristics of the radio hardware platform selected for the Imote2. The Chipcon CC2420 2.4 GHz IEEE 802.15.4 radio transceiver is used as a radio chip in the Imote2 (Crossbow, 2007). Compliant to 802.15.4, which is an IEEE standard, the radio chip is able to provide low power and a high data rate. Although the chip has been widely adopted for various wireless platforms, the low-power feature makes the radiated signals more prone to noise, interference, and distortions (Baccour et al. 2012).

The main causes resulting in irregularity in radio signals can be categorized in to two: device related causes and propagating media related causes. Device related issues may occur due to differences in the power at which the devices transmit (Petrova et al. 2007). Even if the same chips were used in wireless platforms, random factors, such as lower-gain antennas, may have been introduced during the manufacturing processes. Also self-powered wireless nodes may have different voltage levels. The difference in power during radio transmission may result in a non-isotropic connection between nodes (Zhou et al. 2004). Factors causing randomness in radio communication from environments are diverse. Temperature has a strong correlation with communication quality. Bannister et al. (2008) observed a significant attenuation in received signal strength (RSS) with an increase in temperature (8 dB difference in RSS between 25℃ and 65℃). Humidity can also affect the radio quality. Thelen et al. (2005) found a positive influence of humidity on transmission range. Reflection, diffraction, and scattering of radio signal may result in degradation of the signal quality (Shankar, 2001). Reflection and scattering could arise when radio signals encounter objects, such as steel and concrete. Diffraction may result from irregular surfaces. According to a number of tests done by Linderman et al. (2010), negligible degradation in reception rate has been observed from the

interference of a reinforced concrete wall and a concrete masonry unit infill wall, while 10% reduction has been found from steel structures. More significant degradation, 15% reduction, occurred when the radio environment was affected by other wireless networks. Because the radio signal is vulnerable to various factors, concerns regarding the impact of signal attenuation arose accordingly.

In the past years, a non-negligible impact of radio irregularity has been found. For example, influences on the performance and correctness of networking protocols have been observed, regarding range reductions and loss of packets and the like (Zhou et al. 2004; He et al. 2003; Johnson and Maltz, 1996; Karp and Kung, 2000). However, the impact of poor radio performance on structural analysis for SHM has only been studied by a few researchers. Nagayama et al. (2007) reported that data loss arising from unreliable radio communication affects output-only system identification results. Relationships between data loss level and noise of the signal have also been found such that 0.38% of data loss corresponds to an additional 5% noise to the signal. When data with some packet loss is used for damage detection, false detection may be induced (Moinzadeh et al. 2011). Studies imply that radio performance needs to be verified for appropriate use of wireless sensors for SHM purposes.

Thus far, studies on estimating link quality to monitor radio environments have been explored. Typical hardware-based link quality estimators (LQEs) include: Received Signal Strength Indicator (RSSI), Link Quality Indicator (LQI), and Signal to Noise Ratio (SNR). And the quality of the radio signal is represented by Packet Reception Rate (PRR). Descriptions of each parameter follow (Baccour et al. 2012).

- PRR is computed as the ratio of the number of received packets to the number of packets transmitted.

- RSSI is a register reading value that can be provided by the CC2420 radio transceiver. The value corresponds to signal strength of received packets (Chipcon AS, 2007).

- LQI is proposed in the IEEE 802.15 standard (IEEE 802.15.4 standard, 2003). For CC2420 radio transceivers, the measured value corresponds to symbols embedded in received packet. The index ranges from 50 to 110 and a higher value indicates a better quality index (Chipcon AS, 2007).

- SNR is calculated by the difference in decibels between the pure received signal strength and the noise floor (Baccour et al. 2012).

Relationships between PRR and LQEs (RSSI, LQI, and SNR) have validated the applicability of LQEs. For example, an observation that PRR value drops dramatically below a threshold of RSSI indicates that RSSI provides a quick and accurate estimation of radio quality (Srinivasan et al. 2006). In the case of LQI, although LQI does not provide intermediate quality of the radio link, because the value is averaged over a certain number of readings, large variance in LQI can be used for quality estimation (Srinivasan et al. 2006, 2010; Srinivasan and Levis, 2006). However, studies on SNR have found that SNR can be inaccurate for estimating intermediate links (Zuniga and Krishnamachari, 2004). Further, SNR can be used to describe how strong the pure received signal is compared to the receiver noise floor, but cannot be used as standalone estimator of PPR (Yunqian, 2005; Senel et al. 2007; Aguayo, 2004; Lal, 2003). Lin et al. 2006 claimed that the decision of whether the link quality is good or not can be reasonably made using RSSI and LQI with thresholds on each estimator. Despite the fact that most wireless smart sensors are equipped with readily available LQEs, monitoring of radio communication environments has been lacking from long-term deployment plans for civil infrastructures. Especially, when the structure is large and complicated, LQEs can be used to separate a network into sub-networks and secure reliable radio links for each sub-network.

2.6. Summary

This chapter sought to explore general needs for monitoring dynamic behaviors of a railroad bridge in the presence of train loadings. In-depth review on the numerical models have verified that the repetitive forces from sequential wheels of a train, heavier train weights due to increased amount of freight, and faster speeds from demands on high-speed trains cause the interaction problem to be more complicated and time dependent. Also, because most railroads in the United States are nearing their expected life time and used as shared corridors, some of special issues are addressed: investigation of avoidance of resonance speed and estimation of railroad bridge load capacity. Those concerns on the safety of the train and bridge have strengthened the needs to monitor railroad bridges. However, traditional wired SHM systems are not sufficient for such applications due to their high cost and coaxial wiring. With the advances in the mobility of wireless sensors, the possibility of implementing wireless sensors on geographically discrete objects has become available; i.e., wireless sensors can be deployed on the vehicle and the bridge. Nonetheless, the discrete nature of WSSNs induced other challenges. For example, time synchronization is another key issue in the realization of scalable WSSNs. So far, many protocols have been proposed, including a hardware-based approach and a software-based approach. However, full-fledged time synchronization has not been realized. Also, radio communication links are vulnerable to various factors such as temperature and blockages from a structure. The failure to establish secured radio connection may lead to data loss, which further affects the modal analysis of a structure. Although researchers have found that link quality can be estimated using link quality estimators, not many SHM applications have been considered in their applications. The gaps between the potentials of WSSN and the realization of SHM systems for railroad bridge applications need to be filled.

CHAPTER 3. MODELS FOR PREDICTING BRIDGES DYNAMIC RESPONSE

This section develops models for the bridge/train problem: First, a simple beam model for understanding mass effects of vehicle mass on the bridge dynamics efficiently, is presented. Then, a hybrid model is proposed, which is a flexible and efficient solution for estimating bridge responses for arbitrary train configuration and speeds. Herein, the bridge and track are represented, respectively, with an FE model and a continuous slender beam modeled using the assumed modes method, allowing train loads to be applied in a consistent manner. Each component of the system, the bridge and track, is discussed subsequently. Then, the interconnections between the bridge, track, and train are described such that the hybrid model can be employed for both symmetric and asymmetric loading cases.

3.1. Simple beam model

3.1.1. Model formulation
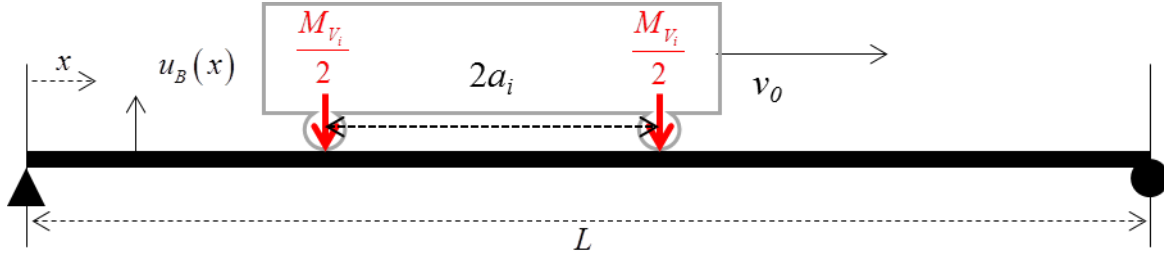
Figure 6. Simply supported beam model.

A simple beam model is developed adopting the approach from Lee (1996). Summing the internal and external virtual work (VW) of the beam, which is modeled using the assumed modes method and subjected to a series of moving point masses (shown in Figure 6), the EOM yields;

$$\left(\mathbf{M}_b + \Delta\mathbf{M}_R\right) \ddot{\mathbf{q}}_b\left(t\right) + \mathbf{C}_b\,\dot{\mathbf{q}}_b(t) + \mathbf{K}_b\,\mathbf{q}_b\left(t\right) = \boldsymbol{p}_R\left(t\right) \tag{7}$$

where

$$\mathbf{M}_b = \int_0^L \rho_b A_b \mathbf{N}_b(x)^{\mathrm{T}} \mathbf{N}_b(x) dx,$$

$$\mathbf{K}_b = \int_0^L \mathbf{N}_b''(x)^{\mathrm{T}} EI_b \mathbf{N}_b''(x) dx,$$

$$\mathbf{C}_b = c_b \int_0^L \mathbf{N}_b(x)^{\mathrm{T}} \mathbf{N}_b(x) dx.$$

Here, $\Delta\mathbf{M}_R$ and $\boldsymbol{p}_R(t)$ are the time varying mass term and the applied force caused by a series of movings car as below;

$$\Delta\mathbf{M}_R(t) = \sum_{i=1}^{N_v} \left(\frac{M_{V_i}}{2} \int_0^L \mathbf{N}_b^{\mathrm{T}}(v_0 t + a_i) \mathbf{N}_b(v_0 t + a_i) \delta(x - (v_0 t + a_i)) dx + \frac{M_{V_i}}{2} \int_0^L \mathbf{N}_b^{\mathrm{T}}(v_0 t - a_i) \mathbf{N}_b(v_0 t - a_i) \delta(x - (v_0 t - a_i)) dx \right) \tag{8}$$

$$\boldsymbol{p}_R(t) = \sum_{i=1}^{N_V} \left(\frac{M_{V_i} g}{2} \int_0^L \mathbf{N}_b^{\mathrm{T}}(v_0 t + a_i) \delta(x - (v_0 t + a_i)) dx + \frac{M_{V_i} g}{2} \int_0^L \mathbf{N}_b^{\mathrm{T}}(v_0 t - a_i) \delta(x - (v_0 t - a_i)) dx \right) \tag{9}$$

The vertical displacement of the beam is $\boldsymbol{u}_b(x,t)$, where

$$\boldsymbol{u}_b(x,t) = \mathbf{N}_b(x) \boldsymbol{q}_b(t) \tag{10}$$

$\mathbf{N}_b(x)$ is a vector of shape functions that satisfies the geometric boundary conditions of the bridge at the two ends, and $\boldsymbol{q}_b(t)$ is the time-dependent generalized displacement.

Other variables used are as follows: L is the length of the beam with $\rho_b A_b$, EI_b, and c_b being mass and stiffness properties and damping coefficient of the beam; a_i is the distance from the center of the car to one set of bogie of i-th car; M_{Vi} is the weight of the i-th vehicle car; N_V is the total

number of cars in a train; g is the gravity; and v_0 is a constant speed of the vehicle. Also, note that $\delta(x)$ indicates the Dirac delta function of x.

The beam properties for this model can be found such that the beam represents both the bridge and track systems. When the maximum vertical deflection of the beam is δ_v under a unit load (i.e., $P = 1$), then properties related to the stiffness of the bridge can be expressed as following (Bowe, 2009).

$$EI_b = \frac{PL^3}{48\delta_v} = \frac{L^3}{48\delta_v} \tag{11}$$

The mass related properties can also be found so that the first natural frequency of the beam dominates the total behavior. When the first vertical natural frequency is f_1,

$$\rho_b A_b = \frac{\pi^2}{4L^4} \frac{EI_b}{\left(f_1\right)^2} \tag{12}$$

Then, in the beam model, the axial strain on the instrumented member can be obtained using its relationships to the shear load (V_b)carried by the bridge at the location, i.e.,

$$V_b = EI_b u_b'''\left(s,t\right), \tag{13}$$

Here, s is the location of the sensor.

3.1.2. Numerical example

To demonstrate vehicle mass effects on the dynamic responses of a railroad bridge, numerical simulations are conducted in this section. Two examples are discussed; a single moving train and a train with multiple cars. These examples will illustrate the importance of including mass effects in assessing railroad bridges.

Single car

In this example, a single car is used (see Figure 6), where the mass is $M_V = 52.63 \times 10^3$ kips, $N_V = 1$ in Eqns. (8) and (9), and front and bogie distance is $a = 20$ ft. The bridge is modeled using five sine functions, where the span length is 310 ft. The bridge deflection under a unit load is assumed $\delta_v = 1.71 \times 10^{-6}$ ft, and the first vertical frequency $f_1 = 4.26$ Hz with damping ratio 0.05%. Total mass ratio of the car mass over the bridge was about 40 %. The simulations started before the car entered the bridge and ended after the car fully exited, so that the transient responses of the beam could be captured. Also, $\Delta t = 0.01$ sec throughout this section.

Figure 7a shows the example of the vertical beam response at the mid-span under the moving mass model (i.e., ΔM_R is considered in Eqn. (7)) when the car crossed the bridge at 40 MPH. The maximum displacement was about 12 inch when the car was passing the center of the beam. Then, using the same car and beam configuration, simulations for the moving load model was performed (i.e, neglected ΔM_R in Eqn. (7)). As can be seen from Figure 7b, the maximum displacement was similar to the moving mass model (about 12 in). However, because the static component is dominating the response, it is hard to differentiate the dynamic effects in the moving mass and load model. Thus, Figure 7c and d shows the high-pass filtered responses of the beam (i.e, static components are effectively removed). The results indicate that at 40 MPH, moving mass and load model show similar degree of maximum dynamic displacements, which is within 0.5 in.
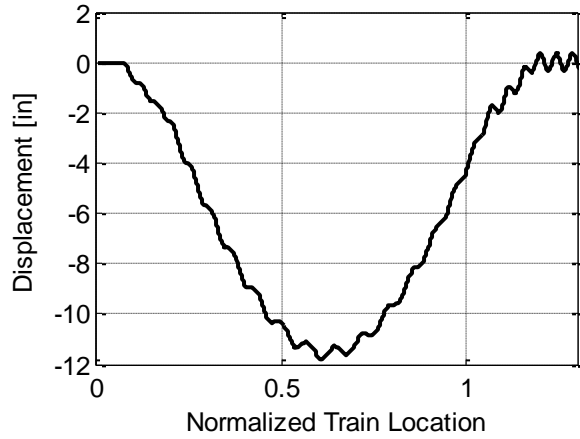
(a) Moving mass model.
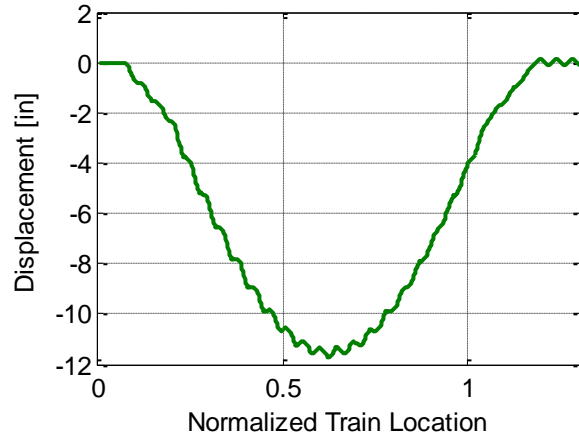
(b) Moving load model.
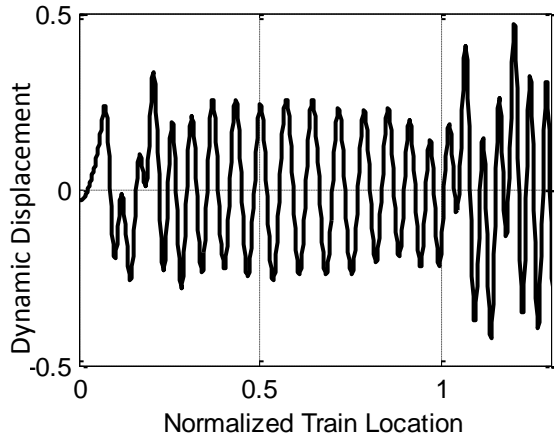
(c) Moving mass model - Dynamic displacement.
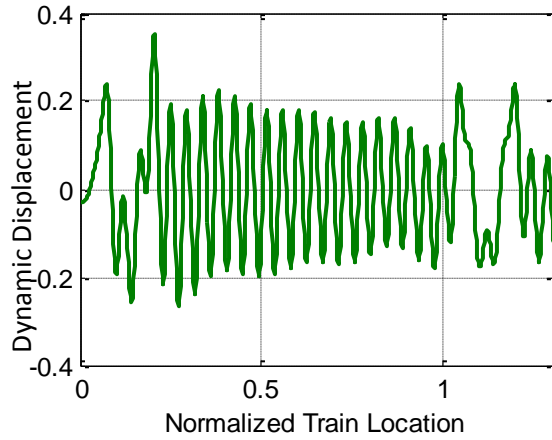
(d) Moving load model - Dynamic displacement.

Figure 7. Vertical displacement of the bridge at the center.

Then, the simulations were performed with the car running at different speeds; from 5 MPH to 60 MPH. Figure 8 compares the dynamic displacements of moving mass and load models. This single car example indicates that within 60 MPH, which the speed is nearly the maximum that a freight car can run on Class I track, moving load model show the similar results with moving mass model.

54
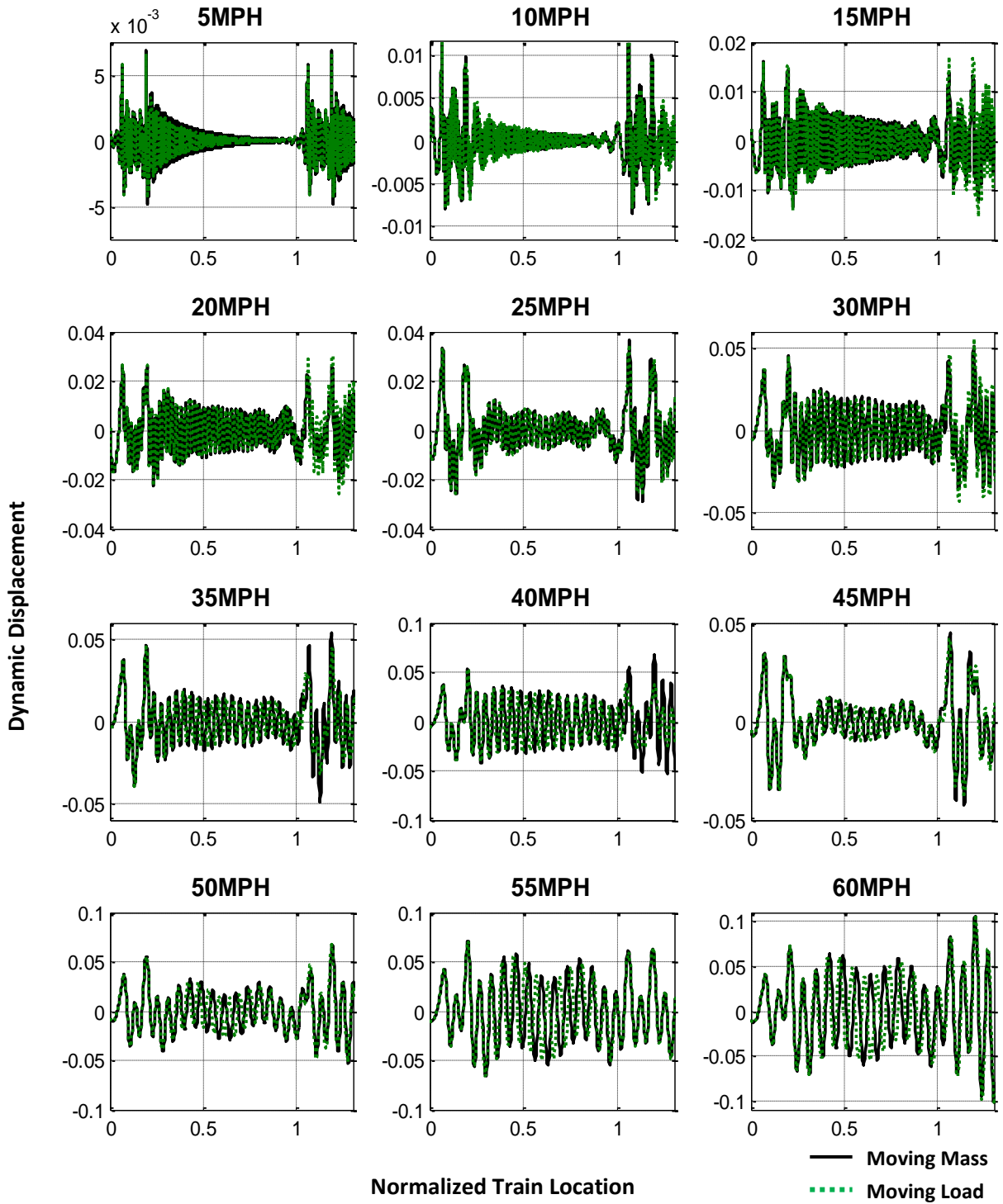
Figure 8. Vertical response of the bridge subject to a single car (in comparison with moving-mass and load model).

55

In comparing the responses from moving mass and load model, the phase differences are observed as the car approaches the center of the bridge. Especially, the phase shift becomes larger as a single car approaches the mid-span of the bridge (see Figure 9). As illustrated in Figure 10, as the car approaches the mid-span of the bridge the first natural frequency changed about 40 %. Note that the frequency at time $t = 0$ and after 1.2 seconds refer to the bridge natural frequency without effects from the mass of the car. (i.e., the first natural frequency shifted from 4.26 to 2.58 Hz).

55MPH
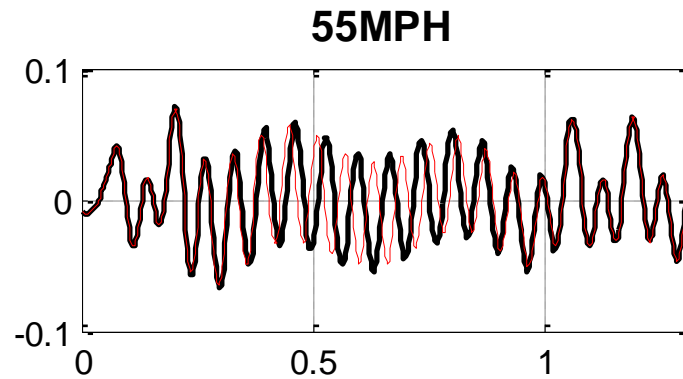
Figure 9. A single car running on a simple beam example.

1st ω_n
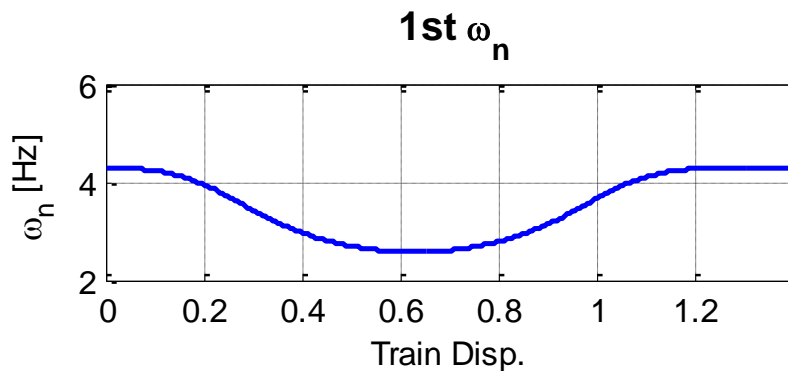
Figure 10. Natural frequency changes as a single car run on the bridge.

Multiple cars

In this example, a train containing multiple cars with different mass and axle distance distributions are used (Figure 11). The train is composed of 8 cars and the total length of the car is equal to the

length of the bridge. The height of each car refers to relative weight of each other and width indicate axle distances. The sum of each mass of a car is set to be 40% of total of the bridge (i.e., the mass ratio of the train to bridge remains the same as the single car example). In the simulations, the speed of the train varied from 5 MPH to 60 MPH. Figure 12 compares the high-pass filtered displacement response of the bridge obtained from moving- mass and load model. As can be seen, although the mass ratio of entire train cars to bridge was the same as in the single moving car example, moving load model shows different dynamic responses; moving load model can underestimated or overestimated the bridge response. Moreover, the differences get larger as more train cars enter the bridge (see Figure 13). Then, the acceleration responses of the bridge at the mid-span are compared in Figure 14 to show that the trends of the responses are similar with that in Figure 12. This result will allow using acceleration responses to capture the critical speeds of the train, which is much simple to obtain in real practice.
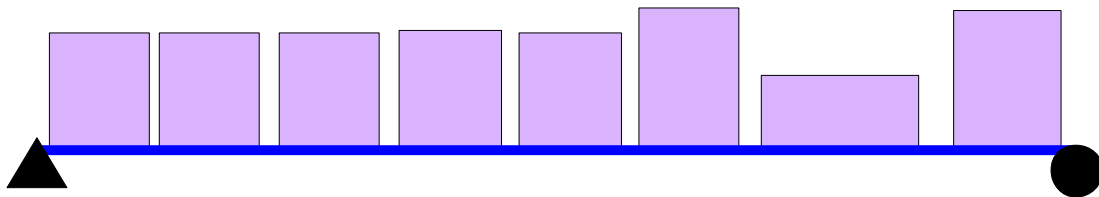
Figure 11. Multiple cars example.

Overall, the simple model and examples presented in this section successfully demonstrated that neglecting the mass effects of a train can result in significant errors in assessing dynamic responses of a railroad bridge. Moreover, because a single car configuration is insufficient, the train representation should be able to accommodate multiple cars easily. The next section will develop a hybrid model, which will allow obtaining more information about the dynamic responses of the bridge under arbitrary train configurations and speeds.
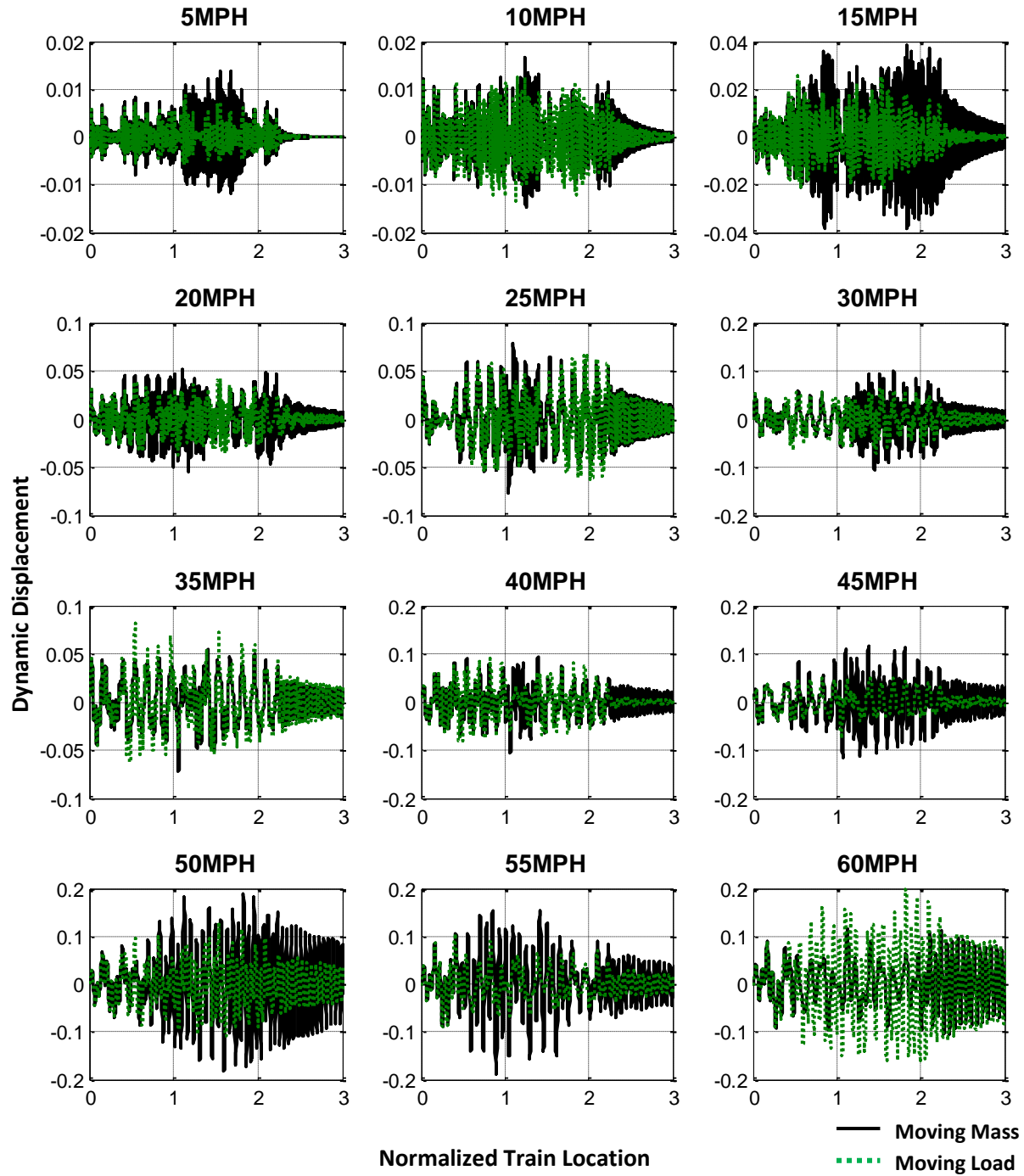
Figure 12. Vertical response of the bridge subject to multiple cars (in comparison with moving-mass and load model).

40MPH

Bridge Displacement [in] vs Normalized Train Location

Entrance of

1 st car   2 nd car   3 rd car   4 th car   5 th car   6 th car   7 th car   8 th car
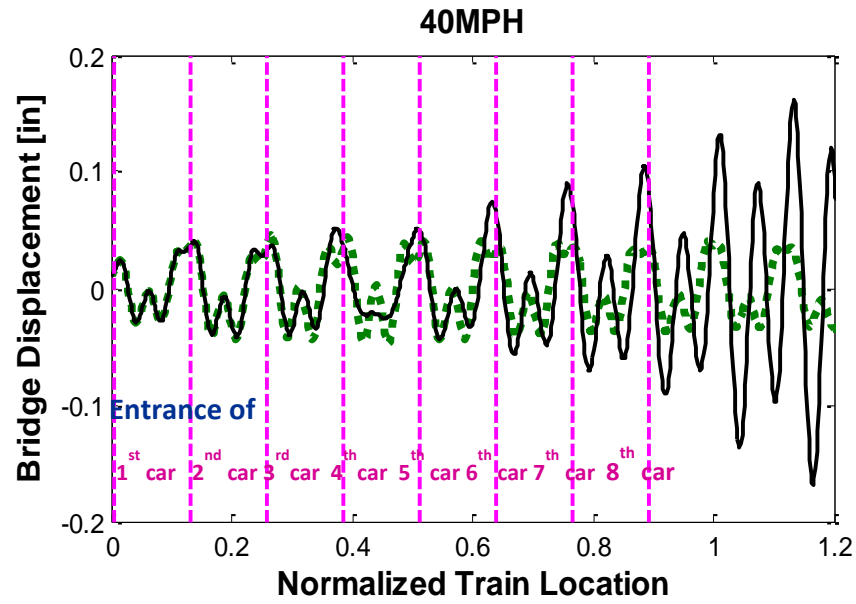
Figure 13. Response of the bridge under moving- mass and load model within the first second.
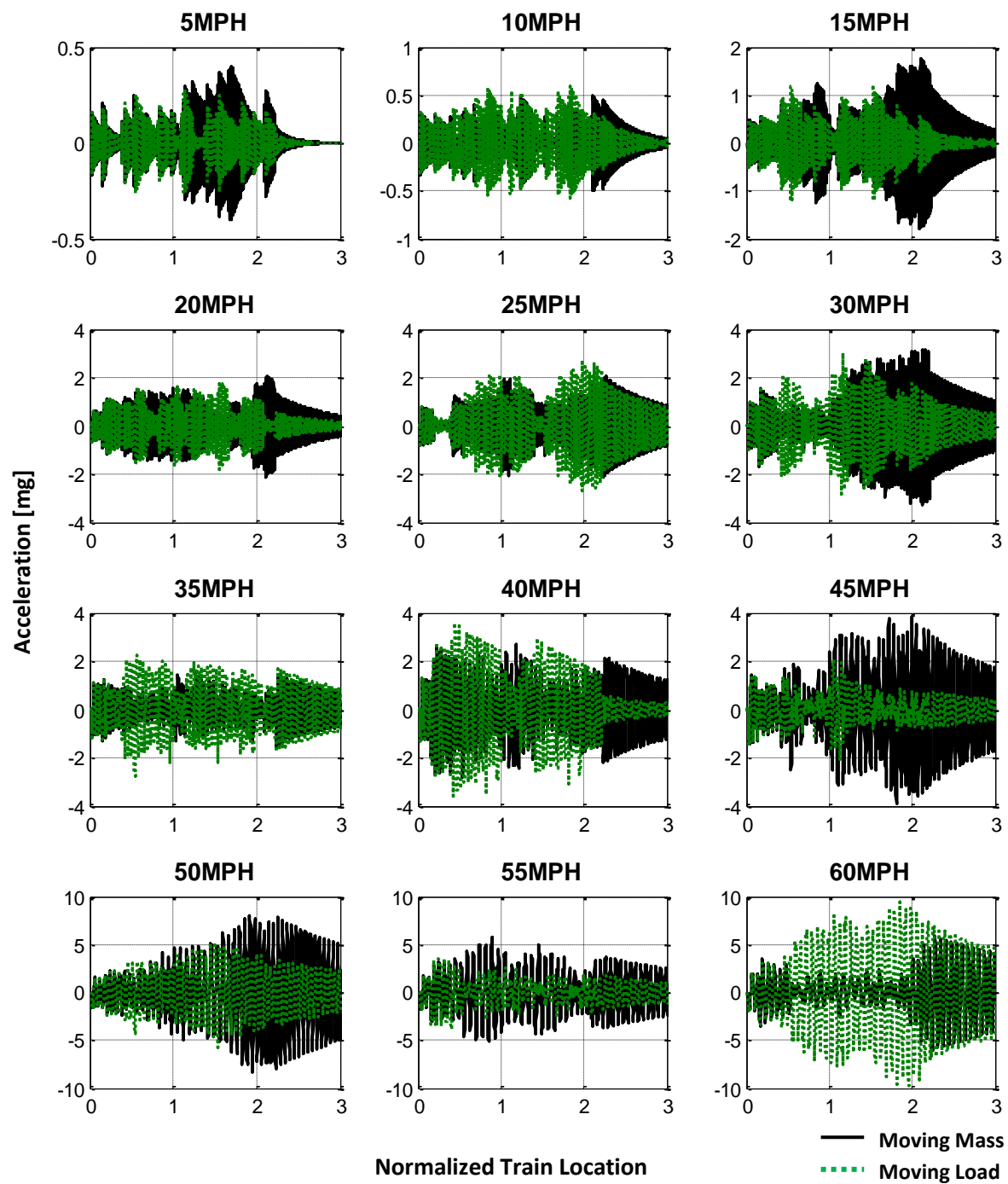
Figure 14. Vertical acceleration of the bridge subject to multiple cars.

3.2. Hybrid model

This section proposes a hybrid model, when the bridge representation is an FE model and the tracks are continuous slender beams using assumed modes methods. Each component of the system, the bridge and tracks, is first presented. Then, the interconnection between the bridge, track, and train are described such that the hybrid model can be applied both for symmetric and asymmetric loading cases.

3.2.1. Bridge/track models
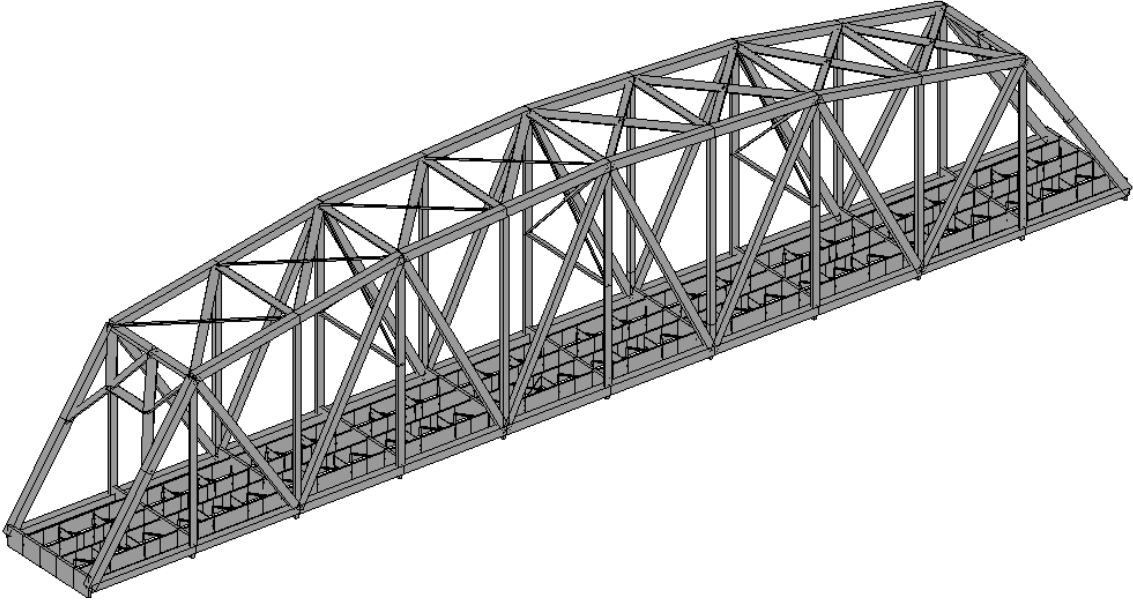
Figure 15. FE model of a railroad bridge.

For a general FE model of a linear elastic time-invariant structure, such as the bridge shown in Figure 15, the equation of motion (EOM) is as follows.

$$\mathbf{M}_B \ddot{\boldsymbol{u}}_B(t) + \mathbf{C}_B \dot{\boldsymbol{u}}_B(t) + \mathbf{K}_B \boldsymbol{u}_B(t) = \boldsymbol{f}_B(t), \tag{14}$$

where $\mathbf{M}_B$, $\mathbf{K}_B$, and $\mathbf{C}_B$ are condensed mass, stiffness, and damping matrices of the bridge. Here, $\boldsymbol{u}_B(t)$ is the displacement vector for the structure and time derivatives are denoted with superscript dots. $\boldsymbol{f}_B(t)$ is a vector of applied forces.

61

The rails are modeled as continuous simple beams using the assumed modes method, which the length is equal to the total bridge length, L. Summing the internal and external virtual work on a rail yields

$$\int_0^L \rho_{R_j} A_{R_j} \ddot{u}_{R_j}(x,t) \bar{u}_{R_j}(x) dx + \int_0^L c_{R_j} \dot{u}_{R_j}(x,t) \bar{u}_{R_j}(x) dx + \int_0^L EI_{R_j} u''_{R_j}(x,t) \bar{u}''_{R_j}(x) dx$$

$$+ \sum_{i=1}^{2N_V} \left(\frac{M_{V_{j,i}}}{2} \ddot{u}_{R_j}\left(x_{V_{j,i}},t\right) \bar{u}_{R_j}(x_{V_{j,i}}) - \frac{M_{V_{j,i}}}{2} g \bar{u}_{R_j}(x_{V_{j,i}}) \right) \tag{15}$$

$$= \bar{q}_{R_j}^{\mathrm{T}} \{ \mathbf{M}_{R_j} \ddot{q}_{R_j}(t) + \mathbf{C}_{R_j} \dot{q}_{R_j}(t) + \mathbf{K}_{R_j} q_{R_j}(t) + \Delta \mathbf{M}_{R_j}(t) - p_{R_j}(t) \} = 0,$$

where $j = 1, 2, ..., NR$ .Therefore, the EOM for the rail/train system is

$$\left(\mathbf{M}_R + \Delta \mathbf{M}_R \right) \ddot{q}_R(t) + \mathbf{C}_R \dot{q}_R(t) + \mathbf{K}_R q_R(t) = p_R(t) \tag{16}$$

Here,

$$\mathbf{K}_R(j,j) = \int_0^L \mathbf{N}''_{R_j}(x)^{\mathrm{T}} EI_{R_j} \mathbf{N}''_{R_j}(x) dx,$$

$$\mathbf{M}_R(j,j) = \int_0^L \rho_{R_j} A_{R_j} \mathbf{N}_{R_j}(x)^{\mathrm{T}} \mathbf{N}_{R_j}(x) dx,$$

$$\mathbf{C}_R(j,j) = \int_0^L c_{R_j} \mathbf{N}_{R_j}(x)^{\mathrm{T}} \mathbf{N}_{R_j}(x) dx,$$

$$\Delta \mathbf{M}_R(j,j) = \sum_{i=1}^{N_V} \frac{M_{V_{j,i}}}{2} \int_0^L \mathbf{N}_{R_j}^{\mathrm{T}} (v_0 t + a_i) \mathbf{N}_{R_j} (v_0 t + a_i) \delta(x - (v_0 t + a_i)) dx$$

$$+ \sum_{i=1}^{N_V} \frac{M_{V_{j,i}}}{2} \int_0^L \mathbf{N}_{R_j}^{\mathrm{T}} (v_0 t - a_i) \mathbf{N}_{R_j} (v_0 t - a_i) \delta(x - (v_0 t - a_i)) dx,$$

$$p_R(j,1) = \sum_{i=1}^{N_V} \frac{M_{V_{j,i}} g}{2} \int_0^L \mathbf{N}_{NR}^{\mathbf{T}} (v_0 t + a_i) \delta (x - (v_0 t + a_i)) dx$$

$$+ \sum_{i=1}^{N_V} \frac{M_{V_{j,i}} g}{2} \int_0^L \mathbf{N}_{NR}^{\mathbf{T}} (v_0 t - a_i) \delta (x - (v_0 t - a_i)) dx,$$

$$\boldsymbol{q}_R(t) = \left\{ \boldsymbol{q}_{R_1}(t) ; \cdots ; \boldsymbol{q}_{R_j}(t) ; \cdots ; \boldsymbol{q}_{R_{NR}}(t) \right\},$$

where $j = 1, 2, ..., NR$. Here, the total number of rails on the bridge is NR and EI_{R_j}, ρ_{R_j}, A_{R_j}, and c_{R_j} denote the flexural rigidity, mass density, cross-sectional area, and the damping coefficient of the j-th rail, respectively. Furthermore, $\boldsymbol{u}_{R_j}(x,t)$ is the vertical deflection of the rail and a prime indicates the derivatives of the function with respect to x. Also, an over-bar represents the virtual displacement. $\mathbf{N}_{R_j}(x)$ is a vector with a series the shape functions that satisfy the geometric boundary conditions at the two ends of the bridge and $\boldsymbol{q}_R(t)$ is the time-dependent generalized displacement of rails, i.e.,

$$\boldsymbol{u}_R(x,t) = \mathbf{N}_R(x) \boldsymbol{q}_R(t);$$

$$\bar{\boldsymbol{u}}_R(x,t) = \mathbf{N}_R(x) \bar{\boldsymbol{q}}_R(t)$$

(17)

Because the size of $\mathbf{N}_{R_j}(x)$ is $1 \times NR$, the size of matrices $\mathbf{M}_R$, $\Delta \boldsymbol{M}_R$, $\mathbf{C}_R$, and $\mathbf{K}_R$ are $NR \times NR$, and vectors $\boldsymbol{q}_R(t)$ and $\boldsymbol{p}_R(t)$ are $NR \times 1$. Having N_V number of cars in a train, $M_{V_{j,i}}$ indicates the mass of the i-th car running over the j-th rail at a constant speed v_0. Figure 16 illustrates a typical configuration of a train car, where the distance between two bogies is *2a*. The front and rear wheel locations at time t can be estimated as $v_0 t + a_i$ and $v_0 t - a_i$, respectively, which at each location the concentrated mass is $M_{V_{j,i}} / 2$.
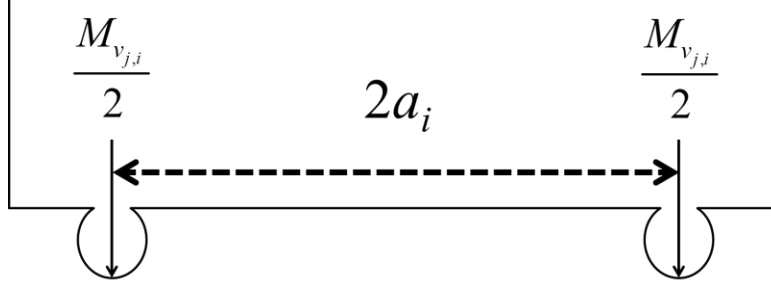
Figure 16. A typical train car configuration.

Combining Eqns. (14) and (16), the EOM for the total system including bridge and rail/train system yields,

$$\mathbf{M}_{\text{total}}\ddot{\boldsymbol{u}}(t) + \mathbf{C}_{\text{total}}\dot{\boldsymbol{u}}(t) + \mathbf{K}_{\text{total}}\boldsymbol{u}(t) = \boldsymbol{p}(t), \tag{18}$$

where

$$\boldsymbol{p}(t) = \{\boldsymbol{p}_R; \boldsymbol{f}_B\},$$

$$\boldsymbol{u}(t) = \{\boldsymbol{q}_R; \boldsymbol{u}_B\}.$$

The next section will discuss the interconnections between rail and bridge system and construct $\mathbf{M}_{\text{total}}$, $\mathbf{C}_{\text{total}}$, and $\mathbf{K}_{\text{total}}$ in Eqn. (18). The coupled terms in the final system of the hybrid model will introduce interactions between rail and bridge. Approaches for both single-track and double-track bridges will be presented.

3.2.2. Bridge-track interconnection

__Symmetric loading case (single-track bridge)__
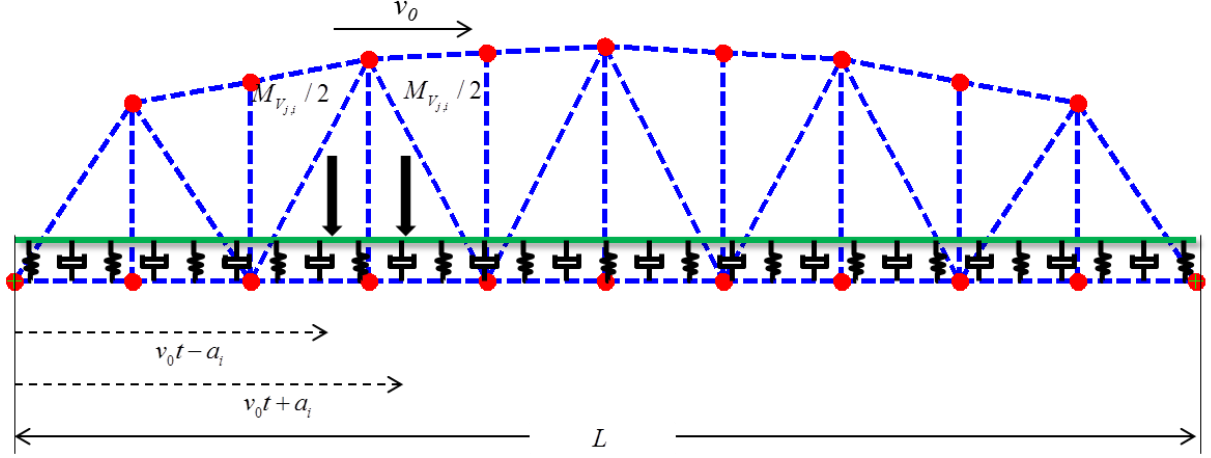
Figure 17. Model of bridge, track and train system.

This section formulates a hybrid model for a single-track bridge, where the loading and the bridge responses are symmetric. Because loads are applied symmetrically, which lacks the out-of-plane forces in the problem, a 2D representation (see Figure 17) is sufficient for solving the problem. Coupling the FE model of the bridge with a continuous track is modeled considering the presence of the ballast layer. For example, if the bridge is an open deck, the interconnections can be modeled as a uniformly distributed suspension system, while a continuous suspension system can represent the ballast deck. Figure 18 depicts a distributed layer between two nodes of the bridge. A series of spring-dashpot units represents rail ties and sleepers (and ballast if needed).
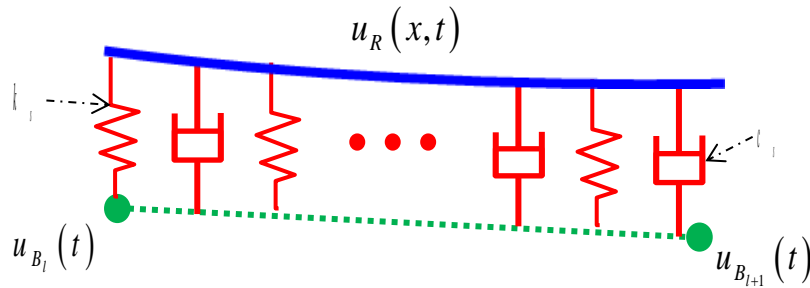
Figure 18. An illustration of the rail-bridge interaction model for the hybrid model.

65

The additional VW due to the suspension system for a discrete spring-dashpot system is

$$\mathbf{VW}_S = k_s \sum_{k=1}^{N_k} \left[\boldsymbol{u}_R(k,t) - \mathbf{H}(k)\left[u_{B_l}; u_{B_{l+1}} \right] \right] \left[\bar{\boldsymbol{u}}_R(k,t) - \mathbf{H}(k)\left[\bar{u}_{B_l}; \bar{u}_{B_{l+1}} \right] \right]$$

$$+ c_s \sum_{k=1}^{N_k} \left[\dot{\boldsymbol{u}}_R(k,t) - \mathbf{H}(k)\left[\dot{u}_{B_l}; \dot{u}_{B_{l+1}} \right] \right] \left[\bar{\boldsymbol{u}}_R(k,t) - \mathbf{H}(k)\left[\bar{u}_{B_l}; \bar{u}_{B_{l+1}} \right] \right], \quad (19)$$

where $l = 1, 2, 3, ..., N-1$

Here, k_s and c_s are the vertical stiffness and the damping of the interaction layer, respectively. N is the number of stringer nodes interacting with rail, N_k is the number of discrete suspension system for ballast between bridge nodes, u_{b_l} and $u_{b_{l+1}}$, $u_R(k,t)$ is the rail displacement estimated at the location of k. $\mathbf{H}(k)$ denotes the shape function at an arbitrary location k, between the node l and $l+1$.

$$\mathbf{H}(k)\left[u_{B_l}; u_{B_{j+1}} \right] = \begin{bmatrix} h1 & 0 & 0 & h4 & 0 & 0 \\ 0 & h2 & 0 & 0 & h5 & 0 \\ 0 & 0 & h3 & 0 & 0 & h6 \end{bmatrix} \begin{Bmatrix} w_l \\ r_l \\ \theta_l \\ w_{l+1} \\ r_{l+1} \\ \theta_{l+1} \end{Bmatrix}, \quad (20)$$

where $h1 = 1 - \dfrac{k}{L_e}$; $\qquad\qquad h4 = \dfrac{k}{L_e}$;

$h2 = 1 - 3\left(\dfrac{k}{L_e}\right)^2 + 2\left(\dfrac{k}{L_e}\right)^3$; $\qquad h5 = 3\left(\dfrac{k}{L_e}\right)^2 - 2\left(\dfrac{k}{L_e}\right)^3$;

$h3 = k - 2L_e\left(\dfrac{k}{L_e}\right)^2 + L_e\left(\dfrac{k}{L_e}\right)^3$; $\qquad h6 = -L_e\left(\dfrac{k}{L_e}\right)^2 + L_e\left(\dfrac{k}{L_e}\right)^3$.

Components in the displacement vector w_k, r_k, and θ_k respectively indicate the lateral, vertical, and rotational displacement at location j, and L_e is the length of the element between nodes l and $l+1$.

Similarly, for a ballast deck the Eqn. (19) becomes,

$$\mathbf{VW}_S = k_s \sum_{j=1}^{N} \int_{x=l}^{x=l+1} \left[\boldsymbol{u}_R(x,t) - \mathbf{H}(x) \left[u_{B_l} ; u_{B_{l+1}} \right] \right] \left[\overline{\boldsymbol{u}}_R(x,t) - \mathbf{H}(x) \left[\overline{u}_{B_l} ; \overline{u}_{B_{l+1}} \right] \right] dx$$

$$+ c_s \int_{x=l}^{x=l+1} \left[\dot{\boldsymbol{u}}_R(x,t) - \mathbf{H}(x) \left[\dot{u}_{B_l} ; \dot{u}_{B_{l+1}} \right] \right] \left[\overline{\boldsymbol{u}}_R(x,t) - \mathbf{H}(x) \left[\overline{u}_{B_l} ; \overline{u}_{B_{l+1}} \right] \right] \qquad (21)$$

$$j = 1, 2, 3, ..., N-1$$

Summing the internal and external VW of bridge and track systems including additional VW due to the interaction layer yields,

$$\mathbf{M}_{\text{total}} \ddot{u}(t) + \mathbf{C}_{\text{total}} \dot{u}(t) + \mathbf{K}_{\text{total}} u(t) = p(t), \text{ or}$$

$$\begin{bmatrix} \mathbf{M}_R + \Delta\mathbf{M}_R & 0 \\ 0 & \mathbf{M}_B \end{bmatrix} \begin{Bmatrix} \ddot{q}_R(t) \\ \ddot{u}_b(t) \end{Bmatrix} + \begin{bmatrix} \mathbf{C}_R + c_s \mathbf{S}_{RR} & -c_s \mathbf{S}_{RB} \\ -c_s \mathbf{S}_{BR} & \mathbf{C}_B + c_s \mathbf{S}_{BB} \end{bmatrix} \begin{Bmatrix} \dot{q}_R(t) \\ \dot{u}_B(t) \end{Bmatrix} \qquad (22)$$

$$+ \begin{bmatrix} \mathbf{K}_R + k_s \mathbf{S}_{RR} & -k_s \mathbf{S}_{RB} \\ -k_s \mathbf{S}_{BR} & \mathbf{K}_B + k_s \mathbf{S}_{BB} \end{bmatrix} \begin{Bmatrix} q_R(t) \\ u_B(t) \end{Bmatrix} = \begin{Bmatrix} p_R(t) \\ 0 \end{Bmatrix},$$

where

$$\mathbf{S}_{RR} = \sum_{k=1}^{N_k} \mathbf{N}_R(k)^{\mathbf{T}} \mathbf{N}_R(k); \qquad \qquad \mathbf{S}_{RB} = \sum_{k=1}^{N_k} \mathbf{N}_R(k)^{\mathbf{T}} \mathbf{H}(k);$$

$$\mathbf{S}_{BR} = \sum_{k=1}^{N_k} \mathbf{H}(k)^{\mathbf{T}} \mathbf{N}_R(k); \qquad \qquad \mathbf{S}_{BB} = \sum_{k=1}^{N_k} \mathbf{H}(k)^{\mathbf{T}} \mathbf{H}(k).$$

As can be seen from Eqn. (22), the hybrid model is expressed through the additional terms in the damping and stiffness matrices. Also, the forces at the wheel-rail contact locations are implicitly included. Note that the proposed 2D hybrid model is limited to a single-track bridge because the model cannot exhibit torsional behavior of the bridge caused by asymmetric loadings of the bridge. Thus, the subsequent section will describe the hybrid model for multiple tracks using a three-dimensional (3D) representation.
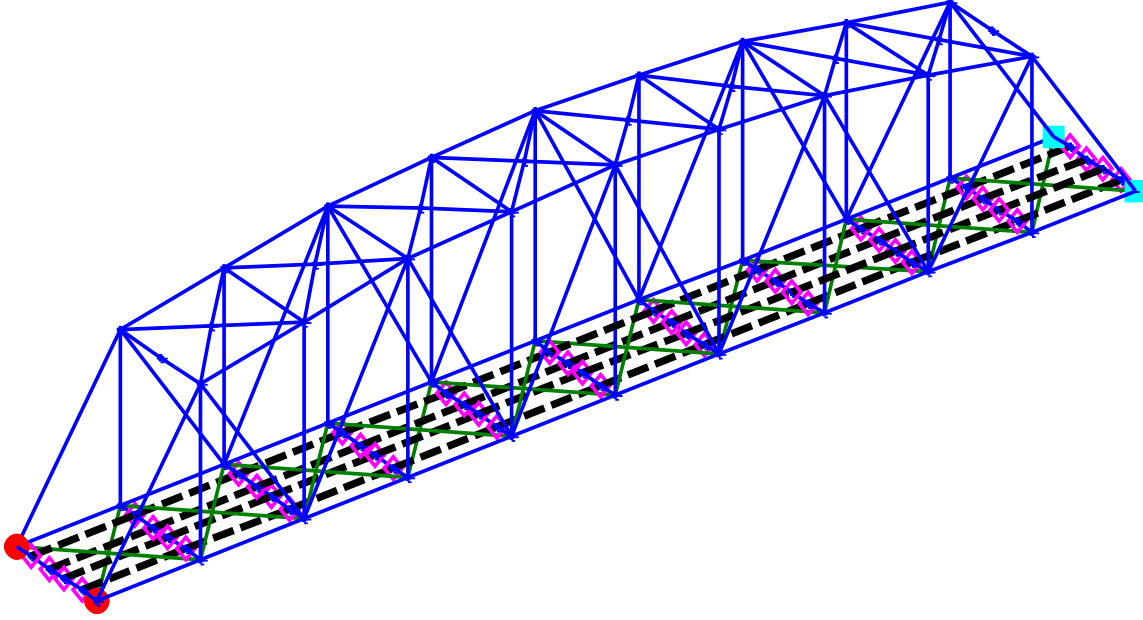
Figure 19. Example of a 3D hybrid model for a double-track bridge.

This section describes the interconnection between track and bridge to build a hybrid model for a multi-track bridge. Because this problem exhibits asymmetric train loading and bridge response, a 3D representation is required (see Figure 19). Here, several additional assumptions are made: First, the loading of the bridge and the rail in the lateral direction is neglected assuming that the vertical loads are dominant in this study. Second, the stiffness of the rail in the lateral direction is assumed negligible, considering that it is much smaller than the stiffness of the bridge. For brevity of the formulation, a double-track bridge, which is a typical example of such a case, is used in this section (i.e. *NR* = 4 in Eqn.(15)). Also, an open-deck bridge is assumed; thus, suspension system will not include the ballast layer. Finally, due to firm connections between the rail and stringers, the stringer displacements are assumed to equal the rail displacements. Then, $\mathbf{M}_B$, $\mathbf{K}_B$, $\mathbf{C}_B$, and $f_b(t)$ in Eqn. (14) can be partitioned as illustrated in Figure 20 for $\mathbf{K}_B$.

$$\left[\mathbf{K}_{B3D}\right]\{u_b\}=$$
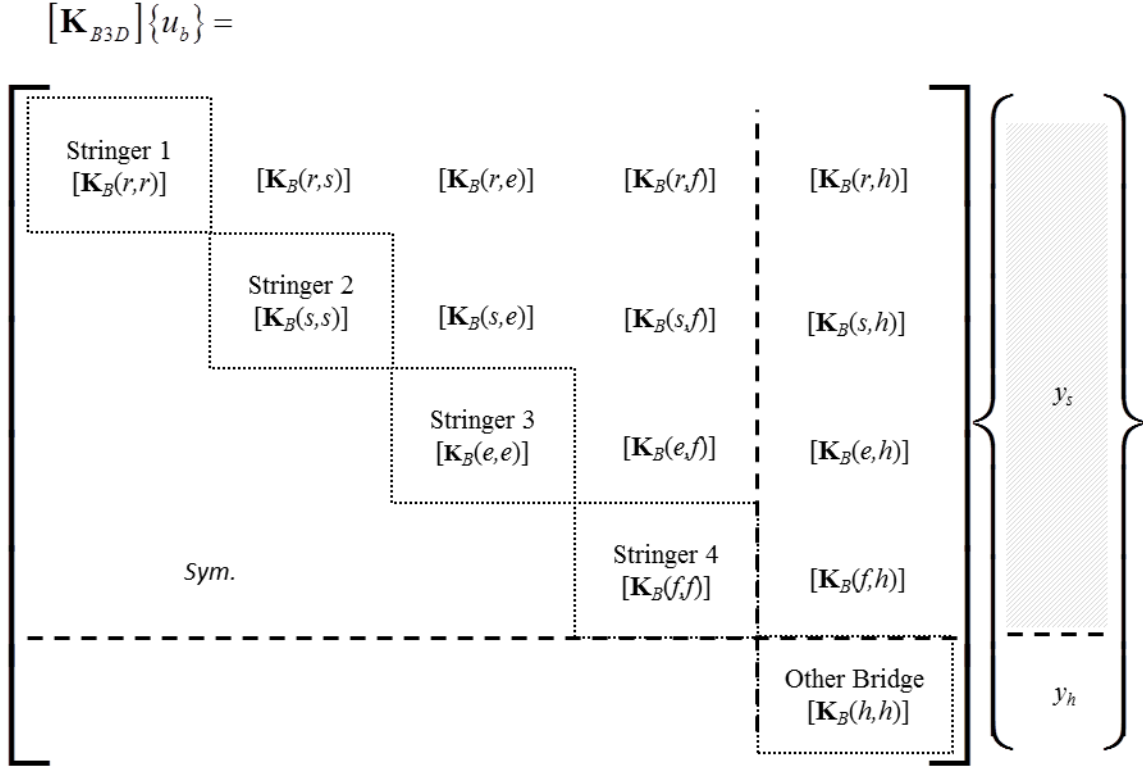
Figure 20. An illustration of the partitioned-stiffness matrix.

Here, the bridge total displacement (u_B) is decomposed into quantities that are related to the stringer (y_s) and the remaining bridge displacements (y_h). The quantities r, s, e, and f represent the vectors of DOFs associated with a stringer underneath each rail. Furthermore, h denotes the bridge DOFs, which excludes four stringers. The off-diagonal terms indicate the coupled stiffness between the rail and the bridge. Then, the displacement vector of the stringers (y_s) at the nodes is determined by

$$\{y_s\}=\left\{\mathbf{N}_{R_1}\left(u_{B_l}\right)q_{R_1}(t);\mathbf{N}_{R_2}\left(u_{B_l}\right)q_{R_2}(t);\mathbf{N}_{R_3}\left(u_{B_l}\right)q_{R_3}(t);\mathbf{N}_{R_4}\left(u_{B_l}\right)q_{R_4}\right\} \tag{23}$$

Here, $\mathbf{N}_{R_1}\left(u_{b_l}\right)\cdots\mathbf{N}_{R_4}\left(u_{b_l}\right)$ are the assumed mode shapes of each rail determined at the stringer nodes ($x=u_{B_l}$) and $q_{R_1}(t)\cdots q_{R_4}(t)$ are generalized displacements. $\mathbf{M}_B$, $\mathbf{C}_B$, and $f_B(t)$ can also be decomposed to obtain condensed matrices and a vector using similar approach.

Summing the internal and external virtual work for the system, including the moving mass, yields,

69

$$\mathbf{M}_{\text{total}}\ddot{u}(t)+\mathbf{C}_{\text{total}}\dot{u}(t)+\mathbf{K}_{\text{total}}u(t)=p(t),\tag{24}$$

where

$\mathbf{M}_{\text{total}} =$

$$\begin{bmatrix}
\mathbf{M}_{R_1}+\mathbf{N}_{R_1}^{\mathrm{T}}\left[\mathbf{M}_{rr}\right]\mathbf{N}_{R_1}+\Delta\mathbf{M}_{R_1} & \mathbf{N}_{R_1}^{\mathrm{T}}\left[\mathbf{M}_{rs}\right]\mathbf{N}_{R_2} & \mathbf{N}_{R_1}^{\mathrm{T}}\left[\mathbf{M}_{re}\right]\mathbf{N}_{R_3} & \mathbf{N}_{R_1}^{\mathrm{T}}\left[\mathbf{M}_{rf}\right]\mathbf{N}_{R_4} & \mathbf{N}_{R_1}^{\mathrm{T}}\left[\mathbf{M}_{rh}\right] \\[4pt]
\mathbf{N}_{R_2}^{\mathrm{T}}\left[\mathbf{M}_{sr}\right]\mathbf{N}_{R_1} & \mathbf{M}_{R_2}+\mathbf{N}_{R_2}^{\mathrm{T}}\left[\mathbf{M}_{ss}\right]\mathbf{N}_{R_2}+\Delta\mathbf{M}_{R_2} & \mathbf{N}_{R_2}^{\mathrm{T}}\left[\mathbf{M}_{se}\right]\mathbf{N}_{R_3} & \mathbf{N}_{R_2}^{\mathrm{T}}\left[\mathbf{M}_{sf}\right]\mathbf{N}_{R_4} & \mathbf{N}_{R_2}^{\mathrm{T}}\left[\mathbf{M}_{sh}\right] \\[4pt]
\mathbf{N}_{R_3}^{\mathrm{T}}\left[\mathbf{M}_{er}\right]\mathbf{N}_{R_1} & \mathbf{N}_{R_3}^{\mathrm{T}}\left[\mathbf{M}_{es}\right]\mathbf{N}_{R_2} & \mathbf{M}_{R_3}+\mathbf{N}_{R_3}^{\mathrm{T}}\left[\mathbf{M}_{ee}\right]\mathbf{N}_{R_3}+\Delta\mathbf{M}_{R_3} & \mathbf{N}_{R_3}^{\mathrm{T}}\left[\mathbf{M}_{ef}\right]\mathbf{N}_{R_4} & \mathbf{N}_{R_3}^{\mathrm{T}}\left[\mathbf{M}_{eh}\right] \\[4pt]
\mathbf{N}_{R_4}^{\mathrm{T}}\left[\mathbf{M}_{fr}\right]\mathbf{N}_{R_1} & \mathbf{N}_{R_4}^{\mathrm{T}}\left[\mathbf{M}_{fs}\right]\mathbf{N}_{R_2} & \mathbf{N}_{R_4}^{\mathrm{T}}\left[\mathbf{M}_{fe}\right]\mathbf{N}_{R_3} & \mathbf{M}_{R_4}+\mathbf{N}_{R_4}^{\mathrm{T}}\left[\mathbf{M}_{ff}\right]\mathbf{N}_{R_4}+\Delta\mathbf{M}_{R_4} & \mathbf{N}_{R_4}^{\mathrm{T}}\left[\mathbf{M}_{fh}\right] \\[4pt]
\left[\mathbf{M}_{hr}\right]\mathbf{N}_{R_1} & \left[\mathbf{M}_{hs}\right]\mathbf{N}_{R_2} & \left[\mathbf{M}_{he}\right]\mathbf{N}_{R_3} & \left[\mathbf{M}_{hf}\right]\mathbf{N}_{R_4} & \left[\mathbf{M}_{hh}\right]
\end{bmatrix};$$

$$\mathbf{C}_{\text{total}}=\begin{bmatrix}
\mathbf{C}_{R_1}+\mathbf{N}_{R_1}^{\mathrm{T}}\left[\mathbf{C}_{rr}\right]\mathbf{N}_{R_1} & \mathbf{N}_{R_1}^{\mathrm{T}}\left[\mathbf{C}_{rs}\right]\mathbf{N}_{R_2} & \mathbf{N}_{R_1}^{\mathrm{T}}\left[\mathbf{C}_{re}\right]\mathbf{N}_{R_3} & \mathbf{N}_{R_1}^{\mathrm{T}}\left[\mathbf{C}_{rf}\right]\mathbf{N}_{R_4} & \mathbf{N}_{R_1}^{\mathrm{T}}\left[\mathbf{C}_{rh}\right] \\[4pt]
\mathbf{N}_{R_2}^{\mathrm{T}}\left[\mathbf{C}_{sr}\right]\mathbf{N}_{R_1} & \mathbf{C}_{R_2}+\mathbf{N}_{R_2}^{\mathrm{T}}\left[\mathbf{C}_{ss}\right]\mathbf{N}_{R_2} & \mathbf{N}_{R_2}^{\mathrm{T}}\left[\mathbf{C}_{se}\right]\mathbf{N}_{R_3} & \mathbf{N}_{R_2}^{\mathrm{T}}\left[\mathbf{C}_{sf}\right]\mathbf{N}_{R_4} & \mathbf{N}_{R_2}^{\mathrm{T}}\left[\mathbf{C}_{sh}\right] \\[4pt]
\mathbf{N}_{R_3}^{\mathrm{T}}\left[\mathbf{C}_{er}\right]\mathbf{N}_{R_1} & \mathbf{N}_{R_3}^{\mathrm{T}}\left[\mathbf{C}_{es}\right]\mathbf{N}_{R_2} & \mathbf{C}_{R_3}+\mathbf{N}_{R_3}^{\mathrm{T}}\left[\mathbf{C}_{ee}\right]\mathbf{N}_{R_3} & \mathbf{N}_{R_3}^{\mathrm{T}}\left[\mathbf{C}_{ef}\right]\mathbf{N}_{R_4} & \mathbf{N}_{R_3}^{\mathrm{T}}\left[\mathbf{C}_{eh}\right] \\[4pt]
\mathbf{N}_{R_4}^{\mathrm{T}}\left[\mathbf{C}_{fr}\right]\mathbf{N}_{R_1} & \mathbf{N}_{R_4}^{\mathrm{T}}\left[\mathbf{C}_{fs}\right]\mathbf{N}_{R_2} & \mathbf{N}_{R_4}^{\mathrm{T}}\left[\mathbf{C}_{fe}\right]\mathbf{N}_{R_3} & \mathbf{C}_{R_4}+\mathbf{N}_{R_4}^{\mathrm{T}}\left[\mathbf{C}_{ff}\right]\mathbf{N}_{R_4} & \mathbf{N}_{R_4}^{\mathrm{T}}\left[\mathbf{C}_{fh}\right] \\[4pt]
\left[\mathbf{C}_{hr}\right]\mathbf{N}_{R_1} & \left[\mathbf{C}_{hs}\right]\mathbf{N}_{R_2} & \left[\mathbf{C}_{he}\right]\mathbf{N}_{R_3} & \left[\mathbf{C}_{hf}\right]\mathbf{N}_{R_4} & \left[\mathbf{C}_{hh}\right]
\end{bmatrix};$$

$$\mathbf{K}_{\mathbf{total}} = \begin{bmatrix} \mathbf{K}_{R_1} + \mathbf{N}_{R_1}^{\mathrm{T}}[\mathbf{K}_{rr}]\mathbf{N}_{R_1} & \mathbf{N}_{R_1}^{\mathrm{T}}[\mathbf{K}_{rs}]\mathbf{N}_{R_2} & \mathbf{N}_{R_1}^{\mathrm{T}}[\mathbf{K}_{re}]\mathbf{N}_{R_3} & \mathbf{N}_{R_1}^{\mathrm{T}}[\mathbf{K}_{rf}]\mathbf{N}_{R_4} & \mathbf{N}_{R_1}^{\mathrm{T}}[\mathbf{K}_{rh}] \\ \mathbf{N}_{R_2}^{\mathrm{T}}[\mathbf{K}_{sr}]\mathbf{N}_{R_1} & \mathbf{K}_{R_2} + \mathbf{N}_{R_2}^{\mathrm{T}}[\mathbf{K}_{ss}]\mathbf{N}_{R_2} & \mathbf{N}_{R_2}^{\mathrm{T}}[\mathbf{K}_{se}]\mathbf{N}_{R_3} & \mathbf{N}_{R_2}^{\mathrm{T}}[\mathbf{K}_{sf}]\mathbf{N}_{R_4} & \mathbf{N}_{R_2}^{\mathrm{T}}[\mathbf{K}_{sh}] \\ \mathbf{N}_{R_3}^{\mathrm{T}}[\mathbf{K}_{er}]\mathbf{N}_{R_1} & \mathbf{N}_{R_3}^{\mathrm{T}}[\mathbf{K}_{es}]\mathbf{N}_{R_2} & \mathbf{K}_{R_3} + \mathbf{N}_{R_3}^{\mathrm{T}}[\mathbf{K}_{ee}]\mathbf{N}_{R_3} & \mathbf{N}_{R_3}^{\mathrm{T}}[\mathbf{K}_{ef}]\mathbf{N}_{R_4} & \mathbf{N}_{R_3}^{\mathrm{T}}[\mathbf{K}_{eh}] \\ \mathbf{N}_{R_4}^{\mathrm{T}}[\mathbf{K}_{fr}]\mathbf{N}_{R_1} & \mathbf{N}_{R_4}^{\mathrm{T}}[\mathbf{K}_{fs}]\mathbf{N}_{R_2} & \mathbf{N}_{R_4}^{\mathrm{T}}[\mathbf{K}_{fe}]\mathbf{N}_{R_3} & \mathbf{K}_{R_4} + \mathbf{N}_{R_4}^{\mathrm{T}}[\mathbf{K}_{ff}]\mathbf{N}_{R_4} & \mathbf{N}_{R_4}^{\mathrm{T}}[\mathbf{K}_{fh}] \\ [\mathbf{K}_{hr}]\mathbf{N}_{R_1} & [\mathbf{K}_{hs}]\mathbf{N}_{R_2} & [\mathbf{K}_{he}]\mathbf{N}_{R_3} & [\mathbf{K}_{hf}]\mathbf{N}_{R_4} & [\mathbf{K}_{hh}] \end{bmatrix};$$

$u(t) = \{y_s(t); u_b(t)\}$; and

$p(t) = \{p_s(t); p_b(t)\}.$

Because the mass and stiffness matrices of the bridge are symmetric, the matrix for the total system is also a symmetric. The inertia of the moving vehicle is considered implicitly at the wheel-rail contact locations; thus, the associated mass matrix is time varying. The time varying quantities in the mass matrix account for the effect of vehicle mass. Neglecting those terms in the EOM will result in the moving-load problem. The off-diagonal terms in the total matrices indicate that the proposed approach can consider interactions between not only the rail and the bridge, but also interactions between each rail even if those were modeled as separate systems, initially.

The performance of the proposed hybrid model using an example of a full-scale railroad bridge will be demonstrated in the subsequent chapter.

3.3. Conclusions

This chapter developed numerical models for assessing dynamic response of a railroad bridge acted by a moving train. A traditional beam model of a bridge was first presented using the assumed modes method. Two simple numerical examples are prepared; a train composed of a single-car and multiple cars with different mass and bogie distance distributions. Bridge responses under moving- mass and load models are compared in those cases to illustrate the importance of mass effects and the appropriate modeling of a train for assessing railroad bridges. The results revealed that the moving load model could introduce significant errors in estimating the beam responses. Moreover, the train model should be able to accommodate multiple cars effectively. Then, the hybrid model has been proposed combining a finite element (FE) method of a bridge with a continuous beam model of the track so that the train loads can be applied consistently. Because the bridge responses are the major concerns in structural health monitoring of a railroad bridge, the vehicles with an arbitrary train configuration and speeds are modeled as a series of moving point masses. At the wheel locations on the rail, the mass effects are implicitly considered in the system equations. The presented approach can be employed for both single-track bridges and multi-track bridges. A two-dimensional hybrid model is suitable for single-track bridge where train loads and the responses are symmetric. A three-dimensional hybrid model is preferred when investigating the bridge dynamics for the multi-track system, which can induce asymmetric loading. The proposed approach provides an efficient way to investigate the moving-mass and moving-load effect on the bridge response under a train with arbitrary axle and bogie distances.

CHAPTER 4. MODEL VALIDATION

This section demonstrates a successful layout of the system and examples of measured data, which is then used for calibrating and validating the developed numerical models. The monitoring system was installed on a railroad bridge owned by Canadian National Railway (CN). The system comprised a set of WSSs, which the basic sensor hardware and software components were developed under Illinois Structural Health Monitoring Project (ISHMP, http://shm.cs.uiuc.edu). The uniqueness of the bridge and careful installation of the system enabled rich collection of the high-quality field data for validating the numerical model.

4.1.   Description of test bridge

The selected railroad bridge for campaign monitoring is a double-track and an open deck truss bridge, located over the Calumet River, near Chicago, Illinois (Figure 21a and b). Over the river, three active identically designed bridges are located. Among those, the West-most bridge in Figure 21b is the Metra lane, a bridge east to the Metra carries CN1 and CN2 and it is the test bridge (an arrow in Figure 21b) track, another truss bridge located the East to the test bridge carries freight and passenger trains, and the East-most bridge is closed for the traffic. The bridge is about 95 m long, 21 m tall, and 10 m wide steel bridge, made of A36 American Society for Testing and Materials (ASTM). The bridge opened for service in 1971, with an expected life of 100 years.

The North end of the bridge has fixed bearings as shown in Figure 21c, and the South end of the bridge has expansion bearings. Girder bridges extend the bridge toward the North and the South to connect the bridge to the land, which the boundary conditions are both fixed near the joints. Figure 21c shows support conditions of stingers of the North approach. On the bridge, the UIC60 type rails, shown in Figure 23, are rigidly connected with the bridge. The weight per meter of the rail is 60.3 kg

and its cross sectional area is $7.686 \times 10^{-3} m^2$. Moment of inertia about the z-axis (see Figure 23) and y-axis are 30.55×10^{-6} m^4 and 5.129×10^{-6} cm^4. Although rail defects are one of the critical components affecting the railroad bridge dynamics, the rail irregularities are neglected from the scope of study, assuming that the rail is well maintained throughout its length.

The test bridge carries two tracks, CN1 track on the West side and CN2 track on the East side, which both are open for South and North bound freight and passenger trains. About ten freight trains and six Amtrak trains run on either CN1 or CN2 track in a daily basis. Those characteristics of the bridge make the bridge suitable and unique for the test bridge: (i) the test bridge is made of steel, which is the most common type in the U.S. (53% of entire railroad bridge inventory, FRA, 2008); (ii) adjacent bridges are open to the traffic exciting the test bridge without changing mass of the bridge by carrying the train loads; and (iii) high traffic with various types of trains on the test bridge allows rich data collection from the monitoring system.
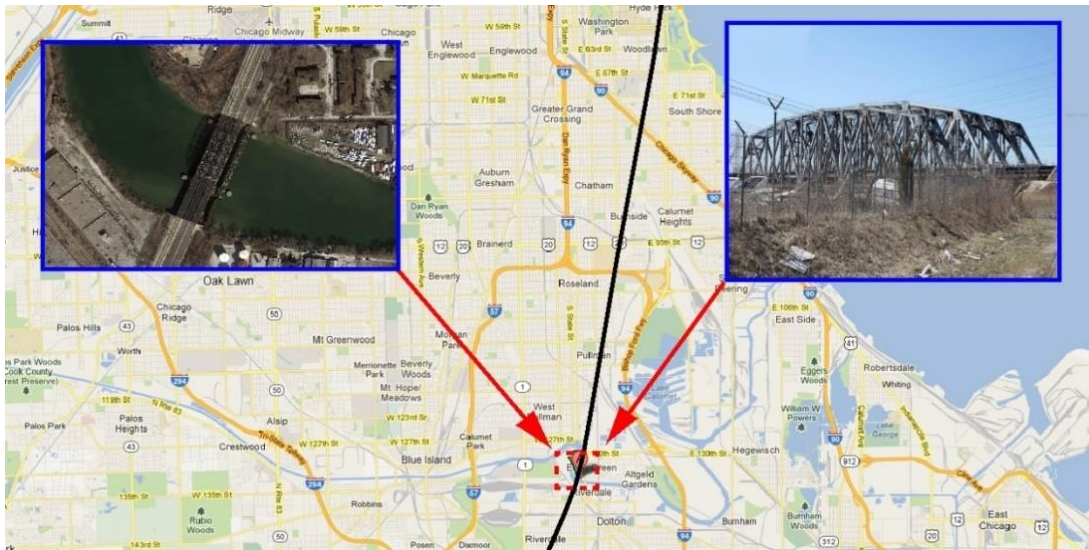
(a) Location of the Calumet Bridge.

Figure 21. Selected test bridge, near Chicago, IL[3].

---

[3] Google Maps (2014), www.maps.google.com.
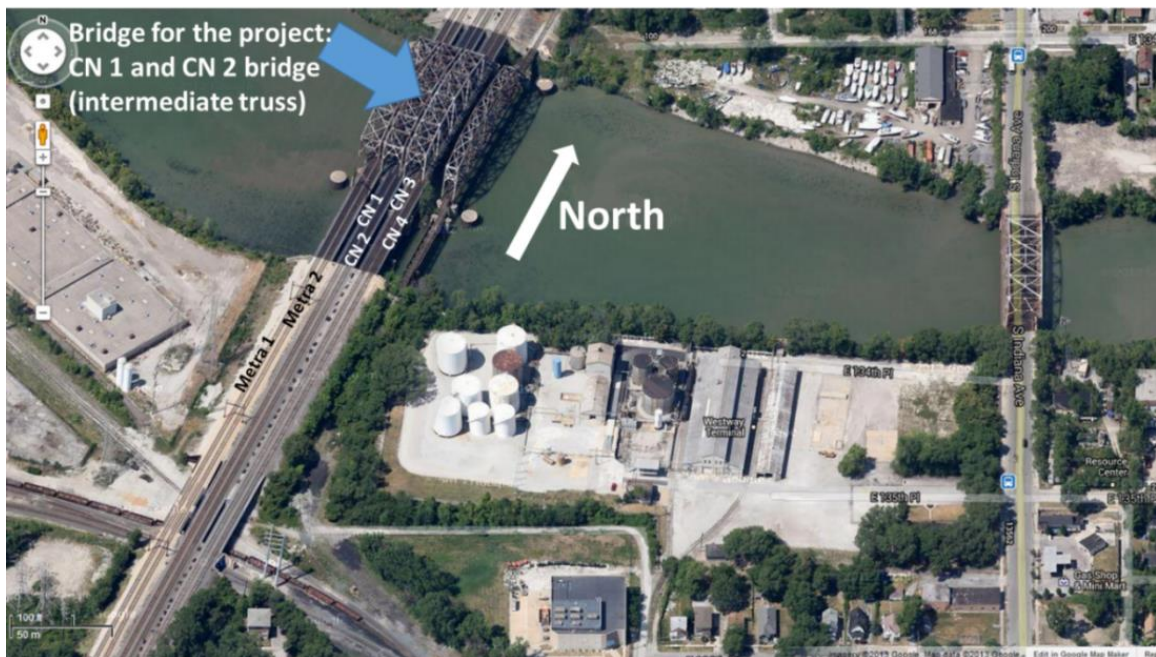
(b) Selected test bridge.

(c) The boundary condition of the bridge.

Figure 21. (cont.)

Figure 22. Stringers support condition from under the bridge[4].
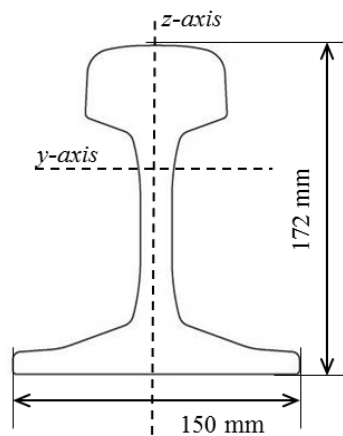
Figure 23. UIC60 rail.

4.2. Monitoring system

WSS networks implemented on the bridge aimed to establish SHM system with different types of

sensors (Kim et al. 2015; Moreu et al. 2015). The scope of this paper is a subset of the deployment,

which includes 10 accelerometers and a strain sensor. A WSS comprises an Imote2 (Figure 24a), the

wireless platform, an sensor board, depends on which type of measurements, an 2.4 GHz antenna, a

---

[4] http://www.historicbridges.org.

solar panel for energy harvesting, and two magnet bases for mounting enclosures. Figure 24b shows an example of prepared enclosure; an ISHM400 board (Figure 24c), a tri-axial accelerometer, is stacked on the Imote2 (Rice, 2008). The essential driver and software for monitoring, such as synchronization and sensing are implemented, adopting services from ISHMP Services Toolsuite. An extensive lab-scale and full-scale implementation from the past research done in ISHMP validated that the hardware and the software is suitable for the campaign-type monitoring services (Rice et al. 2010; Jo et al. 2011).

(a) Imote2.   (b) Enclosure set.   (c) ISM400 board.
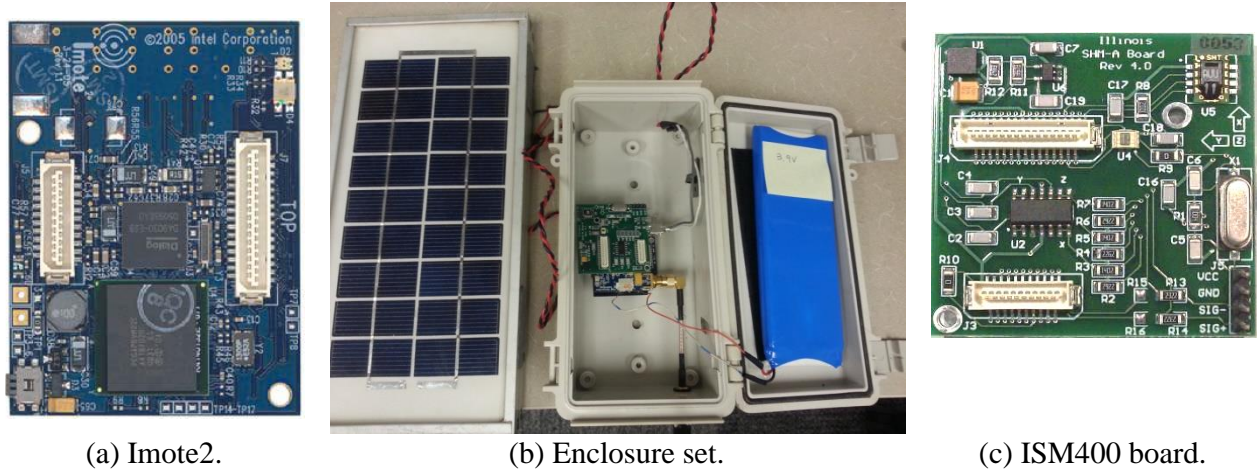
Figure 24. WSS unit.

Figure 25 shows the multi-metric WSS network map used in this thesis. Six WSS nodes with an ISM400 board, which the measurable range is up to ± 2 g, were deployed at each nodal points (A-E and -W, B-E and -W, and C-E and -W in Figure 25) of the truss bridge to provide global behavior. The sensors were located both East and West side of the bridge to provide asymmetric response behavior under train loading on one side of the track. Two WSS nodes with ISM400 board were placed on 2.1 m higher locations from C-E and C-W in Figure 25 to eliminate the spatial aliasing and to capture sway behavior of the bridge. High-sensitivity accelerometers (10 times sensitive than ISM400, Jo et al. 2012) were deployed at D-W and E locations. Jo et al. (2012) found more accurate

modal analysis results when the network uses the higher sensitivity sensor measurements as the reference signals in output-only system identification under low-level vibration. In such way, the total cost to establish a network can be smaller than installing high-sensitivity sensors at all locations, while maintaining the same quality for system identification. Ten accelerometers were synchronized in a network to collect synchronized data at user-selected frequencies (In this work, the sampling rate range from 25 Hz to 100 Hz). A strain sensor (SHM-S board) on a structural element was placed at a diagonal member, about 1.2 m South of C-W in Figure 26. The member was chosen because of its uniqueness that both tension and compression can be experienced as the train passes the bridge. In addition to the sensors on the structure, SHM-S sensors were also deployed on the rails both outside and inside the bridge. Those sensors measured the train wheel loads, but the scope of this study will only cover the measurement from the structure. Finally, a base station PC, located at the North of the bridge (E-E in Figure 25) controlled and collected two WSS networks (acceleration network and strain network). Due to the base station and cellular network connection, both campaign-type and long-term monitoring via remotely controlling the PC of the bridge were available. Thus, the system realized efficient and cost effective WSS networks tailored to monitor the global and local responses of the bridge under the train traffic.
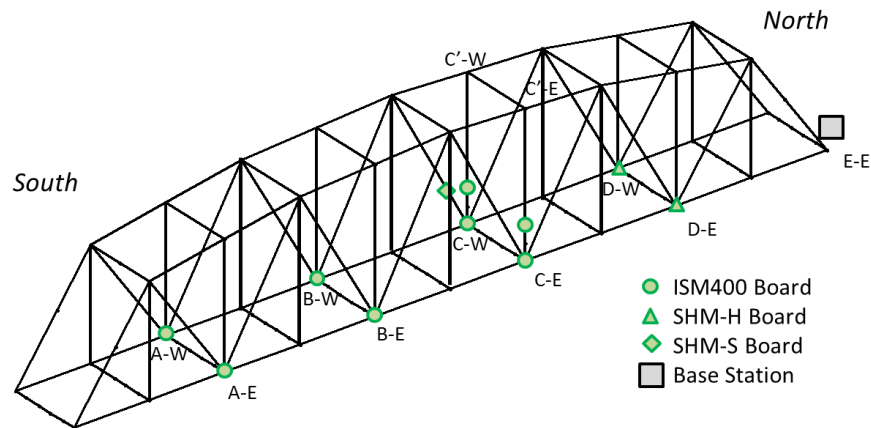
Figure 25. WSS deployment layout.

78
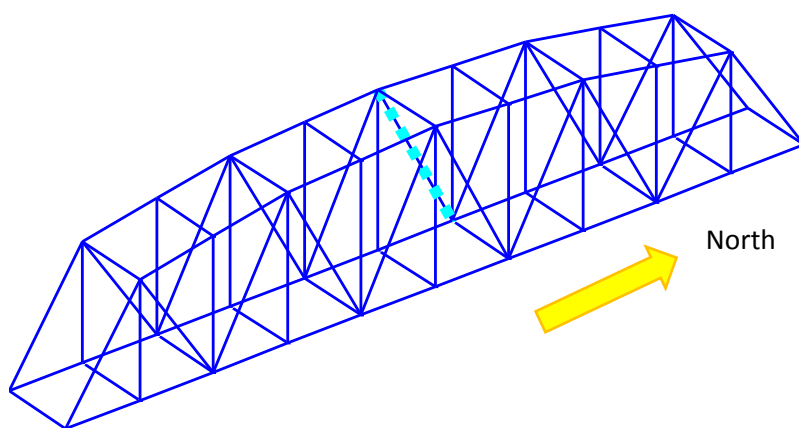
(a) The instrumented member.   (b) The sensor placement.

Figure 26. Bridge indicating the instrumented member.

4.3. Examples of measured data

In this section, examples of measured data from both campaign-type and long-term monitoring services are presented. Here, the campaign-type service refers to the system that can be easily deployed and recovered to enable real-time assessment of the bridge performance under in-service load. The long-term monitoring service refers to a permanent system that can remotely collect and control the networks.

4.3.1. Campaign-type monitoring[5]

The measurements from the monitoring system under various train traffic formed a database for system identification. Figure 27 shows an example of the acceleration response of the bridge when northbound Amtrak was passing the bridge on CN1 track at over 50 MPH. On each plot, the first vertical dashed line around 180 seconds indicates when Amtrak is entering the bridge, while the second vertical line near 190 seconds denotes exiting the bridge. As Amtrak passes the bridge, the

---

[5] Herein, speeds are denoted in MPH to be consistent with the train operational speed.

bridge is excited laterally and vertically at similar degree (±15 mg). However, relatively small accelerations in longitudinal direction inform that Amtrak did not experience much change in acceleration (e.g. neither accelerating nor breaking). Because Amtrak is light and fast, the response of the bridge is similar that under impact tests. The transient responses after Amtrak left the bridge can give rich information of the global characteristics of the bridge.
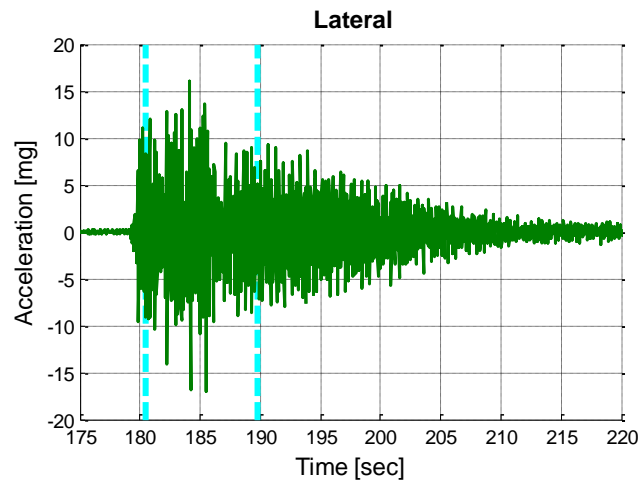
(a) Bridge response in lateral direction.
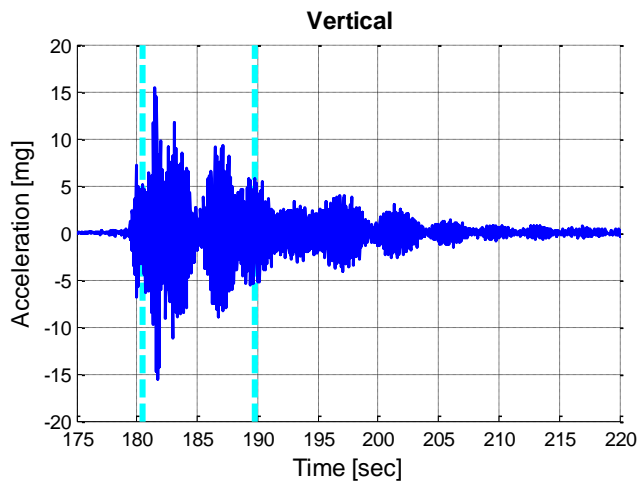
(b) Bridge response in vertical direction.

Figure 27. Bridge responses under northbound Amtrak on CN1 track measured at A-W (located near CN1 track).
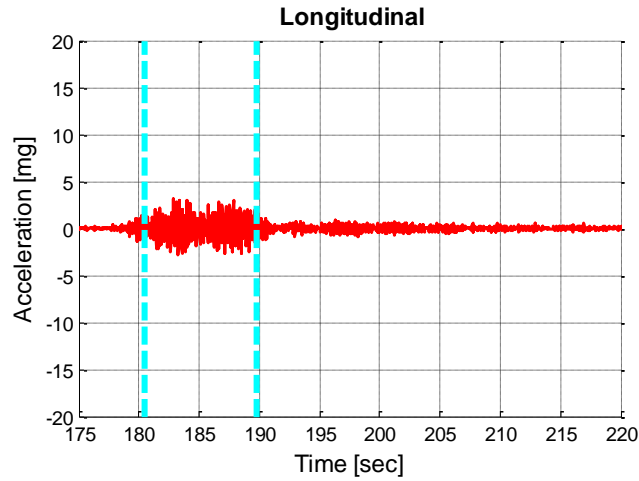
(c)Bridge response in longitudinal direction.

Figure 27. (cont.)

4.3.2. Long-term monitoring

Long-term monitoring service was available from the system due to the base station PC and cellular connections. Without having a person physically accessing the bridge, remote or autonomous control of the networks were available during the period of August, 2013 and July 2014. Data collection was performed autonomously every day in such cases:

- Each node measures voltage level and reports to the base station once a day for sustainability of the network. Sensors were set to go to a deep sleep mode with the lower voltage level (less than 3.7 V), which the sensor charges its Li-ion battery without responding to any commands from the base station.

- Measure accelerations from all WSS nodes in the network when sentry nodes detect vibration level exceed 30 mg, but less than 100 mg. The maximum daily triggering events were set three times.

81

- Measures accelerations from all WSS nodes in the network when sentry nodes detect vibration level exceed 100 mg, with maximum measurement triggered twice a day.

Figure 28 shows the summary of the voltage level measured during the monitoring period. Because of the deep sleep mode function, most nodes were inactive during the winter season (from December to mid-January), when the daylight was short and cloudy with snow. However, as the season changes, some sensors were recovered and became active. These results indicate that the current system with solar rechargeable system, can promise a sustainable long-term SHM system using WSSs.
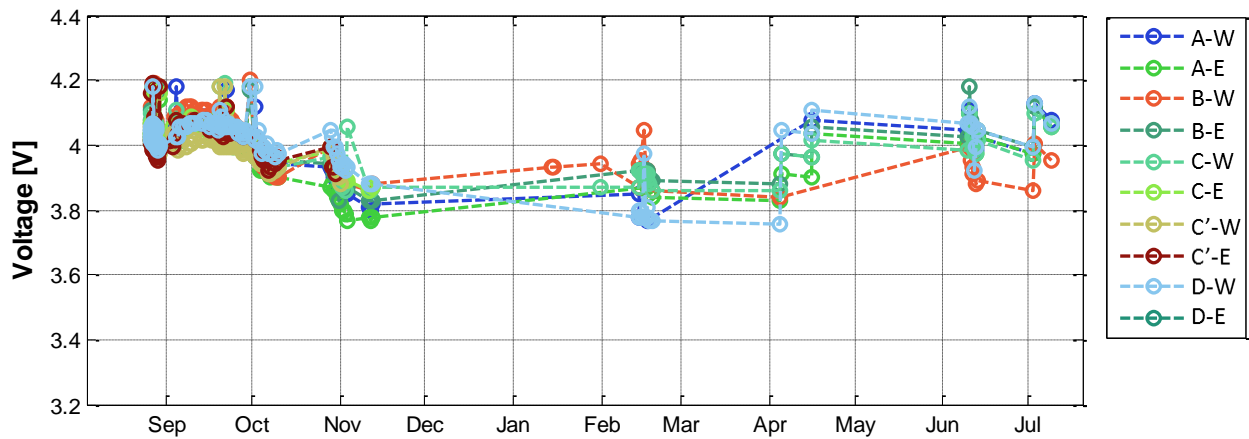
Figure 28. A summary of the voltage report from the WSS nodes.

When the networks were active, the sensors also were able to capture the train passage. An example of vertical axis vibration from September 19, 2013 is shown in Figure 29. The collected acceleration successfully captured a train passing the bridge; a train arrived the bridge around 70 seconds and left the bridge at 100 seconds. Good level of ambient vibrations is followed after the train passage. During the monitoring period, about 46 usable data sets were collected; the data should contain significant vibration level, good number of active sensor nodes, and sufficient length of sensing during transient vibration. This autonomous measurement system successfully showed

82

potential of using the methodology for easy data collection of railroad bridges without physically a

personnel accessing the bridge.
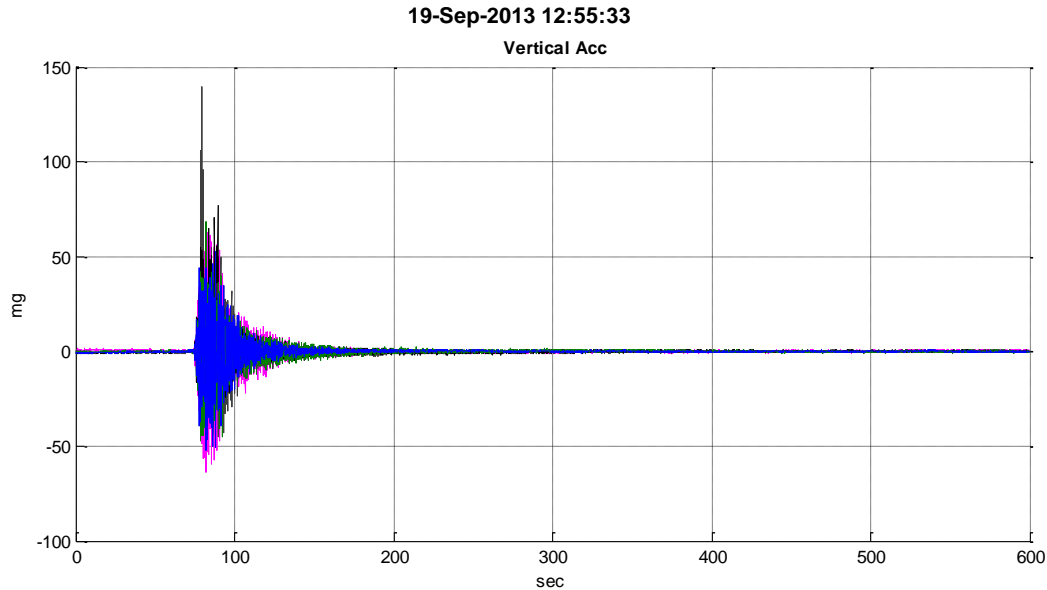
Figure 29. Measurements from the autonomous long-term monitoring service.

4.4.   System identification and model updating

4.4.1. Modal identification

In this section, system identification of the bridge using a set of signals from the acceleration network

is presented. In the modal analyses, peak-picking and NExT ERA methods are employed to find

fundamental characteristics of the bridge. Used measurements are transient responses of the bridge

after Amtrak crossed the bridge. This signal is preferred over other records, such as under or after a

freight train, because the effect of Amtrak increasing the weight of the bridge is negligible due to its

lightweight and fast speed (over 50 MPH). Figure 30(a) shows vertical responses from the West side

of WSSs, which are sampled at 25 Hz. Although the vibration level of the measurements are small,

due to light damping of the structure, the bridge experienced more than 40 seconds of gradual

decrease of the response. Figure 30(b) shows auto spectral density calculated using Hanning Window with 1024 NFFT. The line with '+' marker corresponds to the lateral vibration collected from a sensor at D-W (see Figure 26). This SHM-H sensor shows apparently lower noise level within the frequency zone of interest with clear peaks at fundamental frequencies of the bridge. To benefit the modal analyses by reducing the total noise level in the network, auto spectral density of D-W sensor was used as the reference signal in the identification of the lateral mode shapes.
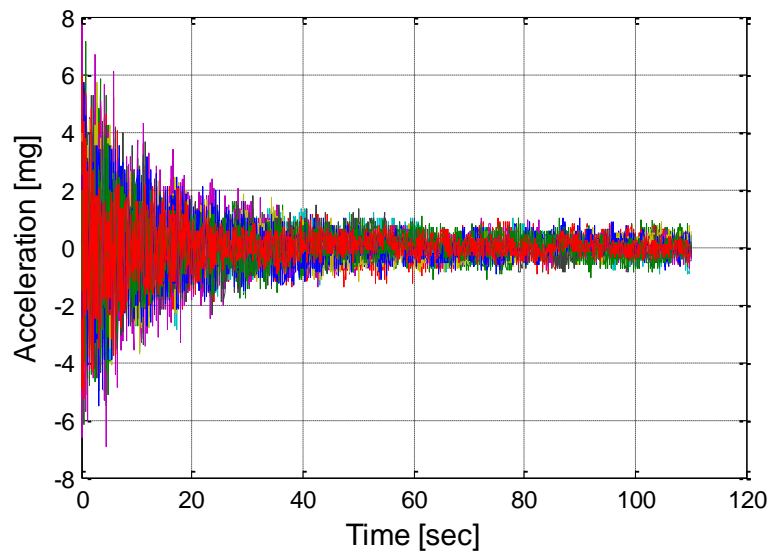
(a) Time history.
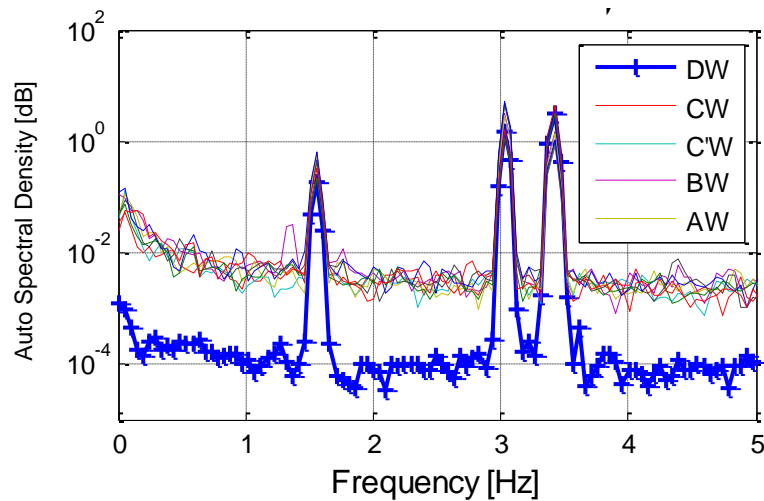
(b) Auto spectral density.

Figure 30. Vertical responses measured from the West side of the truss bridge.

Figure 31 compares mode shapes from peak-picking and NExT ERA methods. In the peak-picking method, the peaks are manually selected from auto spectral density. For visualization purposes and to ease the task of picking peaks from the reference auto spectral density, signals are regulated and divided by the minimum noise level. As a result, they end up having the same noise level. By doing so, the reference signal shows the highest amplitude at the pick. Then, mode shapes are calculated at the selected frequencies by using the reference auto spectral density.

In NExT ERA method, on the other hand, the cross correlation matrix based on the selected reference signals is calculated. Then, the system properties are extracted by employing the eigenvalue problem for the system realization matrix solved through the decomposed of the Hankel matrix (Juang and Pappa, 1986; James et al. 1993). To select only meaningful modes, those with high Extended Modal Amplitude Coherence (EMAC) are chosen (Pappa et al. 1993). Table 2 summarizes differences between natural frequencies identified in two methods. Having less than 2% differences in the results, peak-picking method can be considered as reliable and accurate as NExT ERA method while preserving simplicity and user-friendliness.

Peak-picking	NExT ERA
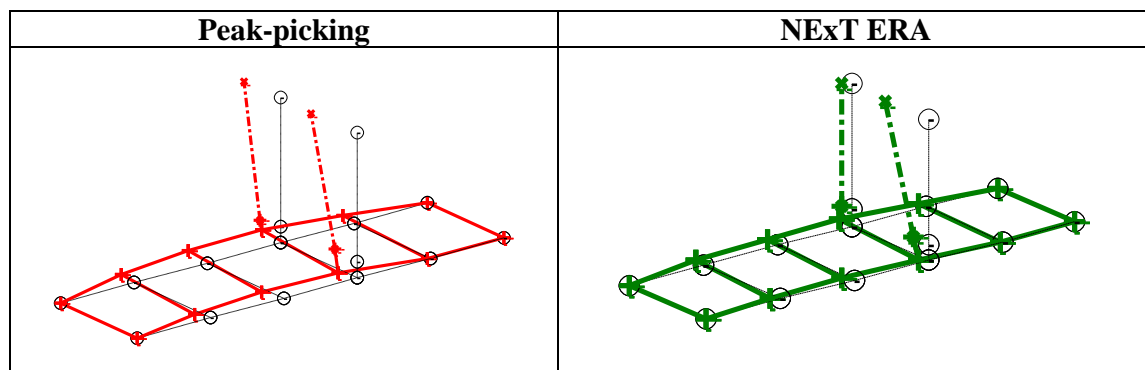
(a) The 1st lateral mode.

Figure 31. Mode shape comparison, peak-picking and NExT ERA comparison.

Peak-picking	NExT ERA
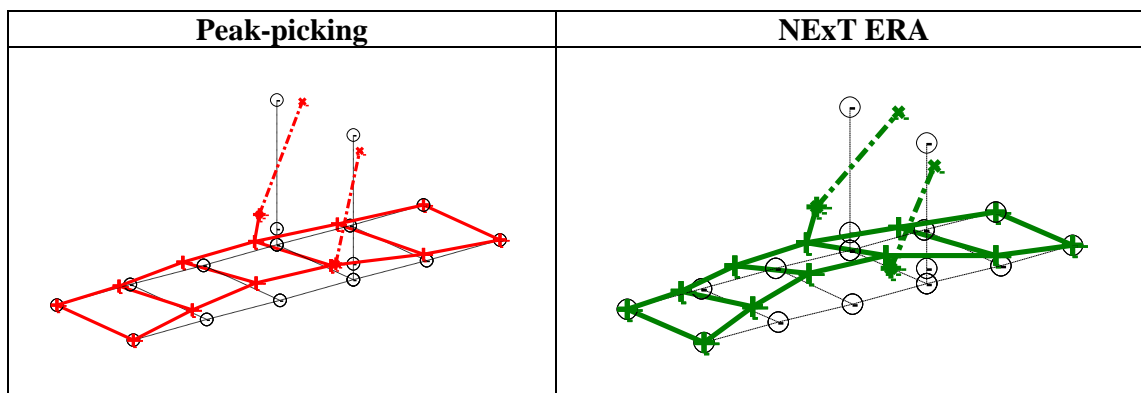
(b) The 2nd lateral mode.

Peak-picking	NExT ERA
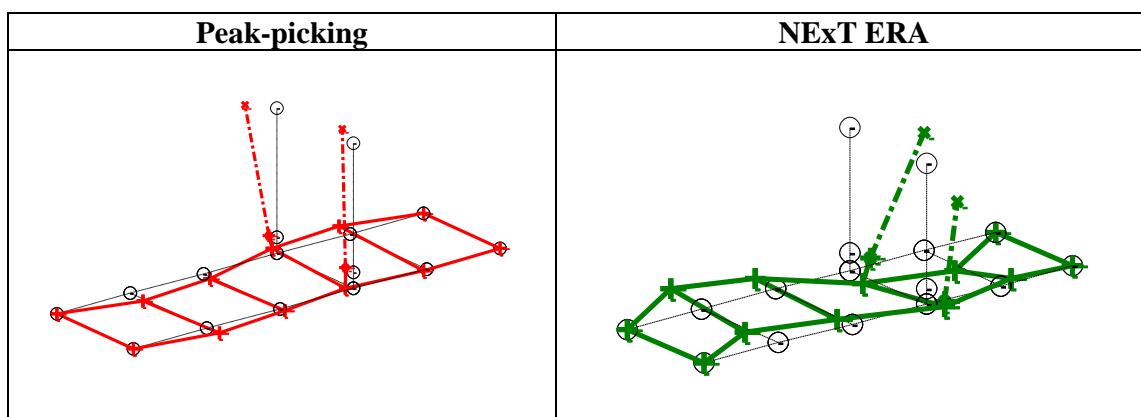
(c) The 3rd lateral mode.

Peak-picking	NExT ERA
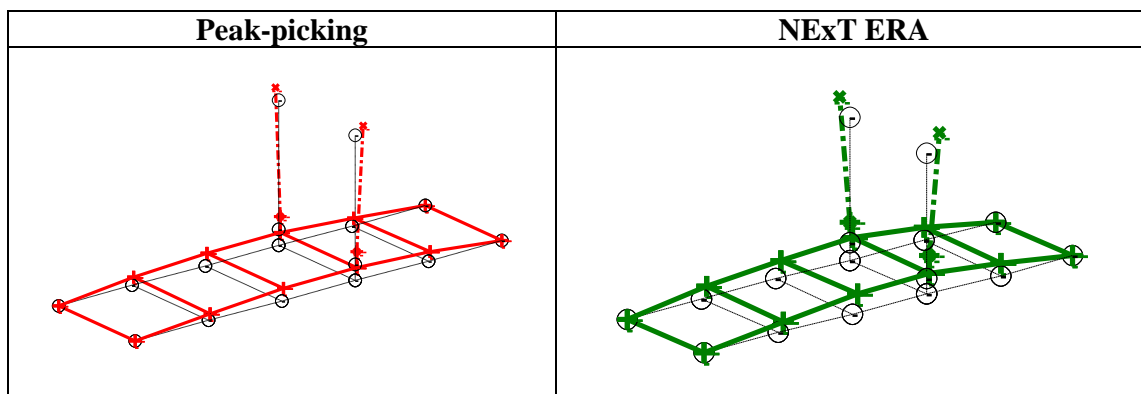
(d) The 1st vertical mode.

Figure 31. (cont.)

Table 2. Natural frequency comparisons; Peak-picking and NExT ERA comparison.

Candidate Modes	Peak-picking [Hz] (Error [%][†])	NExT ERA [Hz] <EMAC>
1st lateral	1.542 (0.065)	1.541 <99.84>
2nd lateral	3.014 (0.660)	3.034 <99.99>
3rd lateral	3.390 (0.732)	3.415 <99.99>
1st vertical	3.592 (1.756)	3.530 <99.92>

† Absolute error: A (|A-B|/B), where A = Peak-picking; B = NExT ERA.

4.4.2. Finite element model

For several decades, FE models have been widely used for simulating and assessing the structural behavior under arbitrary structural conditions. To build a model with such capability, a preliminary analytical FE model is developed in Matlab® using the shop drawings from CN's construction records. The model contains 345 nodes and 724 elements. The boundary conditions at the North and South bearing supports are pin and expandable, respectively. Nodes are frame connected, which can transfer rotational moments to adjacent elements. The initial FE model developed based on the drawing is shown in Figure 32. Table 3 summarizes first four modes identified using this model.
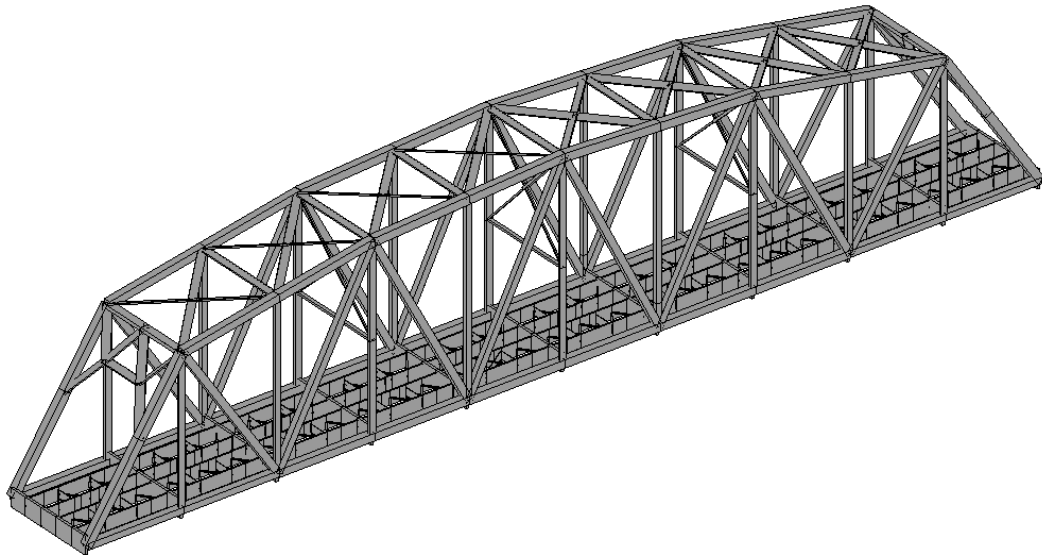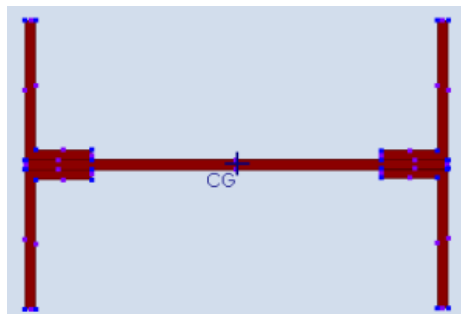
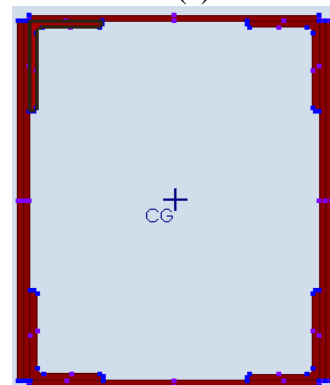**Figure 32. The bridge model.**
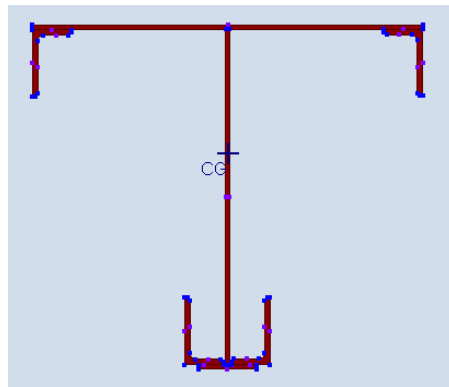
(a) Top End Bracing.
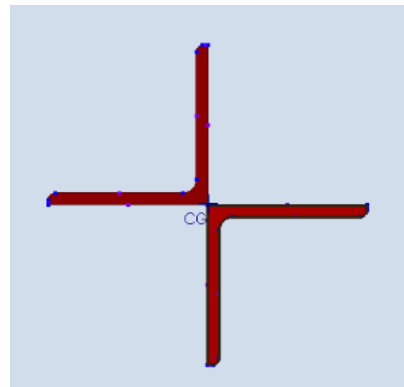
(b) Sway Frame.

(c)

(d) Vertical Member.

(e) Diagonal Member.

Figure 33. Examples of simplified cross section.

Table 3. Natural frequency comparisons between peak-picking and initial FE model.

Candidate Modes	Peak-picking [Hz]	Initial FE model [Hz]	
		Mode [Hz]	Error [%]†
1st lateral	1.542	1.819	17.96
2nd lateral	3.014	2.875	4.612
3rd lateral	3.390	3.774	11.33
1st vertical	3.592	4.025	12.05

† (|A-B|/A), where A = Peak-picking; B = FE model.

As can be seen from Table 3, the initial FE model does not fully represent the current physical state of the bridge. A part of reasons is:

- The initial model represented only the truss structure and did not include track system.

- Most main sections are built-up sections with holes on each side as shown in Figure 34. However, those details were excluded to keep the model simple.

- For brevity of the modeling, all floor systems shared the same neutral axes, while they were in fact located at different levels.

- The boundary conditions and joints between elements were modeled as shown in the drawings, but those may have been changed from the time of original construction.

Thus, the model needs to be updated to better represent the bridge. For example, the shop drawing indicated that the total weight of the bridge is approximately 11,120 kN (2500 kips), which is larger than the preliminary FE model. As discussed earlier, these differences arise from neglecting

track system, rail and fastening, lacings and other utilities (see Figure 34(a) and (b)). For example, the dead load of rail and fastening elements per track are approximately 889.64 N per meter (200 lb_F per feet; Unsworth, 2010). To accommodate the omitted mass, additional mass is distributed and lumped on the floor nodes. After updating the mass, the mass ratio between the bridge and total train represents the actual ratio; a standard Amtrak train composed of one engine and seven cars is about 20% of the bridge weight.

(a) Track system, rail, and fastening.

(b) Lacings.

Figure 34. Bridge additional mass components.

The floor system of the bridge is rigid because three layers are acting as one unit: the lower chords, the floor beams, and the stringers and bottom lateral bracings. To capture such rigidity, the

moment of inertias for those layers is calculated about one reference axis, which is the center of lower chords (see Figure 35). This calculation simplifies the complexity of modeling three layers for the floor system. The following modal analysis of the FE model with updated mass and floor system validates that the model well represents the bridge.
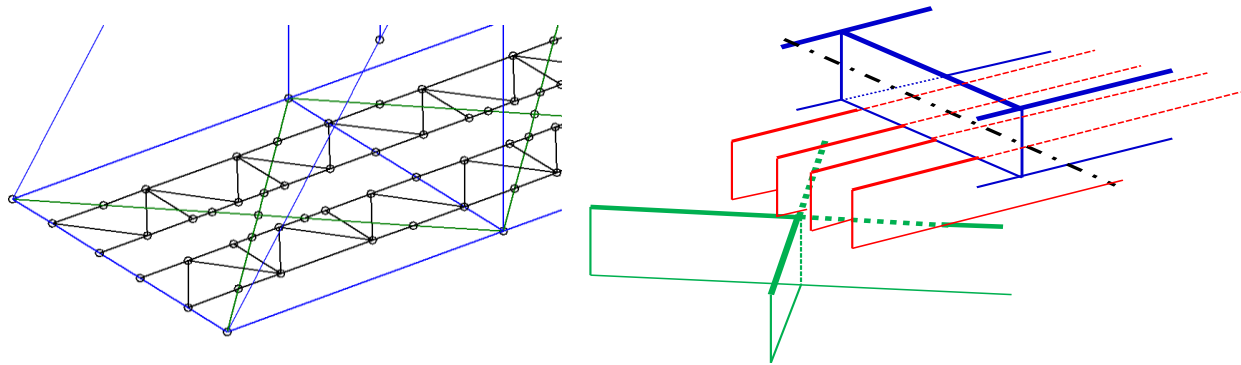

Figure 35. Floor system in detail.

Identified first four modes from the updated FE model show the fundamental dynamic characteristics of the bridge. The first, second and third lateral modes are at 1.551 Hz, 3.054 Hz, and 3.242 Hz, respectively. The first vertical mode is at 3.567 Hz. The next section will show that the model has reached sufficient level of accuracy. Therefore, employing sophisticated model updating techniques such as generic algorithm would be redundant.

4.4.3. Hybrid model development

The hybrid model for the Calumet Bridge is developed in this section using the proposed approach described in CHAPTER 3. Because the selected bridge is a double-track bridge (Figure 19), the bridge is modeled in a 3D hybrid model with frame connection at each node. As can be seen from Figure 36, the stringers are parallel to the rails and the bridge, with a small eccentricity from the rails. Because the rails are symmetrically located above the stringers, the rail displacements are assumed the same as the stringer nodal displacements. A series of diamonds (◊) in Figure 19 indicates the

stringer nodes, which a rail runs over those nodes. Damping of the rails is ignored (i.e. $\mathbf{C}_{R_1} \sim \mathbf{C}_{R_4} = 0$).

Because the cross beams at the end of the bridge are very stiff, the displacements of the stringers are assumed to be zero vertically at the support nodes (see Figure 22). Therefore, sine functions up to the fifth mode are chosen as shape functions. No rail irregularities are introduced at this time. Using the bridge FE model, rail locations, boundary conditions, and admissible functions, a hybrid model described in Eqn. (24) is determined. Note that crossties have been neglected in the modeling and their effect is assumed negligible for this analysis.
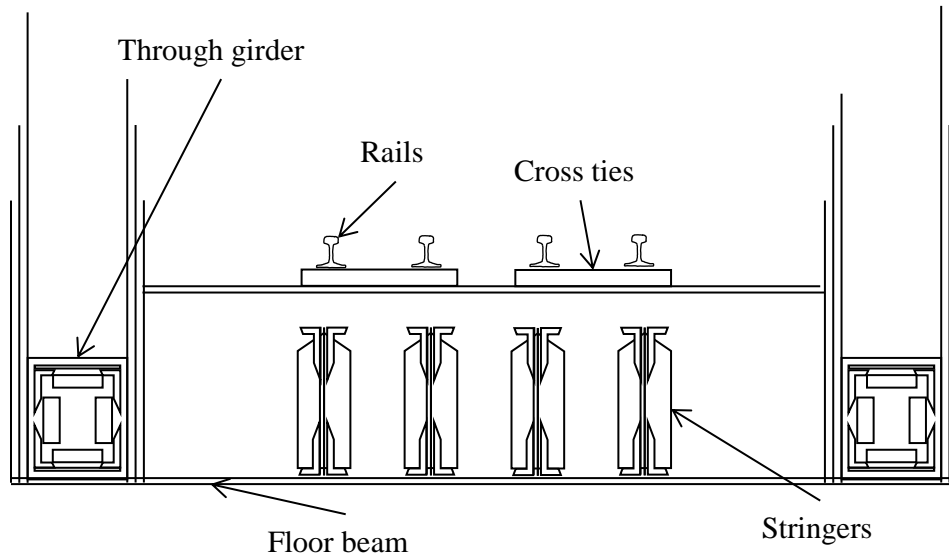
Figure 36. Illustration of cross section of the Calumet Bridge.

4.5. Model Validation

4.5.1. Model validation with global responses

To validate that the FE model can represent the bridge performance in global sense, numerically identified natural frequencies and their mode shapes are compared with experimentally identified results under transient responses after Amtrak, as shown in Figure 37. For efficient visualization, the first column shows the deformed mode shapes of global nodes. To reduce the spatial aliasing, the

second column shows the deformed mode shapes using the deformations only at the locations of the WSSs. The mode shapes in the third column are experimentally identified, with linear extension of the upper chords where the higher sensors are located 2.1 m higher from the bottom chord (dashed-line in the third column). The mode shapes in the FE model agree well with the mode shapes obtained experimentally.
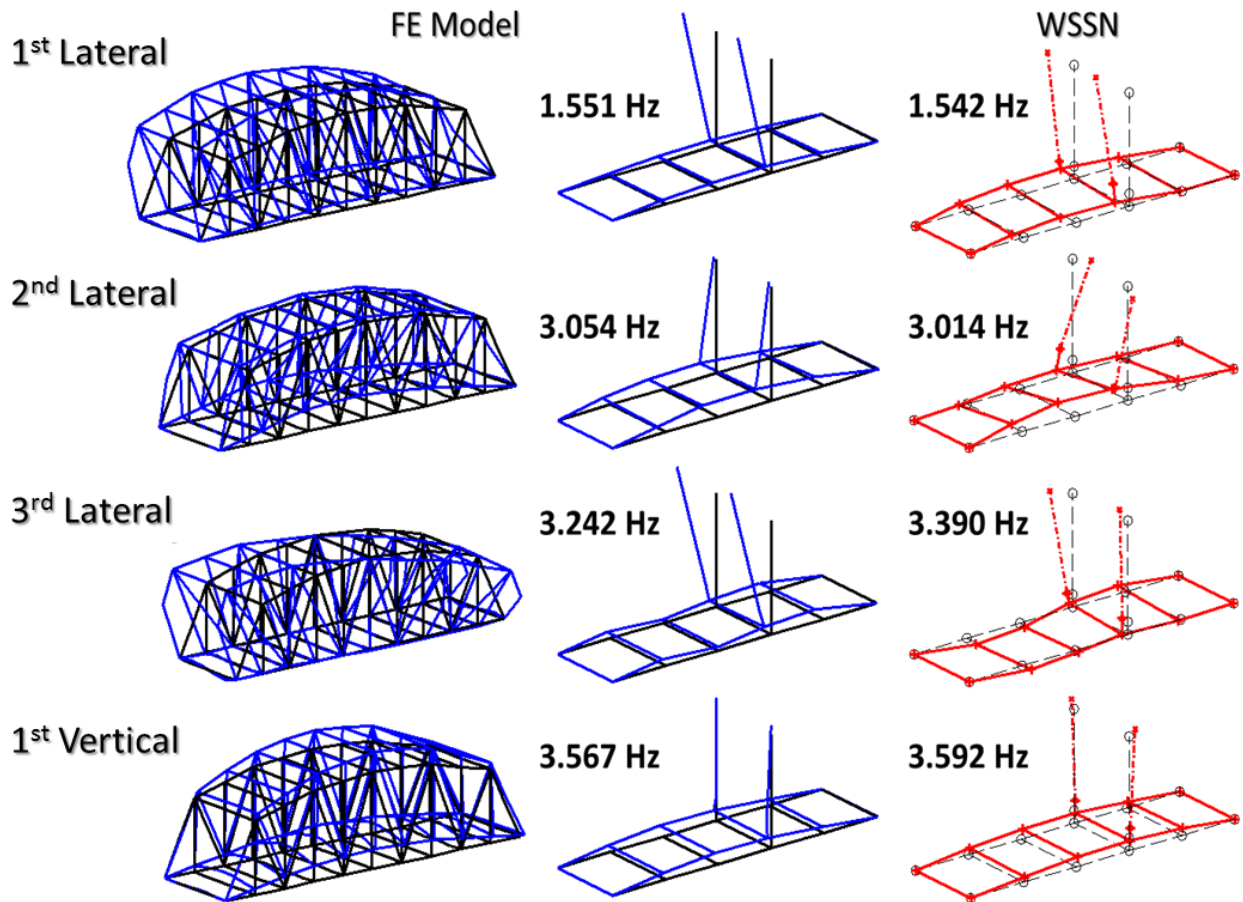

Figure 37. Modal analysis comparison with FE model.

Table 4 summarizes the frequencies at each mode. The model shows a good agreement with the experimentally derived data, with an error of less than 5% for all modes. In addition, numerically obtained mode shapes are correlated with the experimental ones using the modal assurance criterion (MAC). MAC values obtained between the first four mode shapes are shown in Table 3. All modes

93

show MAC values over 90%, indicating that the model well represents the bridge in a global sense. The following section will demonstrate the accuracy of the model in simulating local responses of the bridge, which is important for assessing the state of the bridge under an arbitrary trainload.

Table 4. Mode comparison.

	Peak-picking: WSSN [Hz]	FE model	
		[Hz] (Error [%])†	MAC [%]
1st Lateral	1.542	1.551 (0.584)	91.34
2nd Lateral	3.014	3.054 (1.327)	94.17
3rd Lateral	3.390	3.242 (4.366)	90.97
1st Vertical	3.592	3.567 (0.696)	98.38

† Absolute error: A ($|$A-B$|$/B), where A = Peak-picking; B = FE model.

4.5.2. Model validation using local responses

The predictive capability of the numerical model in local sense is important; a model that can well represent the bridge globally not necessarily can capture local responses. Thus, this section uses measured field strain from a diagonal truss element to validate the local predictability of the models at the axial strain level (see Figure 25 for an instrumented member location). A train crossed the bridge, which the wheel loads were estimated from the strain measurement on the rail. Throughout the experiments, Two WSS networks measured acceleration and strain as the test train moves along the bridge. To reduce the high-frequency noise in the measurements and to have basic response of the bridge, the measured signals were downsampled to have up to 50 Hz frequency components.

Dynamic analysis of the proposed model has been conducted to demonstrate its predictive capability. The simulations are performed by substituting the rail shear to a wheel load in put in the hybrid model, shown in Eqn. (24). First, the assumed modes using sine functions up to fifth modes were used to model the rail and the sample time was $\Delta t = 0.02$ sec. Figure 38 compares the estimated member strain from the hybrid model and the measured strain from the field test. The estimated maximum compression (-72.09 µε) and tension ($+74.99$ µε) strains match well with those from the measurements. In the measured data, the maximum compression and tension strains are -70.32 µε, $+77.38$ µε, respectively. Although maximum strain values are well captured, local peaks, especially about 2 Hz period peaks between 12 and 18 seconds in the plot, are found to be less accurate in the model. To improve the predictive capability of the hybrid model, several adjustments can be made, as will be presented in the subsequent parts.
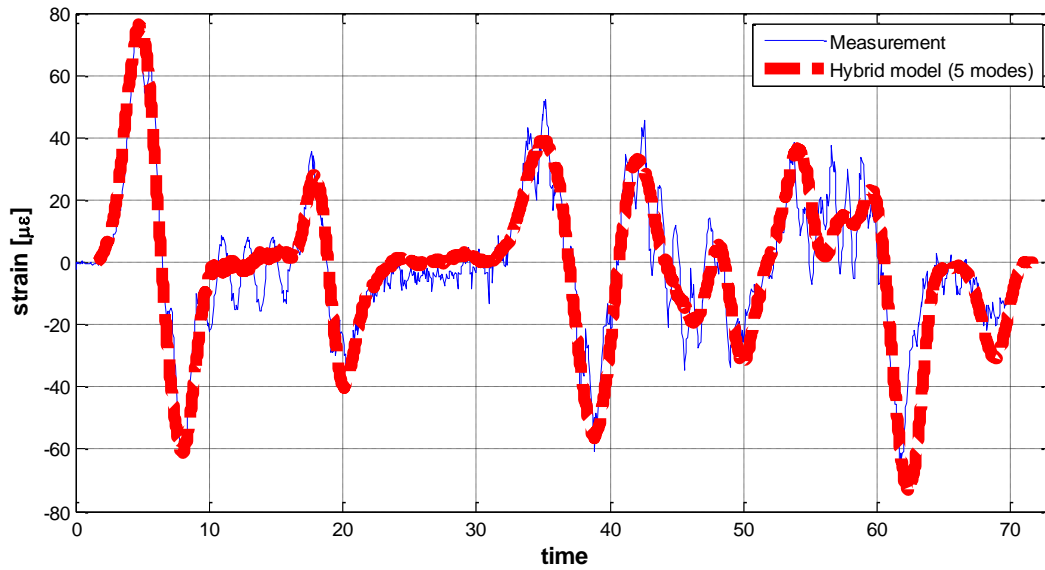

Figure 38. Strain comparison between the hybrid model and measured response.

Refine time step and increase number of assumed modes

The rails were originally modeled using five sine functions (i.e., $N = 5$ in Eqn. (25)) and the simulation time step was 0.02 seconds. However, because the length of the rail was from one end to the other end of the bridge, capturing localized deformation of the rail with only 5 modes at such rough time step may not be sufficient.

$$u(x,t) = \sum_{i=1}^{N} \mathbf{N}_i(x) q_i(t) \tag{25}$$

First, a smaller simulation time step was investigated. Although the time step was refined from 0.02 seconds to 0.01 seconds, only minor differences were found. Thus, time step is not an issue for improving the accuracy of the model. Next, the number of modes are expanded to contain higher modes. Figure 39 compares the results obtained from hybrid model using $N=5$, 10, and 20 modes of sine functions in Eqn. (25). Having 10 modes improved the dynamic responses of the bridge by showing more oscillations in the strain peaks, i.e. between 10 to 18 seconds in the results. Having higher modes also increased the peak strain amplitude slightly. In addition, having 10 modes is sufficient in this problem, showing converging results in 20 modes. Amplitudes at the peaks are also well matched in both 10 modes and 20 modes cases.
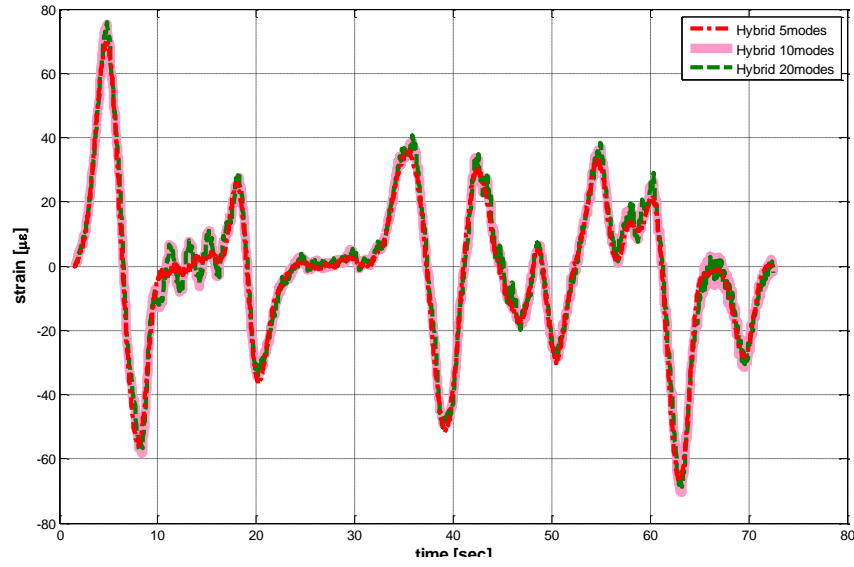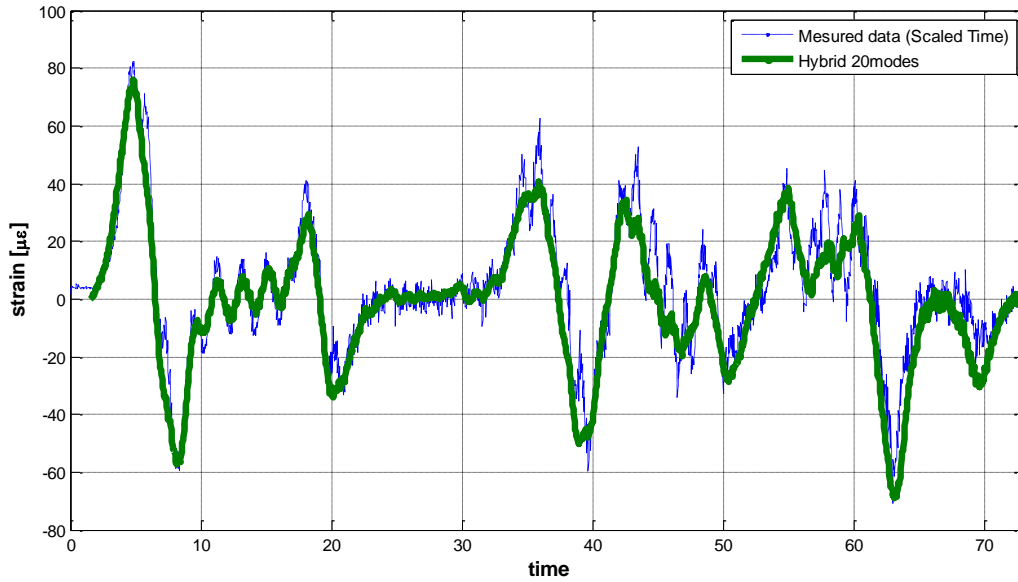
Figure 39. Hybrid model comparison.

Figure 40. Hybrid model in comparison with measured signal.

Then, results from the hybrid model using 20 modes of the assumed modes method are compared with measured signals (Figure 40). To eliminate the error in the measured signals induced from imperfection of the rail and/or rolling of train, a low-pass filter has been applied to the signals, which will allow having the basic responses of the bridge. The model now well captures the strain

trends much better and show the strain peaks occurring between 10 to 18 seconds. This result indicates that to understand bridge dynamics appropriately using proposed hybrid model, having a sufficient number of modes in the rail model is essential.

Damping coefficients

Damping coefficient has been initially estimated to be about 0.5% using the measured transient response of the Calumet Bridge. Such a small damping ratio is typical for a lightly damped truss-type railroad bridge. However, to verify whether the damping has not been over-predicted resulting in error in the simulation, results from different damping coefficients are compared in Figure 41. In the simulation, dynamic analyses using initial damping coefficient ξ=0.5% are compared with ξ=0.3% result. Showing very similar trends for two cases, one can conclude that the initial estimated damping is appropriate and damping has insignificant impact to the bridge dynamic response under a moving train.
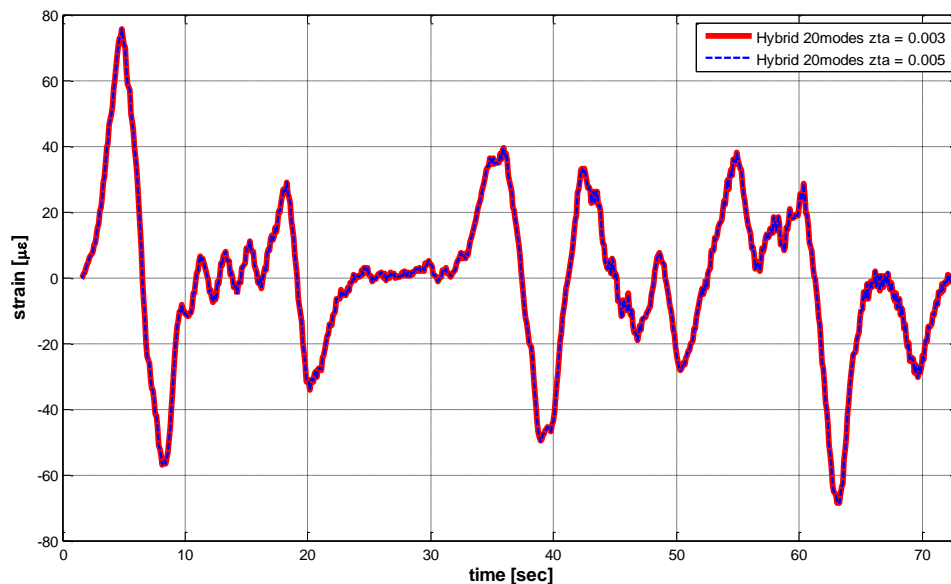

Figure 41. Model comparison varying damping coefficients.

__Power spectrum density of error (between measured and simulated results)__

To better understand the differences in the measured data and estimated signal in Figure 40, a frequency analysis is conducted. Figure 42 shows the PSD of the errors between measured signals and simulated results. The measured signals have been downsampled to have the same time-step as in the simulation. The reference time, at which time one can consider that the measurement and simulation started, is obtained by calculating / searching the least square errors of the two. Thus, the plot in Figure 42 represents the frequencies at which the model could not capture. Figure 42 shows the error the PSD over the entire time record (i.e., $t = 0$ to 73 seconds in Figure 40). Although one can find that the records around 0.9 Hz and 9.5 Hz are the frequencies that are mostly uncaptured, the plot may have averaged the error throughout the entire period. Thus, the signals have been divided into two parts; Figure 42b shows the PSD error using $t < 34$ seconds; Figure 42c shows the PSD error using $t > 34$ seconds. Considering that less than 0.1Hz signals are noise, Figure 42b shows the highest peak at 0.55 Hz, whereas Figure 42c occurred at 0.90 Hz. In addition, Figure 42c shows some peaks at 9.52 Hz, which does not appear in Figure 42b. Thus, one can conclude that errors in 0.5 Hz, 0.9 Hz, and 9.52 Hz ranges are related to specific train cars, rather than the model error. Errors at smaller frequencies (0.5 Hz and 0.9 Hz) may be more related to wheelset imperfection and at larger (9 Hz) may be more related to a car vibration.
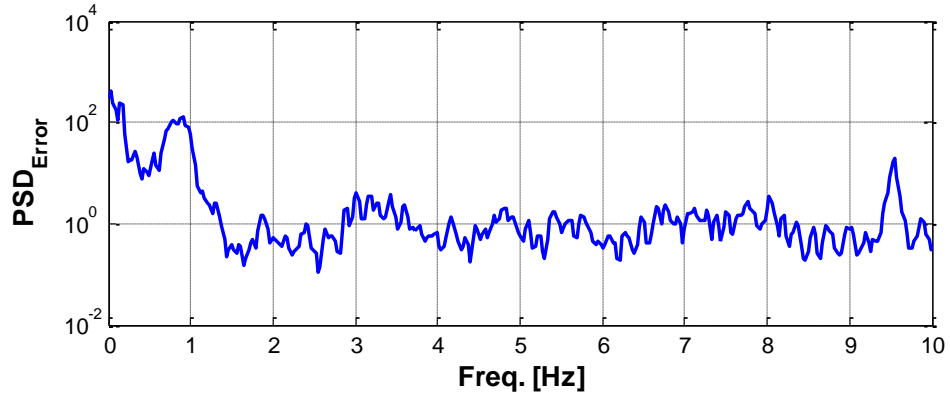
(a) The PSD$_{Error}$ using entire time domain.
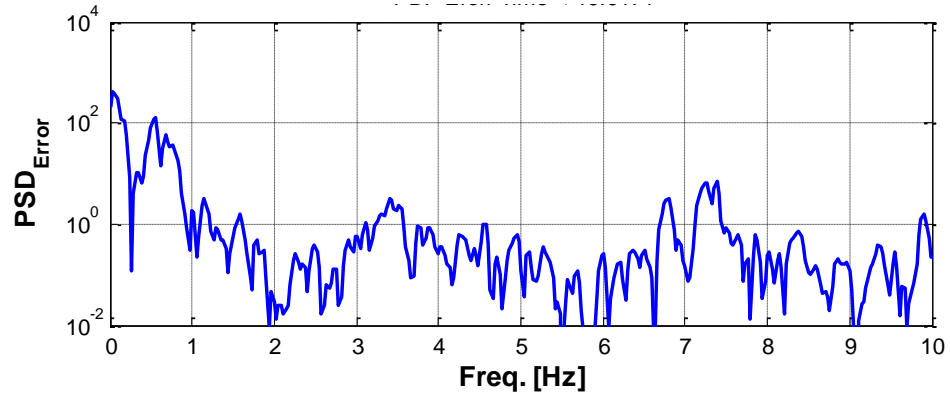
(b) The PSD$_{Error}$ using signals up to t=34 seconds.
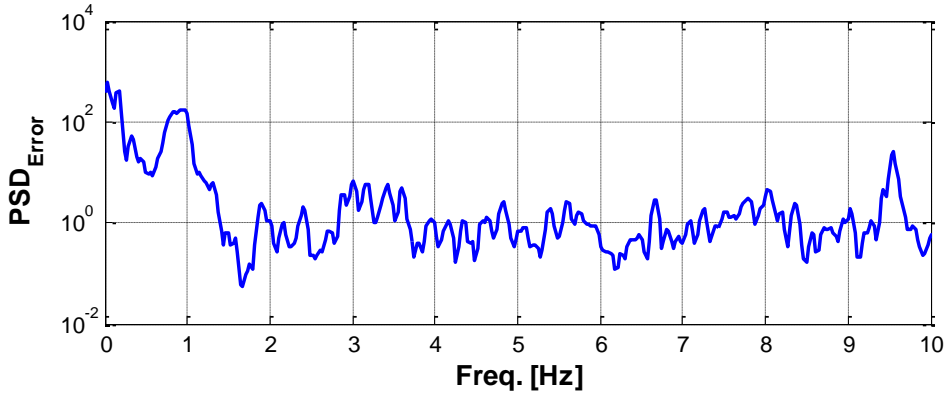

(c) The PSD$_{Error}$ using signals from t=34 seconds.

**Figure 42. The PSD of error.**

Measurement dynamics (Rail shear from inside the bridge)

For the brevity of the computation, input forces are estimated as such; peaks are selected from the

signal (marked as triangle in Figure 43a) if (i) two successive peaks are apart by about 1 ft with each

other and (ii) strain readings are exceeding 40 micro strain. However, as can be seen in Figure 43b, some peaks that might affect the bridge dynamics are unpicked. The reasoning of those double peaks are not clear, while speculations such as wheel imperfection, wheel flats, ovalization of wheel, and rail irregularities can be made.
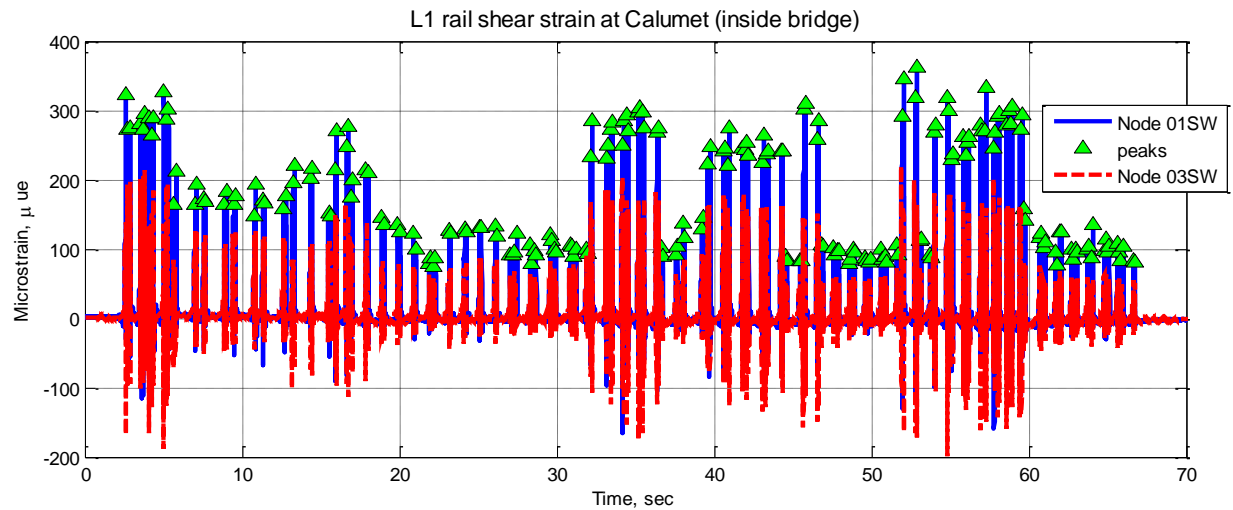
(a) Measured rail shear and selected peaks.
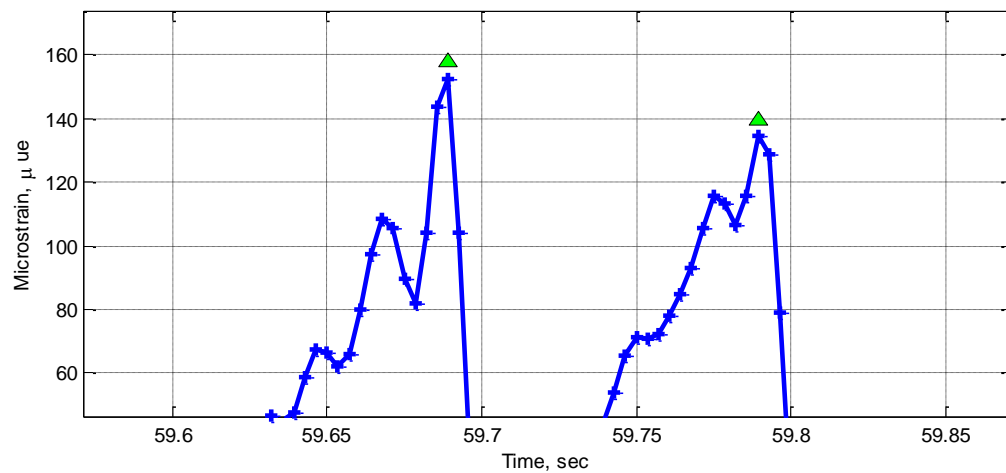
(b) Measured rail shear with unselected peaks.

Figure 43. Rail shear measured from the inside the bridge.

To better visualize the dynamics of the rail shear, Figure 44 plots the PSD of the measured signal. Similar to the previous approach, the signals are first down sampled to 30 Hz and then divided

101

into two; signals before and after t = 34 seconds. Figure 44b show the high PSD peak at near 1 Hz, indicating that the train cars approached after 34 seconds contained the vehicle dynamics, which excited the bridge at about 1Hz. Note that harmonic roll of a train car can be caused at 0.8~1.2 Hz (Moreu et al, 2014). However, 9Hz signals are invisible from the input, indicating that 9 Hz signal may have related to the specific locations of the rail (i.e., rail irregularities), double peaks in the input, or the accelerating or breaking of the train engine.
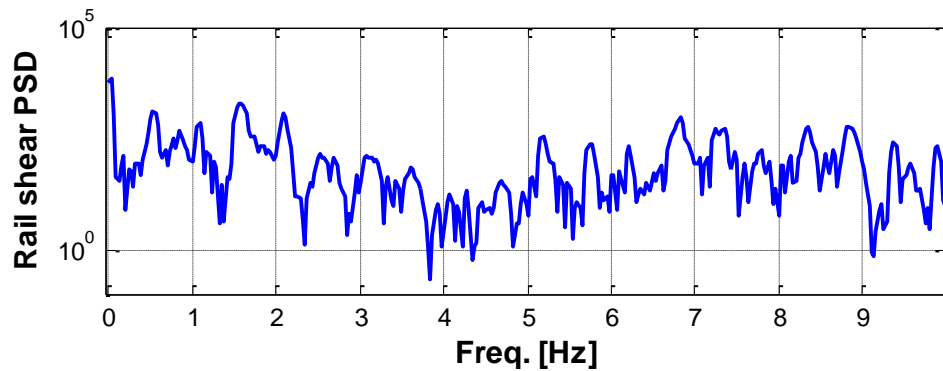
(a) Rail shear using signals up to *t*=34 seconds.
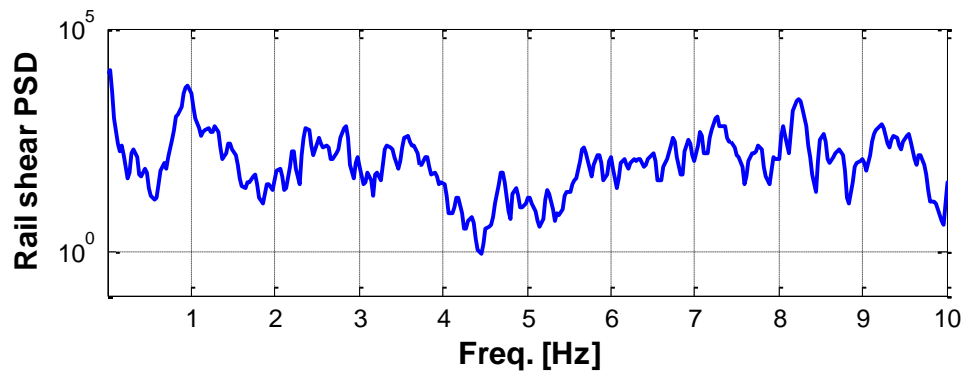
(b) Rail shear using signals after *t*=34 seconds.

Figure 44. Rail shear PSD.

Another Train: Freight car II

During the period of long-term monitoring, another freight train (noted as freight car II, herein) crossed the bridge at 9MPH containing over 200 train cars. The records are compared with the estimated results, which the simulation was performed using 10 modes of assumed modes. Time history of the hybrid model well matches the most peaks in the measured signals as shown in Figure 45. Especially, when looked at the PSD of each results, the hybrid model captured the low-frequencies, i.e., 0.03 Hz and 0.19 Hz (see Figure 46). Note that for better comparison both signals are resampled at 10 Hz. The results validate the predictive capability of the model at lower frequencies, using simple estimation of wheel loads.
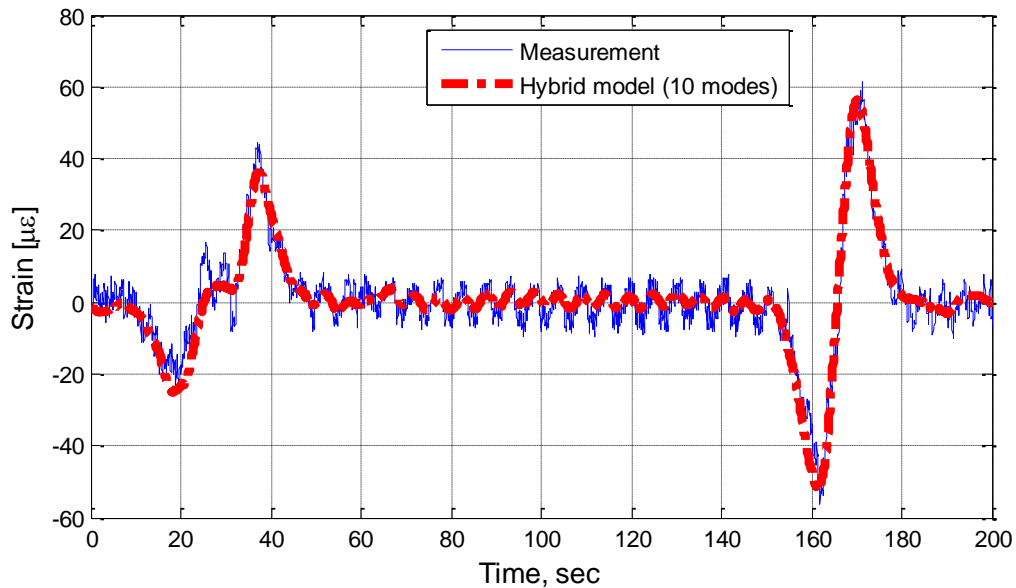

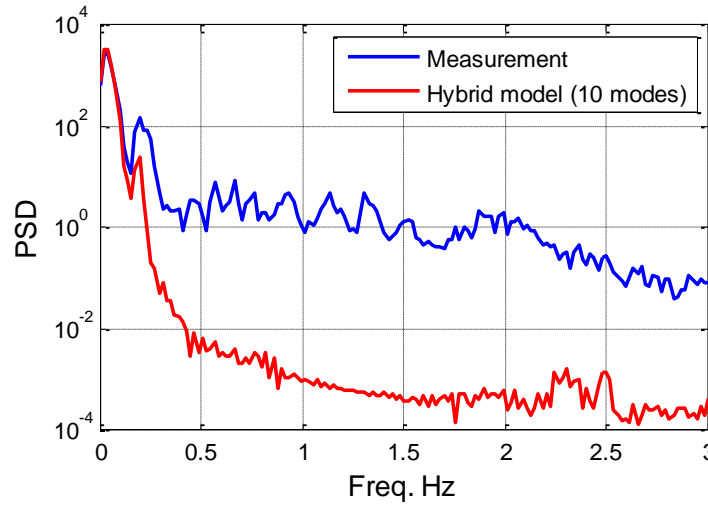**Figure 45. Freight car II crossing the bridge at 9 MPH.**

Figure 46. The PSD of Freight car II.

Now, to see if the errors between measured signal and estimated strain show similar trends as with the previous freight train, the frequency analysis are conducted. Each signal is downsampled at 20 Hz to have the same time-step. Then, the simulation start time has been searched to find the minimum least-square error of the two. Figure 47a plots the PSD of the input (rail shear) and Figure 47b shows the PSD error. The results show that because the input do not contain 1 Hz signal, the error has the low PSD power at 1 Hz. In addition, low power in the error PSD indicates the simulation results are accurate. Because the train started at very low speed, 9 MPH, while crossing the bridge, changes in the train dynamics may have been lesser than the previous example. Thus, in conclusion, the hybrid model can capture general characteristics of the bridge response under moving train, while errors between measured and estimated strain might have been originated from train car dynamics, such as acceleration, breaking, and/or wheel imperfection.
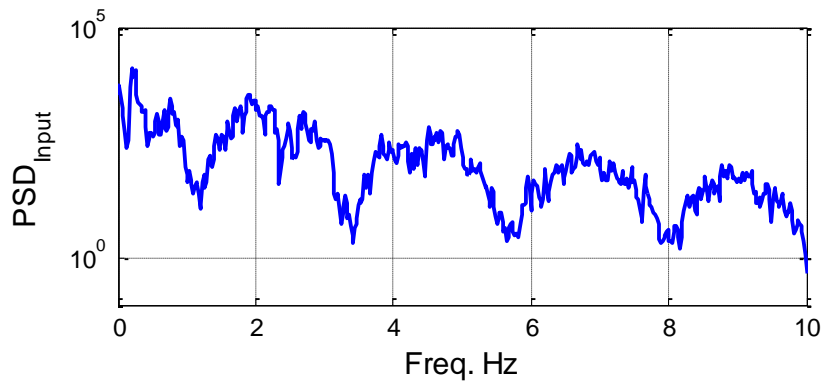
(a) The input PSD (rail shear).
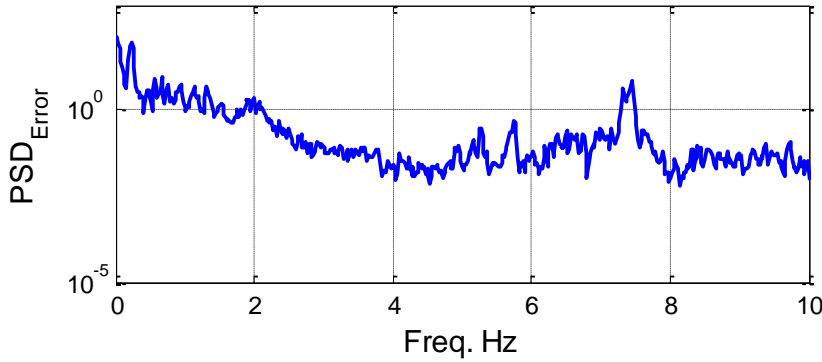
(b) The error PSD between measured and estimated.

Figure 47. The PSD error for freight car II.

4.6. Conclusion

This chapter successfully demonstrated the potentials of using WSSs for SHM railroad bridges. The first part of this chapter demonstrated the implementation of SHM system using WSSs on an in-service railroad bridge near Chicago IL. Careful selection of sensor locations optimized the number of sensors and their locations. The final deployment of the WSS yielded the most important information and reduced the spatial aliasing, with fixed number of sensors. The system supported both campaign type (temporal/short-term installation) and long-term monitoring (permanent installation) services. The long-term monitoring service provided a basis for developing a database of

railroad bridge behavior without having personnel physically accessing the bridge. Such a rich database enabled identification of fundamental characteristics of the bridge.

Then, field data is used to update the FE model. A preliminary FE model following CN bridge drawings was developed. Collected information from the monitoring system was used to update the FE model. The final model closely matched with the experimentally derived natural frequencies and mode shapes.

The subsequent section validated the proposed hybrid models in estimating local response of the bridge responses at the element level. Dynamic analyses were employed using up to five sine functions for the assumed modes of rail, firstly. Although the results showed good agreements in estimating maximum strain, some local strains were not sufficiently accurate. Thus, in an effort to enhance the predictive capability of the hybrid model for estimating member axial strain, the following factors have been studied:

- o **Time step:** Refining time step from 0.02 seconds to 0.01 second showed little impact to the dynamics of the bridge responses.

- o **The number of assumed modes**: Using increased number of modes enhanced the predictive capability of the model. However, as computation time increases with larger number of modes, using a sufficient number is efficient; in this specific example, modes up to 10 was found to be appropriate.

- o **Damping coefficients**: Damping coefficient was initially estimated empirically. Using lighter damping did not affect dynamic responses of the bridge significantly.

- o **The power spectral density (PSD) in error**: Looking at the PSD of error between measured and simulated results, one could identify the frequencies at which the model was not able to capture. In this specific example, the frequencies at 1 Hz and 9 Hz were

not found. Further investigation showed the possibility of the errors correlated to the train cars approached after 34 seconds.

o **Measurement dynamics**: To illustrate that the unestimated frequencies may have arose from input, the PDF of rail shear signals are studied. The PSD of the input signal after 34 second contained 1 Hz signal, indicating that the error was induced by the input excitation.

o **Comparison with another train record**: To validate that the estimation errors are related to specific train car dynamics, the simulation results using another train that ran at much lower speeds are examined. The PSD of input and output errors between measured and estimated are compared. Specific characteristics of the input PSD are not shown at the error PSD indicating most features have been well captured.

Thus, the hybrid model can estimate the local dynamics of the bridge under moving train with high accuracy. However, because the hybrid model assumes that the train runs over the bridge at a constant speed and neglects other dynamics of the train cars, errors can be introduced when the train breaks, accelerates, or contains an imperfect wheel. Future direction to further address the issues will be: (i) instrument various locations of the bridge. Study presented in the thesis only used one diagonal element for model validation. Using multiple locations would help understanding dynamic responses of the bridge more; and (ii) Inclusion of vehicle dynamics: the vehicle dynamics have little impact to the bridge dynamics. However, studies presented in this part revealed that to improve the predictive capability of the hybrid model, introducing vehicle dynamics is beneficial.

Overall, this chapter successfully demonstrated that proposed models are efficient tools for assessing the maximum stress of a member, promising potentials of adopting the approach in monitoring/ detecting local damage, such as fatigue using WSSs.

CHAPTER 5. MODEL INTERPRETATION

This chapter demonstrates the use of the calibrated bridge model for predicting its dynamic responses under arbitrary train scenarios. The section first examines the strain estimation for fatigue, which is one of the critical causes of bridge failure. Based on dynamic analyses of a hybrid moving mass model, a fatigue strain map, which can determine the maximum stresses/strain at arbitrary locations on the bridge, is presented. Then, critical speeds of a train, which can induce resonance vibration of a bridge is explored. Comparisons between the hybrid moving-mass and load models are presented to illustrate the limitation of the moving-load model. Finally, results from a simple beam model are compared, to highlight the applicability of simple mode for predicting dynamic responses of the bridge.

5.1. Strain estimation for fatigue

Fatigue is a progressive and localized damage mechanism, which is one of the most critical causes of steel bridge structures (Fisher, 1984). The designed fatigue life of a steel bridge component is based on the estimated stress history that the member will experience during its life period and durability. Changes in vehicle loads, speeds, and volumes of traffic, in the presence of changing structural conditions, can influence the fatigue life of the bridge (Alampalli, 2006). In addition, most railroad bridges built early 1900s have been designed to carry a percentage a static train loading of those times and not have considered fatigue stress; fatigue life estimation of existing railroad bridges is important for enhancing public safety.

The most direct and accurate way to assess the remaining fatigue life of a bridge member is using measured field strain data (Zhou 2006, Kuhn et al. 2008). However, to apply stress accumulation algorithms such as Palmgren-Miner rule, the entire strain history of the member is

required, which is impractical (Jo and Spencer, 2014). Downing and Socie (1982) proposed a 'one-pass' rainflow-counting algorithm which can be applied for a partial strain history. However, because inspecting every member in a bridge can increase total cost for installation, assessing a full-scale railroad bridge is still challenging. Alternatively, Papadimitriou et al. (2010) proposed a model-based fatigue life estimation of an unmeasured member adopting the Kalman filter. The proposed method demonstrated potentials of using calibrated numerical model and measured strain for estimating an arbitrary locations of the truss bridge.

Because the primary load on the railroad bridges is the train, measuring input force to the bridge is relatively easy; a strain gage installed on a rail can provide highly accurate axle loads. Thus, this section performs dynamic analyses of a calibrated hybrid model and develops fatigue estimation for entire bridge using and measured input train loading. For example, Figure 48a and b show the train configuration estimated from the strain measurement at the rail. Each vehicle has different mass distributions (see Figure 48b) and the loads exerting one side of the rail are summarized in Table 5.

(a) Train configuration

M_{W_1} M_{W_1} M_{W_2} M_{W_2} M_{W_3} M_{W_3} M_{W_4} M_{W_4} M_{W_5} M_{W_5} M_{W_6} M_{W_6} M_{W_7} M_{W_7} M_{W_8} M_{W_8}
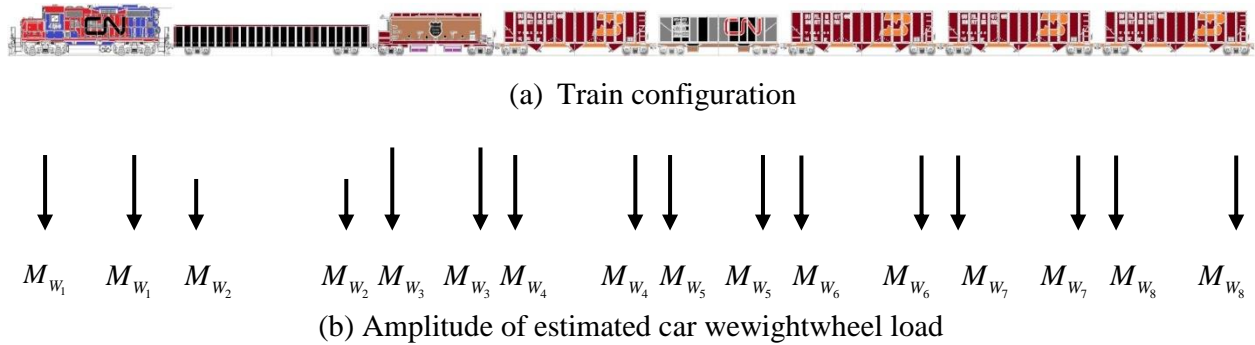
(b) Amplitude of estimated car wewightwheel load

Figure 48. Train configuration.

Table 5. Wheel loads profile.

Wheel number	Wheel loads [ton]	Wheel number	Wheel loads [ton]
M_{W_1}	56.25	M_{W_5}	48.53
M_{W_2}	29.71	M_{W_6}	47.97
M_{W_3}	58.20	M_{W_7}	47.97
M_{W_4}	47.97	M_{W_8}	47.97

In the simulation, strain is calculated for entire bridge at each time-step. Figure 49 provides the evolution of the strain map as the work train crosses the bridge. To the left corresponds to North in the figure. The cyan triangle indicates the estimated locations of the wheels as the work train crosses the bridge. The length of the black lines above the cyan triangles indicates the magnitude of the wheel loads. Members in tension are marked in red, whereas members in compression are marked in blue. The thickness of the colored elements indicates the relative magnitude of the strain in each element. For those elements with strain levels under a specified tolerance limit, the element is marked with a thin black line. The right column of this figure also shows the 3D view of the strain distribution. The asymmetric strain distribution between the West and the East truss planes are due to only one train loading the double-tracked bridge. The information provided by this analysis can verify designs, monitor damage, and assess the fatigue life of bridges under in-service loads. For example, one can construct a histogram of the maximum strain of each member, as shown in Figure 50. This chart can help identifying a critical member under live-train, which can further be used for estimating remaining fatigue life.

110

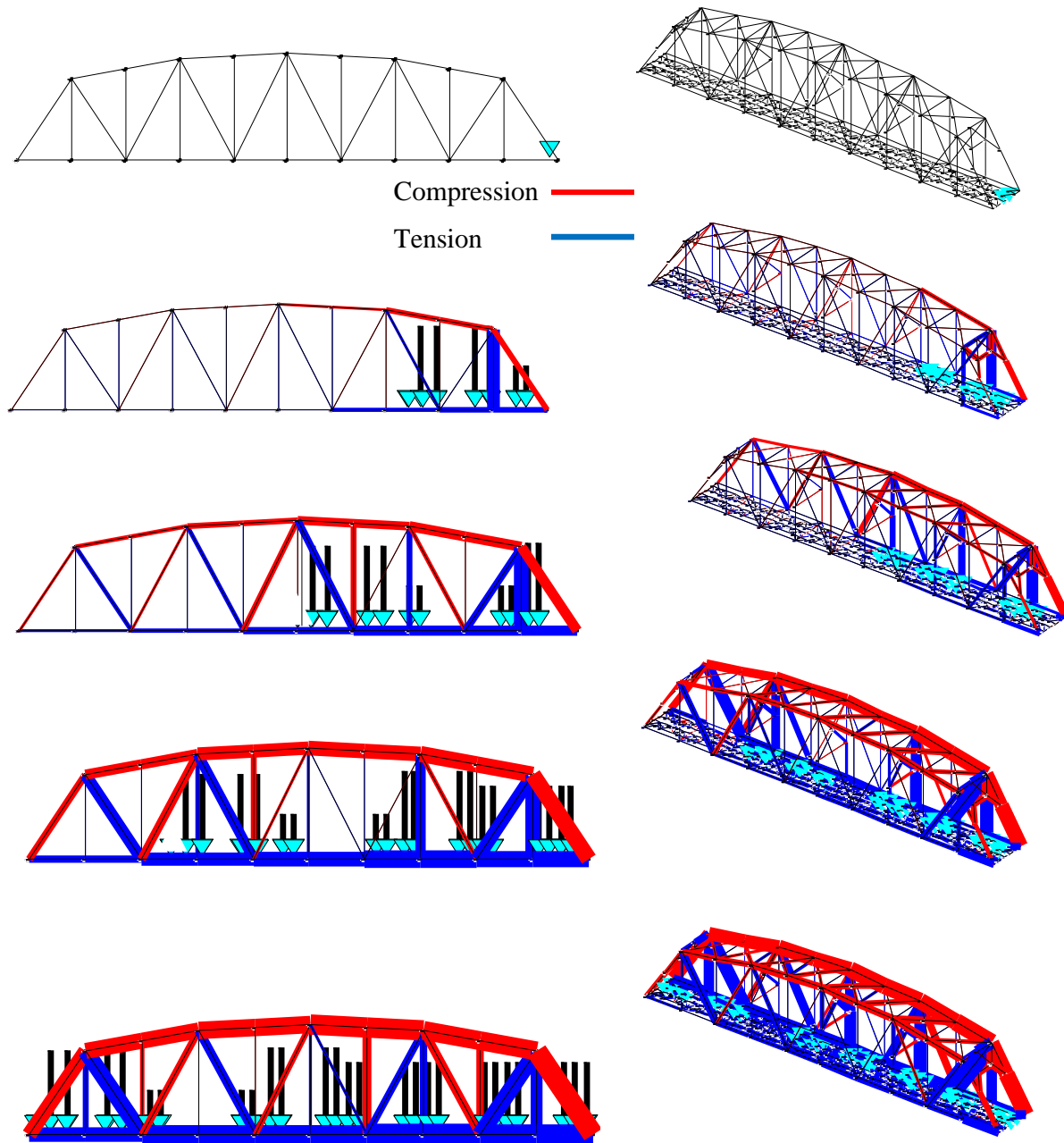An animation of the evolution of the strain map as the train crosses the bridge is at the following link: http://sstl.cee.illinois.edu/BridgeStrainVideo.html.

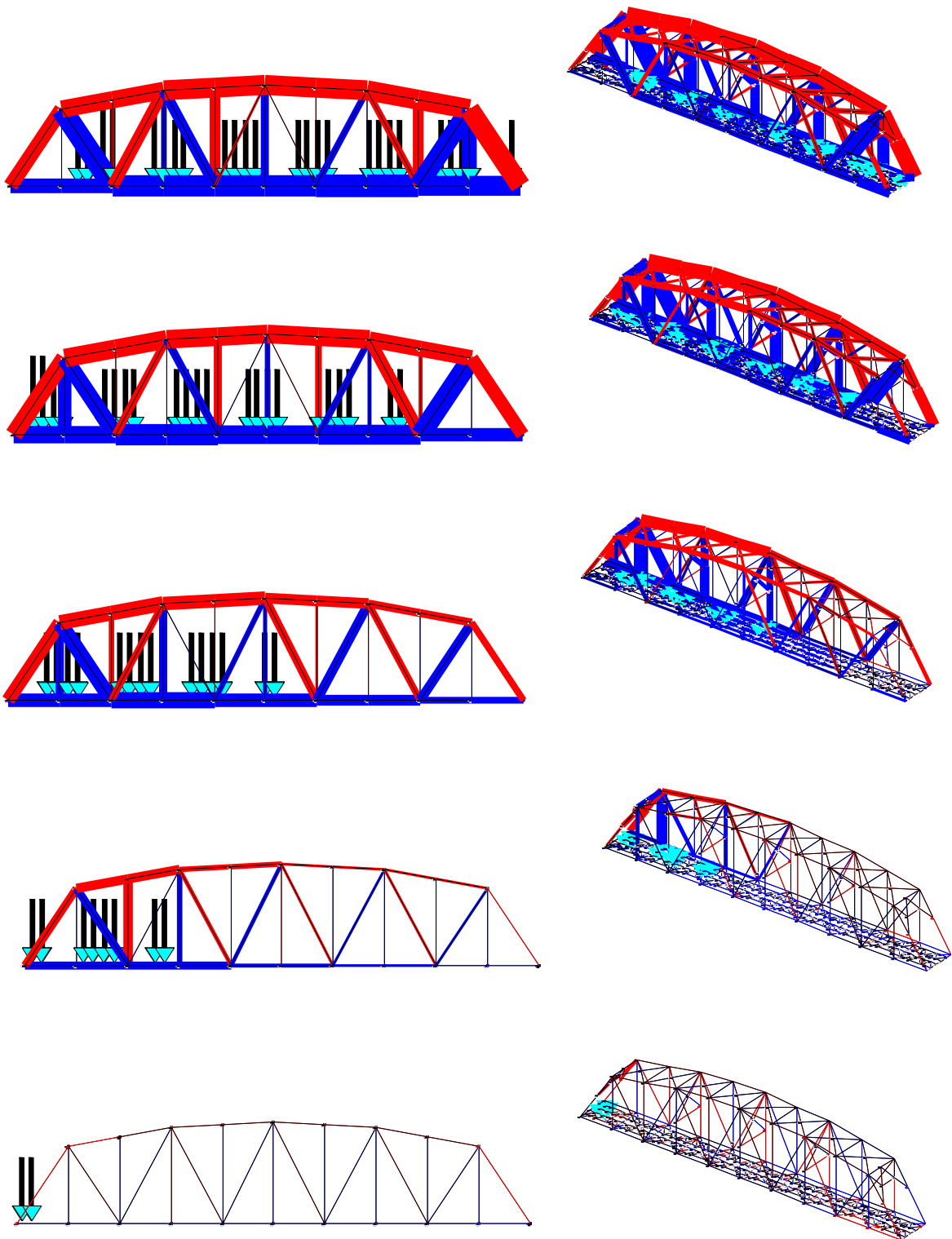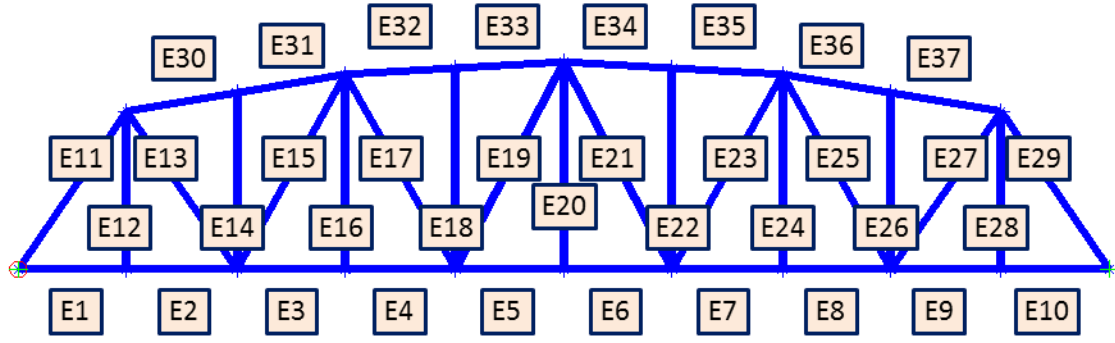**Figure 49. Strain map predicted by the FE model for the work train.**

Figure 49. (cont.)

(a) Member ID.
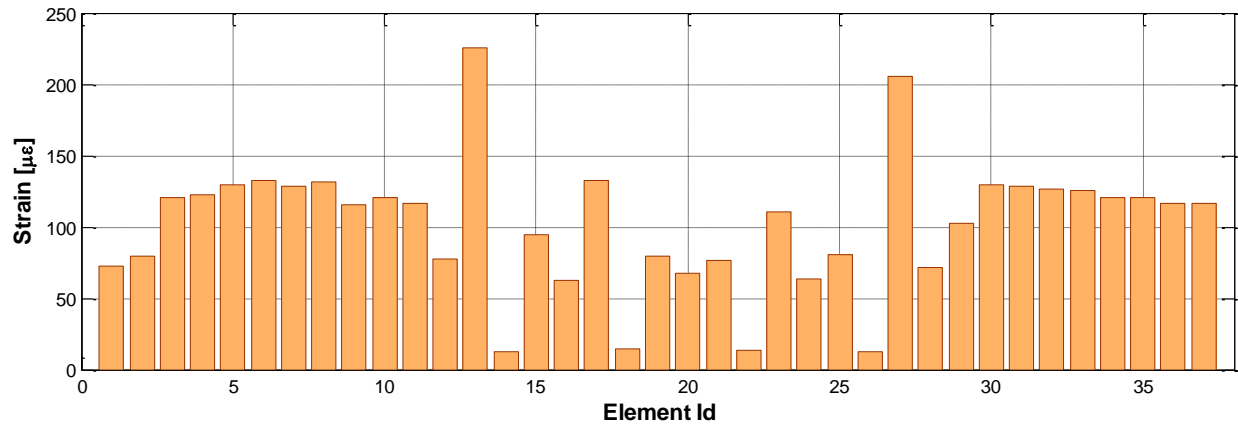
(b) Maximum strain.

Figure 50. Maximum strain at each member.

5.2. Bridge resonance studies

Resonance is another undesirable phenomenon that can raise numerous challenges for railroad bridges. Although resonance phenomena is unusual in dedicated corridors, vehicles running in shared corridors can induce such occurrences resulting in increasing speed of bridge degradation. However, due to the complexities of the phenomena predicting resonance speeds for an in-service structure using a numerical model is difficult; the model requires accurate calibration to represent the status of

the structure and three-dimensional modeling of the vehicle with many DOFs. So far, resonance phenomena have only been considered in the design guide or numerical models are limited to a small number of train cars with the equidistance bogies.

This section presents the estimation of the dynamics responses of the Calumet Bridge at arbitrary speeds of a moving train. The performance of the hybrid model is first presented and then a comparison with the beam model is followed. Any sudden local increase of the maximum value at a given speed is an indication of a critical speed, which will be associated as evidence of the phenomenon of resonance. Comparisons between the moving-mass and load model highlight the limitations of the moving-load model.

5.2.1. Hybrid model

The maximum nodal accelerations of the bridge using the proposed hybrid model are plotted in Figure 51. The accelerations are calculated at the center of the lower chord in the West plane of the bridge, while the train was running on CN1 (track on the West side). In the calculation, the train shown in Figure 48 varied its speeds from 0 MPH to 200 MPH, and both moving-load and moving-mass models were included in the plot. In both models, the simulations were performed with $\Delta t = 0.001$sec and lasted until the bridge response becomes transient after the train exits the bridge. As can be seen in Figure 51, both models show similar maximum accelerations at slower speeds, while differences get larger as the speed increases. Especially, the error in estimating the primary resonance speed is about 50 MPH; the primary critical speed in the moving-mass model is at 125 MPH with amplitude of 210.4 mg; for the moving-load model, it occurred at 174 MPH with 151.1 mg. Figure 52 shows the time history of the accelerations at the resonance of the moving-mass model in comparison with the moving-load model. When the last vehicle left the bridge, marked with a

114

vertical line in Figure 52 ($v_0t/L = 2.24$), the bridge responses of the moving-mass model increase

dramatically. After 1.3 sec, the vibration damps out due to the damping of the bridge. However, in

the moving-load case, the acceleration is bounded within ± 50 mg throughout the entire time history

of the response. This result indicates that the moving-load model overpredicts the critical speeds at

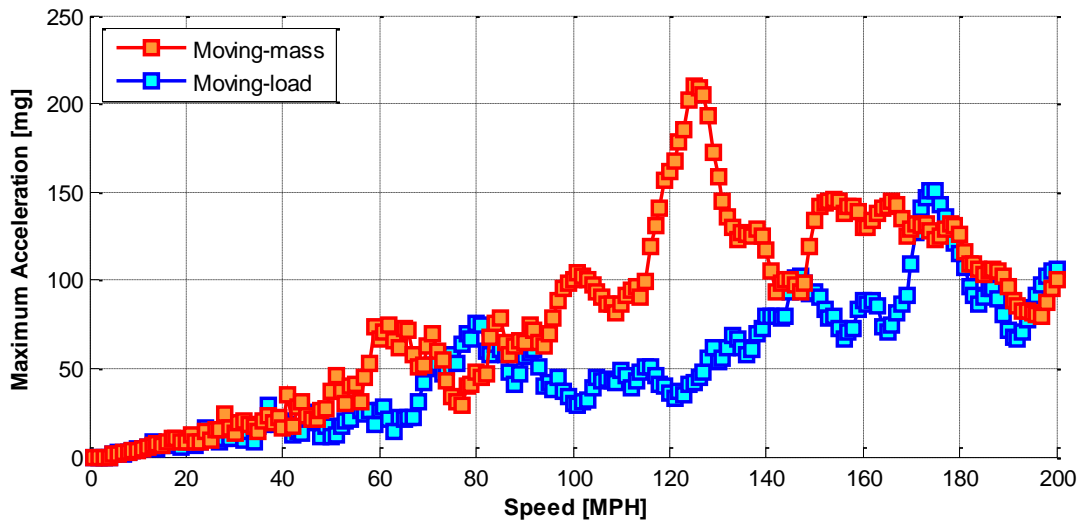resonance and underestimates the maximum acceleration of the bridge under train crossings.

Figure 51. The resonance study comparing the moving-mass and load model.
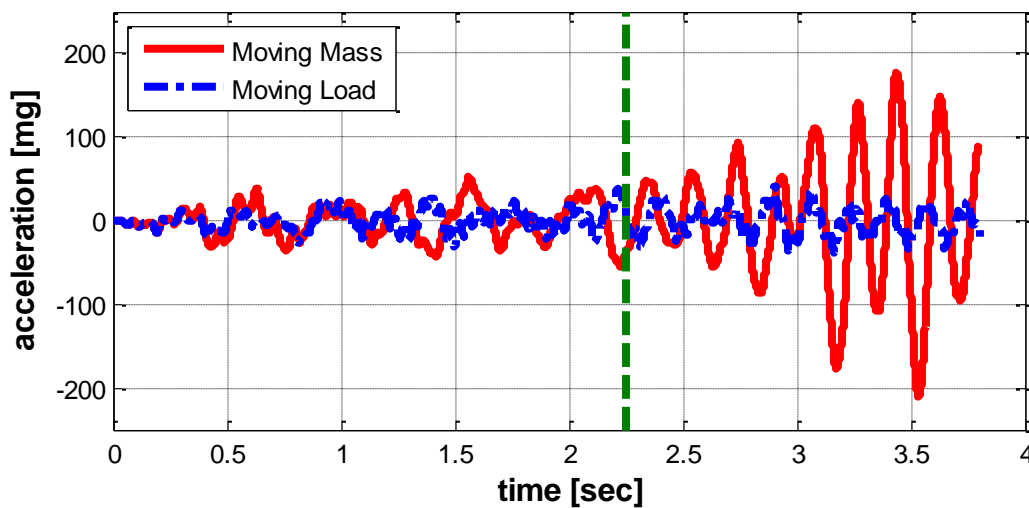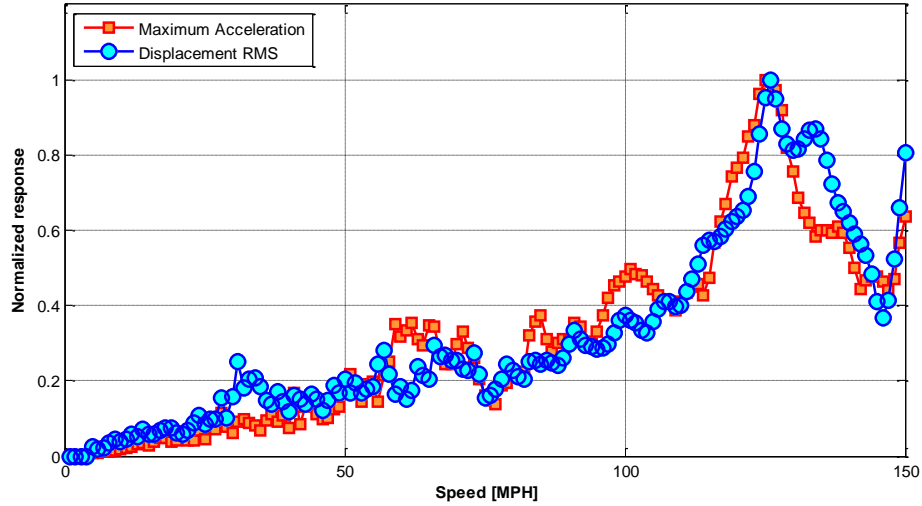

Figure 52. An acceleration history at the resonance.

Figure 53. The resonance study using dynamic displacement and acceleration.

In addition, to verify that the linear effect of ω^2 do not impact estimating critical speeds using acceleration responses are conducted. Figure 53 plots root mean square (RMS) of dynamic responses of displacement and maximum acceleration at each train speed. For direct comparison, results are normalized by the maximum and the results from maximum acceleration are plotted as well. In the simulation, the hybrid model of the moving mass model was used, where the train was composed of 8 train cars (i.e., test train). Trends in the RMS nominally agree with acceleration results having the primary resonance speed around 125 MPH. Thus, one can conclude that to estimate the critical speeds of a train, acceleration response can be used.

5.2.2. Simple beam model

To examine the predictive capability of the beam model, the resonance study varying the speed of the train from 0 MPH to 200 MPH is performed. In the analysis, the sample time is $\Delta t = 0.001 \, \text{sec}$. Figure 54 shows the results of the comparison with the hybrid moving-mass model. The maximum acceleration at each speed is normalized such that the value is 1 at the maximum resonance. As can

be seen, although the speed at which the primary resonance occurs is different between the hybrid model and the beam model, ranges of the local resonances in the hybrid model are captured in the simple model: Increased amplitude in the beam model appears near the speed where the hybrid model exhibits resonances. The corresponding speeds listing in the order of smaller speed are; 51 MPH, 59 to 65 MPH, 85 MPH, 100 MPH, 125 MPH, and 150 MPH to 180 MPH. Thus, using the simple beam model can predict the range of critical speeds while the relative amplitude at its resonance is not as precise.
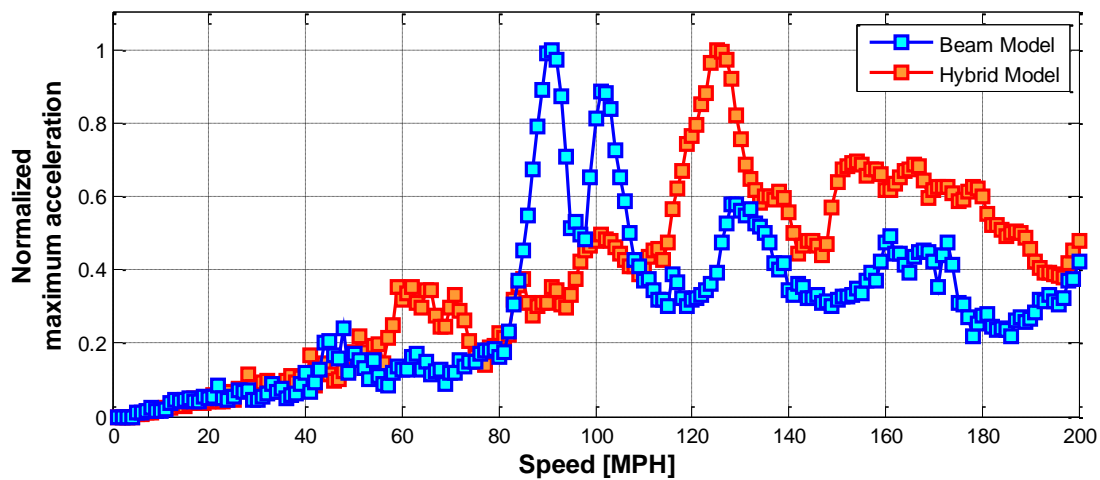
Figure 54. The resonance study of the beam moving-mass model in comparison with the hybrid model.

5.3.   Conclusion

This chapter first explored strain estimation of railroad bridges at an element level, which can potentially lead to the fatigue failure of the bridges that are subjected to increased train loads. Using the calibrated hybrid model, a dynamic strain map was generated for the entire bridge for in-service trainloads. From the map, the maximum stresses/strain at arbitrary locations on the bridge were determined from the dynamic responses of the model. Then, another critical phenomenon, resonance,

that can occur in shared corridors were studied. The presented work highlighted the mass effects in predicting the crucial speeds. Although the moving-load model showed a good estimation in predicting the bridge response at slow speed, unconservative results are observed in the model for predicting critical speeds. Then, a simpler representation of the bridge were used to estimate resonance of the bridge. The simple model showed agreeable results in predicting range of critical speeds from the resonance study when compared with the hybrid model. However, the amplitude at the resonance speeds were less accurate. In conclusion, both the hybrid model and the simple model can be used to assess the bridge responses under moving train of arbitrary configuration and speeds. Studies presented in this chapter will become pivotal for efficiently assessing fatal dynamic phenomena of a railroad bridge such as fatigue and the bridge resonance.

CHAPTER 6. SYNCHRONIZED SENSING FOR RAILROAD BRIDGES USING LOW-COST GPS RECEIVERS

Geographically distributed features of vehicle, track, and bridge (VTB) systems prevent the establishment of a monitoring system using current WSS systems. To obtain meaningful measurements of in-service loads and responses from a railroad bridge, a protocol that can synchronize each components of VTB (i.e. both on the bridge and on the vehicle) must be developed. This chapter proposes a new synchronization strategy, which can achieve high-accuracy synchronized sensing in multiple WSS networks for extended sensing duration. The proposed approach combines hardware- and software-based methods to achieve the necessary accuracy in an efficient manner. The Coordinated Universal Time (UTC) information and the Pulse-Per-Second (PPS) signal provided by low-cost GPS receivers are employed. This protocol first utilizes a hardware-based approach to establish accurate clock synchronization among base stations of individual sub-networks according to the global time from the GPS receivers. Subsequently, a software-based approach is used to provide synchronized sensing within each sub-network, in which the hierarchical root nodes are already synchronized through the hardware-based approach. The method was implemented and verified on the Imote2 sensor platform running TinyOS, showing high-accuracy, long-term, synchronized sensing performance for an arbitrary number of sensor nodes. These results show great potential of the proposed method in facilitating application of WSS networks for monitoring railroad bridges.

6.1. SHM-specific synchronized sensing protocols

Traditional clock synchronization protocols alone do not produce synchronized data. Clock synchronization does not compensate for differences in sampling rate among leaf nodes, fluctuations

in the sampling frequency, and the start time of sensing (Nagayama and Spencer, 2007). For example, although the internal clocks in two leaf nodes shown in Figure 55 were synchronized initially at $t = 0.4$ seconds, clock speed differences resulted in differences in sampling rates and hence unsynchronized measurements. In Figure 56, the nodes have exactly the same sampling rate; however, sensing may not start precisely at the same time in each of the leaf nodes, resulting in the unsynchronized data shown. This section reviews two synchronized sensing protocols tailored for SHM applications that address such issues.
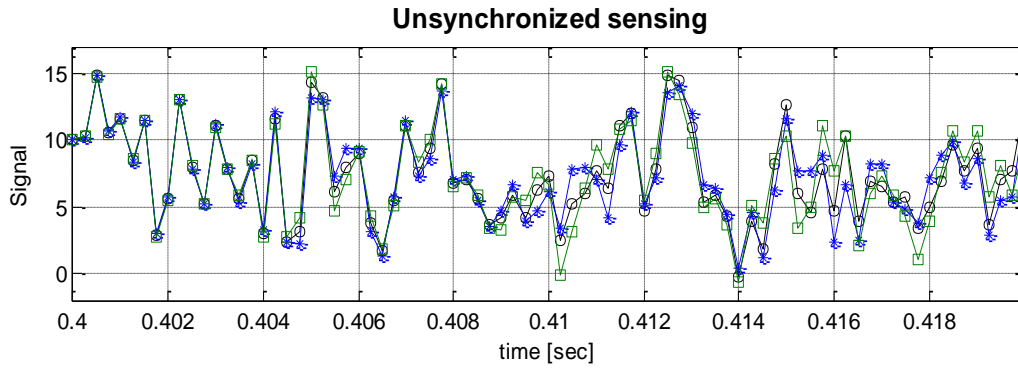

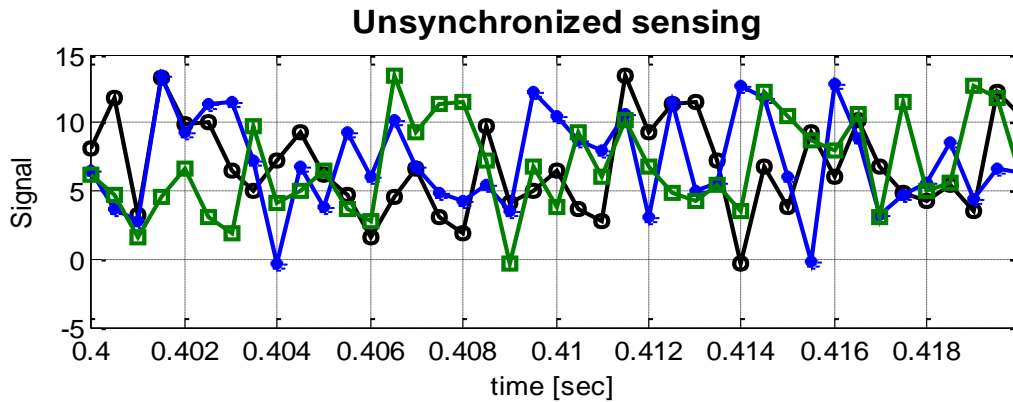**Figure 55. Illustration of unsynchronized data resulting from differences in sampling rate.**

Figure 56. Illustration of unsynchronized data resulting from differences in sensing start time.

6.1.1. Synchronized sensing through resampling

To achieve synchronized sensing, Nagayama and Spencer (2007) developed a protocol that addresses problems with both clock drift and differences in the start of sensing. The proposed method uses a two-step synchronization process: (i) clock synchronization, adopting the FTSP time stamping method, and (ii) a subsequent polyphase resampling of the data to put it all on a common time scale. The clock synchronization step corrects the most common clock errors in discrete clocks, which are offset and clock drift. Clock drift occurs due to imperfect speed differences among clocks; therefore, even if clocks are perfectly synchronized at time $t = 0$, the drift in the clocks will result in an offset between leaf node clocks at future times. To better understand this problem, consider the measured clock offset for nine leaf nodes with respect to the gateway node shown in Figure 57. As seen here, although the nine nodes are synchronized with the gateway node at $t=0$, as time progresses, the offset between the clocks increases linearly.
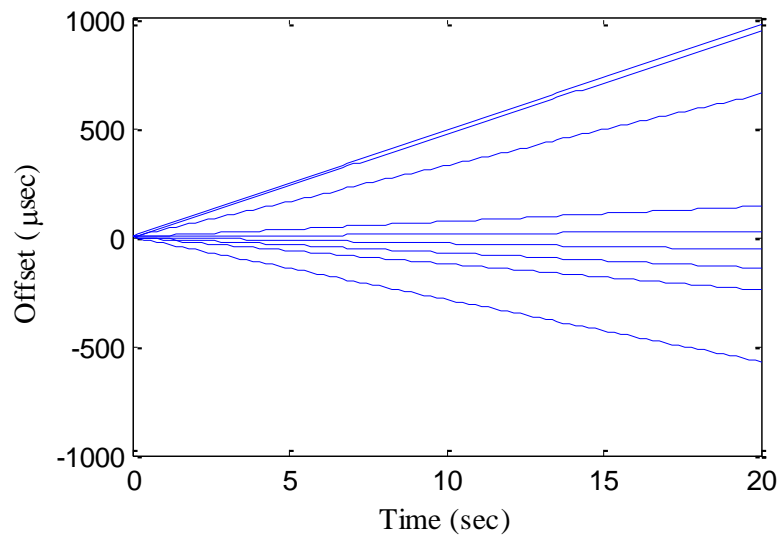

Figure 57. Clock drift in Imote2s (Nagayama and Spencer, 2007).

In this approach, prior to the start of sensing, both clock offset and clock drift rate with relative to the gateway node are estimated for each leaf node, as illustrated in Figure 58. Before the

start of sensing, the gateway node, regularly broadcasts beacon signals for a period of 30 seconds. Each leaf node records the local time at which the signals were received, and estimates the offset for the leaf node clock relative to the gateway's clock. When the gateway node finishes sending beacon signals, the leaf nodes estimate their drift rate with respect to the gateway node based on the collected offset values using linear regression.
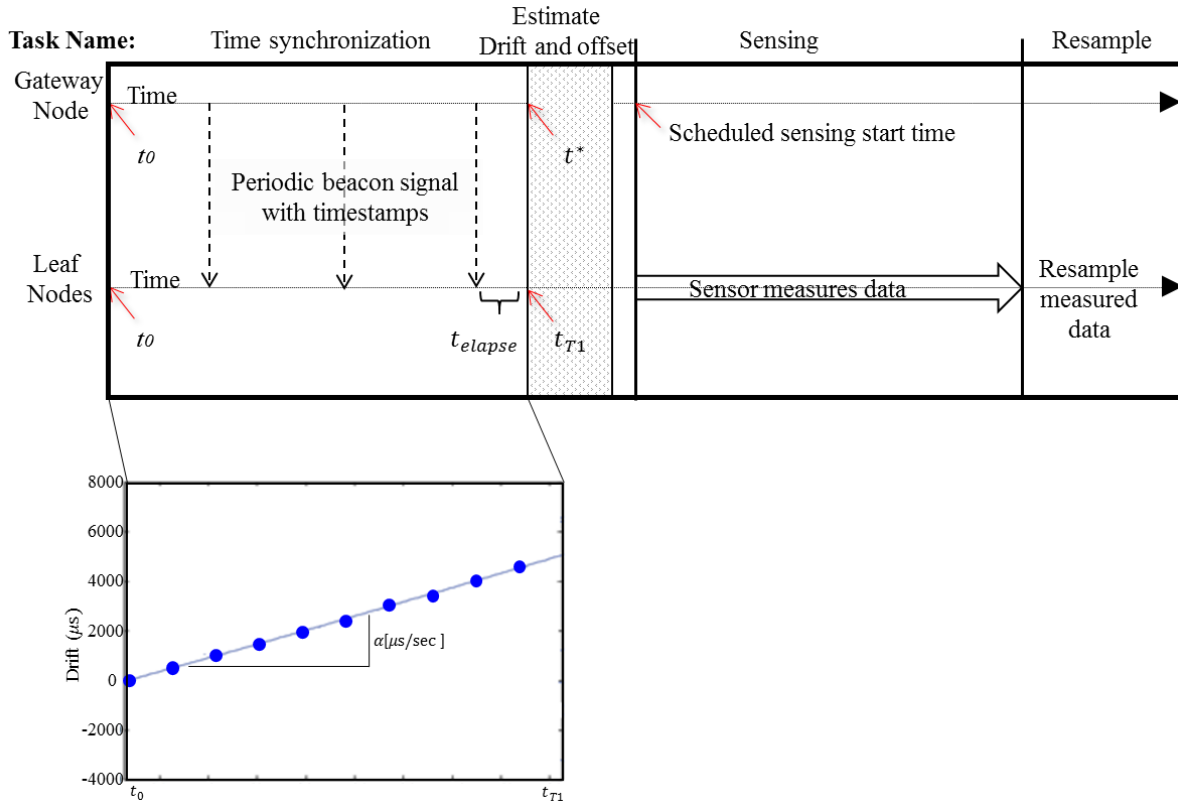
Figure 58. Synchronized sensing scheme with linear clock drift estimation and resampling: gateway node broadcast periodic beacon signals (top box, top line); leaf nodes store received time stamp to estimate drift and offset and start sensing (top box, bottom line); example of drift estimation in a leaf node during the time synchronization (bottom box).

Once the synchronization process has finished, data can be collected from the sensors connected to the leaf nodes. After completion of sensing, polyphase resampling takes place (Figure 58). Based on laboratory tests, the estimated synchronization error of measured data for a small network is about 50 μs (Nagayama and Spencer, 2007). The protocol was then implemented on a

122

full-scale structure, the Jindo Bridge in Korea (Figure 59). The deployment constitutes the world's largest sensor network of its kind with 113 nodes and 669 multi-metric sensing channels. The entire network was divided into four sub-networks using two base station PCs and four gateway nodes (Figure 59). The data from the 4 sub-networks was synchronized in a post-facto manner after being collected on a single computer by comparing the measured responses at nodes in common to the networks. Several limitations were encountered in this approach. First, the 30 seconds required to estimate clock drift rate made capturing transient responses difficult. Additionally, the assumption that the clock drift was linear was found to be invalid, particularly for long acquisition times.
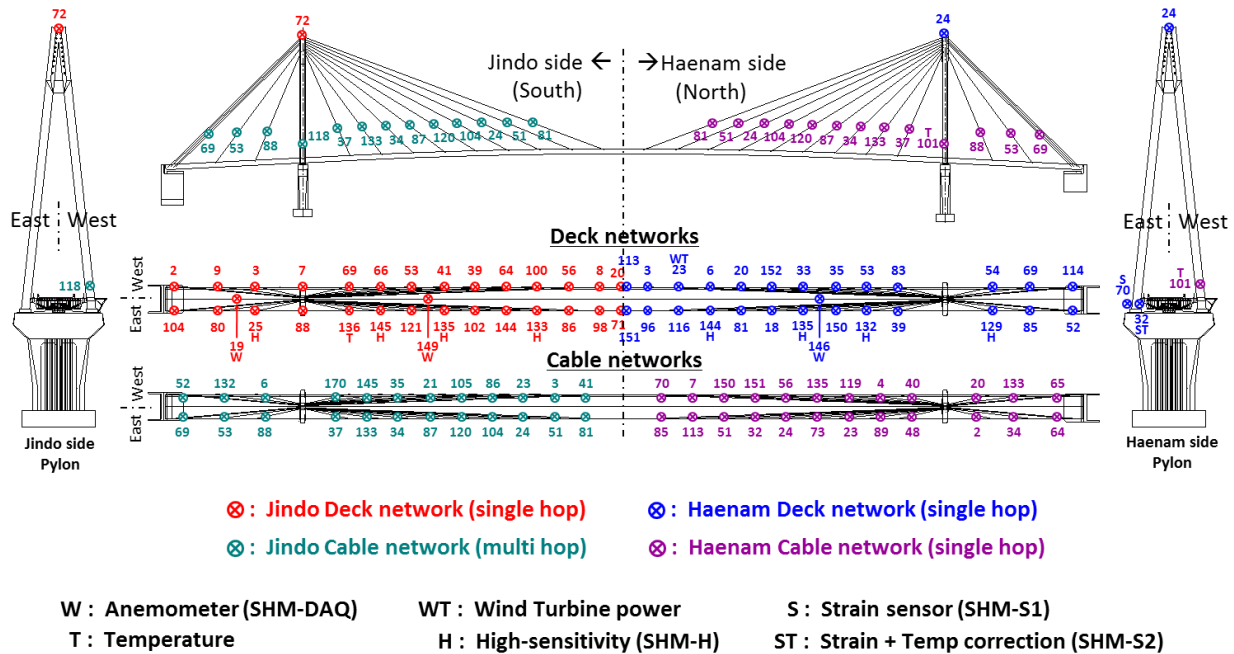
Figure 59. Jindo Bridge sensor deployment (Jo, et al. 2011).

6.1.2. Compensation for nonlinear clock drift

In examining the data collected by the wireless sensors for an extended period of time, the assumption of linear clock drift was found to be invalid. Figure 60 shows clock offset of 4 leaf nodes,

along with the measured temperature of the sensor. As can be seen in the figure, nonlinear clock drift occurs, which is highly correlated to temperature variation of the wireless node. These temperature changes can be attributed to issues such as internal heat generated by the sensor node due to sensing, external heating (e.g., by direct sunlight), etc. Figure 61 shows Node 69, along with the linear drift rate estimated using 30 seconds of data at the beginning of sensing. As can be seen here, after collecting data for 10 minutes, the linearly corrected time on Node 69 would be off by more than 9 ms from the gateway node.

Figure 60. Nonlinear clock drift (Li, et al. 2012).
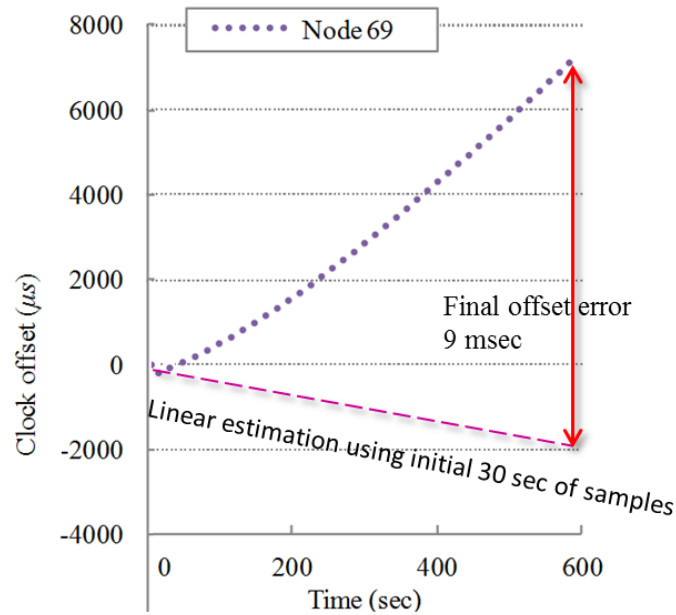
Figure 61. Clock offset error due to nonlinear clock drift.

To address the problem of nonlinear clock drift, Li, et al. (2012) developed a synchronization protocol that enables synchronized sensing over an arbitrary length of sensing duration. On initializing the process, a gateway node broadcasts to the network a single be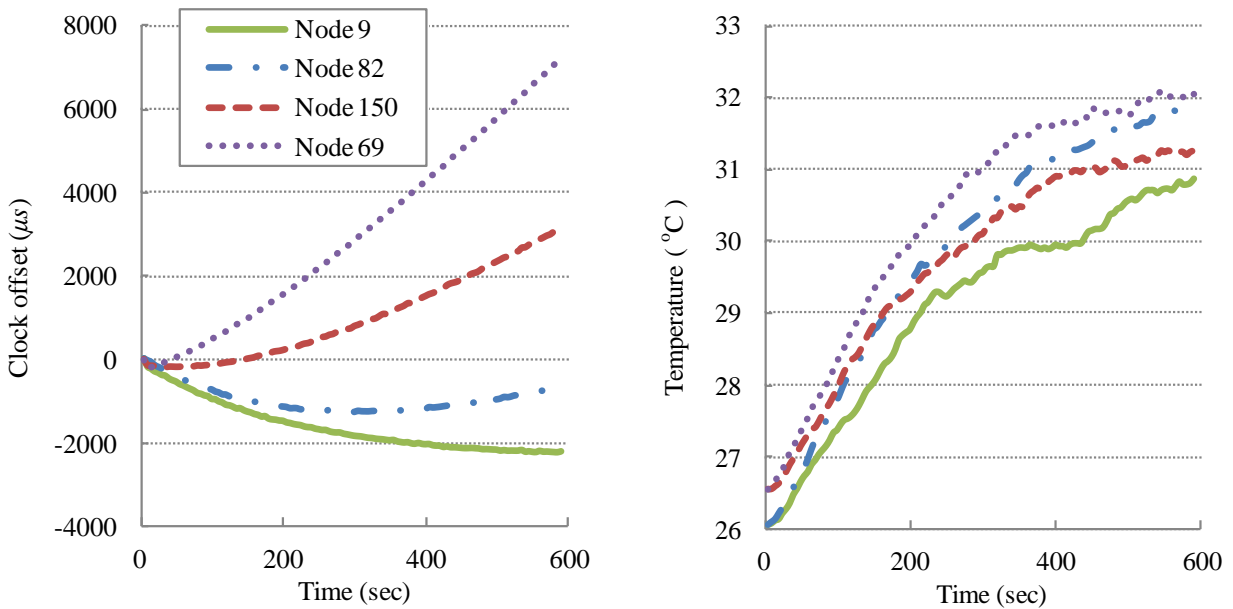acon signal with the global timestamp. Upon reception of the timestamp, leaf nodes calculate the offset and adjust their clocks to synchronize the clocks of the network. Subsequently, the gateway node sends out the sensing start time to the leaf nodes assuming that the clocks do not drift much during the short delay before sensing starts. During sensing, the gateway node periodically broadcasts beacon signals with global timestamps, which is stored in the leaf nodes upon reception. When sensing is finished, timestamps of data are corrected using the nonlinear clock drift estimated with the beacons collected during sensing. Resampling is then performed based on the drift-compensated timestamps, which ensures synchronized measurements among the leaf nodes. Because the leaf node is simultaneously performing sample acquisition and receiving beacon signals from the gateway, conflict between these two tasks may occur, resulting in outliers in the timestamps associated with reception of the beacon signals. The protocol detects and removes these outliers prior to resampling. The proposed protocol

125

achieved synchronized sensing with less than 50 µs synchronization error with gateway clock for long-term data collection in laboratory tests. The protocol also reduced the delay before the start of sensing by eliminating the need to estimate the leaf node's clock drift rate before sensing. However, the application of the protocol is limited to a single network. In addition, the inaccuracy of the gateway clock, which can occur due to temperature changes in the node, is propagated to the leaf nodes. Thus, a unified protocol to address all of the important issues simultaneously is needed.

6.2. GPS-based synchronized sensing for multiple WSS Networks

An efficient protocol that combines the advantages from both hardware-based and software-based approaches is proposed to achieve synchronized sensing. A low-cost GPS used to ensure correct timing on the gateway is combined with the resampling schemes proposed by Nagayama, et al. (2007) and the nonlinear drift compensation strategy proposed by Li, et al. (2012) is employed. This section describes the background and implementation of this combined protocol.

6.2.1. Overview of the proposed synchronized sensing protocol

The proposed protocol aims to achieve the following main goals by combining both hardware- and software-based approaches: i) correct gateway clock errors using a low-cost GPS receiver, and ii) provide synchronized sensing within a sub-network by compensating nonlinear internal clock drift. The hardware-based approach enables maintaining the gateway nodes clock highly accurate among sub-networks. Such a scheme provides scalability by removing communication overhead among sub-networks. In other words, increasing the number of sub-networks does not degrade the performance of synchronized sensing. Moreover, hardware interruption can be handled asynchronously while a gateway node is performing other scheduled tasks; therefore, no delay will be added. Then, the gateway node broadcasts corrected timestamps to its network in beacon signals while leaf nodes

126

perform a sensing task. Leaf nodes, on receiving the signals, store the local clock time and offset from reference clock (Li, et al. 2012). Once measurement is done, the measured data is resampled (Nagayama and Spencer, 2007). This approach removes nonlinear clock drift of leaf nodes as well as the gateway node to achieve highly precise synchronized sensing within each sub-network.

Figure 62 summarizes the scheme of the proposed synchronized sensing algorithm. The approach achieves efficiency for multiple networks by removing the communication between different networks, while preserving high accuracy within a network. The gateway nodes are synchronized with GPS signals assuring similar degree of synchronization throughout the networks. Scalability is secured with reduced size of networks.
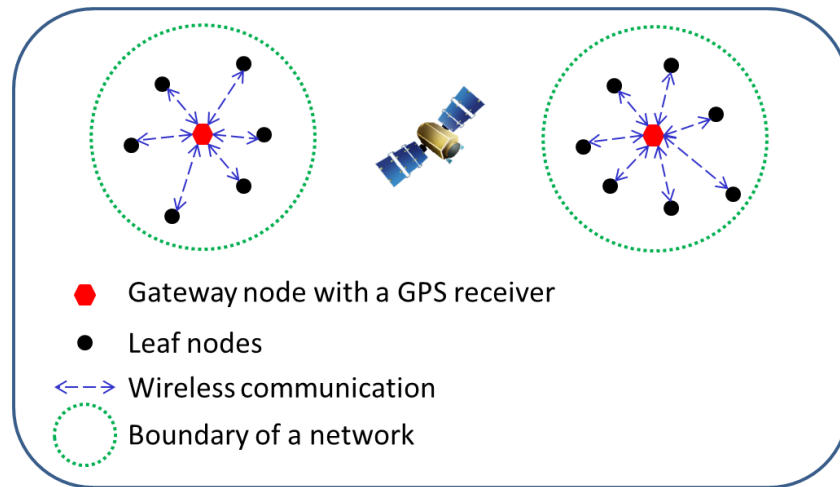
Figure 62. Illustration of the proposed synchronized sensing approach.

6.2.2. GPS-based synchronized sensing: hardware setup for the Imote2

A low-cost GPS receiver, GlobalTop GMS-u1LP, is chosen to provide UTC time to networks and to output PPS signals (Figure 63a). The chipset on the receiver is MediaTek GPS MT3329 solution that supports up to 66 channels of satellite searching (GlobalTop, 2010). The typical power consumption is only 24 mA when tracking satellites and 30 mA during acquisition (GlobalTop, 2010). Also, the

receiver is relatively small in size (16×16×6 mm) and inexpensive ($20 USD / unit). With those features, the selected GPS module is both cost and energy efficient and is therefore suitable for WSN applications.

(a) GPS module   (b) Receiver pin specification
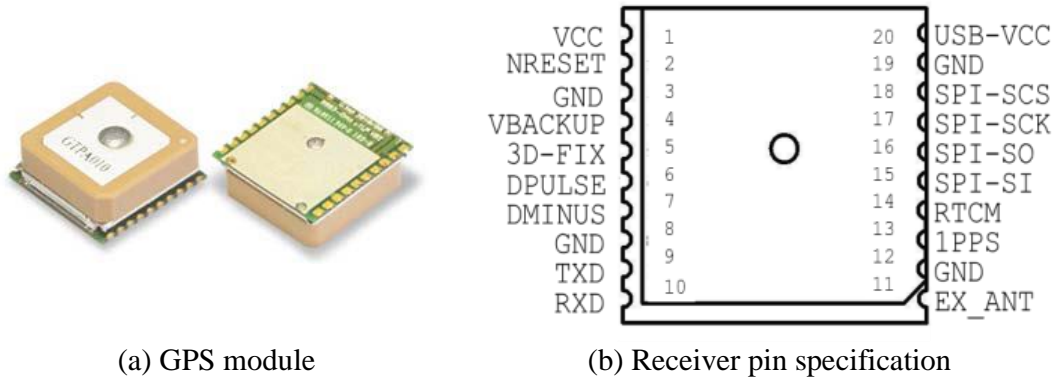
Figure 63. GlobalTop GMS-u1LP GPS receiver.
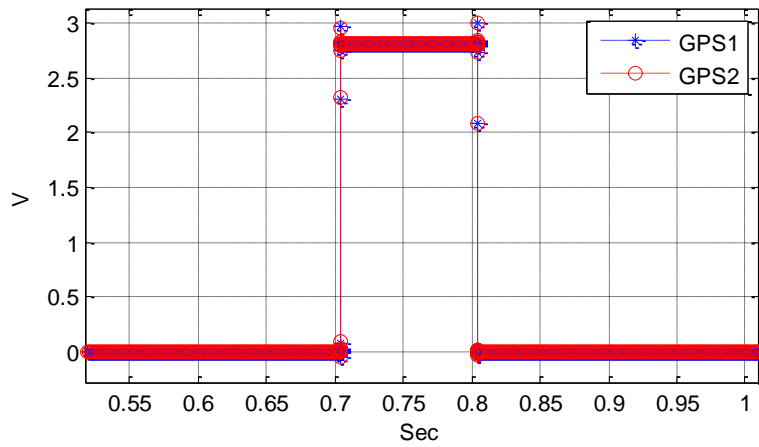
(a) PPS signal sampled at 102400 Hz.

Figure 64. A typical GPS pulse (Kim, et al. 2012).
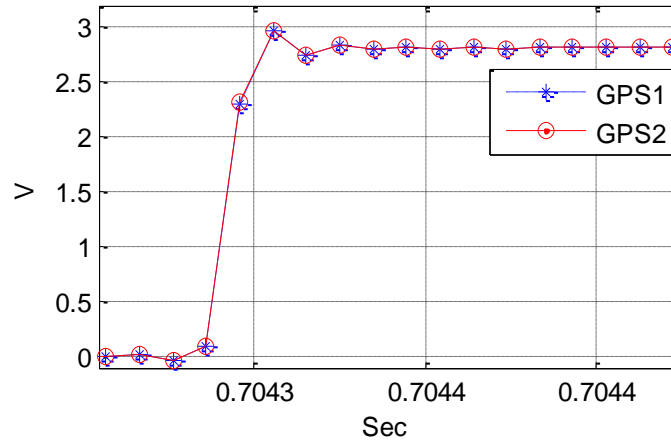
(b) Zoomed PPS rise.

Figure 64. (cont.)

To verify the applicability of the selected GPS receivers, the PPS pins, as shown in Figure 63b, from two receivers are connected to a VibPilot (www.mpihome.com 2010) and data is collected at a high frequency (112,400 Hz). As shown in Figure 64a and b, when the two GPS receivers are in locked status, the PPS signals measured from them are identical, which provides the basis for nearly perfect clock synchronization if the gateway nodes of two sub-networks are connected to them (Kim, et al. 2012).

Hardware pin connections from a GPS receiver to an Imote2 enabled the use of PPS and serial data output directly from the Imote2 platform. The PPS pin is connected to one of the General Purpose Input Output (GPIO) pin on an Imote2 (see Figure 65a, b). The serial data output for NMEA sentence with UART Transistor-transistor Logic (TTL) communication, and thus a TXD port on the GPS receiver (Figure 63b) is connected to an UART RX pin on the Imote2 (Figure 65,b).

129
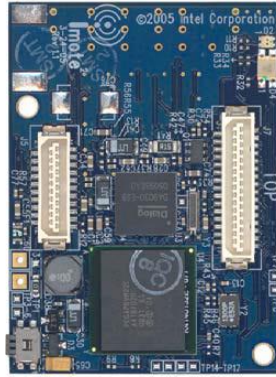
(a) The top view.
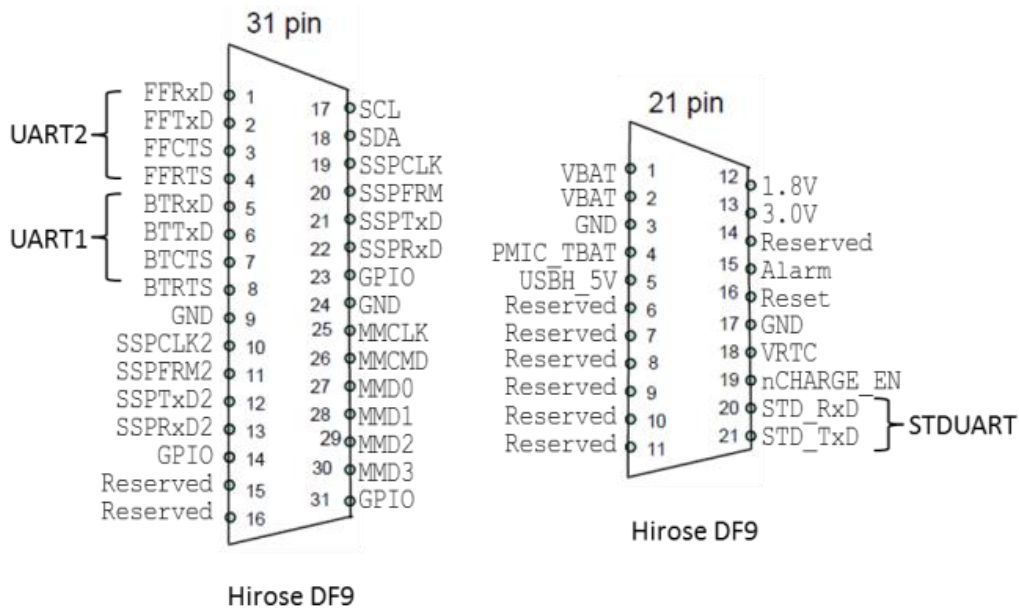
(b) Connector pin specification.

Figure 65. The Imote2 platform.

Hardware interrupts through PPS signals control the entire algorithm to ensure that subsequent tasks are executed concurrently on gateway nodes when a network consists of multiple sub-networks. Each PPS signal passing the GPIO register performs tasks depending on the status of the algorithm at which the hardware is interrupted (see Figure 66). For example, 1) Upon initialization of the protocol, the GPIO interrupt handler is enabled to capture the first PPS signal. Once the signal is successfully captured, the handler is disabled until the following tasks are done to

ignore the subsequent PPS signals. 2) While the handler is disabled, UART port parses NMEA sentence and gets UTC information. Baud rate for the port is set 9600 bps (bits per seconds) to match with supporting speed of the GPS receiver. The port parses data every byte and closes and clears the buffer after reading the first valid UTC information. 3) Once the UTC time is obtained, the GPIO interrupt handler is re-enabled and the following PPS signals periodically adjust the Imote2 internal clock to maintain the GPS time throughout the processes. Although the standard TinyOS scheduler follows a FIFO (First In, First Out) rule, the variation of the processing time of PPS signals can be ignored because the handlers are signaled asynchronously by hardware and no other tasks are asynchronously scheduled (Gay, et al. 2003). Thus, when PPS signal interrupt occurs, the scheduled event will follow immediately.
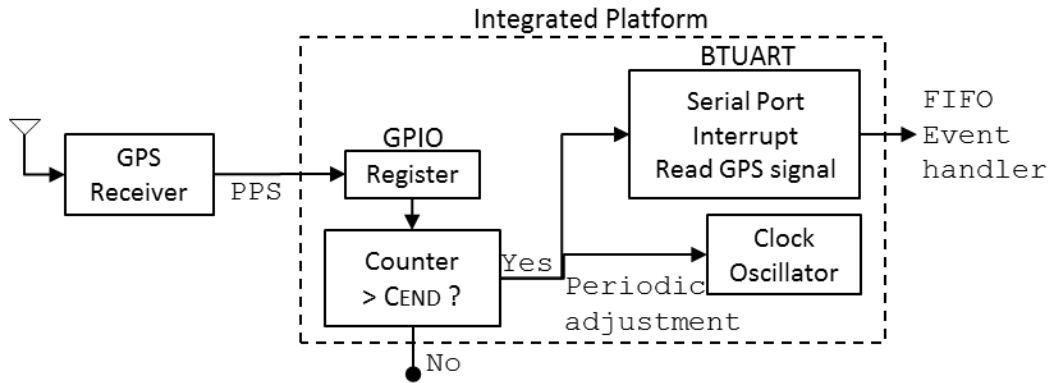
Figure 66. Hardware interrupt scheme.

6.2.3. GPS-based synchronized sensing: software development

This section describes software development to achieve synchronized sensing The proposed algorithm implemented in PPS_based_RemoteSensing[6], a stand-alone application which aims to provide accurate synchronized sensing for multiple networks using PPS signals from GPS receivers.

---

[6] An Calibri font refer to the name of middleware service embedded in TinyOS.

The application is composed of three main processes: (i) the clock synchronization of the gateway nodes based on PPS and UTC time, (ii) the synchronization of the clocks of leaf nodes, and (iii) data synchronization of leaf nodes within each sub-network. Because the PPS signal is globally synchronized with satellites, the application does not require any signal exchange among networks, hence ensuring the scalability of the proposed approach. At the same time, the communication overhead is kept the same as what is required for single network synchronization. The remainder of this section first describes the general approach needed to achieve synchronized sensing in multiple networks and then describes the specific details of the implementation on Imote2s using TinyOS.

Clock synchronization of the gateway nodes in multiple sub-networks

The clocks on multiple gateway nodes are synchronized through the hardware interrupt and UTC information. As the sensing application starts, PPS signals interrupt the GPIO pin on the Imote2. The interrupt handler passes the signals until time reaches the input UTC time. As shown in Figure 67, at the desired UTC time, all gateway nodes adjust their local clocks to a common value (For example, zero as implemented in the application). Once the local clocks are adjusted to a common value, the gateway nodes broadcast the synchronized time stamps and the calculated sensing start time to the leaf nodes in their sub-network. Because the timestamps on the gateway nodes are synchronized, leaf nodes in multiple networks are expected to synchronize their clock based on the same timestamps without requiring message exchanges among sub-networks.
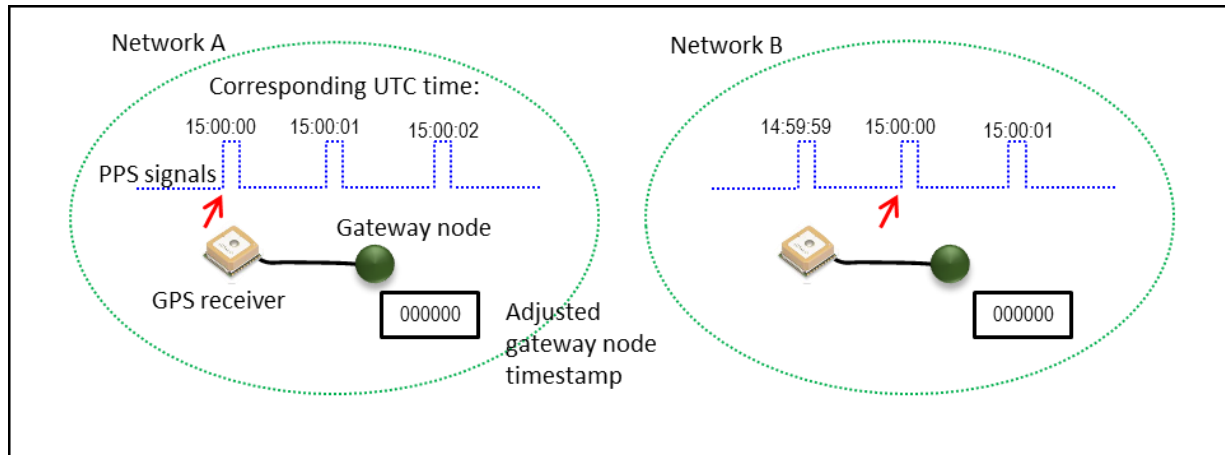
Figure 67. Gateway node clock synchronization on the embedded application.

<u>Clock synchronization and data synchronization of the leaf nodes in multiple sub-networks</u>

Before sensing starts, the clocks on leaf nodes are synchronized based on the clock information broadcasted from the gateway node (see Figure 68). Then, the clock offsets between the leaf node and the gateway node are stored on the leaf nodes. Once the clock is synchronized, gateway node broadcast a message with wait time to start measurements. Based on the stored offset, leaf nodes calculate the timestamp at which each should start sensing. Once sensing is finished, resampling takes place to achieve data synchronization by eliminating the initial start time error and randomness in the leaf node's clock speeds. Because the clocks of all gateway nodes are synchronized initially, the resultant data after resampling is expected to have the same starting timestamp among leaf nodes in different sub-networks.

133
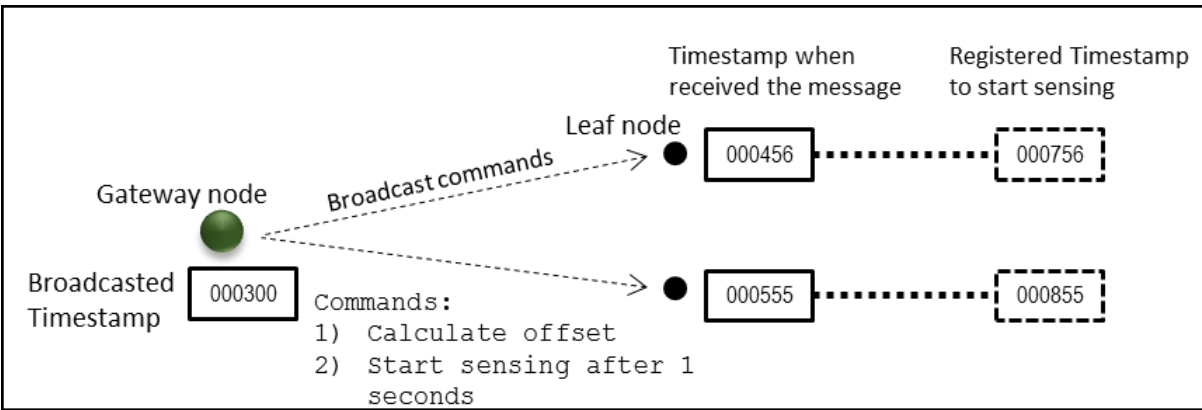
Figure 68. Leaf nodes clock synchronization on the embedded application.

Implementation on Imote2s

Implementation of the algorithms on Imote2s to achieve synchronized sensing for multiple sub-networks is non-trivial due to random delays in hardware operation, clock oscillator speed uncertainty, task scheduling in TinyOS, etc. As a result, although the clocks of the gateway nodes are synchronized initially, this synchronization cannot be guaranteed over extended periods of time. Any errors in synchronization on the gateway nodes will be propagated subsequently to the leaf nodes, making collection of synchronized data impossible. An application PPS_based_RemoteSensing is developed to address these problems using the PPS signal from the GPS.
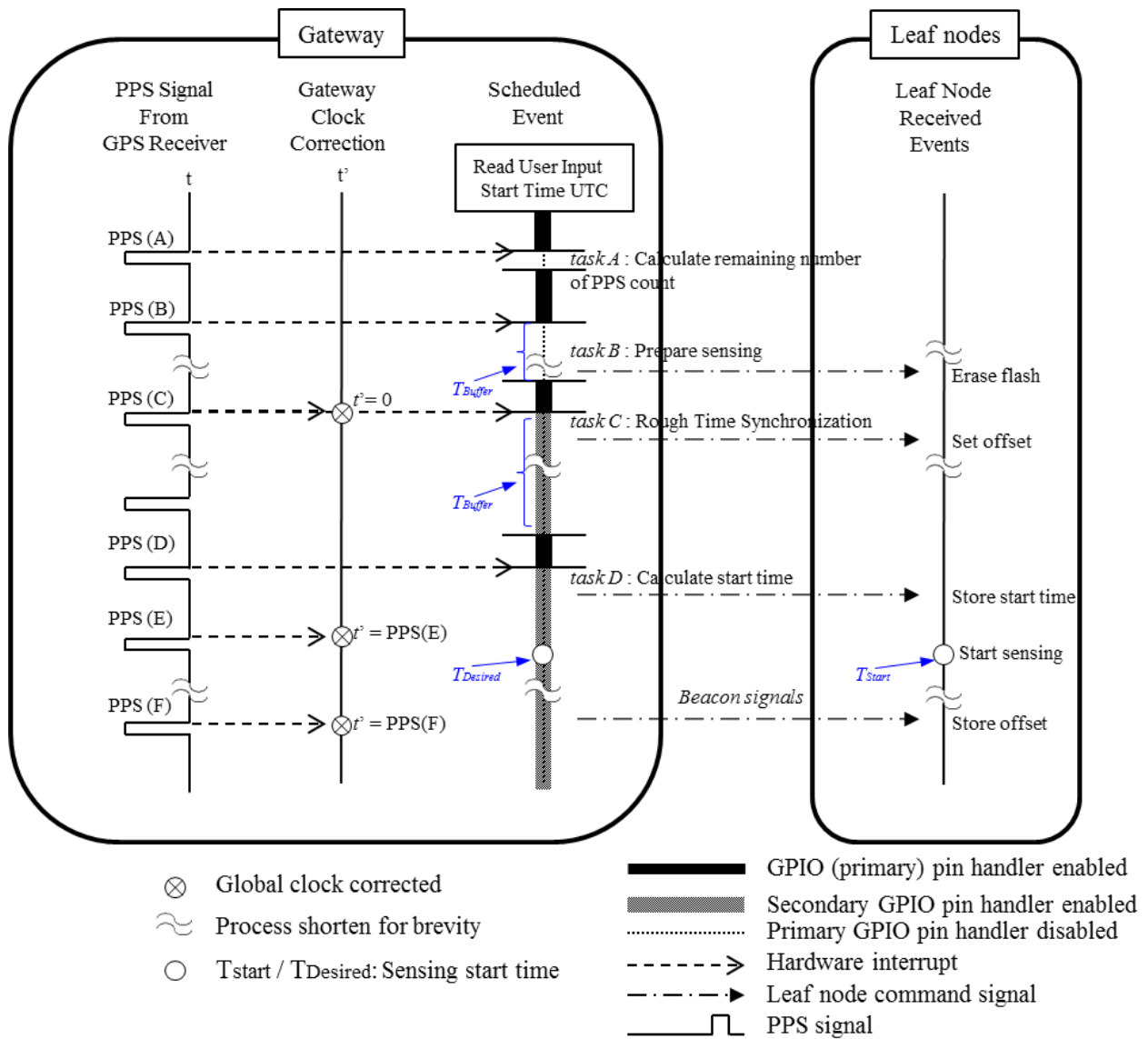
Figure 69. Flow of PPS_based _RemoteSensing algorithm.

The flow of PPS_based_RemoteSensing is shown in Figure 69, where the sequence of events

occurring in a gateway (the left box), and in a leaf node (in the right box). The leftmost column in the

gateway represents the PPS signal input coming from a GPS receiver to the gateway Imote2's GPIO

pin. The middle column illustrates time flow in the gateway clock. The clock is adjusted to specific

values as the algorithm requires. The rightmost column in gateway outlines the list of events

scheduled at each step. Similarly, the column for the leaf nodes shows the list of events occurring

upon receiving the commands from the gateway. The dashed arrows indicate the PPS signal interrupting the gateway hardware to trigger clock adjustment or initiate scheduled events. The dashed-dot arrows represent wireless communication from the gateway to leaf nodes to cast commands. The main function of this flow is to provide fundamental service used for obtaining synchronized measurements such as acceleration and strain.

To start measurements on participating leaf nodes in networks, the application requires users to input the same UTC time on all gateway nodes. Once the input parameters are entered, they are stored in the local flash memory. Then the primary GPIO interrupt handler is enabled and it waits for the PPS signal interrupts. To capture the first rising edge of the PPS signal, C_{end} (Figure 66) is set to 1 at the beginning. The first PPS interrupt triggers the execution of *task A: Calculate remaining number of PPS count*[7] (see Figure 69). This step ensures that the task is synchronized for all participating gateway nodes. Once the task A is successfully executed, the GPIO pin is disabled in order not to be further interrupted by consecutive PPS signals. At the same time, the gateway reads NMEA sentences received from the UART port. The sentence is parsed by every byte and the port will be closed when valid UTC information (T_{UTC}) is obtained. Finally, T_{UTC} is compared with the user defined start time ($T_{Desired}$). Time elapsed to perform those processes may vary on different Imote2 platforms on gateway nodes. Therefore, the next task is queued on following PPS interrupts so that the task can be executed at the same time for all participating gateway nodes. This restriction requires T_{Wait}, sufficient time before time reaches $T_{Desired}$; if the remaining time is larger than T_{Wait}, i.e. $T_{Desired} - T_{UTC} > T_{Wait}$, the C_{End} is updated as $C_{End} = T_{Desired} - T_{UTC}$. Otherwise, if $T_{Desired} - T_{UTC} < T_{Wait}$, the user will be informed that $T_{Desired}$ should be larger. For example, T_{Wait} may be set to 5 seconds to let the gateway nodes finish the calculation.

---

[7] *Italic* font refers to the task identified in Figure 15.

After Task A, the gateway nodes identify the participating nodes in the networks and prepare sensing through *Task B: Prepare sensing*. The gateway first re-enables the primary GPIO interrupt hander and bypasses PPS signal interrupts till the counter reaches C_{End}, i.e., waits until $T_{Desired}$. At PPS (B) (Figure 69) task B is executed and disables the GPIO pin not to be interrupted by following PPS signals. During the task B, two events are scheduled. 1) The gateway commands out to the participating leaf nodes to erase flash memories. 2) Set an oscillator-based timer on the gateway for T_{Buffer}. Although execution of the first event does not require precise task synchronization among multiple network, the latter requires synchronization. The purpose of T_{Buffer} is to allow leaf nodes successfully erase the already stored data before any sensing tasks so that measured data set can be stored. T_{Buffer} can be set for a non-integer value in second, such as 2.5 seconds. This buffer time will prevent gateways triggered by different PPS signals at the moment when T_{Buffer} expires, which may arise from processing time differences. Once the timer for T_{Buffer} is fired, the primary GPIO interrupt handler is re-enabled and C_{End} is set to 1 to capture the first rising edge of the PPS signal. A successful capture of C_{End} will disable the GPIO pin.

Periodic clock correction on the gateway and clock synchronization on leaf nodes are performed during *Task C: Rough Time Synchronization*. When PPS (C) is reached, three events, which all requires task sycnrhozation, are scheduled in the algorithm. 1) Global clocks of the gateway nodes are set to zero (*t' = 0*). This process ensures that all the gateway nodes set their internal clock to the same value. Because all sub-networks processes the task at the same UTC time and the corresponding PPS interrupt, UTC information can be lost. 2) Start another timer T_{Buffer} and broadcasts a single beacon signal to the network containing global clock of gateway. A non-integer value in second for T_{Buffer} is required not to be interrupted with different PPS interrupt. Depends on the size of the network, T_{Buffer} can be set for 3.5 seconds for small sub-networks (less than 10 leaf

nodes within visible range). A leaf node that receives the signal adjusts its offset so that network is roughly clock synchronized. Once tasks are executed, the primary GPIO interrupt handler is enabled again and waits for the next PPS signal interruption ($C_{End} = 1$). A successful capture of the PPS signal will disable the GPIO pin and move on to the following task, the Task D. 3) Schedule a periodic counter (C_{Update}) to update global clock to prevent clock drift. This process timestamps the global time (T_{Prev}) and enables a secondary GPIO interrupt handler with a counter, C_{Update}. For example, if C_{Update} is set to 5, the secondary GPIO handler bypasses four consecutive pulses and interrupts itself at the fifth PPS pulse. Then, global clock adjusts its clock by adding elapsed time to previously stored time information. Figure 70 depicts the above process. The clock is assumed to be linear within C_{Update} and does not drift much. The process repeats till the sensing task is finished. The purpose of C_{Update} is to ensure synchronization among gateways by controlling clocks to increase according to PPS signals. Since the periodic updates of the gateway clocks are scheduled asynchronously as hardware interrupts, the clocks of the gateway nodes can be kept very accurate and hence accurately synchronized with each other.

```
Case (TaskC)
set.clock(0);    // Clock initialization
while( SensingTask == True) { //Repeat if the sensing Task is not ended
      T_prev = get.Time(); // Read Time stamp
      // enable secondary GPIO pin
            if(count == Cupdate){
                time = T_prev+get.ClockRate()*Cupdate;
                // disable secondary GPIO pin
            }else
            count++;
}
```

Figure 70. Periodic clock offset correction scheme.

Time for leaf nodes to actually start measurement will be commanded through *Task D: Calculate start time*. When PPS (D) interrupts GPIO pin the gateway calculates T_{Start} and broadcast the time to the leaf node. When leaf nodes receive the message, waiting time (waitTime) is calculated based on leaf node current time (T_{Leaf}) and T_{Start} (i.e. waitTime $= T_{Start} - T_{Leaf}$). Since all leaf nodes in a sub-network are synchronized with the gateway clock at the beginning, leaf nodes start sensing roughly at the same time. Leaf nodes in multiple networks also start measurement nearly at the same time because gateway node clocks are initially synchronized and the task D has been synchronized using the PPS signals.

The uncertainty of sensing start time in the networks will be compensated through resampling after sensing is finished. Gateway broadcasts beacon signals periodically and leaf nodes in the network stores offset and corresponding local time for regression analysis to estimate nonlinear clock drift when sensing is finished (Li, et al. 2012). Finally, data synchronization, resampling, is applied after sensing is finished to eliminate the errors from uncertainties of start timing and randomness of the clock speeds.

139

6.3. Performance evaluation

Laboratory tests validated the proposed synchronized sensing protocols for both single network and multiple-network synchronized sensing. Tests are performed for short-term (1 min and 5 min) and long-term measurements (30 min) and measured random signals to compare the synchronization accuracy. Also, the stability of the clock is checked by compensating the clock drift with either linear or 5th order curve fitting. The results of the tests prove the prospective use of the algorithm for scalable WSS Networks aiming at long-term monitoring of civil structures.

6.3.1. Synchronized sensing protocols comparison in a single network

A small-scale network in which all leaf nodes can measure the identical random signals is prepared in an indoor laboratory to check the single network synchronized sensing (Figure 71). The network consists of an Imote2 as a gateway and three Imote2s as leaf nodes. A GPS receiver is connected to the gateway and periodically updated the clock based on PPS signals (every 5 PPS signals) when proposed protocol was used. An ISM400 sensor board capable of measuring external analog signals is stacked on the Imote2 of each leaf node (MEMSIC, 2010). An analog signal generator, VibPilot (www.mpihome.com, 2010), generated Band Limited White Noise (BLWN) with 100 Hz bandwidth. To provide identical signals to three leaf nodes, the signal is split using connectors and fed to the sensor board. The test setup assures that all leaf nodes measure identical BLWN signals, which facilitate accurate estimation of synchronized sensing error in the measured data.
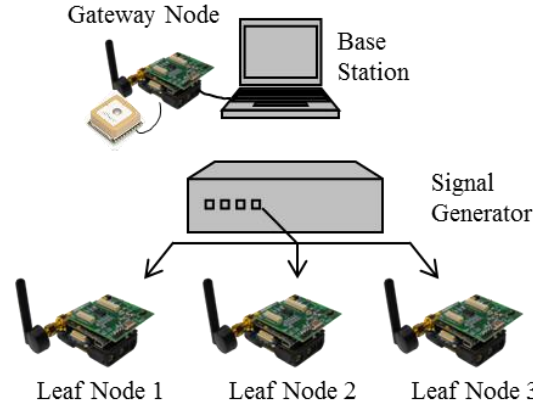
Figure 71. Test setup for synchronized sensing accuracy estimation.

Synchronized sensing error can be quantified using the phase angle of the cross PSD between the collected signals. Once the cross PSD is calculated, the slope of the phase angle of the cross PSD is found using linear curving fitting (Nagayama and Spencer, 2007). Then, the synchronized sensing error is estimated by the following equation, in which θ is the angle of the phase angle curve.

$$\text{Time Synchronization error} = \frac{\theta}{2\pi} \times 10^6 \ (\mu s) \tag{26}$$

In calculation of the cross PSD, Hanning window with 1024 Fast Fourier Transformation points and 50% overlapping are used. The frequency range used for linear curve fitting the phase angle curve (the slope of phase angle) can be chosen based on the cut-off frequency used to measure the data with an ISM400 board. Throughout the experiment, sampling frequency of 100 Hz and corresponding cut-off frequency of 40 Hz is used. Thus, the frequency range used for linear fitting used is from 0 to 35 Hz. Figure 72 shows an example of calculated phase angle of the cross PSD between two measured signals. By linear curve fitting the phase angle the synchronized sensing with the frequency range 0 to 35 Hz is about 13 µs.
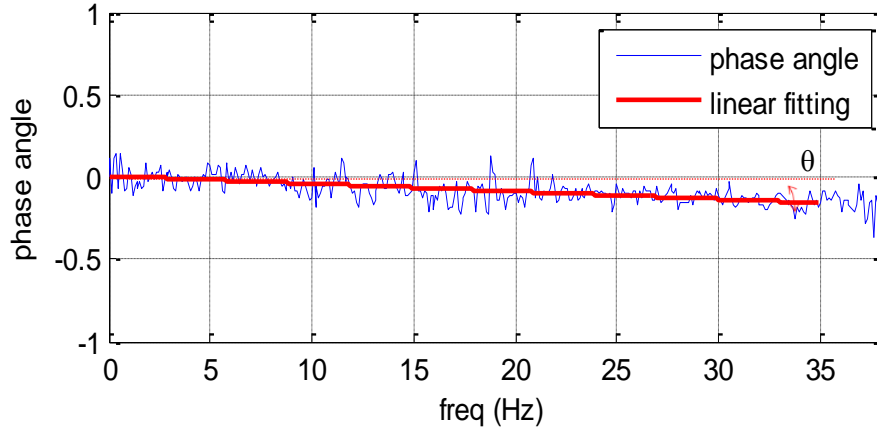
Figure 72. Example of phase angle of the cross PSD.

Three protocols are compared to validate the proposed synchronized sensing method in a single network: (i) synchronized sensing with linear drift estimation, (ii) synchronized sensing with nonlinear drift compensation, and (iii) the proposed algorithm. Both piecewise linear and fifth-order curve fitting were used for the comparison in the nonlinear drift compensation algorithm and proposed protocol. The sampling frequency of data acquisition with WSSs was 100 Hz, and sensing durations were varied from short-term (1 min), mid-term (3 min), and to long-term (30 min) measurements. As shown in Table 6, when the error was calculated based on the base station local clock, similar degree of synchronized sensing error, about 33 μs on average, are observed in all protocols for short-term tests. The Linear drift estimation showed increased synchronized sensing error (over 50 μs) for mid-term test, whereas other methods showed similar error sizes with short-term tests. Significant effects of nonlinear clock drifts in the leaf nodes are observed in long-term tests: Two sensor measurements are unsynchronized showing the synchronization error as large as 1 ms. Nonlinear clock drift compensation ensured that the similar degrees of synchronized errors in long-term measurements for other cases. The higher-order regression of the clock drift enhanced the performance; an approximately 15% increase for both protocols. The results validated that the

142

proposed method provides synchronized sensing with error less than 50 μs in a single network for an arbitrary length of time.

Table 6. Synchronized sensing errors.

Synchronized Sensing Protocols	Synchronized sensing error [μs] - compared with base station local clock		
	1 min	3 min	30 min
Linear drift estimation	28.95	55.16	-1175.8
Nonlinear drift compensation (piecewise linear)	30.92	31.00	23.73
Nonlinear drift compensation (5th order)	35.83	36.71	19.71
Proposed algorithm (linear)	35.26	35.28	34.05
Proposed algorithm (5th order)	34.84	24.87	26.29

6.3.2. Multiple-network synchronized sensing accuracy

Two WSS networks, as shown in Figure 73, are prepared to validate two main goals of the proposed algorithm: (i) periodic correction of gateway node's clocks with PPS signals to compensate nonlinear drift, and (ii) achieve synchronized sensing between different sub-networks. In the test setup, Network A consists of one leaf node, Leaf Node 1, and Network B consists of two leaf nodes, Leaf Node 2 and Leaf Node 3. Each gateway node is connected to a base station computer and a GPS receiver. Each leaf node's Imote2 is connected to an ISM400 sensor board to measure external analog signals. Since the two networks are closely located, two different radio communication channels are designated to each network. When the frequency range of the selected radio channels are apart from each other, mutual interference can be avoided (Linderman, et al. 2010). Synchronization accuracy between the two networks is estimated by comparing the signals measured

143

by the sensor boards. To provide the same signal to all sensors, random signals generated from VibPilot are split and fed into the 4th channel of the ISM400 boards. The sampling frequency of all wireless sensors is 100 Hz.
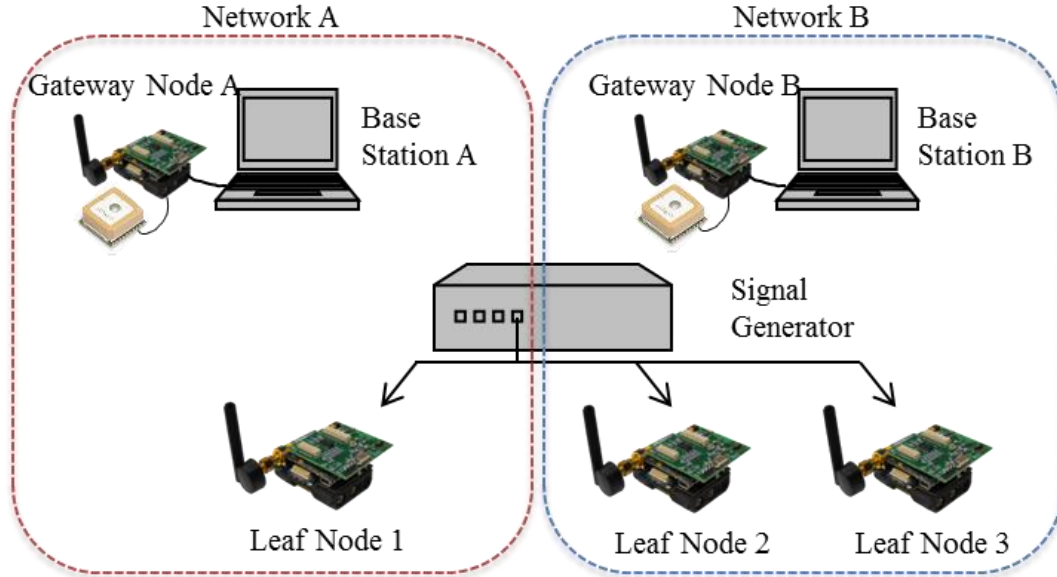
Figure 73. Test setup for evaluating synchronized sensing for multiple networks.

The first test demonstrated the effectiveness of periodic correction of gateway node's clocks by comparing the measurements without and with gateway clock adjustments. At the beginning of sensing, both gateway nodes are clock synchronized to the UTC time. However, the differences between the clock frequencies of the two gateway nodes are not corrected and are broadcasted to their leaf nodes. The phase angle of the cross PSD calculated using signals measured for 3 min period showed relatively large error of -138 μs based on the phase angle with the frequency range between 0 to 35 Hz. When both gateway clocks are updated periodically after every 5 PPS signals during the sensing period and are broadcasted to leaf nodes, the slope of the phase angle of the cross PSD is much smaller. The synchronization error was -20 μs based on the phase angle with the frequency range. The results indicate that the clock drift on the gateway nodes is not negligible and their clocks should be adjusted to provide synchronized sensing among multiple networks.

144

Further tests are performed for extended sensing periods to validate synchronized sensing between multiple networks. The test combinations have different sensing durations (1 min, 3min, and 30 min) and different clock drift compensation (linear and 5th order curve fitting). Table 7 summarizes averages and standard deviations of the synchronization errors over a number of tests for each test combination. Accurate synchronized sensing, which is less than 50 µs, is obtained from the leaf nodes in different sub-networks. Moreover, the error size did not increased significantly as the sensing time increases indicating the stability of the protocol. Due to periodic gateway node clock correction, which assured the linearity of the clock drift, linear curve fitting result showed similar degree of accuracy compared with 5th order curve fitting. In summary, both single network and multiple-network test results achieved synchronized sensing with less than 50 µs errors. Therefore, the proposed protocol is suitable for long-term monitoring of scalable WSS networks.

Table 7. Multiple-network synchronization error comparison.

		Multiple-network synchronized sensing error [µs]		
		1 min	3 min	30 min
Linear Curve fitting	Average	19.55	21.06	33.49
	<Std*>	<4.23>	<6.25>	<5.09>
5th-order Curve fitting	Average	16.21	11.08	30.60
	<Std>	<4.40>	<6.45>	<2.43>

<Std>: Standard deviation

6.4. Future implication of the synchronization for monitoring railroad bridges

Field tests were performed to show the potential use of the proposed synchronized sensing protocols for monitoring responses of a railroad bridge and input loading. Along with the bridge network on the selected railroad bridge in Figure 25, another network was prepared on the locomotive of the test train described in Figure 48. A laptop inside the engine reached the gateway node on the side rail and controlled the train sensors. Three leaf nodes shown in Figure 74 captured the responses of the front and rear bogies, as well as the responses of the car body.
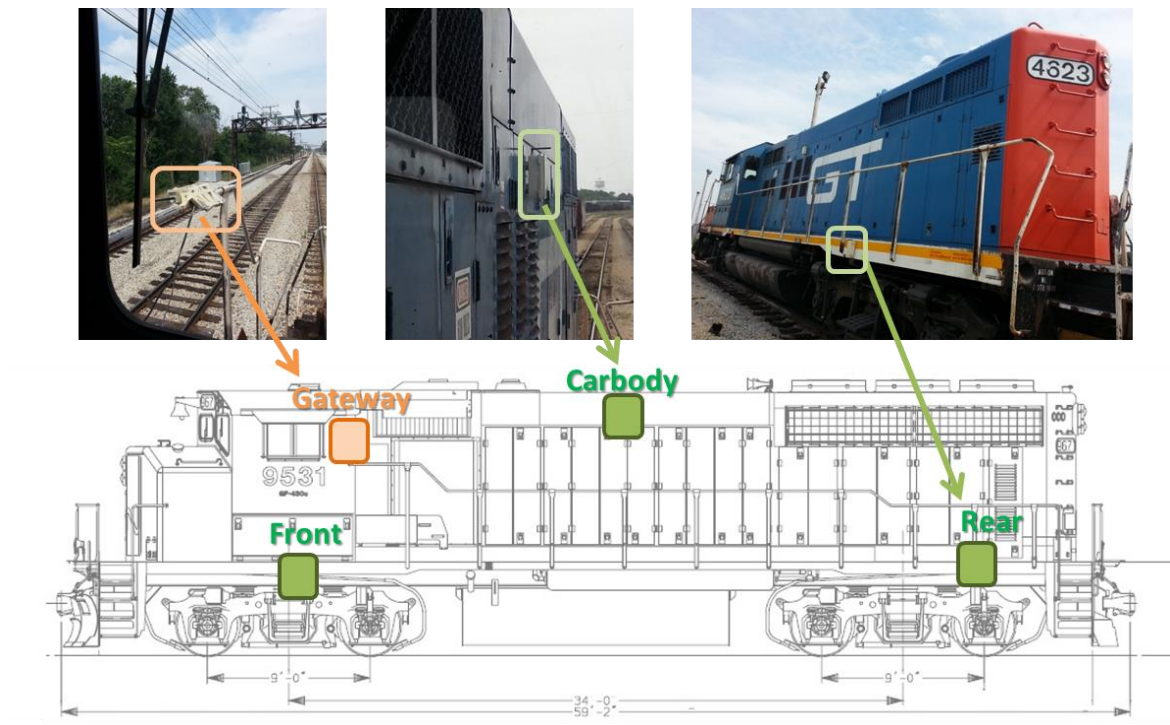
Figure 74. Train sensors setup.

An example of measured signals while the test train crossed the bridge is shown in Figure 75. Leaf nodes in two networks initiated sensing with the same input; same UTC time, sampling frequency (25 Hz) and measurement period (over 10 min). Train reached the bridge at 5 MPH from the South. When the train fully crossed the bridge, train fully stopped. After a minute of rest, the train re-approached the bridge and stopped in the middle of the bridge for about 20 seconds. The train

exited the bridge by moving towards the South end of the bridge. As can be seen in Figure 75, acceleration signature of the bridge agrees well with the train log indicating that two networks were synchronized with each other. These results demonstrates the potential of using synchronized data to identify input to the structure and to validate the numerically developed VTB interaction models that will lead to better understanding the state of the railroad bridges.
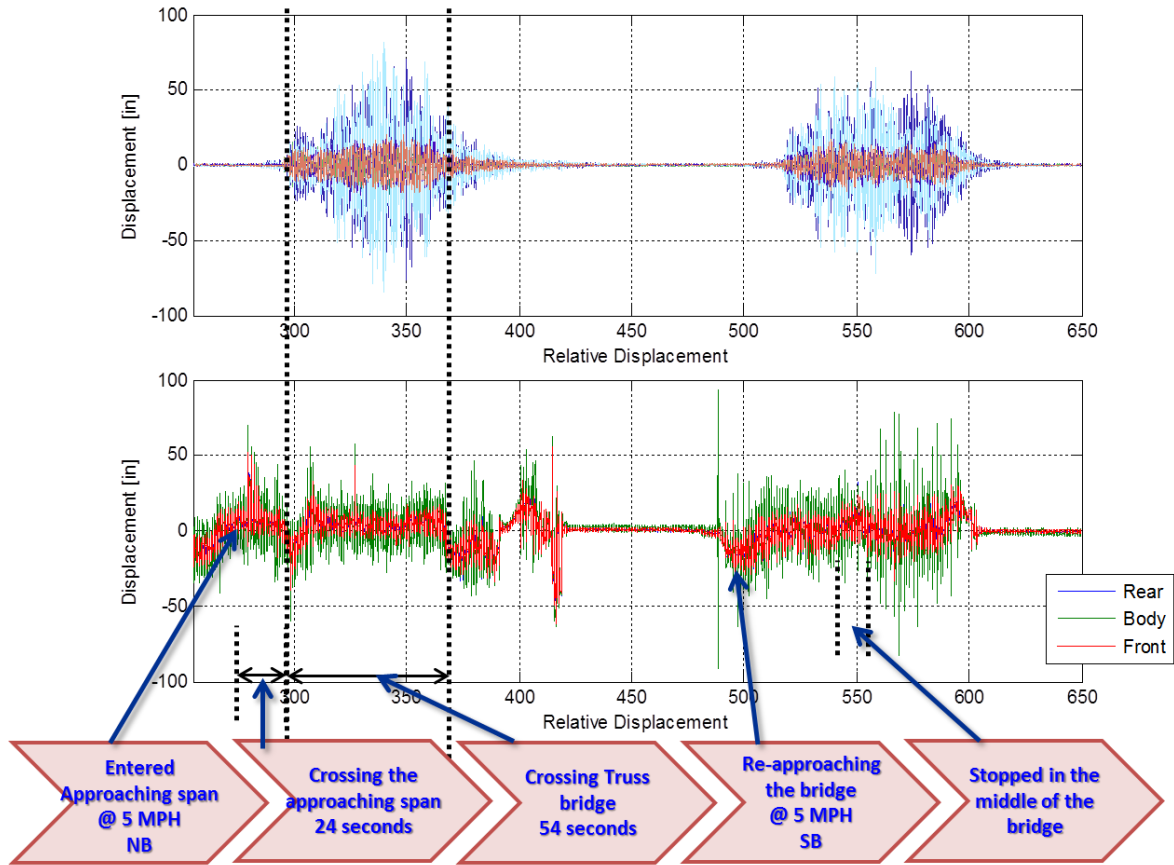
Figure 75. An example of synchronized sensing.

6.5. Conclusion

In this chapter, a scalable protocol that provides effective synchronized sensing among multiple networks has been presented. The protocol used the Pulse-Per-Second signals from low-cost GPS receivers. The method was implemented on the Imote2 sensor platform and achieved two following main goals; i) periodic clock correction of gateway nodes to compensate nonlinear clock drift, and ii)

achieve 50 μs synchronized sensing accuracy from leaf nodes in different networks. The results demonstrated that the proposed approach is highly scalable, realizing precise synchronized sensing for an arbitrary duration of data collection. The proposed method provides a foundational base for monitoring interaction dynamics in a railroad bridge application.

CHAPTER 7. APPLICATION-LEVEL RELIABILITY ASSESSMENT OF WSS NETWORKS

WSSs offer low-cost, easy installation, and on-board processing of raw data promising that this new technology can reduce the cost and complexity of bridge assessment tasks. However, because of their distributed nature, maintaining highly robust and reliable networks can be challenging, limiting their wider implementation. So far, studies on network quality assessment have been focused on communication-level reliability using temporal signal indicators. Because the WSS networks for SHM purpose often require a large amount of data transfer, application-level reliability, which can assess the network quality based on the completion of a task, should be considered. Thus, this chapter proposes a new approach to assess application-level reliability of WSS networks deployed for SHM application. Following a framework for assessing application-level reliability of WSS networks is presented. Two common tools to assess the reliability of a system (i.e., Monte Carlo Simulation (MCS) and First-Order Reliability Methods (FORM) are employed along with collected communication-level data. Examples using small-scale and full-scale WSS networks are considered to demonstrate the practical use of the proposed approach. The proposed approach provides a tool that can quickly evaluate the reliability of WSS networks for SHM using readily available data.

7.1. Example of unpredictable WSS performance

This section illustrates the unpredictable performances of Imote2s even under identical communication circumstances. Applications in the ISHMP Services Toolsuite aim to provide robust performances. Figure 76 shows an example of a WSS network. When a command is sent from a central base station to leaf nodes in its network, the individual leaf nodes resend a packet to the base station once the application is successfully completed. When the message does not arrive within a certain amount of time, the base station acknowledges that the application has been failed at the leaf

node. Such a failure may be caused by i) the failure of the node while performing the tasks, ii) the failure of communication such that the commands from the base station have not arrived, or iii) the failure of communication such that the acknowledgement message from the node is not received. Reset[8] is one of the simplest applications among those services. A message from the base station node only contains a reset command. The acknowledge message will be immediately sent back once the command is received. Because of its simplicity, the application failure will provide a good indicator of communication failure during sending/receiving the messages.
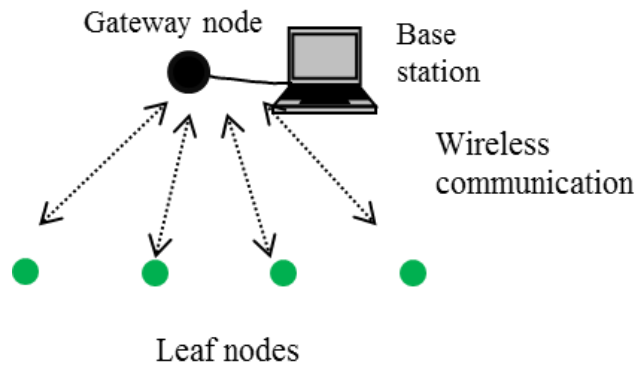
Figure 76. Illustration of a wireless network.

Ten Imote2s were prepared in an outdoor environment, in which all leaf nodes are located about 100 m from the base station node. Stable DC power was provided to the nodes from an 80-Watt power supply. Thus, the communication environment and the power source were identical. The test performed 12 trials, in which the base station broadcasted the reset command to ten leaf nodes. Figure 77 summarizes the returned packets from each leaf node acknowledging the completion of Reset. Although the application is simple and the communication circumstance was identical, each leaf node showed different performance. The number of failures and the trials at which a sensor failed varied among sensors. Node ID (5) had only one failure, while Node ID (73) failed four times.

---

[8] An Arial font indicates the name of an application.

The test results indicate that the performance of an application may vary with each nodes and also with other unknown factors. This type of communication uncertainty is always present in the wireless communication network. To use such failure prone WSSs in a SHM application requiring high data throughput, appropriate models for these failures, as well as a means to analyze their impact on the overall network, must be developed.

Figure 77. Application test under identical communication circumstances.

151

7.2. Measures of communication link quality

This section investigates long-term wireless performance of the Imote2s to understand relationships between application-level performance and commonly adopted link quality indicators. Various researchers have proposed statistical methods to characterize the quality of the wireless links. Those studies used indices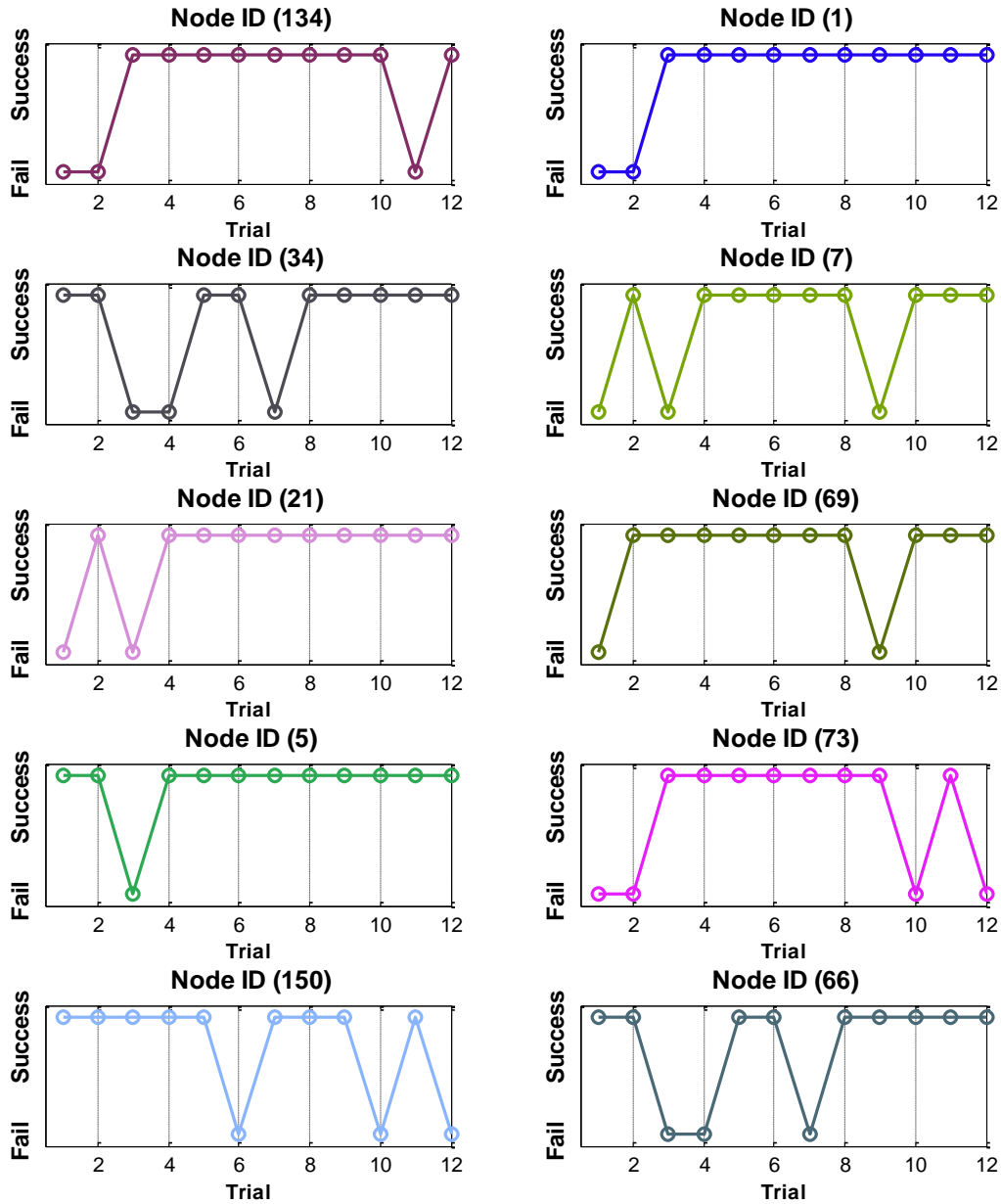 that can provide instantaneous measure of link instability and radio signal strength such as Radio Signal Strength Indicator (RSSI) and Link-Quality Indicator (LQI). RSSI is the measure of power in the received radio signals and LQI estimates how easily the signals can be modulated in the presence of noise in the channel (Benkic et al. 2008). Gungor et al. (2010), and Rondinone et al. (2008) related the radio communication quality to Packet Reception Rates (PRR) by measuring RSSI and LQI. Although previous studies found some correlations between those indices have been found, such relationships provide only instantaneous measure of link characteristics. Therefore, those proposed methods are not directly applicable to WSS networks for SHM applications.

An application, TestRadio, was selected to identify the extended relationships between RSSI, LQI, and long-term performance of the wireless link using the Imote2 platforms. A built-in radio chip, in the Imote2 can provide digital RSSI and LQI. The dynamic range of RSSI is from −100 dB to 0 dB and LQI ranges from 0 to 255 which 110 indicates the maximum quality and 50 is the lowest detectable value (Chipcon, 2004). Figure 78 shows an example of TestRadio that attempted to send 1,000 round-trip packets to a leaf node (node ID: 53). The gateway node sent out 1,000 packets to the leaf node. On receiving the packets, the leaf node returned the packets to the gateway node, with information about RSSI and LQI of each packet. Returned RSSI (rrssi[9]) and returned LQI (rlqi) represent communication qualities at the leaf nodes. Then the gateway calculates PRR (r%) using the

---

[9] A Courier New font indicates the parameter shown in Figure 78.

ratio between received and sent packets, which indicates the measure of data loss. Thus, PRR can be a measure of reliability and goodness of the links. In this example, the gateway node aimed to transmit 1,000 packets and received 1,000 packets back, thus, `r%` is 100 %. Output of TestRadio indicates application-level performance of the nodes because the application provides cumulated `r%` and averaged `rrssi` and `rlqi` over a number of packets, that were communicated in between the gateway node and the leaf node.


```
BluSH>TestRadio 1000 53
BluSH>Sending 1000 packets to 1 node(s): 53
Request successfully sent to 1 node(s).
Sending data messages...
Data messages sent.
Querying node 53...
Finished receiving responses from node 53.
addr    cnt    %      rssi   lqi    noise   rcnt   r%     rrssi  rlqi noi
se
53      1000   100    -37    106    -96     1000   100    -36    107 -99
```

Figure 78. TestRadio example.

Table 8. The radio test setup.

Number of lead nodes	3
Distance from a gateway (m)	5
Packets sent in each trial	100
Number of trials	500

TestRadio was performed extensively using three leaf nodes to measure averaged `rrssi` (noted as RSSI hereafter), `rlqi` (also noted as LQI) and `r%` (averaged PRR). Test setup is summarized in Table 8. In this test, hardware related bias was reduced by using three different Imote2s. Figure 79 plots three-dimensional and two-dimensional relationships among PRR-LQI-RSSI. Overturned 'L-shape' relationships, which PRR decreases sharply as both RSSI and LQI value

decrease are observed. The sharper edge in PRR-RSSI (Figure 79b) indicates that RSSI itself is inaccurate to predict PRR due to high fluctuations in the domain RSSI < −90 and due to low sensitivity with higher RSSI (i.e. RSSI > −90).
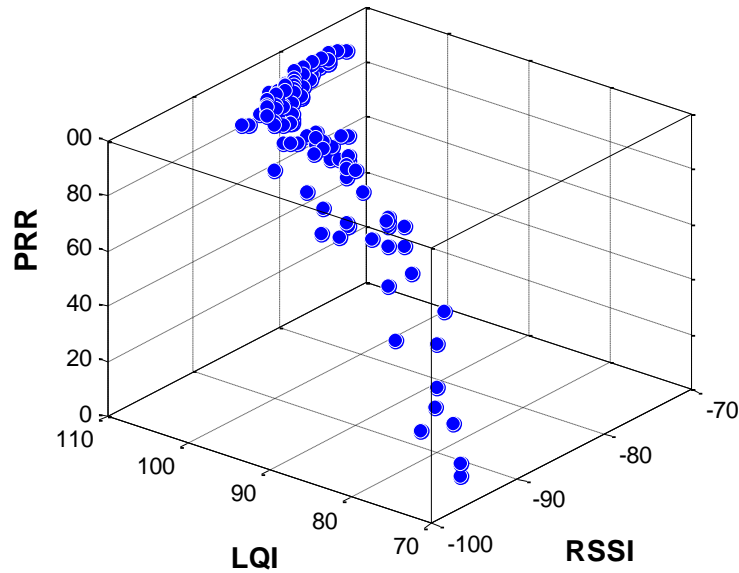
(a) RSSI-LQI-PRR.
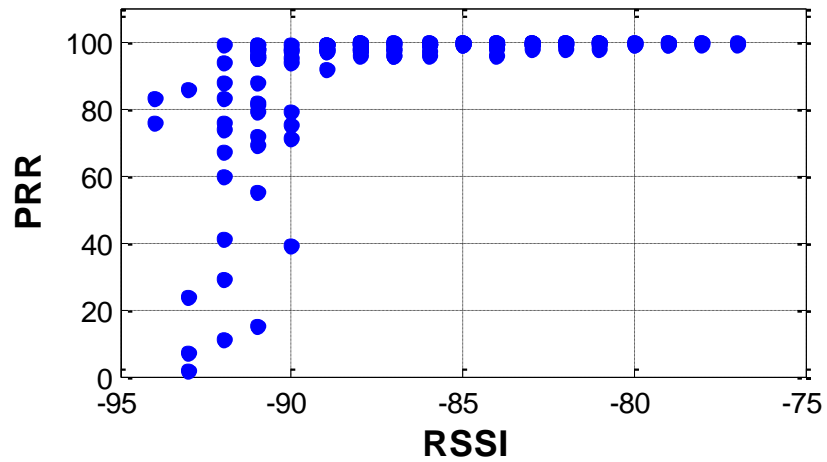
(b) RSSI-PRR.

Figure 79 Relationships with the PRR.
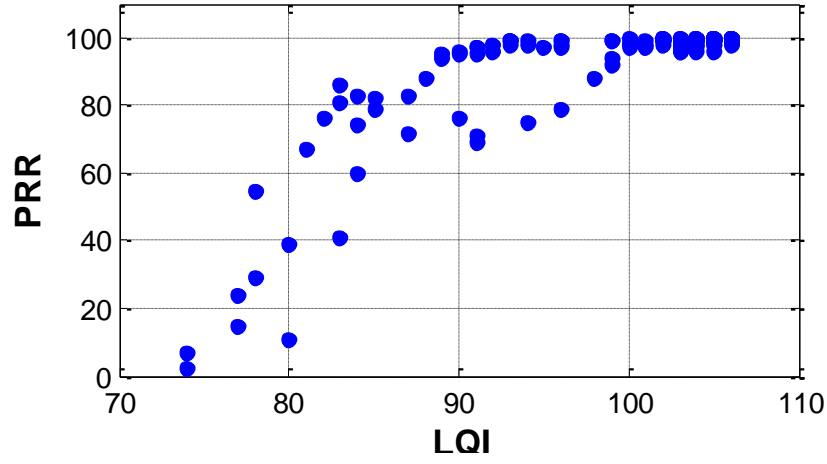
(c) LQI-PRR.

Figure 79. (cont.)

Using the relationships observed in the measured data, estimated PRR, PRR_{EST}, can be expressed as a function of RSSI and LQI. For example, using a second-order polynomial model

$$PRR_{EST} = a + b(RSSI) + c(LQI) + d(RSSI^2) + d(RSSI)(LQI) + e(LQI^2) \tag{27}$$

where a, b, c, d, and e are constants obtained from nonlinear regression of the measured PRR on the measured RSSI and LQI. As shown in Figure 80a-c, the regression model captures trends of measured PRR over the measurement range of RSSI and LQI reasonably well. However, because of the randomness in measured RSSI and LQI, an empirical equation in Eqn. (27) alone cannot represent their relationship with PRR accurately. Thus, using Eqn. (27), a stochastic approach will be adopted in assessing the application-level network communication quality in the next section.

155
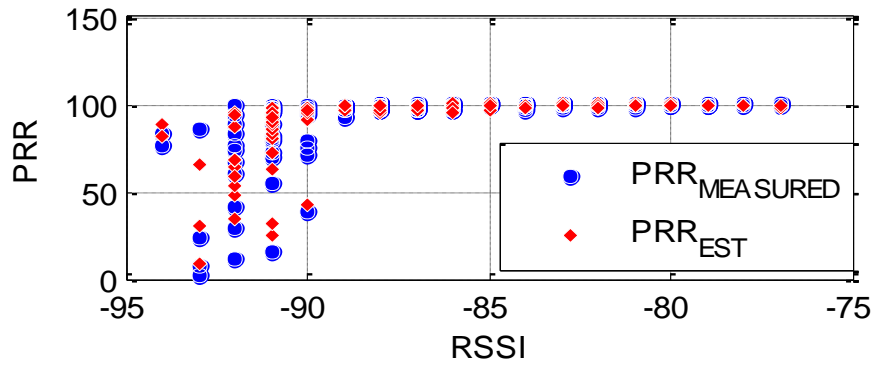
(a) RSSI-PRR relationship.
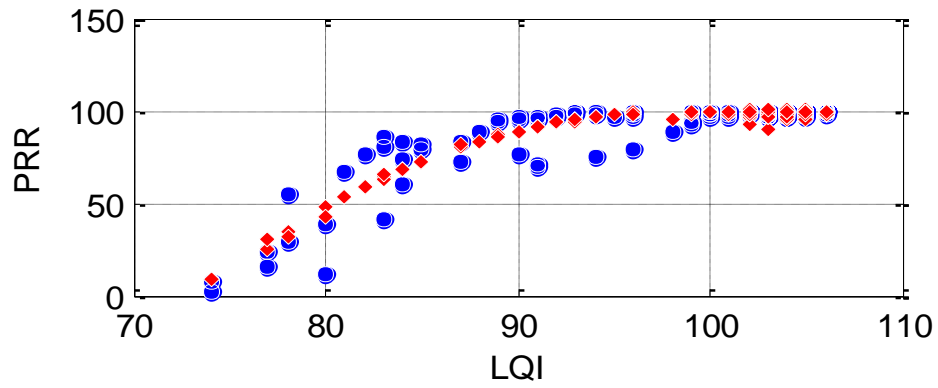
(b) LQI-PRR relationship.
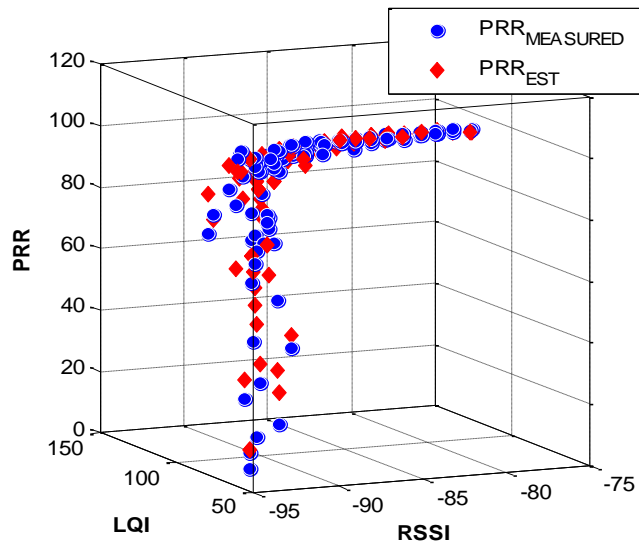
(c) RSSI-LQI-PRR relationship.

Figure 80. Estimated PRR.

156

7.3. Framework for application-level reliability assessment

This section defines framework for the reliability assessment of WSS networks. The limit state function is defined first and then the uncertainty is added in the model.

7.3.1. Limit state function

A failure state of a leaf node in SHM applications is defined as an event that a leaf node fails to send measured signals to a gateway node due to excessive amount of packet loss occurred during the transmission. Knowing packet loss before sending data, however, is challenging. Instead, the PRR can be estimated, PRR_{EST}, using empirical relationships shown in Eqn. (27), and compared with a threshold PRR, PRR_{LIMIT}. Eqn. (28) shows such a state; when PRR_{EST} is lower than PRR_{LIMIT}, the communication environment is considered harsh and a leaf node is likely to give up completing data transmission to the base station.

$$g(x) = PRR_{EST} - PRR_{LIMIT} + \varepsilon \tag{28}$$

An additional term (ε), which represent the epistemic error, is added in the equation. One can adopt the central limit theorem for ε, to compensate such a model error. The distribution model of ε is assumed to follow the normal distribution with zero mean and standard deviation σ, determined during regression analysis $\varepsilon(RSSI, LQI) \sim N(0, \sigma)$. A linear regression method is used to find an unbiased estimation of the conditional variance of ε for given values of RSSI and LQI (Straub and Der Kiureghian, 2010). Then, a constant for PRR_{LIMIT} should be determined depends on the application requirement. For example, a high number should be used for an application, which the application aims near real-time data acquisition and each packet is irreplaceable. On the other hand, if an application can transmit the same packet for a certain trials to assure the packet has received, a

157

relatively low constant can be used. Then, a set will be determined either a failure set when $g(x)$ is lower than 0, a limit state when $g(x)=0$, or a safe set $g(x)>0$.
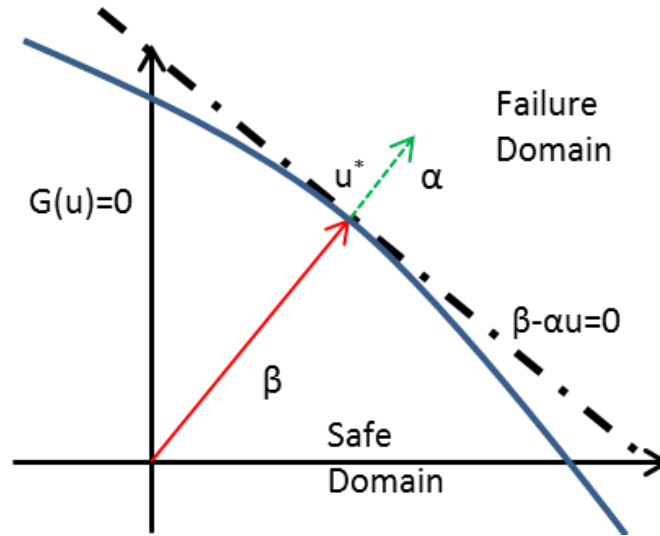
Figure 81. An illustration of FORM approximation.

A number of different methods can be adopted to solve the limit-state function with random variables. Two most common methods are First Order Reliability Method (FORM) and Monte Carlo Simulation (MCS). FORM is advantageous when the application is stringent on computational complexities. In FORM, the limit-state function is replaced by a tangential hyper-plane at the failure point (u^*) as depicted with the dashed line in Figure 81. The approach uses a relatively small number of computations on the limit-state function and its gradient. Der Kiureghian (1996) emphasized the effectiveness of FORM analysis by showing that the number of computations of each limit state function and its gradient is of order 10-100. MCS is a powerful tool to estimate P_E, because the method allows direct consideration of any type of probability distribution, easy to implement at the desired precision (Cardoso et al. 2008). However, due to the difficulties in producing truly random samples and the possible high computational cost for low-probability events, MCS is often criticized as impractical for some engineering applications (Der Kiureghian, 1996). Here, both approaches will

be applied in assessing the network reliability with the known distribution of the random variables, RSSI and LQI, which will be described in the next section.

7.3.2. Uncertainty Modeling in the Network

This section determines the distribution types of the random variables in the Eqn. (28) using the measured RSSI and LQI in the test described in Table 8. In selecting distribution models, the maximum likelihood estimation method was adopted with the following criteria:

1. The shape of the selected Probability Density Function (PDF) of a random variable should well represent that of the histogram.

2. The boundary of each distribution must not violate physical limitations of random variables.

For example, from the measured data sets, PDF of RSSI can be the normal distribution (see Figure 82a) with mean value (μ_{RSSI}) of -92.60 dB and standard deviation (σ_{RSSI}) of 1.43. For PDF of LQI, the gamma distribution (see Figure 82b) can be used with the following parameters: $\mu_{LQI}=$ 97.50, $\sigma_{LQI}= 36.24$, $a_{LQI}= 262.335$ and $b_{LQI}= 8.6\times10^{-4}$. Note that a_{LQI} and b_{LQI} refer to the shape and scale parameters of the gamma distribution, respectively. The histogram of RSSI has discontinuities, as can be seen in Figure 82, because RSSI is a quantized integer value. The mean and variances of RSSI and LQI are susceptible to the environmental changes such as the distance and nearby material types. However, distribution types are less likely to change because hardware related biases are considered by using three different Imote2s. Thus, the usage of the application will collect smaller amounts of data to find the parameter fitting for the distribution types. This approach enhances in-place applicability.

(a) RSSI.

(b) LQI.
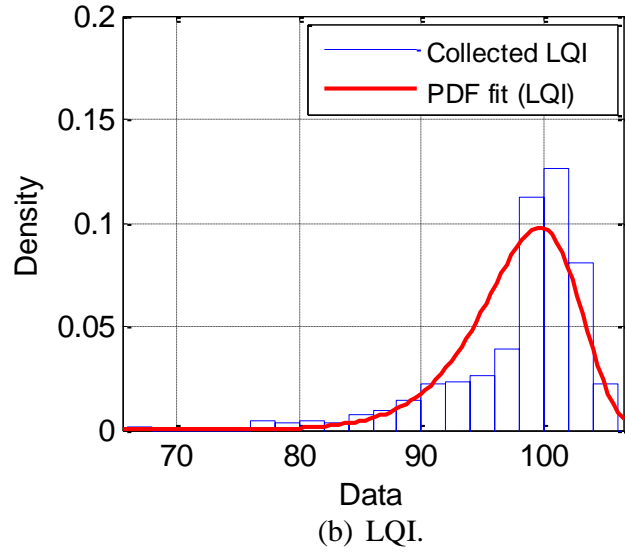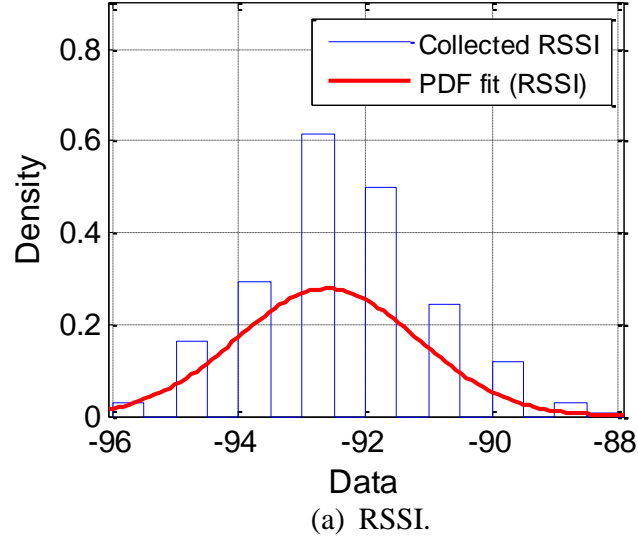
Figure 82. Histogram and PDFs.

Nataf joint distribution model is applied to describe the correlation among random variables in the standard normal random variable space (Nataf, 1962). Correlation coefficient ($\rho_{RSSI,LQI}$) of transformed standard normal random variables (z_{RSSI}, z_{LQI}) can be expressed as follows.

$$\rho_{RSSI,LQI} = \int_{-\infty}^{\infty}\int_{-\infty}^{\infty}\left(\frac{x_{RSSI} - \mu_{RSSI}}{\sigma_{RSSI}}\right)\left(\frac{x_{LQI} - \mu_{LQI}}{\sigma_{LQI}}\right)\varphi_2\left(z_i, z_j, \rho_{0,RSSI,LQI}\right)dz_{RSSI}dz_{LQI} \tag{29}$$
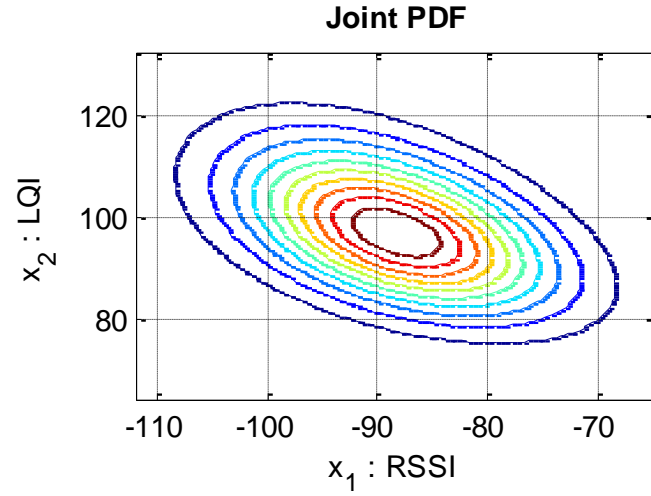
(a) Joint PDF.
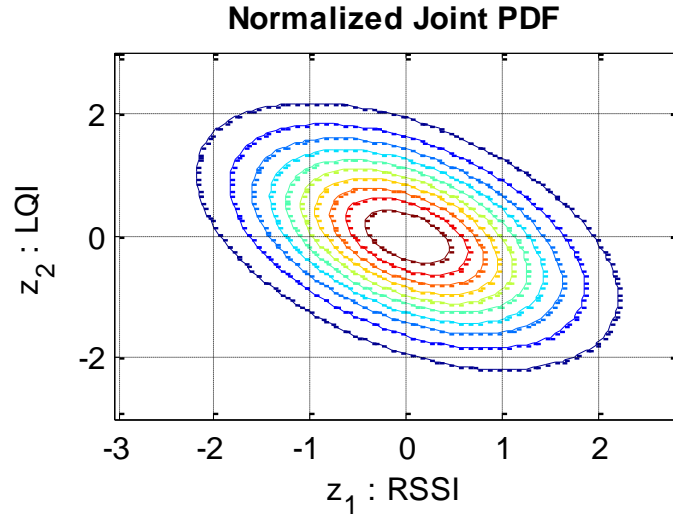
(b) Standard normal PDF.

Figure 83. Joint PDF and standard normal PDF.

where, x_{RSSI} and x_{LQI} are random variables, φ_2 is the bivariate standard normal PDF and $\rho_{0,RSSI,LQI}$ is

the correlation coefficient of x_{RSSI} and x_{LQI} (Der Kiureghian and Liu, 1986). Using the measured

data from the test setup described in Table 8, $\rho_{LQI,PRR} = 0.80$ for LQI and PRR$_{MEASURED}$ and

$\rho_{RSSI,PRR} = 0.49$ for RSSI and PRR$_{MEASURED}$. Differences between $\rho_{LQI,PRR}$ and $\rho_{RSSI,PRR}$ indicate that,

as can be seen in the sharp edge of an overturned 'L-shape' in Figure 79b, PRR$_{MEASURED}$ is less

sensitive to the change in RSSI than LQI. Figure 83 shows the calculated joint PDF and the transformed standard normal PDF from the measurements. Finally, probability of a failure is defined as follows.

$$P_E = \int\limits_{x \in \Omega_E(x)} f(x)dx, \tag{30}$$

where P_E denotes the probability of failure, $f(x)$ is a standard joint normal PDF, and $\Omega_E(x)$ is the failure domain determined by limit-state functions.

So far, the reliability model to assess the application-level wireless communication quality has been determined; A limit state function using the measured variables and estimated PRR are defined. Distribution types for random variables are also chosen using the measured data. Here, the distribution shapes of the random variables and PRR are rather deterministic because the tests contains an wide range of LQI and RSSI and eliminated hardware-related bias. However, the constants in the equation may be sensitive to the environmental effects; i.e. distance from the gateway to leaf nodes, radio blockage, etc. Therefore, the proposed approach will require a priori tests with less number of data sets for the following reasons: i) determine the characteristics of two random variables (RSSI and LQI), ii) curve fit the predetermined equation to obtain constants in the Eqn. (27). The following section will demonstrate the applicability of the proposed method to assess application-level reliability of wireless networks.

7.4. Performance evaluation of the proposed method on WSS networks

This section evaluates the performance of the developed model on a small-scale WSS network and a full-scale network for reliability assessment. For computation of failure probabilities two methods are included for small-scale WSS network; FORM approximation and MCS. For full-scale network, only MCS is performed due to ease of computation.

162

7.4.1. Small-scale WSS network application
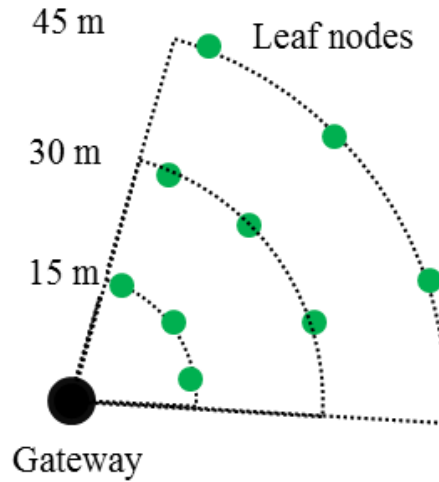
Figure 84. Small-scale test topology.

A temporal outdoor WSS network was prepared to assess the performance of the model developed in the section 4. In total, nine leaf nodes were prepared at three different locations; i.e. at each distance, 3 leaf nodes were located to mitigate hardware related bias (Figure 84). Three locations were measured from the base station, which were 15 m, 30m, and 45 m. Leaf nodes were lifted about 1m above from the ground to remove the signal blockage (Linderman et al. 2010). A polymer Li-ion battery provided a stable power of 3.7 V and 10 Ah to all sensors.

A set of radio of radio test determined the parameters for the distributions of two random variables and curve-fitted the limit-state function in Eqn. (30). The test averaged RSSI and LQI value over 100 packets and performed 100 times. From heuristic relationships between packet loss rate and the successful collection of a long data set from a leaf node to a gateway, PRR_{limit} was set to 85%. Once the model is identified, FORM and MCS are both followed on the measured radio test data to evaluate the network failure probability. FORM approximation analyses were performed using educational software developed at the University of California, Berkeley, FERUM (Finite Element Reliability Using Matlab), (Der Kiureghian et al. 2006). Table 9 summarizes the results obtained

from FORM analyses of the WSS network. P_E denotes the failure probability and β is the reliability index. The geometric meaning of β is the distance in the normalized space from the origin to the limit state surface (Ditlevsen and Madsen, 1996). The last two columns denote the most likely failure RSSI and LQI pairs. P_E increases with distance from the base station increases, confirming that the distance is one of the factors that affect application-level reliability. However, the value of P_E in all the cases are as small as 0.1772, indicating that within the distance of 50 m, the WSS network using the Imote2 platform is robust enough to complete the application, e.g. transmitting measured data in this case.

Table 9. FORM analyses results.

Location from Base Station	P_E	β	Failure point	
			RSSI	LQI
15 m	0.0584	1.5681	−77.25 dB	106.16
30 m	0.1182	1.1838	−82.35 dB	102.20
45 m	0.1772	0.9262	−82.16 dB	99.78

MCS can serve as a good alternative method over FORM approximation when large amount of sample is hard to obtain from the approximation. MCS has applied on the radio test data to check the applicability of the simulation in assessing the network reliability. During the simulation, c.o.v. (δ_{P_E}) validated the simulation size. Converging c.o.v. (δ_{P_E}) with a small value indicates that the sufficient number of samples has generated. For example, Figure 85a and b shows the converging P_E

and c.o.v. (δ_{P_E}) for test results obtained from 15 m WSSs. Approximately 10^4 samples give

confidence for the P_E and the size is used for simulating 30m and 45m test sets.
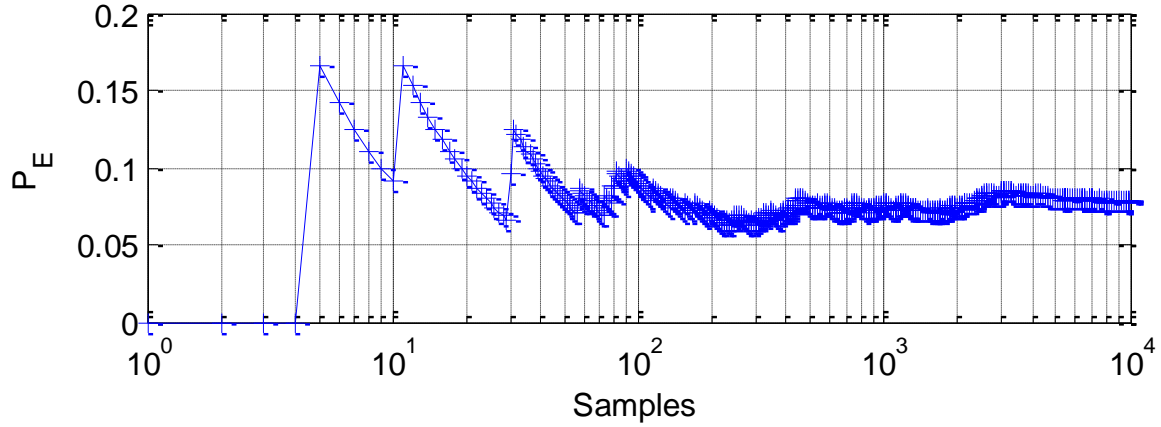
(a) Probability of failure.
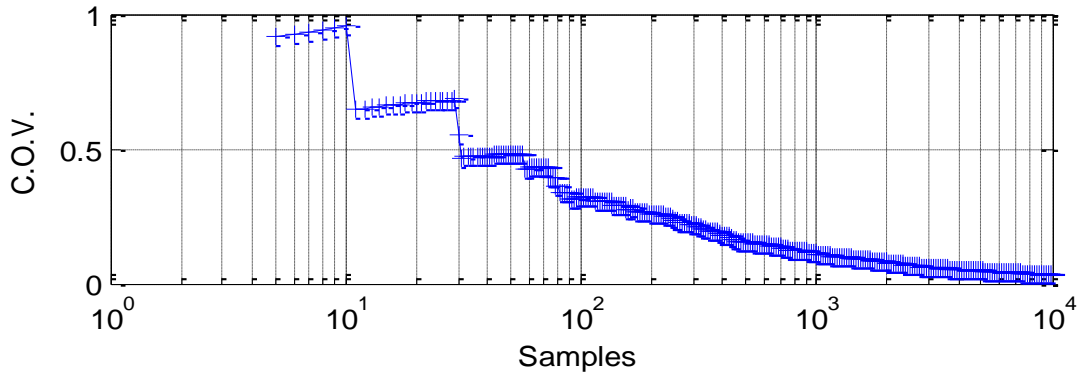
(b) c.o.v.
Figure 85. MCS results.

Table 10 summarizes P_E obtained from MCS (10^4 samples) and compares it with that of

FORM. As distance from the base station increases, P_E gradually increases both in MCS and in

FORM. However, MCS results are larger than FORM with roughly a 40% difference. Such large

differences may occur when the limit state function shows nonlinear behavior near the failure points.

Figure 86a~c confirm that the limit state surface experiences high nonlinearities, both in RSSI and in

LQI, near the design points found in Figure 81. In this case, MCS analysis is more powerful and

faithful tool that provides a more accurate result. Note that MCS analysis is efficient for solving this

problem because of the simple limit state function, which leads to low computational cost and fast

convergence time

Table 10.MCS results (comparison with FORM results).

| Distance | P_E | | Difference |
	FORM	MCS	[%]
15	0.0584	0.0771	24.25
30	0.1182	0.2013	41.28
45	0.1772	0.2855	37.93
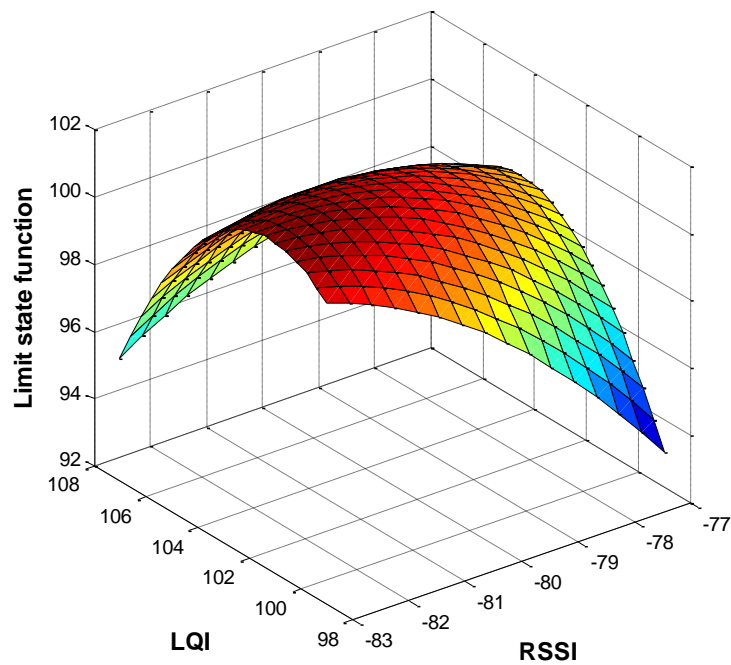
(a) An air view.

Figure 86. The limit state function near the failure points.
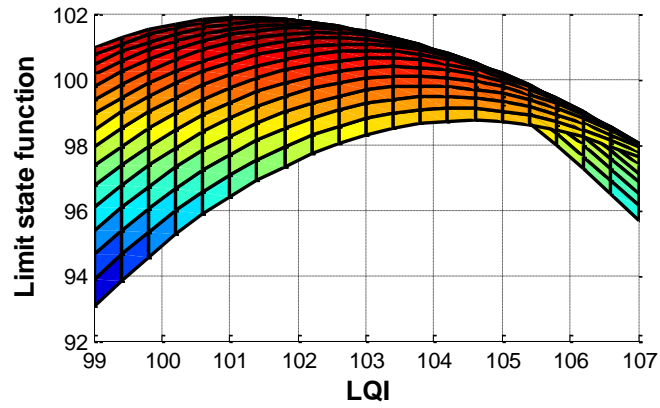
(b) The limit surface projected on the RSSI axes.
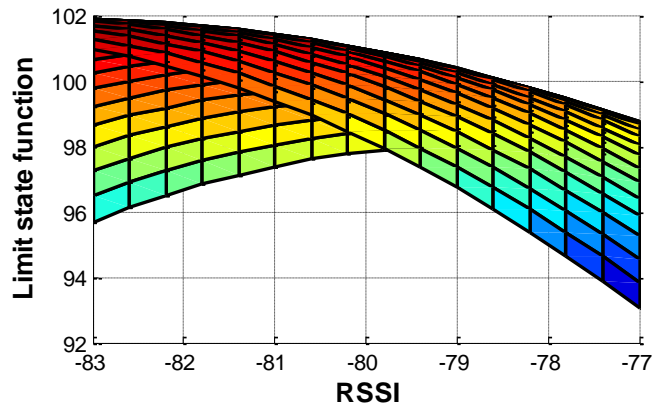
(c) The limit surface projected on the LQI axis.

Figure 86. (cont.)

7.4.2. Full-scale WSS network: The Jindo Bridge

Network Description

The world's largest full-scale WSS networks were deployed on the 2nd Jindo Bridge, Korea using the

Imote2 platform and the ISHMP Services Toolsuite for long-term monitoring of the structure (Rice et

al. 2009; Jo et al. 2011). The bridge is a steel cable stayed bridge, which connects the Jindo Island

and Korean Peninsula (see Figure 87). The fact that the bridge is made of steel, which blocks the

passage of the radio signal, and that the bridge is often subject to high humidity due to frequent fog

and harsh winds, which weakens the signal, interference in the radio communication was expected to be high. Thus, several efforts were made in the design of WSS networks for the Jindo Bridge to enhance the network communication. First, the entire network was decomposed into four subnets with two central base station PCs to reduce the number of nodes in each subnet and the distance between the base station and the respective nodes (Figure 87). The maximum communication distance from a central server to a WSS was no more than 170 m (note that the Imote2 can cover up to 300 m distance at its ideal condition). Second, radio transmission channels were selected that were not in use by other users. Third, two types of antennas are used. Each base station sensors, which all sensor node in each sub-network transfer data packets to, had a 8 dBi antenna (see Figure 88a, PM-0M07 8dB Volcado, Daeheung) whereas, the other sensor nodes deployed on the bridge had 2 dBi (see Figure 88b, PM-DI02A, Daeheung). Among four subnets, a subnet on the bridge deck near Haenam side (shown in a box in Figure 87) is selected in this paper as a benchmark in assessing the reliability of the network.
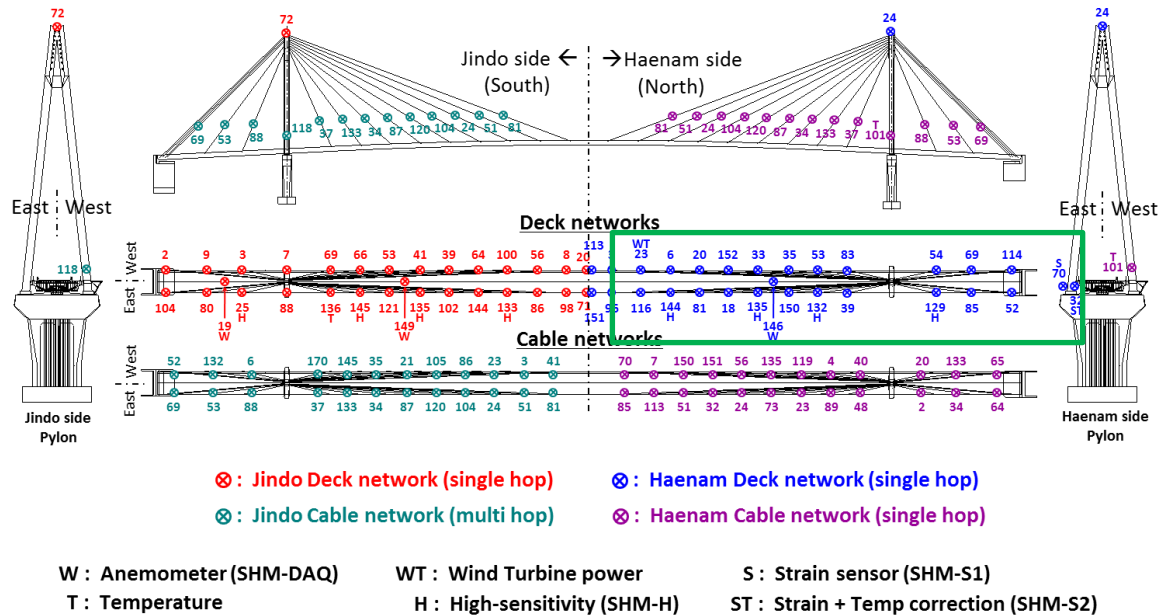
Figure 87. Jindo Bridge WSS networks layout.

168
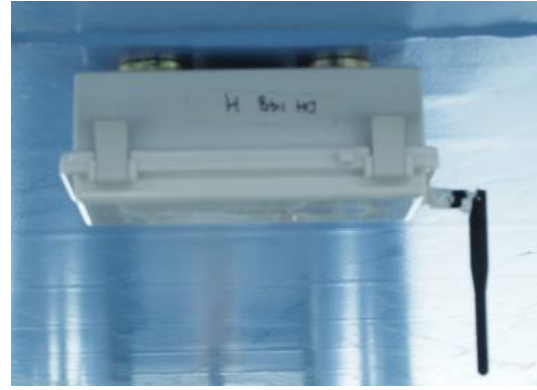
|(a) Base station.|(b) Sensor node.|

Figure 88. Antenna selection.

Performance Evaluation

Application-level reliability model has been applied to full-scale WSS network infrastructure deployed on the Jindo Bridge. Figure 89 shows the distribution of WSSs in the selected subnet. The base station for this subnet was on the pylon pier at Haenam side. As shown in Figure 88a, the base station has an antenna with higher gain than leaf nodes. However, the developed model assesses the network using the communication quality indicators estimated at the leaf node side, which has a lower gain antenna.
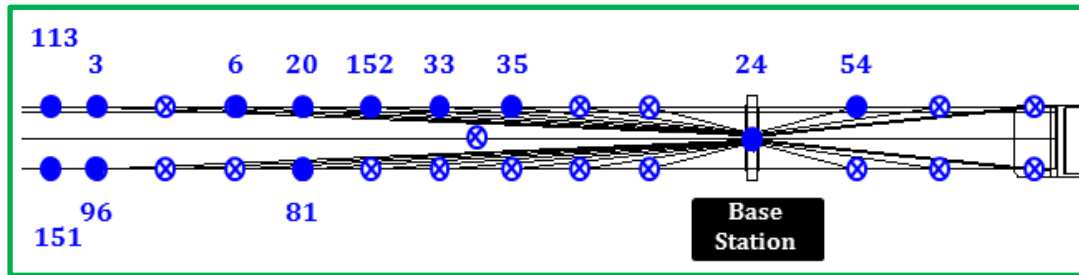
Figure 89. Sensor topology used for WSS networks reliability assessment.

A set of radio test determined the fundamental characteristics of RSSI, LQI and the limit state function. Two random variables are averaged over 100 packets for each radio test and tests were tried over 100 times. Only MCS method using 10^4 numbers of samples is applied for the analyses. Using MCS was beneficial over FORM approximation mainly because (i) sampling a large number of live

data set is inefficient considering the power consumption occurring during the test and (ii) the limit state function may show nonlinearity near the failure points as found in the earlier section. One can assume from the previous results that MCS method gives conservative and accurate results over FORM approximation with this simple model.

Table 11 summarizes the results from MCS method at each WSS in the sub-network. With converging c.o.v., obtained P_E values are very small regardless of the distance from the base station, except for Node Id 3. The sub-network is highly robust and reliable in the application-level. The result indicates that the extra antenna installed at the base station enhanced overall communication-quality of the subnet.

Table 11. MCS results.

Node Id	c.o.v.	P_E	Node Id	c.o.v.	P_E
54	0.0863	0.0013	81	0.0478	0.0043
24	0.0180	0.0298	6	0.0596	0.0028
35	0.0460	0.0047	3	0.0048	0.3059
33	0.0448	0.0050	96	0.0354	0.0001
152	0.0406	0.0060	113	0.0510	0.0010
20	0.0415	0.0058	151	0.0333	0.0001

Further actions can be driven to improve the WSS networks. For example, although P_E at Node Id 3 is still low, the node can be replaced to a nearby location to the base station to maintain

similar degree of P_E over the sub-network. The lower radio power from the leaf node can be selected to reduce the excessive power use. Also, the network design can be optimized to have subnets with larger domain.

7.5. Conclusion and future implication of the network reliability for monitoring railroad bridges

Low-cost and on-board computational capabilities of wireless smart sensors (WSS) have shown potentials of wide applications for monitoring civil infrastructure. However, due to distributed and unreliable nature of WSSs, maintaining highly robust and reliable networks is challenging. Quantitative assessment of WSS network communication quality before and after finalizing a deployment is critical to achieve a successful WSS network for structural health monitoring (SHM) purposes.

This chapter presented model assessed application-level reliability of the WSS network using readily available indicators. Using communication-level measurements from a WSS, First Order Reliability Method (FORM) and Monte Carlo Simulation (MCS) analysis assessed the failure probability (P_E) of the network reliability, which is defined as data transfer failure due to excessive packet loss. The proposed method first determined the distribution types for selected two random variables, radio signal strength indicator and link quality indicator. The reliability of the measurement were enhanced by averaging over a number of data set and performing an extensive number of test sets. Then, packet reception rate was estimated using two random variables and determined the failure state of the data transfer in the limit state function. The error in the regression model has been compensated following the central limit theorem. The proposed approach has been verified under a small-scale temporal WSS network and a full-scale network. In a small-scale test,

both FORM and MCS were applied. Both methods provided quantitative assessments of the WSS network at application-level. However, large differences in P_E were found between FORM and MCS analyses. The main reason for such results was due to the nonlinearity of the limit state function near the failure points, indicating that MCS is a more conservative and accurate tool for solving the proposed model. Thus, MCS has been applied to assess the network reliability of the Jindo Bridge, Korea, which the sensor locations were pre-defined. The strengthened radio power and extra Antenna device on the base station enhanced the communication quality showing fairly low P_E on a subset of the Jindo Bridge. Proposed approach showed an effective way to assess the reliability of WSS networks at application-level. The approach can be also used in designing a long-term deployment to obtain robust WSS networks. Depending on the required degrees of the robustness, not only the distances between sensors but also radio power and antenna devices can be determined. Periodic assessment is also required to understand the quality of sensors, which are easily affected by temporal changes in the environment. Early inspection of WSS network reliability using the proposed approach in this study in a design phase along with a periodic assessment will lead to a successful long-term SHM using WSSs.

The proposed method can be applied to long-term SHM systems for monitoring railroad bridges using WSSs. Constructing a robust network is important in such applications, because the communication may become harsh in the presence of a freight train on the bridge. Therefore, although study presented system reliability to assess the overall quality of the WSS networks, the method can be expanded to include both system and component reliability. For example, system reliability can be first applied in the design phase of the system. To reach the required degrees of the robustness, several decisions such as the distances between sensors, radio power, and antenna devices can be determined. Periodic assessment of the network communication quality will lead to

the sustainable WSS networks. Then, component reliability can be applied to the networks such that each sensor transmits measured data to the gateway and the base station only if the P_E is larger than a certain limit. Sensors with low P_E can timestamps the undelivered data itself and re-transmit afterwards. Therefore, by adopting the proposed approach in sensor networks for monitoring railroad bridges, an optimized sensor topology and data collection strategies can be achieved that will be able to deliver robust and reliable performance.

CHAPTER 8. CONCLUSIONS and FUTURE WORK

8.1.   Conclusions

This research presented modeling and monitoring railroad bridges for understanding salient features of the dynamic responses of the bridge under moving train. To this end, a hybrid model has been developed to capture the bridge dynamics efficiently. Wireless smart sensor (WSS) networks have been deployed on an in-service railroad bridge leveraged updating and calibrating the proposed models. Performance of the hybrid model has been validated with field measurements to prove that the model can effectively simulate dynamic responses of the bridge under arbitrary train loading and speeds. To enhance the usability of WSSs for railroad bridges, application-level reliability analyses of the network have been proposed. In addition, software and hardware designed and produced realized the accurate synchronization of multiple WSS networks. The results of this research overcome issues that have limited understanding railroad bridge dynamics.

A thorough background of existing numerical models and structural health monitoring (SHM) system of railroad bridges has been provided, addressing practical challenges limiting model-based assessments of those bridges. In addition, the current regulations on railroad bridge inspection are presented; these inspections are mostly visual in nature. Previous monitoring systems based on dynamic tests and model calibration have been focused on highway bridge applications, where the mass of the vehicles crossing highway bridges is assumed to be relatively small compared to the mass of the bridge itself; as a result, the vehicles are often treated as random loads on the bridge. SHM systems that have been implemented on railroad bridges are presented as necessary background for the successful framework that has obtained global characteristics of the bridges under ambient vibration.

Studies on numerical models of railroad bridges were subsequently presented. A simple beam model allowed capturing salient features of the bridge responses under a moving train. A hybrid model, which combined the finite element (FE) approach of the bridge and the assumed modes methods of rails, was proposed. Unlike traditional approaches, where contact forces explicitly considered, the proposed approach implicitly included the contact force in the system equations, assuring efficiencies and consistencies in the formulation and computation. The models were able to be employed both for single-track bridges and double-track bridges. The hybrid model was shown to provide a flexible and efficient tool for estimating bridge responses for arbitrary train configurations and speeds.

The proposed model was then validated from measurement data obtained from an in-service railroad bridge. A finite element (FE) model was updated so that the model well represent the bridge. The final model was validated using both global and local bridge responses. Acceleration responses of the bridge validated the global features of the bridge. Measured strain demonstrated that the model also could well capture the local responses at the element level of the truss bridge. The comparison of the dynamic bridge responses obtained from the model to the field measurements highlighted that the model can be used to provide an accurate assessment of the response of the bridge.

Using the calibrate models, further interpretations were made to enhance maintainability of the bridge. First, the hybrid model was used to develop a fatigue map. Results obtained from the dynamic analysis of the model allowed identifying the members with highest strain under revenue train loadings. Then, resonance studies were presented and the performances of hybrid moving mass and load models were compared. The results showed unconservative results from the traditional moving-load model, emphasizing the importance of moving-mass effects. The results of the studies

revealed that the hybrid model is a tool for prediction of bridge responses for arbitrary train configurations and speeds, portending the future potential of monitoring railroad bridges effectively.

The aforementioned results opened questions in utilizing WSSs for capturing the vehicle-track-bridge interaction, which is one of the key issues for characterizing bridge responses under high-speed passenger trains, as well assessing passenger comfort. Some critical challenges of current wireless sensing technologies and solutions for enabling monitoring railroad bridges were identified.

The first component discussed was providing synchronized sensing for multiple networks. In the case of high-speed passenger rails, because the trains run over shared corridors, ensuring ride comforts is critical. To monitor vehicle-track-bridge interaction adequately, both input forces and responses of sub-structure must be measured simultaneously. However, due to geographically distributed and mobile feature of vehicle-track-bridge system, conventional monitoring strategies using wired sensor systems or WSSs have been recognized to be insufficient. As one solution, a scalable protocol that provides effective synchronized sensing among multiple networks has been developed and presented. The protocol used the Pulse-Per-Second signals from low-cost GPS receivers. The method was implemented on the Imote2 sensor platform and achieved the following two main goals; i) periodic clock correction of gateway nodes to compensate nonlinear clock drift, and ii) less than 50 μs synchronized sensing accuracy from leaf nodes in different networks.

Moreover, geographically distributed WSS networks challenge the ability to maintain highly robust and reliable networks. Thus, a model that can assess the application-level reliability of the WSS network using readily available communication-level indicators was proposed. Quantitative assessment of WSS network communication quality before and after finalizing a deployment offers achieving a successful network for monitoring complex civil infrastructure, such as railroad bridges.

In conclusion, this research provided a modeling and monitoring techniques for railroad bridges toward understanding the dynamics responses by identifying gaps in the model-based approach and in the implementation of monitoring systems using WSSs. The results of this research successfully demonstrated the potentials of using wirelessly measured data to perform model development and calibration that led to better understand the dynamic responses of railroad bridges and to provide an effective tool for prediction of bridge response for arbitrary train configurations and speeds.

8.2. Future studies

This section describes suggested future directions and studies to extend the developed framework to be more applicable for monitoring railroad bridges.

8.2.1. Sudden event monitoring of bridges using wireless smart sensors

Bridges form a critical link in the transportation networks, both in the railway and highway systems, with over 691,000 in the USA. inventory, while those are generally susceptible to various types of hazards, e.g. earthquake, hurricanes, impacts, etc. A report from the Federal Highway Administration revealed that over 500 bridges failed in the USA. between 1989 and 2000 (FHWA, 2001). Collisions, along with floods, are the most frequent causes of those collapses; especially, overloaded vehicles and lateral impact forces from truck/ships, and trains form 20% of the total bridge failures. Figure 90 shows an example of a bridge collapse due to a cargo ship collision. Once such collision occurs, accurate and rapid condition assessment, including measure of impact, estimation of potential primary/secondary damage, of those bridges are critical. However, due to unpredictable nature of such events and lack of key technologies, an integrated structural health monitoring system for detecting collision impact has not been developed.

177

Figure 90. A cargo ship collision in 2012, causing Eggner Ferry Bridge, KY, collapse.

Critical issues with current wireless sensing technologies are related to power management during long-term operation and construction of a rapid and reliable wireless communication networks. Thus, hardware and software components for building frameworks for monitoring these relatively common and high-risk events will be developed. For hardware development, a sensor chip with a low-power accelerometer will be selected for developing a sensor board. The sensor should be programmable to meet the following requirements of the sensor (i) user-selectable power management plans; (ii) ability to detect and be triggered by an impact; (ii) capability to read buffer for processing the impact event. A number of software and algorithms will be development as well. The efforts will include, but not limited to proposing (i) a new time synchronization algorithm for rapid data synchronization, (ii) a rapid notification of the events to networks, and (iii) a schedule for immediate sensing to capture the sudden events.

The ultimate objective of the proposed research, therefore, is to establish a monitoring system that can address the gaps in the current technology. Techniques developed are expected to inexpensively and effectively detect, sense, quantify, and report bridge impacts by over-height vehicles (highway traffic collisions).

178

8.2.2. Unattended autonomous monitoring: mobile data collection

A typical WSS network for structural health monitoring consists of a base station PC and a set of wireless sensors. Because WSSs run on battery power, no additional power supply is required. However, the base station PC that retrieves collected data from those nodes requires a power supply. Subsequently, when the supply is not available, establishing the network for long term monitoring becomes challenging.

Therefore, an alternative data collection scheme needs to be developed for wide applicability of SHM system using WSSs. For example, a base station PC mounted on a train can travels along bridges to retrieve already collected data from a sentry node in the bridge network (Figure 91 shows the scheme). To facilitate such a monitoring strategy, two-level of data collection algorithms will be developed. The first level is the data retrieval to the sentry node from sensor nodes in the network; after regularly scheduled sensing is done, each sensor node in the network will transfer data to the sentry node. The sentry node only collects and stores data in consecutive order until the train with the base station reaches the bridge. The second level is the communication for data collection from the sentry node to the moving base station; the base station will travel while sending out strong beacon signals that can be heard by the sentry node. When the signal is received, the sentry node will start sending out collected data to the base station. To facilitate such a monitoring strategy, understanding the radio performance of WSSs under mobile condition is essential.

Realization of the scheme will make obsolete the need to install the base station on the bridge and potentially enable a wide range of applications involving unattended autonomous monitoring of civil infrastructure at reduced cost.
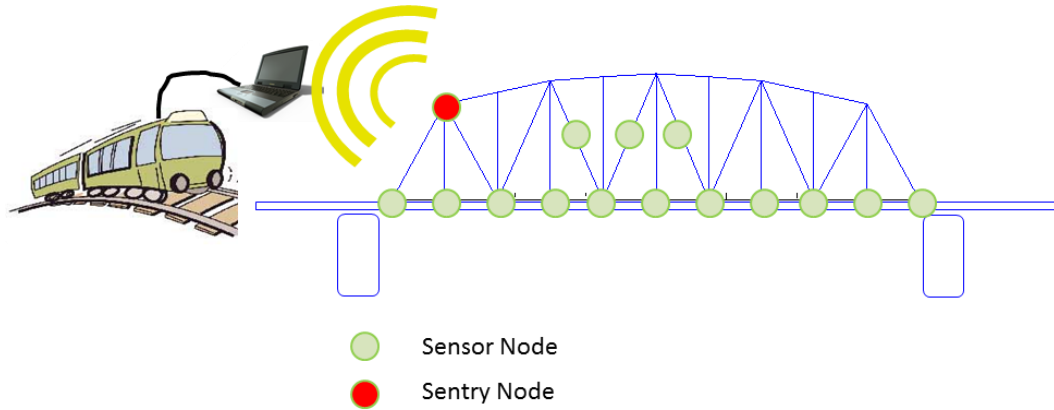
Figure 91. Unattended autonomous monitoring scheme.

8.2.3. Extension of hybrid model to assess derailment of a train

Shared corridors are common in the USA., while vehicles running at high speeds in those tracks raise numerous challenges for railroad bridges. Due to large variances in operation speeds, vehicle weights, etc., degradation of the bridge and track systems in the shared corridors is faster than those used only for high-speed passenger trains. As a consequence, resonance phenomena in the bridge may occur, which can lead to derailment of a train, especially when the conditions of a bridge are unknown. However, because the problem is time dependent and coupled, adequate vehicle-track-bridge-interaction models for studying train derailment has been lacking.

Therefore, continuing efforts on the development of hybrid model, which effectively represented the bridge dynamics considering train mass effects, I plan to expand the model to include a number of degrees of freedom of vehicle. For example, a two-dimensional model shown in Figure 92 considers pitching effect of the vehicle body and elastic and damping effects of the suspension systems. On top of predicting capability of the hybrid model presented in Chapter 5 (i.e., the bridge and rail dynamics), this new model can provide vehicle dynamics such as resonance of vehicle. When the model is expanded for a three-dimensional representation, one can obtain simulation that is

180

more practical. For example, the risk of derailment of a vehicle running over the bridge can be investigated. Therefore, enhanced models will represent the salient features of train and bridge and track dynamic responses considering train mass and dynamic effects.

Through the proposed study, the following outcomes are expected: (i) Effective means for predicting the risk of derailment of a train under arbitrary speeds. (ii) Validate existing regulations on the derailment and design.
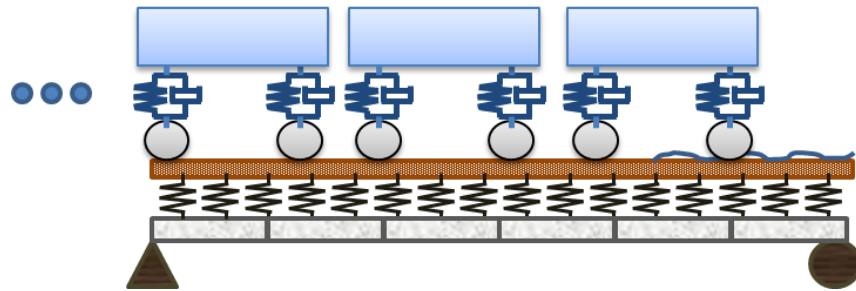
Figure 92. Hybrid model expanded to consider detailed vehicle representation.

REFERENCE

[1]   Abdel-Ghaffar, A.M. and Scanlan, R.H., (1985), "Ambient vibration studies of golden gate bridge: I. suspended structure", Journal of Engineering Mechanics, 111(4), 463-482.

[2]   Adler, R., Flanigan, M., Huang, J., Kling, R., Kushalnagar, N., Nachman, L., et al., (2005), "Intel mote 2: An advanced platform for demanding sensor network applications", Proc. of the 3rd International Conference on Embedded Networked Sensor Systems, 298-298.

[3]   Ahmadi, H.R., and Daneshjoo, F. (2012), "A harmonic vibration, output only and time-frequency representation based method for damage detection in Concrete piers of complex bridges", International Journal of Civil and Structural Engineering, 2(3).

[4]   Alampalli, S., and Lund, R. (2006), "Estimating fatigue life of bridge components using measured strains", Journal of Bridge Engineering, 11(6), 725-736.

[5]   American Short Line and Regional Railroad Association (2003). ???,

[6]   Association of American Railroads (2012), "An Overview of America's Freight Railroads External Link".

[7]   Ayre, R. S. and Jacobsen, L. S. (1950). "Transverse vibration of a two-span beam under the action of a moving alternating force," J. Appl. Mech., 17(3), 283–290.

[8]   Ayre, R. S., Ford, G., and Jacobsen, L. S. (1950). "Transverse vibration of a two-span beam under action of a moving constant force," J. Appl. Mech., 17(1), 1–12.

[9]   Bai, F. & Krishnan, H. (2006), Reliability Analysis of Dsrc Wireless Communication for Vehicle Safety Applications, Intelligent Transportation Systems Conference, 2006. ITSC'06. IEEE, IEEE, pp. 355-362.

[10]   Bandyopadhyay, S. & Coyle, E. J. (2003), An Energy Efficient Hierarchical Clustering Algorithm for Wireless Sensor Networks, INFOCOM 2003. Twenty-Second Annual Joint Conference of the IEEE Computer and Communications. IEEE Societies, IEEE, pp. 1713-1723.

[11]   Benkic, K., Malajner, M., Planinsic, P. & Cucej, Z. (2008), Using Rssi Value for Distance Estimation in Wireless Sensor Networks Based on Zigbee, Systems, Signals and Image Processing, 2008. IWSSIP 2008. 15th International Conference on, IEEE, pp. 303-306.

[12]   Bennett, R., Hayes-Gill, B., Crowe, J. A., Armitage, R., Rodgers, D. and Hendroff, A., (1999), "Wireless Monitoring of Highways, in Smart Systems for Bridges, Structures and Highways", Proc. of the SPIE, Vol. 3671, 173–182.

[13]   Biggs, J. M. (1964). Introduction to Structural Dynamics, McGraw-Hill, New York, N.Y.

[14] Bocca, M., Eriksson, L. M., Mahmood, A., Jäntti, R. & Kullaa, J. (2011), A Synchronized Wireless Sensor Network for Experimental Modal Analysis in Structural Health Monitoring, Computer-Aided Civil and Infrastructure Engineering, 26(7), 483-499.

[15] Brenner, B., Bell, E., Sanayei, M., Pheifer, E., Durack, W., Fay, S., and Thorndike, L. (2010), Structural modeling, instrumentation, and load testing of the Tobin Memorial Bridge in Boston, Massachusetts,Proc., 2010 Structures Congress.

[16] Brincker, R., Zhang, L., and Andersen, P. (2001), "Modal identification of output-only systems using frequency domain decomposition", Smart materials and structures, 10(3), 441.

[17] Brownjohn, J. (2003), "Ambient vibration studies for system identification of tall buildings", Earthquake engineering & structural dynamics, 32(1), 71-95.

[18] Brownjohn, J. M. W., (2007), "Structural health monitoring of civil infrastructure. Philosophical Transactions of the Royal Society A: Mathematical, Physical and Engineering Sciences", 365, 589-622.

[19] Brownjohn, J.M., and Xia, P.-Q. (2000), "Dynamic assessment of curved cable-stayed bridge by model updating", Journal of Structural Engineering, 126(2), 252-260.

[20] Bu, J. Q., Law, S. S., & Zhu, X. Q., (2006), "Innovative bridge condition assessment from dynamic response of a passing vehicle", Journal of engineering mechanics, 132(12), 1372-1379.

[21] Caicedo, J. M., Clayton, E., Dyke, S. J., Abe, M. and Tokyo, J., (2002), "Structural health monitoring for large structures using ambient vibrations", Proc. of the ICANCEER Conference, Hong Kong, August, 15-20.

[22] Cambridge Systematics, Inc. "National Rail Freight Infrastructure Capacity and Investment Study." Cambridge, Massachusetts, September, 2007.

[23] Cardoso, J. B., de Almeida, J. R., Dias, J. M. & Coelho, P. G. (2008), Structural Reliability Analysis Using Monte Carlo Simulation and Neural Networks, Advances in Engineering Software, 39(6), 505-513.

[24] Catbas, F.N., Ciloglu, S.K., Hasancebi, O., Grimmelsman, K., and Aktan, A.E. (2007), "Limitationsin structural identification of large constructed structures", Journal of Structural Engineering,133(8),1051-1066.

[25] Catbas, F.N., Susoy, M., and Frangopol, D.M. (2008), "Structural health monitoring and reliability estimation: Long span truss bridge application with environmental monitoring data", Engineering Structures, 30(9), 2347-2359.

[26]   Celebi, M. and EERI, M., (2006), "Real-time seismic monitoring of the new cape girardeau bridge and preliminary analyses of recorded data: An overview", Earthquake Spectra, 22, 609.

[27]   Chatterjee, P. K. and Datta, T. K. (1995). "Dynamic analysis of arch bridges under travelling loads," Int. J. Solids Struct., 32(11), 1585–1594.

[28]   Chen Y., Q. Wang, M. Chang, and A. Terzis, Ultra-Low Power Time Synchronization Using Passive Radio Receivers, In Proceedings of the Information Processing in Sensor Networks (IPSN), 2011 10th International Conference on 2011. 235-245.

[29]   Cheng, Y. S., F. T. K. Au, and Y. K. Cheung. "Vibration of railway bridges under a moving train by using bridge-track-vehicle element." Engineering Structures 23, no. 12 (2001): 1597-1606.

[30]   Chipcon, A. (2004), Cc2420 2.4 Ghz Ieee 802.15. 4/Zigbee-Ready Rf Transceiver, Chipcon AS, Oslo, Norway, 4.

[31]   Cho S., H. Jo, S. Jang, J. Park, H-J Jung, C-B Yun, B. F. Spencer, Jr., and J-W Seo, Structural Health Monitoring of a Cable-Stayed Bridge Using Wireless Smart Sensor Technology: Data Analyses, Smart Structures and Systems, 6, 5-6 (2010). 461-480.

[32]   Cho, S., Giles, R.K., and Spencer, B.F. (2014), "System identification of a historic swing truss bridge using a wireless sensor network employing orientation correction", Structural Control and Health Monitoring.

[33]   Christians P. P., The dynamic response of horizontally curved bridges subjected to moving loads. Ph.D. thesis presented to Carnegie-Mellon University at Pittsburgh. PA (1967).

[34]   Crossbow Technology Inc. (2009), Imote2 - High-performance Wireless Sensor Network Node, Available   at http://www.xbow.com/Products/Product_pdf_files/Wireless_pdf/Imote2_Datasheet.pdf

[35]   Crossbow Technology, Inc., (2007), "ITS400, Imote2 Basic Sensor Board", San Jose, CA.

[36]   Crossbow, I. (2007), Imote2 Hardware Reference Manual: Revision A.

[37]   Deng, L., and Cai, C. (2009), "Bridge model updating using response surface method and genetic algorithm", Journal of Bridge Engineering, 15(5), 553-564.

[38]   Der Kiureghian, A. & Liu, P.-L. (1986), Structural Reliability under Incomplete Probability Information, Journal of Engineering Mechanics, 112(1), 85-104.

[39]   Der Kiureghian, A. (1996), Structural Reliability Methods for Seismic Safety Assessment: A Review, Engineering Structures, 18(6), 412-424.

[40]   Der Kiureghian, A., Haukaas, T. & Fujimura, K. (2006), Structural Reliability Software at the University of California, Berkeley, structural safety, 28(1), 44-67.

[41] Ditlevsen, O. & Madsen, H. O. (1996), Structural Reliability Methods, Wiley New York.

[42] Downing, S. D., and Socie, D. F. (1982), "Simple rainflow counting algorithms," International Journal of Fatigue, 4(1), 31-40.

[43] Dugush, Y. A. and Eisenberger, M. (2002). "Vibrations of non-uniform continuous beams under moving loads," J. Sound & Vibr., 254(5), 911–926.

[44] Elson J., and K. Römer, Wireless Sensor Networks: A New Regime for Time Synchronization, ACM SIGCOMM Computer Communication Review, 33, 1 (2003). 149-154.

[45] Elson J., L. Girod, and D. Estrin, Fine-Grained Network Time Synchronization Using Reference Broadcasts, ACM SIGOPS Operating Systems Review, 36, SI (2002). 147-163.

[46] Ember, (2008), Boston, MA.

[47] Farrar, C. R., Allen, D. W., Ball, S., Masquelier, M. P. and Park, G., (2005), "Coupling Sensing Hardware with Data Interrogation Software for Structural Health Monitoring", Proc. of the 6th International Symposium on Dynamic Problems of Mechanics (DINAME), Ouro Preto, Brazil, February 29–March 4.

[48] Federal Highway Administration, (1999), "Recording and coding guide for the structure inventory and appraisal of the nation's bridges".

[49] Federal Railroad Administration (2010), National Rail Plan Progress Report.

[50] Federal Railroad Administration, (1992), "Railroad Bridge Safety Survey".

[51] Federal Railroad Administration, (1999), "Interim Statement of Policy on the Safety of Railroad Bridges".

[52] Federal Railroad Administration, (2010), "Bridge Safety Standards; Final Rule".

[53] Felber, A.J. (1993), "Development of a hybrid bridge evaluation system", Ph.D. Dissertation, University of British Columbia.

[54] Fisher, J.W. (1984), "Fatigue and Fracture in Steel Bridges: Case Studies", Wiley. New York.

[55] Foster, W., (1897), "A Treatise on wooden trestle bridges: According to the present practice on American railroads", Wiley, New York.

[56] Foutch, D. A., Tobias, D. and Otter, D. E., (1996), "Analytical investigation of the longitudinal loads in an open-deck through-plate-girder railway bridge", Rep. R-894, Association of American Railroads, Washington, D.C.

[57] Foutch, D. A., Tobias, D., Otter, D. E., LoPresti, J. A. and Uppal, A. S., (1997), "Experimental and analytical investigation of the longitudinal loads in an open-deck plate girder railway bridge", Rep. R-905, Association of American Railroads, Washington, D.C.

[58]   Fujino, Y. (2010), "Flexible smart sensor framework for autonomous structural health monitoring", Smart Structures and Systems, 6(5-6), 423-438.

[59]   Fujino, Y., Murata, M., Okano, S. and Takeguchi, M., (2000), "Monitoring system of the Akashi Kaikyo Bridge and displacement measurement using GPS", Proc. of SPIE, nondestructive evaluation of highways, utilities and pipelines IV, 229–236.

[60]   Gay D., P. Levis, P, D. Culler, and E. Brewer, nesC 1.1 Language Reference Manual. (2003), http://today.cs.berkeley.edu/tos/tinyos-1.x/doc/nesc/ref.pdf.

[61]   Gbadeyan, J. A. and Oni, S. T. (1995). "Dynamic behaviour of beams and rectangular plates under moving loads," J. Sound & Vibr., 182(5), 677–695.

[62]   Giles, R., Kim, R., Sweeney, S., Spencer, B., Bergman, L., Shield, C., and Olson, S. (2014), "Multimetric monitoring of a historic swing bridge", Bridges, 10, 9780784412374.014.

[63]   Giles, R.K., Kim, R., Spencer Jr, B.F., Nathan, M., Newmark, A.M., Bergman, L.A., Shield, C.K., and Sweeney, S.C. (2011), Structural health indices for steel truss bridges Editi,n ed., Springer.

[64]   Giles, R.K., Kim, R., Sweeney, S.C., Spencer Jr., B.F., Bergman, L.A., Shield, C.K. and Olson, S., (2012), "Multimetric Monitoring of a Historic Swing Bridge", Proceedings of the 20th Analysis and Computation Specialty Conference. 2012: 151-162.

[65]   GlobalTop, www.gtop-tech.com, 2010.

[66]   Government Accountability Office (GAO), Railroad Bridges and Tunnels.

[67]   Green, M. F. and Cebon, D., (1997), ''Dynamic interaction between heavy vehicles and highway bridges", Comput. Struct., 62 (2), Pages 253–264.

[68]   Gungor, V. C., Lu, B. & Hancke, G. P. (2010), Opportunities and Challenges of Wireless Sensor Networks in Smart Grid, Industrial Electronics, IEEE Transactions on, 57(10), 3557-3564.

[69]   Hill, J. (2000), A Software Architecture Supporting Networked Sensors, Department of Electrical Engineering and Computer Sciences, University of California.

[70]   Hill, J. L. & Culler, D. E. (2002), Mica: A Wireless Platform for Deeply Embedded Networks, Micro, IEEE, 22(6), 12-24.

[71]   Hill, J., Szewczyk, R., Woo, A., Hollar, S., Culler, D. & Pister, K. (2000), System Architecture Directions for Networked Sensors, ACM SIGOPS operating systems review, ACM, pp. 93-104.

[72]   Hollar, S. E.-A. (2000), Cots Dust.

[73]   Humar, J. L. and Kashif, A. M., (1993), "Dynamic response of bridges under travelling loads", Can. J. Civ. Eng., 20, 287–298.

[74]   Inglis, C. E. (1934). A Mathematical Treatise on Vibration in Railway Bridges, The University Press, Cambridge, England.

[75]   Jackson, Donald C., (1988), "Great American Bridges and Dams". Wiley.

[76]   Jaishi, B., and Ren, W.-X. (2005), "Structural finite element model updating using ambient vibration test results", Journal of Structural Engineering, 131(4), 617-628.

[77]   James III, G.H., Carne, T.G., and Lauffer, J.P. (1993), "The natural excitation technique (NExT) for modal parameter extraction from operating wind turbines", NASA STI/Recon Technical Report N, 93, 28603.

[78]   Jang, S.A., Jo, H., Cho, S., Mechitov, K.A., Rice, J.A., Sim, S.H., Jung, H.J., Yun, C.B., Spencer Jr., B.F. and Agha, G., (2010), "Structural health monitoring of a cable-stayed bridge using smart sensor technology: deployment and evaluation", Smart Structures and Systems, 6(5-6), 439-459.

[79]   Jeffcott, H. H. "VI. On the vibration of beams under the action of moving loads."The London, Edinburgh, and Dublin Philosophical Magazine and Journal of Science 8, no. 48 (1929): 66-97.

[80]   Jo, H., Sim, S.-H., Mechitov, K.A., Kim, R., Li, J., Moinzadeh, P., Spencer Jr, B., Park, J.W., Cho, S., and Jung, H.-J. (2011), Hybrid wireless smart sensor network for full-scale structural health monitoring of a cable-stayed bridge, Proceedings of the SPIE Smart Structures/NDE Conference.

[81]   Jo, H., Sim, S.-H., Nagayama, T., and Spencer Jr, B. (2011), "Development and application of high- sensitivity wireless smart sensors for decentralized stochastic modal identification", Journal of Engineering Mechanics, 138(6), 683-694.

[82]   Jo, Hongki, and B. F. Spencer, (2014), Multi-metric model-based structural health monitoring, Proceedings of the SPIE Smart Structures/NDE Conference.

[83]   Juang, J.-N., and Pappa, R.S. (1985), "An eigensystem realization algorithm for modal parameter identification and model reduction", Journal of guidance, control, and dynamics, 8(5), 620-627.

[84]   Juang, J.-N., and Pappa, R.S. (1986), "Effects of noise on modal parameters identified by the eigensystem realization algorithm", Journal of Guidance, Control, and Dynamics, 9(3), 294-303.

[85]   Kahn, J. M., Katz, R. H. & Pister, K. S. (1999), Next Century Challenges: Mobile Networking for "Smart Dust", Proceedings of the 5th annual ACM/IEEE international conference on Mobile computing and networking, ACM, pp. 271-278.

[86]   Kantwell, Evan N., ed. America's Bridges???. Nova Publishers, 2008.

[87]   Kawatani, M. and Kim, C. W. (2001). "Computer simulation for dynamic wheel loads of heavy vehicles," Struct. Eng. & Mech., 12(4), 409–428.

[88] Kim R., T. Nagayama, H. Jo, and B. F. Spencer, Jr., Preliminary Study of Low-Cost Gps Receivers for Time Synchronization of Wireless Sensors, In Proceedings of the SPIE Smart Structures/NDE 2012, pp. 83451A-83451A-83459.

[89] Kim, J, Lynch, J.P., Lee, J.J. and Gee, C.G., (2011), "Truck-based mobile wireless sensor networks for the experimental observation of vehicle-bridge interaction", Smart Mater. Struct. 20 065009.

[90] Kling, R. M. (2003), Intel Mote: An Enhanced Sensor Network Node, Int'l Workshop on Advanced Sensors, Structural Health Monitoring, and Smart Structures, pp. 12-17.

[91] Kling, R., Adler, R., Huang, J., Hummel, V. and Nachman, L., (2005), "Intel mote-based sensor networks", Structural Control and Health Monitoring, 12, 469-479.

[92] Kou, J. W. and DeWolf, J. T. (1997). "Vibrational behavior of continuous span highway bridge — Influencing variables," J. Struct. Eng., ASCE, 123(3), 333–344.

[93] Kuhn, B., Lukic, M., Nussbaumer, A., Gunther, H.-P., Helmerich, R., Herion, S., Kolstein, M.H., Walbridge, S., Androic, B., Dijkstra, O., and Bucak, O. (2008), "Assessment of Existing Steel Structures: Recommendations for Estimation of Remaining Fatigue Life", Joint Report Prepared under the JRC-ECCS cooperation agreement for the evolution of Eurocode 3 (programme of CEN / TC 250).

[94] Lee, H. P. "Dynamic response of a beam with a moving mass." Journal of sound and vibration 191.2 (1996): 289-294.

[95] Lee, W., Lee, J., Henderson, C., Taylor, H. F., James, R, Lee, C. E., Swenson, V., Atkins, R. A. and Germeiner, W. G., (1999), "Railroad Bridge Instrumentation with Fiber-Optic Sensors", Appl. Opt., 38(7), 1110-1114.

[96] Li J., T. Nagayama, K. A. Mechitov, and B. F. Spencer Jr., Efficient Campaign-Type Structural Health Monitoring Using Wireless Smart Sensors, In Proceedings of the SPIE Smart Structures/NDE 2012, pp. 83450U-83450U-83411.

[97] Lin, C. W., & Yang, Y. B., (2005), "Use of a passing vehicle to scan the fundamental bridge frequencies": An experimental verification. Engineering structures, 27(13), 1865-1878.

[98] Linderman, L. E., Rice, J. A., Barot, S., Spencer, B. F., Jr & Bernhard, J. T. (2010), Characterization of Wireless Smart Sensor Performance, Journal of engineering mechanics, 136(12), 1435-1443.

[99] Lord Rayleigh, The Theory of Sound, vol. 1, The Macmillan Company1877 (reprinted 1945 byDover Publications, New York).

[100] Lou, P., and Q. Y. Zeng. "Formulation of vertical equations of motion of finite element form for vehicle-bridge interaction system." J. Struct. Eng (2004).

[101] Lowan, Arnold N. "LIV. On transverse oscillations of beams under the action of moving variable loads." The London, Edinburgh, and Dublin Philosophical Magazine and Journal of Science 19, no. 127 (1935): 708-715.

[102] Lu, Y., Mao, L., & Woodward, P., (2012), "Frequency characteristics of railway bridge response to moving trains with consideration of train mass", Engineering Structures, 42, 9-22.

[103] Luo, Wenjun, and Songliang Lian. "The Characteristic Analysis of Vibration for Coupling System of High-Speed Train-Ballastless Track-Bridge System." ICTIS 2013@ sImproving Multimodal Transportation Systems-Information, Safety, and Integration. ASCE.

[104] Lynch J. P. , An Overview of Wireless Structural Health Monitoring for Civil Structures, Philosophical Transactions of the Royal Society A: Mathematical, Physical and Engineering Sciences, 365, 1851 (2007). 345-372.

[105] Lynch J. P., K. H. Law, A. S. Kiremidjian, E. Carryer, C. R. Farrar, H. Sohn, D. W. Allen, B. Nadler, and J. R. Wait, Design and Performance Validation of a Wireless Sensing Unit for Structural Monitoring Applications, Structural Engineering and Mechanics, 17, 3-4 (2004). 393-408.

[106] Lynch J. P., Y. Wang, K. H. Law, J. H. Yi, C. G. Lee, and C-B Yun, Validation of a Large-Scale Wireless Structural Monitoring System on the Geumdang Bridge, In the Proceedings of 9th International Conference on Structural Safety and Reliability 2005. 19-23.

[107] Lynch J. P., Y. Wang, K. J. Loh, J-H Yi, and C-B Yun, Performance Monitoring of the Geumdang Bridge Using a Dense Network of High-Resolution Wireless Sensors, Smart Materials and Structures, 15, 6 (2006). 1561.

[108] Lynch, J. P. and Loh, K. J. (2006), A Summary Review of Wireless Sensors and Sensor Networks for Structural Health Monitoring, Shock and Vibration Digest, 38(2), 91-130.

[109] Lynch, J.P., Law, K.H., Kiremidjian, A.S., Kenny, T.W., Carryer, E. and Partridge, A., (2001), "The Design of a Wireless Sensing Unit for Structural Health Monitoring", Proc. of the 3rd International Workshop on Structural Health Monitoring, Stanford, CA, September 12–14.

[110] Mannermaa J., K. Kalliomaki, T. Mansten, and S. Turunen, Timing Performance of Various Gps Receivers, in Frequency and Time Forum, 1999 and the IEEE International Frequency Control Symposium, 1999., In Proceedings of the 1999 Joint Meeting of the European. 287-290.

[111]   Maróti M., B. Kusy, G. Simon, and Á. Lédeczi, The Flooding Time Synchronization Protocol, In Proceedings of the 2nd International Conference on Embedded Networked Sensor Systems 2004. ACM, 39-49.

[112]   Mechitov, K., Kim, W., Agha, G. and Nagayama, T., (2004), "High-Frequency Distributed Sensing for Structure Monitoring", Proc. First Intl. Workshop on Networked Sensing Systems, Tokyo, Japan, 101–105.

[113]   Mee, B., McCown, B., Davids, G.A., Nejikovsky, B., Cotton, K., (1994), "Overview of Railroad Bridges and Assessment of Methods to Monitor Railroad Bridge Integrity", United States Department of Transportation Federal Railroad Administration, DOT/FRA/ORD-94/20, June 23, Final Report.

[114]   MEMSIC, Inc., ISM400, Imote2 Structural Health Monitoring Board, Andover, MA 2010.

[115]   MicroStrain, (2008), Williston, VT, http://www.microstrain.com.

[116]   Mills D. L , Internet Time Synchronization: The Network Time Protocol, Communications, IEEE Transactions on, 39, 10 (1991). 1482-1493.

[117]   Mishra, D., Tutumluer, E., Stark, T.D., Hyslip, J., Chrismer, S. and Tomas, M., (2012), "Investigation Differential Movement at Railroad Bridges through Geotechnical Instrumentation". Journal of Zhejang University-Science A, Vol. 13, No. 11, www.zju.edu.cn/jzus or www.springerlink.com, pp. 814-824.

[118]   Mitchell, K., Rao, V.S. and Pottinger, H.J., (2002), "Lessons Learned About Wireless Technologies for Data Acquisition", Proc. of the SPIE, San Diego, CA.

[119]   Morassi, A., and Tonon, S. (2008), "Dynamic testing for structural identification of a bridge", Journal of bridge engineering, 13(6), 573-585.

[120]   Moreu, F. and LaFave, J.M., (2012), "current research topics: railroad bridges and structural engineering". NSEL Report Series Report No. NSEL-032.

[121]   Morrison, S., and J. Moses. "Benefits and Uses of FE Modeling in Bridge Assessment and Design." Elastic 1 (1993).

[122]   Nagayama, B. F. Spencer, Jr., and Y. Fujino. Synchronized sensing for structural health monitoring using smart sensors, World Forum on Smart Materials and Smart Structures Technology: In Proceedings of SMSST'07, World Forum on Smart Materials and Smart Structures Technology (SMSST'07), 22-27.

[123]   Nagayama, S. H. Sim, Y. Miyamori, and B. F. Spencer Jr., Issues in Structural Health Monitoring Employing Smart Sensors, Smart Structures and Systems, 3, 3 (2007). 299-320.

[124] Nagayama, T. and Spencer, B., F, Jr. (2007), Structural Health Monitoring Using Smart Sensors, Newmark Structural Engineering Laboratory. University of Illinois at Urbana-Champaign.

[125] Nagayama, T., Abe, M., Fujino, Y., and Ikeda, K. (2005), "Structural identification of a nonproportionally damped system and its application to a full-scale suspension bridge", Journal of structural engineering, 131(10), 1536-1545.

[126] Nagayama, T., Ruiz-Sandoval, M., Spencer Jr., B.F., Mechitov, K.M. and Agha, G., (2004), "Wireless Strain Sensor Development for Civil Infrastructure", Proc. of First International Workshop on Networked Sensing Systems, Tokyo, Japan, 97-100.

[127] Nagayama, T., Ushita, M., Fujino, Y., Ieiri, M., and Makihata, N. (2010), The combined use of low-cost smart sensors and high accuracy sensors to apprehend structural dynamic behavior, SPIE Smart Structures and Materials+ Nondestructive Evaluation and Health Monitoring.

[128] Nataf, A. (1962), Détermination Des Distributions De Probabilitiés Dont Les Marges Sont Données, Comptes Rendus de l'Academie des Sciences,, Paris, pp. 42-43.

[129] Ni, Y. Q., Ye, X. W. and Ko, J. M., (2010), "Monitoring-based fatigue reliability assessment of steel bridges: analytical model and application", Journal of Structural Engineering, 136(12), 1563-1573.

[130] Noh K.L, E. Serpedin, and K. Qaraqe, A New Approach for Time Synchronization in Wireless Sensor Networks: Pairwise Broadcast Synchronization, Wireless Communications, IEEE Transactions on, 7, 9 (2008), 3318-3322.

[131] Otter, D. E. and LoPresti, J. A., (1997), "Longitudinal forces in an opendeck steel deck plate-girder bridge", Railw. Track Struct., 935,14–15.

[132] Otter, D. E. and LoPresti, J. A., (1998), "Longitudinal forces in three open-deck bridges", Proc., Annual Conf. American Railway Engineering and Maintenance-of-Way Association, Landover, Md.

[133] Otter, D. E. and LoPresti, J. A., (1999), "Longitudinal forces in a singlespan, ballasted deck, steel-plate-girder bridge", Rep. R-935, Association of American Railroads, Washington, D.C.

[134] Otter, D. E., LoPresti, J. A. and Sweeney, R. A., (2001), "Longitudinal forces in bridges due to heavy haul freight operations", Proc., 7th Int. Heavy Haul Conf., International Heavy Haul Association, Virginia Beach, Va., 565–568.

[135] Pakzad S. N. , G. L. Fenves, S. Kim, and D. E. Culler, Design and Implementation of Scalable Wireless Sensor Network for Structural Monitoring, Journal of Infrastructure Systems, 14, 1 (2008). 89-101.

[136] Pakzad, S.N. and Fenves, G.L., (2004), "Structural Health Monitoring Applications Using MEMS Sensor Networks", Proc. of the 4th International Workshop on Structural Control, Columbia University, New York, 47-56.

[137] Papadimitriou, C., Fritzen, C.P., Kraemer, P., and Ntotsios, E. (2011), "Fatigue predictions in entire body of metallic structures from a limited number of vibration sensors using Kalman filtering", Structural Control and Health Monitoring, 18(5), 554-573.

[138] Pappa, R.S., Elliott, K.B., and Schenk, A. (1993), "Consistent-mode indicator for the eigensystem realization algorithm", Journal of Guidance, Control, and Dynamics, 16(5), 852-858.

[139] Pesterev, A. V., Bergman, L. A., Tan, C. A., Tsao, T. C., and Yang, B. (2003). "On asymptotics of the solution of the moving oscillator problem," J. Sound & Vibr., 260, 519–536.

[140] Pesterev, A. V., Yang, B., Bergman, L. A., and Tan, C. A. (2001). "Response of elastic continuum carrying multiple moving oscillators," J. Eng. Mech., ASCE, 127(3), 260–265.

[141] Pottie, G. J. and Kaiser, W. J., (2000), "Wireless integrated network sensors", Magazine Communications of the ACM CACM Homepage archive, Vol. 43, Issue 5, Pages 51-58.

[142] Rao, G. V. (2000). "Linear dynamics of an elastic beam under moving loads," J. Vibr. & Acous., ASME, 122(7), 281–289.

[143] Rice J. A., and B. F. Spencer Jr., Flexible Smart Sensor Framework for Autonomous Full-Scale Structural Health Monitoring, 2009 Newmark Structural Engineering Laboratory. University of Illinois at Urbana-Champaign.

[144] Rice, J.A. and Spencer Jr., B.F., (2009), "Flexible smart sensor framework for autonomous full-scale structural health monitoring", NSEL Report Series 018, University of Illinois at Urbana-Champaign.

[145] Rice, J.A., and Spencer Jr, B. (2008), Structural health monitoring sensor development for the Imote2 platform, The 15th International Symposium on: Smart Structures and Materials & Nondestructive Evaluation and Health Monitoring.

[146] Rice, J.A., Mechitov, K., Sim, S.-H., Nagayama, T., Jang, S., Kim, R., Spencer Jr, B.F., Agha, G., and and Fujino, Y. (2010). "Flexible Smart Sensor Framework for Autonomous Structural Health Monitoring," Journal of Smart Structures and Systems 6(5-6), pp. 423-438.

[147] Ritter, M.A., (1990), "Timber Bridges: Design, Construction, Inspection and Maintenance", United Stated Department of Agriculture, Forest Service, Washington, DC.

[148] Roche M., Time Synchronization in Wireless Networks, CSE574S: Advanced Topics in Networking: Wireless and Mobile Networking (Spring 2006), Washington University in St. Louis, 23.

[149] Rodrigues, C. ,Cavadas, F., Félix, C. and Figueiras, J., (2012), "FBG based strain monitoring in the rehabilitation of a centenary metallic bridge", Journal of Engineering Structures, Vol. 44, pp. 281-290, doi:10.1016/j.engstruct.2012.05.040.

[150] Rondinone, M., Ansari, J., Riihijärvi, J. & Mähönen, P. (2008), Designing a Reliable and Stable Link Quality Metric for Wireless Sensor Networks, Proceedings of the workshop on Real-world wireless sensor networks, ACM, pp. 6-10.

[151] Rytter, A., (1993), "Vibration based inspection of civil engineering structures", Ph.D. Dissertation, Department of Building Technology and Structural Engineering, Aalborg University, Denmark.

[152] Sazonov E., V. Krishnamurthy, and R. Schilling, Wireless Intelligent Sensor and Actuator Network-a Scalable Platform for Time-Synchronous Applications of Structural Health Monitoring, Structural Health Monitoring, 9, 5 (2010). 465-476.

[153] Sazonov, E., Janoyan, K. & Jha, R. (2004), Wireless Intelligent Sensor Network for Autonomous Structural Health Monitoring, Smart Structures and Materials, International Society for Optics and Photonics, pp. 305-314

[154] Shankar, P. M. (2002), Introduction to Wireless Systems, Wiley New York.

[155] Sim, S. H. and Spencer Jr., B.F., (2009), "Decentralized strategies for monitoring structures using wireless smart sensor networks", NSEL Report Series 019, University of Illinois at Urbana-Champaign.al of Smart Structures and Systems.

[156] Siringoringo, Dionysius M., and Yozo Fujino. "Estimating bridge fundamental frequency from vibration response of instrumented passing vehicle: Analytical and experimental study." Advances in Structural Engineering 15.3 (2012): 417-434.

[157] Soyoz, S. & Feng, M. Q. (2009), Long-Term Monitoring and Identification of Bridge Structural Parameters, Computer-Aided Civil and Infrastructure Engineering, 24(2), 82-92.

[158] Spencer Jr. B.F., Nagayama T., and Rice J. A., Decentralized Structural Health Monitoring Using Smart Sensors, In Proceedings of the The 15th International Symposium on: Smart Structures and Materials & Nondestructive Evaluation and Health Monitoring 2008, pp. 693202-693202-693214.

[159] Spencer Jr., B. F., Nagayama, T., Rice, J. A. and Agha, G. A., (2007), "Smart sensing technology: a new paradigm for structural health monitoring", Proc. 39th Joint Panel Meeting on Wind and Seismic Effects, UJNR, Tsukuba, Japan.

[160] Spencer, B. F., Jr, Ruiz-Sandoval, M. E. & Kurata, N. (2004), Smart Sensing Technology: Opportunities and Challenges, Structural Control and Health Monitoring, 11(4), 349-368.

[161] Sridharan, N. and Mallik, A. K. (1979). "Numerical analysis of vibration of beams subjected to moving loads," J. Sound & Vibr., 65, 147–150.

[162] Stanišić, M. M. and Hardin, J. C. (1969). "On the response of beams to an arbitrary number of concentrated moving masses," J. Franklin Inst., 287, 115–123.

[163] Stokes, G. G. (1849). "Discussion of a differential equation relating to the breaking of railway bridges," Trans. Cambridge Phil. Soc., 8(5), 707–735.

[164] Straser, E. G and Kiremidjian, A. S., (1998), "A modular, wireless damage monitoring system for structures", Report No. 128, John A. Blume Earthquake Engineering Center, Department of Civil and Environmental Engineering, Stanford University, Stanford, CA.
Straub, D. & Der Kiureghian, A. (2010), Bayesian Network Enhanced with Structural Reliability Methods: Methodology, Journal of engineering mechanics, 136(10), 1248-1258.

[165] Su, D., Fujino, Y., Nagayama, T., Hernandez Jr, J.Y., and Seki, M. (2010), "Vibration of reinforced concrete viaducts under high-speed train passage: measurement and prediction including train–viaduct interaction", Structure and Infrastructure Engineering, 6(5), 621-633.

[166] Tan, C. P. and Shore, S. (1968a). "Dynamic response of a horizontally curved bridge," J. Struct. Div., ASCE, 94(3), 761–781.

[167] Tan, C. P. and Shore, S. (1968b). "Response of horizontally curved bridges to moving load." J. Struct. Div., ASCE, 94(9), 2135–2151.

[168] Timoshenko, S. P. "CV. On the forced vibrations of bridges." The London, Edinburgh, and Dublin Philosophical Magazine and Journal of Science 43, no. 257 (1922): 1018-1019.

[169] Tobias, D. H., Foutch, D. A., Lee, K., Otter, D. E. and LoPresti, J. A., (1999), "Experimental and analytical investigation of longitudinal forces in a multi-span railway bridge", Rep. R-927, Association of American Railroads, Washington, D.C.

[170] Unsworth, J.F. (2010), Design of modern steel railway bridges Editioned., CRC Press.

[171] Uppal, A. S., Otter, D. E., Doe, B. E., Foutch, D. A. and Kim, T. W., (2001), "Longitudinal forces in a long railroad trestle", Proc., Annual Conf., American Railway Engineering and Maintenance-of-Way Association, Landover, Md.

[172] Van Damme, S., Boons, B., Vlekken, J., Bentell, J., and Vermeiren, J. (2007), "Dynamic fiber optic strain measurements and aliasing suppression with a PDA-based spectrometer", Measurement Science and Technology, 18(10), 3263.

[173] VibPilot, m+p international, (2010). www.mpihome.com.

[174] Wang Y., J. P. Lynch, and K. H. Law, Wireless Structural Sensors Using Reliable Communication Protocols for Data Acquisition and Interrogation, Ann Arbor, 1001 (2005). 48109.

[175] Wang, T. L., Huang, D. and Shahawy, M., (1992), "Dynamic response of multi-girder bridges", J. Struct. Engrg., ASCE, 118(8),2222-2238.

[176] Wang, Ton-Lo, Vijay K. Garg, and Kuang-Han Chu. "Railway bridge/vehicle interaction studies with new vehicle model." Journal of Structural Engineering117.7 (1991): 2099-2116.

[177] Wang, Y., Lynch, J. P. and Law, K. H., (2005), "Wireless Structural Sensors Using Reliable Communication Protocols for Data Acquisition and Interrogation", Proc. of the 23rd International Modal Analysis Conference (IMAC XXIII), Orlando, FL, January 31– February 3.

[178] Willis, R. (1849). "Appendix to the report of the commissioners appointed to inquire into the application of iron to railway structures," H. M. Stationary Office, London, England.

[179] Windl U. , D. Dalton, H. Packard, and M. Martinec, M, The NTP FAQ and HOWTO Understanding and using the Network Time Protocol, (2006). http://www.ntp.org.

[180] Wong, K.Y., (2004), "Instrumentation and health monitoring of cable-supported bridges", Structural Control and Health Monitoring, 11(2), 91-124.

[181] Wong, K.Y., (2007), "Design of a structural health monitoring system for longspan bridges", Structure and Infrastructure Engineering, 3,169–185.

[182] Wu, J. S. and Dai, C. W. (1987). "Dynamic responses of multispan nonuniform beam due to moving loads," J. Struct. Eng., ASCE, 113(3), 458–474.

[183] Wu, Y. S. and Yang, Y. B. (2003). "Steady-state response and riding comfort of trains moving over a series of simply supported bridges," Eng. Struct., 25(2), 251–265.

[184] Wu, Y. S., Yang, Y. B., and Yau, J. D. (2001). "Three-dimensional analysis of train–rail–bridge interaction problems," Vehicle Syst. Dyn., 36(1), 1–35.

[185] Xu N., S. Rangwala, K. K. Chintalapudi, D. Ganesan, A. B., R. Govindan, and D. Estrin, A Wireless Sensor Network for Structural Monitoring, In proceedings of the 2nd international conference on Embedded networked sensor systems 2004. ACM, pp. 13-24.

[186] Yang, Y. B. and Lin, B. H., (1995), "Vehicle–bridge interaction analysis by dynamic condensation method", J. Struct. Eng., ASCE, 121(11), 1636–1643.

[187] Yang, Y. B. and Yau, J. D. (1997). "Vehicle–bridge interaction element for dynamic analysis," J. Struct. Eng., ASCE, 123(11), 1512–1518 (Errata: 124(4), 479).

[188] Yang, Y. B., Chang, C. H., and Yau, J. D. (1999). "An element for analyzing vehicle–bridge systems considering vehicle's pitching effect," Int. J. Num. Meth. Eng., 46, 1031–1047.

[189] Yang, Y. B., J. D. Yau, and Y. S. Wu. Vehicle-bridge interaction dynamics. World Scientific Publishing Company, 2004.

[190] Yang, Y. B., Liao, S. S., and Lin B. H. (1995). "Impact formulas for vehicles moving over simple and continuous beams," J. Struct. Eng., ASCE, 121(11), 1644–1650.

[191] Yang, Y. B., Lin, C. L., Yau, J. D., and Chang, D. W. (2004). "Mechanism of resonance and cancellation for train-induced vibrations on bridges with elastic bearings," J. Sound & Vibr., 269(1–2), 345–360.

[192] Yang, Y.B. , Lin, C.W., Yau, J.D., (2004), "Extracting bridge frequencies from the dynamic response of a passing vehicle", Journal of Sound and Vibration, 272, pp. 471–493

[193] Yang, Y.B. , Yau, J.D., and Wu, Y.S., (2004), "Vehicle-Bridge Interaction Dynamics - With Applications To High-Speed Railways", WSP.

[194] Yau, J. D., Wu, Y. S. and Yang, Y. B., (2001), "Impact response of bridges with elastic bearings to moving loads", J. Sound and Vibr., 248(1), 9–30.

[195] Zhang, Y., Lie, S. T., & Xiang, Z., (2012), "Damage detection method based on operating deflection shape curvature extracted from dynamic response of a passing vehicle", Mechanical Systems and Signal Processing.

[196] Zhang, Z. C., J. H. Lin, Y. H. Zhang, W. P. Howson, and F. W. Williams. "Non-stationary random vibration analysis of three-dimensional train–bridge systems." Vehicle System Dynamics 48, no. 4 (2010): 457-480.

[197] Zheng, D. Y., Cheung, Y. K., Au, F. T. K., and Cheng, Y. S. (1998). "Vibration of multi-span non-uniform bridges under moving loads by using modified beam vibration functions," J. Sound & Vibr., 212, 455–467.

[198] Zhou, Y.E. (2006), "Assessment of bridge remaining fatigue life through field strain measurement", Journal of Bridge Engineering-ASCE, 11(6), 737-744.

APPENDIX: NOTATION

This appendix lists the variables used in this thesis.

A_b	cross-sectional area of the beam
A_{R_j}	cross-sectional area of the jth rail
a_i	axle distance of ith vehicle on the bridge
$\mathbf{C}_b$	damping matrix of the beam
$\mathbf{C}_B$	damping matrix of the bridge structure
$\mathbf{C}_{R_j}$	damping matrix of the jth rail
c_b	damping of the beam
c_{R_j}	damping of the jth rail
c_s	damping coefficient of ballast
EI_{R_j}	flexural rigidity of the jth rail
EI_b	flexural rigidity of the beam
e, f, r, s, f	vectors of DOFs associated with four stringers nodes
$f_B(t)$	externally applied nodal forces on the bridge
f_1	the first vertical natural frequency of the beam
g	gravity

$\mathbf{H}(k)$	interpolation matrix for bridge element between u_{b_j} and $u_{b_{j+1}}$ evaluated at distant k from u_{b_j}
h	all DOFs of bridge excluding four stringers
$h1 \sim h6$	coefficients in the interpolation matrix $\mathbf{H}(k)$
i	i^{th} vehicle on the bridge
j	j^{th} rail on the bridge
$\mathbf{K}_b$	stiffness matrix of beam
$\mathbf{K}_B$	stiffness matrix of the bridge structure
$\mathbf{K}_{R_j}$	stiffness matrix of the jth rail
k	position of ballast suspension between bridge node u_{b_j} and $u_{b_{j+1}}$
k_s	stiffness of ballast
L	span length of bridge
L_e	length of the bridge element between u_{b_l} and $u_{b_{l+1}}$
$\mathbf{M}_b$	mass matrix of beam
$\mathbf{M}_B$	mass matrix of the bridge structure
$\mathbf{M}_{R_j}$	mass matrix of the jth rail
$M_{V_{j,i}}$	time varying mass matrix caused by rear bogie of the ith vehicle on the rail, on j-th rail at time t
N	total number of stringer nodes (bridge nodes interacting with rail)
$\mathbf{N}_b(x)$	mode shape of the beam

198

$\mathbf{N}_R(x)$	mode shape of the rail
$\mathbf{N}_{R1}(x) \sim \mathbf{N}_{R4}(x)$	mode shape of the rail, R1~ R4 for double-track
N_k	total number of discrete suspension system for ballast between two stringer nodes
N_V	number of vehicles on the bridge at time t
NR	total number of rails in the bridges
P	applied external load of the beam
$\boldsymbol{p}_R, \boldsymbol{p}_{R_j}$	load vector applied on the rail (total and on the jth rail, respectively)
$\boldsymbol{p}(t)$	total applied force vector
$\boldsymbol{p}_s(t)$	applied force on stringers DOFs
$\boldsymbol{p}_h(t)$	applied nodal force excluding DOFs related to stringer nodes
$\mathbf{q}_b(t)$	generalized coordinate of the beam
$\mathbf{q}_{R_j}(t)$	generalized coordinate of the jth rail
r_k	vertical displacement at bridge node k
s	location of the sensor on the beam
t	time
$u(t)$	total displacements considering bridge-track interaction
$u_B(t)$	nodal displacements of bridge element
$u_b(x,t)$	the vertical deflection of beam at x and time t
u_{B_l}	displacement of element l

$u_R(x,t)$	deflection of rail at x and t
V_b	shear force
v_0	vehicle speed
w_k	lateral displacement at bridge node j
x	*beam axis*
$x_{V_{j,i}}$	location of ith vehicle on the jth rail
y_s	displacements of stringers
y_h	nodal displacements excluding DOFs related to stringer nodes
$\Delta\mathbf{M}_R, \Delta\mathbf{M}_{R_j}$	time varying mass term caused by moving point mass (total and on the jth rail, respectively)
δ	Dirac delta
δ_v	the maximum vertical deflection of the beam under P
θ_k	rotation at bridge node k
ρ_{R_j}	mass density of the jth rail
ρ_b	mass density of the beam